Simulation of cavitation and surface erosion on marine propellers

Melissaris, Themistoklis

DOI
10.4233/uuid:68eaa272-e222-4216-aba8-42c86fdf12fb

Publication date
2023

Document Version
Final published version

Citation (APA)
Melissaris, T. (2023). *Simulation of cavitation and surface erosion on marine propellers*. [Dissertation (TU Delft), Delft University of Technology]. https://doi.org/10.4233/uuid:68eaa272-e222-4216-aba8-42c86fdf12fb

Simulation of Cavitation and Surface Erosion on Marine Propellers

SIMULATION OF CAVITATION AND SURFACE EROSION ON MARINE PROPELLERS

Proefschrift

ter verkrijging van de graad van doctor
aan de Technische Universiteit Delft,
op gezag van de Rector Magnificus Prof. dr. ir. T.H.J.J. van der Hagen,
voorzitter van het College voor Promoties,
in het openbaar te verdedigen op donderdag 12 januari 2023 om 15:00 uur

door

Themistoklis MELISSARIS

Master of Naval Architecture and Marine Engineering,
Technische Universiteit Athene, Athene, Griekenland,
geboren te Athene, Griekenland.

Dit proefschrift is goedgekeurd door de

promotor: Prof. dr. ir. T.J.C. van Terwisga
copromotor: Prof. dr. ir. C. Poelma

Samenstelling promotiecommissie:

Rector Magnificus,	voorzitter
Prof. dr. ir. T.J.C. van Terwisga,	Technische Universiteit Delft
Prof. dr. ir. C. Poelma,	Technische Universiteit Delft
Onafhankelijke leden:	
Prof. dr. R. Bensow,	Chalmers Teknika Högskola
Prof. dr. ir. B.J. Boersma,	Technische Universiteit Delft
Prof. dr. J. Carlton,	City University of London
Prof. dr. ir. S. Hickel,	Technische Universiteit Delft
Overige leden:	
Dr. N. Bulten,	Wärtsilä Netherlands BV

This research was funded by the European Union Horizon 2020 Research and Innovation programme, Grant Agreement No. 642536, and by Wä rtsil ä Netherlands BV, R&D Propulsion Technology department.

Keywords: Cavitation Erosion, Propellers, Implosion loads, Surface accumulated energy

Printed by: GILDEPRINT

Front & Back: Cavitating propeller during operation behind a ship hull, showing the vapor volume development and the corresponding estimated erosion risk on the propeller blades.

An electronic version of this dissertation is available at
http://repository.tudelft.nl/.

The only true wisdom is
in knowing you know nothing.

Socrates

To my family

CONTENTS

SUMMARY

Cavitation is the formation of vapor pockets in a liquid due to a pressure drop or an increase in speed. Cavitation nuisance can be disastrous for mechanical components, and therefore needs to be controlled from an early design stage. However, predicting cavitation dynamics using CFD (Computational Fluid Dynamics) and therefore the performance of different designs in cavitating flow, can be very challenging and computationally expensive. In this study, we make an attempt to understand the mechanisms of cavitation erosion and predict the erosion risk on the blades of marine propellers operating in behind condition. Cavitation erosion is a result of extreme pressure loads taking place at the final stage of the collapse, and the prediction of those requires very small scales in time and space. For engineering applications, it is extremely costly to resolve such small scales, and therefore additional modeling is required to reduce the computational cost.

A novel erosion model is applied for the first time on marine propellers. The erosion model follows an energy balance approach to simulate the energy cascade during a cavity collapse. The potential energy initially contained in the cloudy structures that are shed from partial cavities, is proportional to the vapor volume of the structures, and the pressure difference between the driving pressure and the pressure within the cavities. During the collapse, the potential energy is converted into kinetic energy, and slowly focused towards the collapse center. At the final stage of the collapse, the kinetic energy is partially converted into internal, rebound and acoustic energy. For relatively high driving pressures ($\sim$ 1 bar) internal energy can be neglected. Rebound energy is associated with the non-condensable gas content in the cavities, and could be neglected if we do not account for non-condensable gas. Thus, for the cases concerned in this thesis, we can assume that all the kinetic energy before the collapse is converted into shock wave energy and it is radiated to the surrounding liquid.

For the correct implementation of the erosion model special attention should be paid to two main aspects. First, the exact computation of the instantaneous change of potential energy, and afterwards the correct projection of the radiated energy to the surrounding surfaces. The computation of the instantaneous change of potential energy involves the calculation of the material derivative of the vapor volume fraction and the estimation of the pressure field driving the collapse. The material derivative of the vapor volume fraction can be computed either from the velocity divergence or from the source term of the cavitation model. The reconstruction of the velocity divergence introduces significant errors to the eventual change of potential energy, and therefore it is suggested that the cavitation source term is used to compute the change in potential energy. Nevertheless, the cavitation rate can differ depending on the solver and the cavitation model in use, and thus it is recommended to always monitor the reconstructed material derivative of the vapor volume fraction, so that it gives the right amount of potential energy change. The driving pressure field is estimated from the statistical average of the instantaneous pressure in cavitating flow over a certain time sample period.

The correct projection to the adjacent surfaces is associated with the calculation of the solid angle. An approximation of the exact solid angle is used to circumvent the difficulties of the analytical expression of the solid angle. However, for sources very close to the surface, the solid angle approximation may lead to values much higher than the maximum solid angle, and result in significant increase of the surface accumulated energy. Therefore, the approximated solid angle in such cases should always be bounded to the maximum solid angle.

The main contribution of this study is the implementation and improvement of a novel erosion model for the prediction of the surface accumulated energy and the erosion risk on full-scale marine propellers. An accurate estimation of the erosion risk on the surface of a mechanical component requires proper quantitative predictions of the cavitation implosion loads, so that a good distinction of the erosion risk for different designs and different operating conditions can be achieved. An extensive verification and validation study is presented on four test cases, a hydrofoil, a model-scale propeller, a full-scale thruster propeller and a full-scale open propeller behind a Ro-Ro container vessel. Best practice guidelines for the use of the erosion model are developed and it is demonstrated that quantitative predictions of the implosion loads are possible. Predicting the cavitation implosion loads allows for estimation of the erosion risk based on the surface energy distribution. Moreover, a distinction between extreme events and events of lower amplitude is possible by using filters that attenuate the low amplitude events. However, simulating the exact erosion rate requires models involving the material properties and response. In future work, this erosion model could possibly be coupled to fluid structure interaction models able to simulate the material response due to the cavitation implosion loads, and to compute the actual surface erosion rate.

SAMENVATTING

Cavitatie is de vorming van een regio van damp in een vloeistof als gevolg van een druk die lager is dan de dampdruk. Een dergelijk lage druk kan optreden door bijvoorbeeld een lokale drukval of toename in snelheid. Omdat dit fenomeen potentieel zeer schadelijk kan zijn voor mechanische onderdelen dient er al in een vroeg ontwerpstadium rekening mee te worden gehouden. Het voorspellen van het dynamisch gedrag van cavitatie, en de daarbij horende prestaties van verschillende ontwerpen, met behulp van numerieke stromingsleer kan echter erg lastig zijn en veel rekenkracht kosten. In dit onderzoek wordt er getracht om het mechanisme achter cavitatie-erosie te begrijpen en om het risico op erosie aan de bladen van scheepspropellers onder normale vaart te voorspellen. Cavitatie-erosie is het gevolg van extreme drukken die optreden tijdens de laatste fase van het imploderen van een cavitatiebubbel. Het voorspellen van deze drukken en de resulterende krachten vereist zeer kleine tijd- en ruimteschalen wat erg duur is voor het gebruik in alledaags commercieel, technisch werk. Om de kosten te verminderen, dienen er aanvullende modellen ontwikkeld te worden.

Een nieuw erosiemodel wordt voor het eerst toegepast op scheepsschroeven. Dit erosiemodel maakt gebruik van een energiebalans om de cascade van energie gedurende de implosie van een dampholte te kunnen simuleren. De potentiële energie die aanvankelijk opgeslagen zit in wolkencavitatie, welke is ontstaan door het afschudden van delen van vliescavitatie, is proportioneel aan het volume van de dampstructuren en aan het drukverschil tussen de aandrijvende druk en de druk binnen de holtes. Gedurende het krimpen van een holte wordt de potentiële energie omgezet in kinetische energie en langzaam geconcentreerd op het middelpunt van de ineenstorting. Tijdens het laatste moment van het instorten wordt een deel van deze kinetische energie verder omgezet in interne, weerkaatste en akoestische energie. Bij relatief hoge aandrijvende drukken (~ 1 bar) kan de interne energie worden verwaarloosd. De weerkaatste energie is gerelateerd aan het gehalte van niet-condenseerbaar gas in de dampregio en kan worden verwaarloosd wanneer niet-condenseerbaar gas niet wordt meegenomen in het model. Derhalve kan voor de gevallen bestudeerd in dit proefschrift worden aangenomen dat alle kinetische energie wordt omgezet in schokgolfenergie en wordt overgedragen aan de omliggende vloeistof.

Voor een juiste implementatie van het erosiemodel dient er speciale aandacht te worden geschonken aan twee aspecten: een nauwkeurige berekening van de ogenblikkelijke verandering in potentiële energie en een goede projectie van uitgestraalde energie naar de omliggende oppervlakken. Voor het bepalen van de ogenblikkelijke verandering in potentiële energie dient de materiële afgeleide van de dampvolumefractie berekend te worden en het drukveld te worden afgeschat. De materiële afgeleide kan worden berekend middels de divergentie van de snelheid of via de bronterm van het cavitatiemodel. De reconstructie van snelheidsdivergentie resulteert echter in significante afwijkingen in de verandering van potentiële energie. Het gebruik van de bronterm van het cavitatiemodel geniet dan ook de voorkeur bij het berekenen van de verandering in potentiële

energie. Desalniettemin kan de cavitatiesnelheid verschillen afhankelijk van de gebruikte numerieke algoritmes en het cavitatiemodel. Het wordt dan ook aanbevolen om altijd de gereconstrueerde materiële afgeleide van de dampvolumefractie te monitoren om te controleren of de verandering in potentiële energie juist is. Het drukveld dat de implosie aanjaagt kan worden afgeschat op basis van het statistische gemiddelde van de ogenblikkelijke druk in de caviterende stroming gedurende een gespecificeerd tijdsbestek.

De correctie projectie van energie naar de omringende oppervlaktes behelst het berekenen van de solide hoek. Gezien de analytische oplossing voor de solide hoek gepaard gaat met verschillende moeilijkheden, kan een benadering van de exacte solide hoek worden gebruikt. Deze benadering resulteert soms echter in hoeken die veel groter zijn dan de maximale solide hoek en daarmee ook tot significant hogere hoeveelheden opgehoopte energie op het oppervlak. De benaderde solide hoek moet dan ook altijd worden gelimiteerd tot de maximale solide hoek.

De grootste bijdrage van dit onderzoek is de implementatie en verbetering van een nieuw erosiemodel voor het voorspellen van de oppervlakte geaccumuleerde energie en het risico op erosie bij propellers op ware grootte. Een nauwkeurige afschatting van het erosierisico op bladen van verschillende propellerontwerpen bij uiteenlopende condities vereist een kwantitatieve voorspelling van de cavitatie-implosiekrachten. Uitgebreide verificatie- en validatieonderzoeken zijn uitgevoerd voor vier verschillende situaties: een vleugelprofiel, een modelschaal propeller, een roerpropeller op ware grootte en een open propeller gemonteerd op een Ro-Ro containerschip op ware grootte. Daarnaast zijn er richtlijnen opgesteld voor het gebruik van het erosiemodel en is er aangetoond dat het maken van kwantitatieve voorspellingen voor de implosiekrachten mogelijk is. In de toekomst kan het erosiemodel mogelijk worden gekoppeld met vloeistof-structuurinteractie modellen om het gedrag van het materiaal als gevolg van de cavitatie-implosiekrachten te voorspellen.

1

INTRODUCTION

1.1. PROPELLER CAVITATION

Cavitation involves the development of vapor structures in a liquid flow due to local acceleration and consequent pressure drop below a critical value, usually close to vapor pressure. Figure 1.1 shows the phase diagram of water. Phase change can occur either at constant pressure, with an increase in temperature (e.g. boiling) or at (almost) constant temperature, with a decrease in pressure (e.g. cavitation). Cavitation is not a major problem by itself, but the collapse of the developed vapor structures, when transported by the main flow to pressure recovery regions, leads to pressure wave emissions of high amplitude and very short duration. The emitted pressure waves interact with neighboring solid walls, and the resulting impulsive loads often lead to vibrations (typically caused by cavity dynamics and not necessarily by implosions) and erosion damage of mechanical components, for instance, hydro pumps and turbines, fuel injectors, impellers, ship propellers and rudders. Cavitation erosion, when experienced, normally leads to significant repair and maintenance costs, safety issues or component replacement.

In the maritime industry, propeller cavitation is basically unavoidable, as in practice, efficient designs cavitate. Cavitation can be avoided, but this comes at the cost of efficiency or extra capital investments. A propeller without cavitation on the blades during operation is often regarded as a sub-optimal design, unless a cavitation free design is the target. On the other hand, extensive cavitation on the blades may result in unwanted phenomena, e.g., propeller noise, hull vibrations, thrust breakdown, and severe surface erosion. Most often, the fuel efficiency of the propulsion systems is sub-optimal, because countermeasures needed to prevent cavitation nuisance. Cavitation nuisance and efficiency, show typically opposite trends in efficiency. Hence, it is crucial to understand when cavitation becomes harmful in operation, and to find the balance between the propeller efficiency and cavitation nuisance. To this end, cavitation noise and erosion prediction at an early stage of the design phase becomes more and more critical.

The growing importance of fuel efficiency of ships and their propulsion units (e.g., Energy Efficiency Design Index-EEDI) impose another challenge on propeller designs.

1

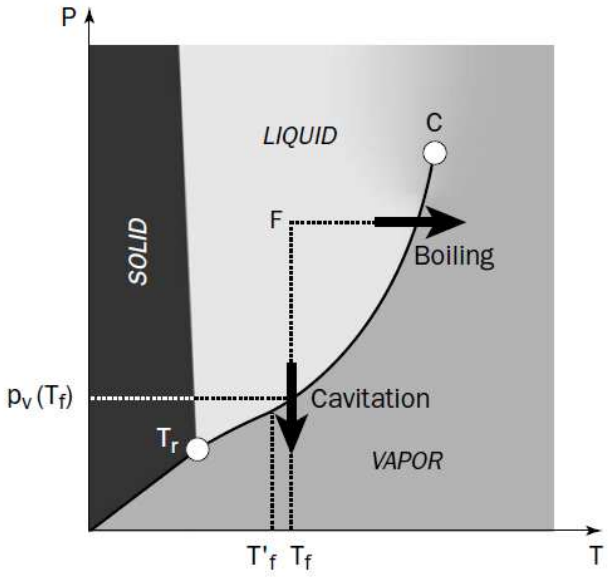

Figure 1.1: Phase Diagram of Water [1]

The trend to increase the energy efficiency of ships stimulates continuous innovation and technological development of all the components influencing the fuel efficiency of a ship from its design phase. Propulsion units are one of the main contributors to fuel efficiency, and thus the importance of efficient propeller designs is increasing. Consequently, there is a clear need for designs which are stretched to the limits. This means reducing the safety margin against unwanted cavitation phenomena as much as possible, in favor of higher propulsive and fuel efficiency. As illustrated in Figure 1.2, propeller performance is strongly influenced by an increase of cavitation dynamics. In the design process of a propeller, a trade-off has to be made between the propulsive efficiency on the one hand and cavitation behavior on the other. If cavitation erosion on the blades can be predicted with higher accuracy than the safety margin, then the safety margin can be reduced from point A to point A', with a consequent efficiency gain. In an ideal situation, where the accuracy of prediction is maximum, and the safety margin is minimum, the optimal performance can be achieved, in terms of cavitation dynamics.

Propeller cavitation has been a major challenge in engineering for many years. The history of cavitation began already a couple of centuries ago, when Euler, in the mid-eighteenth century, discussed the possibility of a phenomenon which influenced the performance of water wheel. The first to introduce the phenomenon as it is known today was Reynolds in 1850's, by discussing the effect it had on the performance of a screw propelled steamer [2, 3]. However, the first observer of cavitation in real operating conditions was Parsons, whose ship, Turbinia, suffered from severe thrust breakdown due to cavitation [4]. Since then, plenty of knowledge has been gained on cavitation dynamics on propellers; however the underlying physics behind the mechanisms of cavitation

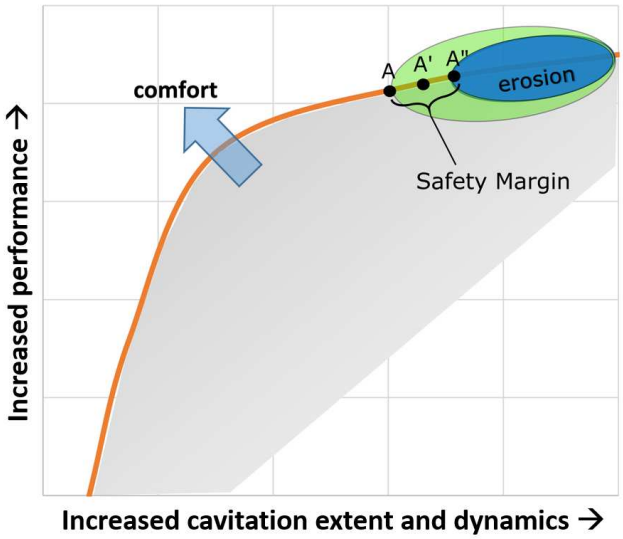

Figure 1.2: Trade-off of main targets in propeller design process

erosion due to the implosion of cavitating structures in the vicinity of the propeller surface, remain yet unclear. And even though cavitation dynamics and cavitation behavior on marine propellers have been extensively investigated, for more than a century experimentally [5], and over 20 years numerically, cavitation erosion prediction is still a major challenge. Despite the long-lasting problems associated with cavitation erosion, computational models that could simulate cavitation and identify locations of erosion have still not been thoroughly developed due to lack of physical understanding.

Nowadays, model scale observations of the propeller performance in a depressurized towing tank is the most conventional way to get an estimation of the erosion risk on the propeller blades. In specific cases (on the ship owner's demand), experimental paint tests are conducted, in order to get a qualitative prediction of the high erosion risk areas on the blade. However, the results of such tests can be very sensitive to the selection of the paint coating, and their repeatability is often questionable. On the other hand, numerical simulations can provide more information on the erosive potential of cavitating structures, offering the possibility of a quantitative analysis, at a much lower cost. For instance, the exact amount of vapor volume on the blades can be quantified, as well as the whole pressure field around the propeller. This kind of information is essential for the estimation of cavitation impact loads on the surface, and getting that information is rather difficult during a model test. Besides, with Computational Fluid Dynamics (CFD) several propeller designs can be assessed much faster, and even simultaneously, something that would be rather impractical and prohibitively expensive to do in a towing tank. Thus, the evaluation of different designs requires numerical tools and methods, capable of providing accurate and reliable prediction of cavitation impact loads, within a reasonable amount of time, to secure the selection of the best design.

However promising, currently, the assessment of cavitation erosion risk from numer-

ical flow simulations is still a major challenge. Despite many previous efforts to characterize and simulate cavitation erosion, it still remains a fluid dynamics problem, that we only recently started to understand, due to the multi-scale character of the complex physical phenomena that govern it. While the size of the cavitating structures developed on a Full-scale propeller blade are in the order of cm, the erosive potential of the consequent impact loads strongly depends on flow phenomena acting on extremely small scales in space and time. Considering the current computational resources, trying to resolve the cavity dynamics on a micro-scale would require extremely high resolution in space and in time, and thus high computational effort. Hence, predicting cavitation erosion on a Full-scale propeller in the design phase requires a method which can be applied on a macroscopic scale, thereby considering the dynamics of especially the large scale cavitating structures.

1.2. ENERGY BALANCE IN CAVITATION EROSION

Cavitation erosion is a challenging issue, because it involves the interaction between fluid dynamics and solid mechanics. Predicting the actual cavitation erosion damage, and the instantaneous surface erosion rate, requires models that can reliably predict the impact loads coming from the fluid side, and the material response, as well as the interaction between them. However, it is wise to isolate the problems before we start looking at the interaction between the fluid and the structure.

The notion that the aggressiveness of cavitation could be assessed through a consideration of energy conversion was already acknowledged by Hammit [6]. Thus, in order to investigate the erosive potential of large scale cavitating structures, and to characterize the intensity of the emitted pressure waves, we should focus on the overall energy balance. It is, thereby, crucial to determine how the energy is transferred between the collapsing structure and the generated pressure waves. Assuming a spherical bubble of a certain size, its energy content is proportional to its volume and the pressure difference between the ambient pressure and the pressure within the bubble. When the ambient pressure is higher than the vapor pressure inside the bubble, the bubble will start to condense, and the potential energy will gradually convert into kinetic energy. At the final stage of the collapse, where all the potential energy has been converted to kinetic energy, Tinguely *et al.* [7] have shown that the kinetic energy is eventually partitioned into shock wave energy E_{SW}, dissipative thermal energy ΔU and rebound energy E_{reb}, such that

$$E_0 = E_{SW} + \Delta U + E_{reb} \tag{1.1}$$

In case of a structure collapsing close to a solid wall, a microjet is formed, and thus, a part of the initial potential energy will go into the formation of a microjet. Then, the energy partition becomes

$$E_0 = E_{SW} + \Delta U + E_{reb} + E_{jet} \tag{1.2}$$

The dissipative thermal energy ΔU has been shown to be negligible [7]. The rebound energy depends strongly on the amount of non-condensable gas, contained initially in the bubble, and the pressure driving the collapse. It becomes relevant only for low ambient pressures, significantly lower than $1 bar$. Furthermore, in order to estimate the part of the

energy absorbed by the microjet formation, we need to resolve each individual bubble close to the surface, which requires very high spatial and temporal resolution. Eventually, when an attempt is made to assess the energy transfer to the surface, all the above need to be taken into consideration.

Unfortunately, none of the developed methods for predicting cavitation impact loads found in the literature can ensure that the overall energy balance is satisfied. Fortes-Patella and Reboud [8] were one of the firsts to introduce the energy balance approach for cavitation erosion prediction. Many studies have been based on this approach. Leclercq *et al.* [9], for instance, incorporated the energy balance of the cavity collapse into a cavitation erosion model to compute the local impact power caused by imploding cavities. Even though it has been shown that the overall energy is conserved at the end of a cavity collapse, the cavitation intensity approach still cannot reflect the spatial and temporal focusing of the potential cavity energy, as described by Tinguely *et al.* [7].

Other erosion models focus mainly on the collapse of individual bubbles. For example, the erosion model by Dular and Coutier-Delgosha [10] is based on the microjet formation. It considers only individual bubbles collapsing near a wall. Apart from the high resolution, which is required to resolve every single bubble, this model does not account for the overall energy balance either. Only the energy for the microjet formation is considered from the initial potential energy, while any impact from shock waves emitted from the eventual collapse of the bubbles is neglected.

The capabilities and the accuracy provided by the cavitating flow solver should also be taken into account in the design of erosion models. For industrial applications, pressure based solvers are mostly used. The reason for that is mainly their robustness and the rather low computational cost, especially for incompressible flow regimes. Cavitating flows are modeled, then, by using mass transfer source terms, where compressibility is mimicked only in regions where phase transition occurs, while the pure phases are considered incompressible. Schenke and van Terwisga [11] have demonstrated the limitations of such solvers on predicting cavitating flows. Local peak pressures are strongly dependent on both resolution (spatial and temporal) and mass transfer magnitude, and are not reliably predicted. Thereby, erosion models that require a reliable prediction of the maximum pressure are not applicable, even though they might be energy conservative. A good example is the "collapse detector" by Mihatsch *et al.* [12], which was developed for a high fidelity fully compressible density based solver. However, even a density based solver requires extremely high spacial and temporal resolution, in order to get a grid independent solution, for a fixed acoustic Courant number.

Finally, even though quite a few attempts to predict the erosion risk on propeller blades are reported, all of them are just an implementation of existing models, while none of them has proven to be energy conservative. This inevitably leads us to seek for a cavitation erosion model which can be applied on an Unsteady Reynolds Averaged Navier-Stokes (URANS) pressure based solver, is energy conservative and reflects the spatial and temporal focusing of the initial potential cavity energy.

1.3. AIM OF THE THESIS

The aim of this thesis is to investigate the possibility to estimate the cavitation erosion risk on the blades of marine propellers, using the URANS equations when the propeller is op-

erating behind the ship (behind condition). It would be of great significance to develop an erosion model which is based on the correct overall energy balance during a cavity collapse and which can reliably estimate the cavitation impact loads on the propeller surface, within a reasonable amount of time. Such a method could be integrated into the design process and could help to push propeller designs to the limits, and increase their total efficiency.

To reach this goal of erosion risk prediction, a novel method to estimate the cavitation impact loads on a surface is presented, which has been developed within the European project "CaFE", by Schenke *et al.* [13]. The model is based on a time accurate energy balance during a cavity collapse. It allows for the conversion of the initial potential energy, contained in a vapor structure, to local surface impact power. As a vapor structure (or a cloud of structures) collapses, the potential energy is continuously stored as kinetic energy at the interface, and it is getting focused towards the collapse center. At the final stage of the collapse, the kinetic energy is eventually converted into shock wave energy and radiated to the surroundings. The main advantage of this method is that the total energy is conserved and the time accurate energy balance is satisfied, giving a more physical representation of collapsing cavitating structures, without the need to handle the increased difficulty with multiple scales when going to full scale.

One of the main challenges is to implement the model in such a way that the overall energy balance is satisfied, and the total energy is conserved. This can be done by eliminating all the modeling and numerical errors involved in the reconstruction of the radiated energy, and its projection to the surrounding surfaces. Close attention will be paid to the different error sources, in order to make sure that our method remains energy conservative, also numerically. The next challenge is to implement the erosion model successfully on propeller test cases. To increase the confidence, we validate the method against both model and full scale propeller designs. Therefore, the simulated cavitation erosion risk can be compared to experimental paint tests, and real propeller damage. Finally, we focus on how to interpret the surface accumulated energy into cavitation erosion risk, and how to differentiate between extreme events and repetitive loads of lower amplitude.

All in all, the main goal of this thesis is to demonstrate the potential of our fully conservative method, for practical use, to predict cavitation impact loads on the propeller blades, in behind condition, already in an early design phase.

1.4. OUTLINE

In Chapter 2, the physical mechanisms responsible for cavitation erosion are presented. An attempt for separation of scales in cavitating flows from a physical and a numerical point of view is made to understand the different modeling approaches and how to estimate the erosion potential of larger cavitating structures. The energy balance during the cavity collapse is illustrated, as well as the key components for an accurate prediction of the cavitation implosion loads and the eventual energy impact distribution on the solid surface.

Chapter 3 includes a review of the current cavitation erosion models/approaches. Three erosion models from the literature are thoroughly examined, in view of their reliability and applicability to a multiphase URANS solver. We conclude that the energy

balance approach, where it is assumed that the potential energy contained in a vapor structure is proportional to the volume of the structure, and the pressure difference between the surrounding pressure and the pressure within the structure, provides the best framework for erosion risk assessment. Based on this framework, a validation and verification study is conducted on the ability of a URANS solver, to predict the developed cavity structures around the Delft Twist 11 hydrofoil, and the consequent energy transfer to the surface. The results are compared with experimental observations and paint tests.

In chapter 4, the accuracy of a URANS solver to estimate cavitation impact loads on a propeller surface, is investigated. The novel approach by Schenke *et al.* [13] is employed, where we account for the focusing of the potential energy into the collapse center before it is converted into shock wave energy. The local surface impact power is estimated following different considerations for the vapor volume destruction rate. We first simulate a single cavitating bubble collapsing in an infinite liquid and near a wall, where we verify that when the vapor volume destruction is estimated using the mass transfer source term, then all the energy is conserved and the total energy balance is satisfied. The model is further applied on a model propeller test case. The obtained impact distribution agrees well with the experimental paint test results, illustrating the potential for practical use of our fully conservative method to predict cavitation impact loads on the propeller blades.

In Chapter 5, the erosion model is applied on a full-scale thruster propeller, which is responsible for the main propulsion of a tug boat. Three designs of this vessel suffered from pressure side cavitation erosion. The capability of the erosion model to distinguish different cavitation aggressiveness levels and compute the magnitude of implosion loads at different conditions and different designs is demonstrated. The specific energy distribution shows the total impacted area on the blades, and pinpoints the areas with the highest energy density (and possibly the highest erosion risk). The importance of the solid angle calculation for computing the right fraction of radiated energy that is projected to the surface, especially for sources very close to the wall, is also discussed in this chapter.

Finally, in Chapter 6, the erosion model is applied on a full scale propeller operating in behind condition. Two propeller designs, fitted in a Ro-RO container vessel, suffered from pressure side cavitation erosion. Erosion indicators are used to identify the extreme loads on the propeller blades and differentiate the risk from repetitive events of lower magnitude.

REFERENCES

[1] J. P. Franc and J. M. Michel, *Fundamentals of Cavitation* (Kluwer Academic Publishers, Dordrecht, 2004).

[2] O. Reynolds, *The causes of the racing of the engines of screw steamers investigated theoretically and by experiment,* Trans. Inst. Naval Arch. **14**, 56 (1873).

[3] O. Reynolds, *On the internal cohesion of liquids and the suspension of a column of mercury to a height of more than double that of the barometer,* Mem. Manchester Lit. Phil. Soc. **7**, 3rd Series, 1 (1882).

[4] C. Parsons, *The steam turbine on land and at sea,* Lecture to the Royal Institution, London (1906).

[5] E. A. Weitendorf, *On the history of propeller cavitation and cavitation tunnels,* in *Proceedings of the* 4^{th} *International Symposium on Cavitation* (California Institute of Technology, Pasadena, USA, 2001).

[6] F. G. Hammit, *Observations on cavitation damage in a flowing system,* J. Basic Eng **85**, 347 (1963).

[7] M. Tinguely, D. Obreschkow, P. Kobel, N. Dorsaz, A. de Bosset, and M. Farhat, *Energy partition at the collapse of spherical cavitation bubbles,* Phys. Rev. E **86** (2013).

[8] R. Fortes-Patella and J. L. Reboud, *A new approach to evaluate the cavitation erosion power,* Journal of Fluids Engineering **120**, 335 (1998).

[9] C. Leclercq, A. Archer, R. Fortes-Patella, and F. R. F. Cerru, *Numerical cavitation intensity on a hydrofoil for 3d homogeneous unsteady viscous flows,* Int. J. Fluid Mach. Syst. **10**, 254 (2017).

[10] M. Dular and O. Coutier-Delgosha, *Numerical modelling of cavitation erosion,* Int. J. Numer. Meth. Fluids **61**, 1388 (2009).

[11] S. Schenke and T. J. C. van Terwisga, *An energy conservative method to predict the erosive aggressiveness of collapsing cavitating structures and cavitating flows from numerical simulations,* Journal of Multiphase Flow **111**, 200 (2019).

[12] M. S. Mihatsch, S. J. Schmidt, M. Thalhamer, and N. A. Adams, *Numerical prediction of erosive collapse events in unsteady compressible cavitating flows,* in *Proceedings of IV International Conference on Computational Methods in Marine Engineering* (Lisbon, Portugal, 2011).

[13] S. Schenke, T. Melissaris, and T. J. C. van Terwisga, *On the relevance of kinematics for cavitation implosion loads,* Phys. Fluids **31**, 052102 (2019).

2

PHYSICAL MECHANISMS OF CAVITATION EROSION

In this chapter we discuss the physical mechanisms responsible for cavitation erosion from the hydrodynamic side. The material response is not within the scope of this study. The energy balance of a collapsing cavity is presented, from the initial potential energy to the accumulated surface energy after the collapse. We discuss the separation of scales, where we mainly focus on the large scale dynamics and how they contribute to surface erosion in comparison to the micro scale dynamics of isolated cavities collapsing close to the surface. Furthermore, we elaborate on the effect of the pressure driving the collapse and its role on the surface impact power. Finally, we demonstrate a novel erosion model together with the advantages and limitations of predicting the implosion loads from the collapse of cavitating structures with a URANS solver.

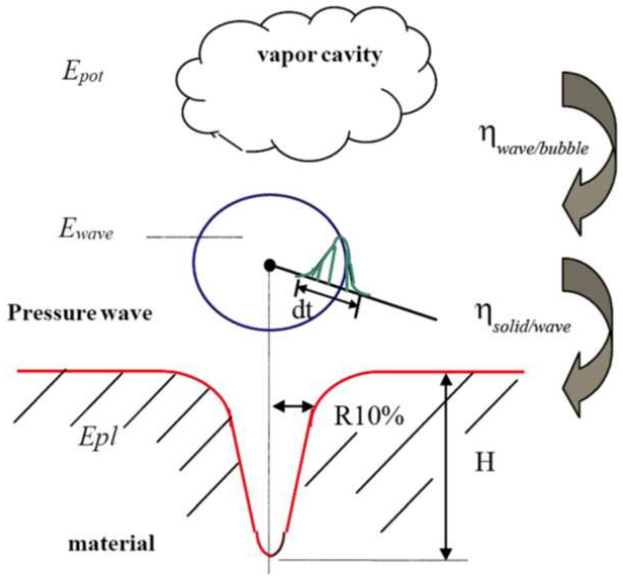

Figure 2.1: Shock wave mechanism shown by the collapse of a cloudy structure at some distance away from the surface [1].

Two main mechanisms are generally held responsible for cavitation erosion and material damage. The first and more common mechanism is the so-called "shock wave" mechanism. Pressure waves of short period and high amplitude are emitted from the collapse of cloudy cavity structures when they enter a high pressure region (see Fig. 2.1 [1]). The produced "shock wave" after the collapse, travels towards the surrounding surface, and the implosion loads depend strongly on the orientation and the distance from the collapse center [2].

Cloudy structures are usually the consequence of partial cavities, which under certain conditions (angle of attack and cavitation number) can experience a strong dynamic behavior. Looking at the flow around a hydrofoil or a section of a propeller blade, at a certain angle of attack and flow speed, the flow on the suction side, close to the leading edge, will accelerate such that the pressure drops below the vapor pressure. Thus, a partial sheet cavity is formed (See Fig. 2.2), which can be either relatively stable or oscillate in length, and periodically shed clouds of smaller vapor structures [3].

As the cavity grows, the minimum pressure occurs within the cavity itself, and the curvature of the surrounding flow tends to direct the streamlines towards the cavity. Thus, usually the cavity reattaches to the solid wall, resulting in a stagnation point at the trailing edge of the cavity. This stagnation point leads to a re-entrant jet which travels upstream, carrying liquid within the cavity, which is responsible for the break-up and the shedding of the partial cavity into smaller vapor structures (See Fig. 2.3). When those structures reach a region of increased pressure, they collapse violently producing a shock wave, that is emitted into the domain.

The re-entrant jet mechanism is the most common mechanism responsible for the

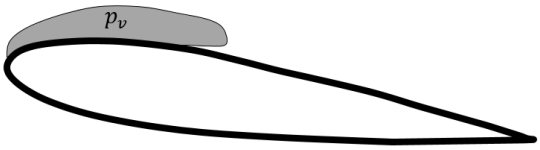

Figure 2.2: Partial cavity formed at the leading edge of a hydrofoil

dynamic behavior of partial cavities, however, it is not the only one. Ganesh [4] recently demonstrated that another mechanism can lead to shedding of partial cavities, the "bubbly shock mechanism". In this particular case, the collapse-induced pressure waves from previously shed clouds are responsible for the shedding of new clouds from the partial cavity. This mechanism usually starts to play a role at low cavitation numbers and high vapor volume fractions within the cavity [5]. The "bubbly shock mechanism" is characterized by a propagating discontinuity. A void fraction front is present that spans along the complete cavity height and propagates upstream due to the shock wave induced by the collapse of the downstream cloudy structures. When the void front reaches the leading edge, the attached cavity separates and a new cycle occurs. Consequently, the partial cavity dynamics in the bubbly shock regime are shock-wave driven, whereas in the re-entrant jet regime they are inertia driven. From experimental observations in an axisymmetric converging diverging nozzle, it was shown by Jahangir [6] that for a cavitation number $\sigma > 0.95$ the cavity shedding was caused by the re-entrant jet mechanism, while for $\sigma < 0.75$ the bubbly shock mechanism was responsible for the periodic shedding. Both mechanism were observed in the transition region, $0.75 < \sigma < 0.95$.

The second mechanism responsible for cavitation erosion is the liquid-jet mechanism. When a vapor structure is collapsing close to a wall, the driving pressure field is a-symmetric, resulting in a high speed liquid-jet formation on the vapor surface away from the wall. The liquid jet is directed towards the surface, and its velocity can be up to 1000 m/s or even higher in a few cases. At the moment of the jet incidence, a short high amplitude water hammer shock occurs, followed by a stagnation pressure of lower magnitude. Fig. 2.4 shows the liquid jet formation for a single bubble collapsing close to a solid boundary.

One of the long lasting debates for the last few decades concerns the question which of the two erosion mechanisms is mainly responsible for the material damage on components that suffer from cavitation. Research on cloud cavitation and bubble dynamics has shown that both mechanisms are able to generate implosion loads high enough to cause erosion on material surfaces. However, it remained unclear whether one of the two is always more dominant or material damage is a combination of both mechanisms. Recently, Joshi *et al.* [7] have shed some light on the potential plastic deformation of each mechanism. They used a SPH (Smooth Particle Hydrodynamics) axisymmetric solver to simulate the collapse of a single cavitation bubble close to an elastic-plastic material, and they

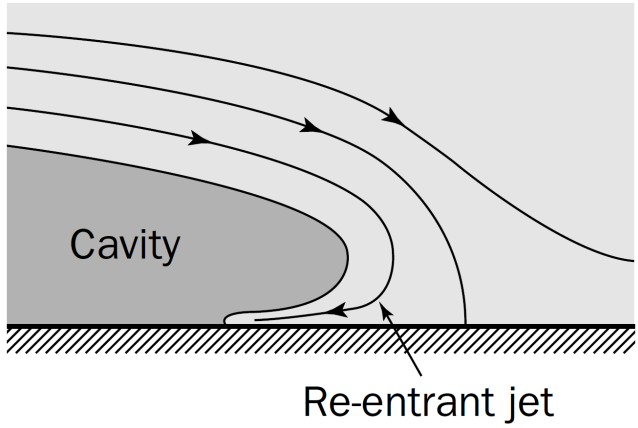

Figure 2.3: Re-entrant jet mechanism, showing the surrounding flow streamlines that are directed towards the cavity, causing a stagnation point at the cavity closure which leads to the formation of the re-entrant jet [3].

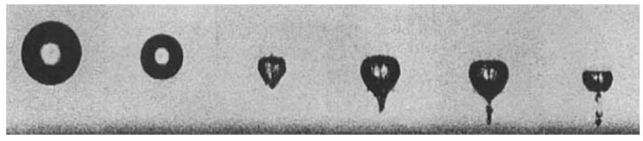

Figure 2.4: Liquid Jet formation observed in experiment by Vogel and Laterborn [8].

demonstrated the plasticity formation and hence material erosion. They concluded that a micro-jet can produce twice the maximum plastic deformation compared to a shock wave, while the shock wave can plastify a much larger volume of material (almost 800 times larger). Hence, the erosion rate should be higher for a shock wave impact.

On top of that, cloudy structures collapsing further away from the wall, could possibly have much larger volume than the structures collapsing close to a solid surface. Consequently, these cloudy structures contain a much larger amount of potential energy (due to the larger volume) and inevitably lead to implosion loads of higher amplitude. Finally, the time scales of the micro-jet formation and the water hammer shock are typically smaller than the time scales of the shock wave formation from the collapse of larger cavitating structures, even smaller than the material incubation time. Therefore, in many cases the material does not have time to react to the liquid-jet impact, as demonstrated by Joshi *et al.* [7]. Considering all these, large cloudy structures collapsing in the broader vicinity of a surface are expected to have a significantly larger erosion potential than smaller structures collapsing close to the wall.

2.1. SCALE SEPARATION IN CAVITATING FLOWS

In the context of the present work, the different scales in cavitating flows can be classified from both a physical and a numerical point of view. From a physical point of view, cavitation can be analyzed on a microscopic or macroscopic level. Analysis of cavitating flows on a microscopic level concerns the interaction between cavities (or bubbles) and fluid particles, and whether the flow satisfies (or not) thermodynamic and mechanical equilibrium. Such analysis is very relevant for cavitation inception investigation, where water quality and the number and size of nuclei in the flow seem to play a major role in determining the inception pressures. Microscopic characteristics of the flow (nuclei, small gas bubble etc.) may cause deviations from the phase diagram, and possible delays in phase transition. On a macroscpic scale, the focus is mainly on the kinematics of the cavitating structures and the mass transfer between the different phases. A homogeneous mixture is usually assumed which consists of liquid and vapor, and possibly non-condensable gas. Additional classification can be made between the smaller scales, where bubble dynamics are concerned, and the larger scales, where the implosion loads of large cloudy structures are of main interest.

From a modeling point of view, the representation of the cavitating flows could be classified first with regard to the frame of reference. The most common and popular approach for engineering applications is the eulerian mixture approach. The homogeneous mixture experiences phase change which is described by one set of equations for the whole field, in the Eulerian reference frame. This results in a no-slip condition between the two phases, that share the same velocity at the interface. Accounting for the slip velocity between the two phases, requires another set of equations. In this case, each phase is represented by one set of equations in the Eulerian frame of reference. However, a coupling between the phases is required for the momentum and the mass transfer. Since this approach is computationally more expensive, it is only recommended for cases where the slip velocity between the phases is important. On a macroscopic scale, slip velocities between the liquid and the vapor phases has been found to be negligible, nevertheless they seem to play an important role between the liquid and gaseous phases of a cavitating combustion spray [9].

Furthermore, a Langragian approach can be employed for the vapor phase, when high accuracy for sub-grid structures is required. The liquid phase is then described by one set of equations in the Eulerian reference frame, while the vapor phase is described by individual spherical bubbles or parcels of bubbles in a Lagrangian reference frame. One equation for the momentum transport and one for the phase transition needs to be solved for each bubble, and then a coupling for the momentum transfer between the phases is required. This method is the most expensive in terms of computational effort, however, it can provide high-fidelity predictions for the smallest scales in cavitation phenomena, such as the effect of dissolved gas, bubble-bubble and bubble-wall interaction, turbulence effects on bubble motion and break-up, surface tension effects on small bubbles etc. Ghahramani *et al.* [10] proposed a hybrid model, where larger cavities are still modeled using a Eulerian frame of reference, while small sub-grid structures as well as sparse bubble clusters are tracked as Lagrangian bubbles. Such an approach can reduce significantly the computational effort compared to a Lagrangian approach, while still providing high accuracy on simulating sub-grid cavitating structures. However, the computational

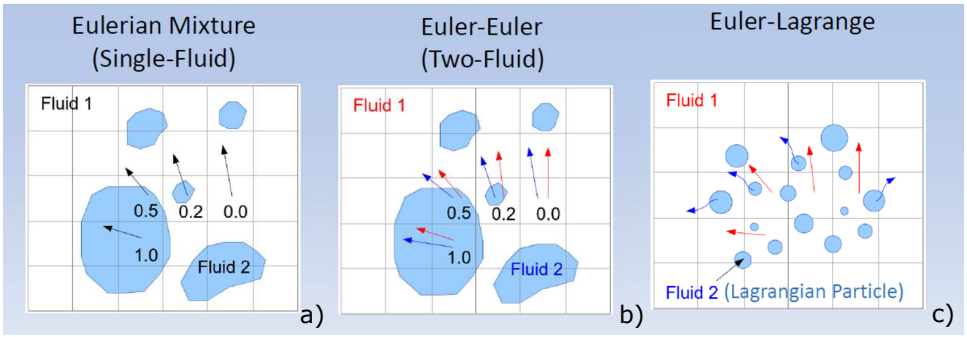

Figure 2.5: Numerical representation of cavitating flows. Single fluid approach a), two-fluid approach b), and Eulerian-Lagrangian approach c).

cost is still much higher than the Eulerian mixture approach, and yet not very attractive for industrial applications.

Secondly, cavitation modeling can be split into equilibrium and non-equilibrium models. Equilibrium models are assumed to satisfy phase equilibrium, on a macroscopic scale, of all involved variables at any time instant. That means that the macroscopic flow states of density, pressure and temperature are unique. An equation of state (EoS) is needed to describe the dependency between the flow state quantities. In some cases, thermodynamic tables are used to increase numerical efficiency [11, 12]. An additional transport equation is solved to achieve closure and describe the changes of internal energy in the system. In homogeneous equilibrium approaches, the fluid is often treated as fully compressible. However, the fact that the pure phases are almost incompressible leads to quite a few numerical challenges, due to the large range of Mach numbers involved. Therefore, in many cases barotropic equations of state are used, where the pressure is directly linked only to the fluid density [13–15]. Barotropic models do not always obey thermodynamic equilibrium, nevertheless, they usually are able to provide a realistic sound speed distribution of the cavitating mixture flow. A detailed classification between equilibrium and non-equilibrium cavitation models can be found in Schenke [16].

Moreover, mass transfer models are often used to model phase transition. Mass transfer models do not assume thermodynamic equilibrium, and they require an additional transport equation to be solved for the vapor volume fraction. The phase transition is controlled by a finite mass transfer source term, and the flow states are not unique, as in thermodynamic equilibrium models, but they are highly dependent on the source term of the vapor volume fraction transport equation. A cavitation model is required to determine the mass transfer rate included in the mass transfer source term. The pure phases are modeled as fully incompressible, while compressibility is mimicked only in the mixture regime. Mass transfer models are encountered usually in large scale engineering applications, and even though they violate the thermodynamic equilibrium, they can work very efficiently under certain flow conditions, providing high computational efficiency and robustness.

The reason why mass transfer models can work efficiently for engineering applications is attributed to the pressure scales at which transition occurs, and the fact that these

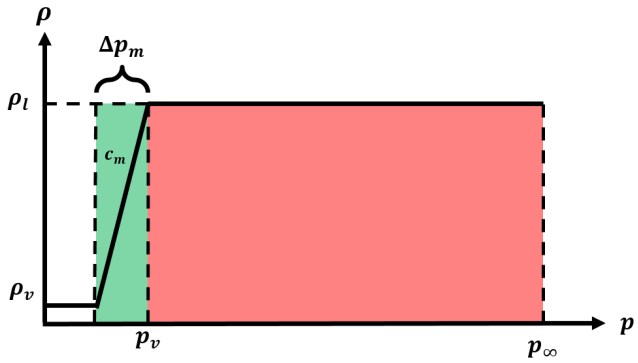

Figure 2.6: Representation of the transition from vapor to liquid phase at constant mixture sound speed c_m, and the pressure scales of typical engineering applications

scales are typically separated from the characteristic pressure difference driving the inertial dynamics in most applications. Schenke [16] proposed the inverse Mach number to separate the flow scales such that

$$Ma^{-1} = \frac{c_m}{v_{inert}} \approx \sqrt{\frac{\Delta p_m}{p_\infty - p_v}} \tag{2.1}$$

where c_m is the mixture sound speed, v_{inert} the inertial flow velocity that is characteristic of a collapsing cavity, and Δp_m is the pressure range during which phase transition occurs. The inverse Mach number is a measure of the inertial dynamics, and shows to what extent a cavitating flow is inertia driven.

Figure 2.6 illustrates the density transition of vapor to liquid and vice versa, when the flow is subjected to a driving pressure difference $p_\infty - p_v$. In most engineering applications, where the ambient pressure is $p_\infty \approx 1bar$ or higher, $Ma^{-1} \ll 1$, and the flow can be characterized as inertia driven. The pressure range where the mixture fluid exists, Δp_m, is relatively small compared to the pressure range of the liquid phase. Therefore, for relatively high driving pressures the flow is mainly governed by the pressure difference. So, the only implication in that case is to correctly represent the dynamics of the collapsing cavities and the phase transition form vapor to liquid. It becomes obvious then, that semi-empirical non-equilibrium mass transfer models can give realistic predictions of the inertial driven flows, including the representation of the phase transition, as long as the density-pressure trajectories obtained from the mass transfer model are steep enough, so that $p_\infty - p_v \gg \Delta p_m$. In cases, where Ma^{-1} is closer to 1, the pressure scales where phase transition occurs, are of higher interest, as the inertial forces become less and less dominant in the flow. In those cases, the density pressure trajectory becomes increasingly important, and a more accurate representation of the flow state is required.

In the present work, a semi-empirical mass transfer model is employed to simulate the mass transfer between the liquid and the vapor phases. The cavitation model by Schnerr and Sauer [17] is employed for the mass transfer source term, which is conceptually based on sub-grid bubble dynamics considerations. As our main focus is to resolve the largest

scales that are shed from partial cavities, and since high driving pressure differences are involved, the main concern is to achieve a sufficiently steep density-pressure trajectory and a quick transition form vapor to liquid phase. The phase transition is then controlled by the vaporization and condensation coefficients of the Schnerr-Sauer cavitation model. More details on that aspect are discussed in Chapter 4.

2.2. ENERGY BALANCE OF A COLLAPSING CAVITY

The potential energy contained in a cavity is proportional to its volume, V_v, and the pressure difference between the driving pressure, p_d and the pressure within the cavity, p_v

$$E_{pot} = (p_d - p_v) \cdot V_v \tag{2.2}$$

In every computational cell, the instantaneous volume specific change of potential energy is given by

$$\dot{e}_{pot} = \frac{DE_{pot}/Dt}{V_{cell}} = (p_d - p_v) \cdot \frac{D\alpha_v}{Dt} + \frac{Dp_d}{Dt} \cdot \alpha_v \tag{2.3}$$

It becomes quite clear that the energy content within a cavity depends strongly on its size (the larger the volume the larger the energy) and the driving pressure difference (the higher the driving pressure difference the more violent the collapse of a cavity of a certain volume). As Eq. 2.2 indicated, the potential energy initially contained in a cavity before its collapse will be equal to the sum of the internal, shock wave and rebound energy after the collapse. For moderate ambient pressures ($\approx$ 1 bar) and by neglecting any presence of non-condensable in the liquid (thus no rebounds), we can assume that all the potential energy will convert into shock wave energy at the final stage of the collapse. Consequently, the change of potential energy can lead us to the radiated energy that will be emitted and distributed to any surrounding surface. It is important then to isolate the two terms on the r.h.s of Eq. 2.3 and understand which term can contribute to the radiated energy. A detailed analysis of the contribution of each term can be found in Chapter 4, showing that energy cannot be radiated without any change in vapor volume, and therefore only the first term of the r.h.s of Eq. 2.3 may contribute to the emitted shock wave energy after the collapse.

Therefore, the change in potential energy can be identified by computing the material derivative of the vapor volume fraction and the driving pressure distribution. However, the determination of both quantities is not that straightforward. The material derivative of the vapor volume fraction, by definition, involves the partial derivative of the vapor volume fraction and an advective term. While, the partial derivative can be computed quite accurately, the advective term needs to be reconstructed, which may introduce significant numerical errors. Considering the mixture density and the mass continuity, the material derivative of the vapor volume fraction could also be computed using the velocity divergence or the mass transfer model source term $\dot{m}$ such that

$$\frac{D\alpha_v}{Dt} = \left(\frac{\partial \alpha_v}{\partial t} + u \cdot \nabla \alpha_v \right) = \frac{\rho}{\rho_l - \rho_v} \nabla \cdot \mathbf{u} = \frac{\rho}{\rho_l} \dot{m} \tag{2.4}$$

The velocity divergence term, computed from the face fluxes, may also introduce high numerical errors, due to interpolations from the cell faces to the cell center. When only

condensation is taking place, those numerical errors can be corrected from the total volume change. Nevertheless, in more complex situations, the velocity divergence introduces high uncertainty. Therefore, it is suggested that the material derivative of the vapor volume fraction is computed from the mass transfer model source term (cavitation rate). However, it is also suggested to always monitor the reconstructed material derivative of the vapor volume fraction, since even the cavitation rate might be different depending on the solver or the cavitation model in use. A more elaborate discussion on the numerical and modeling error sources in the computation of the potential energy change can be found in Chapter 4. Finally, the uncertainty introduced by the selection of the driving pressure field is discussed in the following section.

2.3. EFFECTIVE DRIVING PRESSURE OF COLLAPSING CAVITATING STRUCTURES

One of the key components and one of largest uncertainties in cavitation erosion modeling is introduced by the effective driving pressure term in Eq. 2.2. The pressure driving the collapse is responsible first of all for the actual potential energy contained in the cavities. For a certain volume, the potential energy will change if the driving pressure changes. Furthermore, the driving pressure determines the aggressiveness of the collapse. The higher the driving pressure the faster and the more violent a cavitating structure will collapse, leading to higher radiation of acoustic energy, increasing the risk of surface erosion.

For a spherical bubble collapsing in an infinite liquid, the pressure development in time and space in the liquid domain can be obtained by the Rayleigh-Plesset Eq. [18] after neglecting surface tension and viscous effects

$$\frac{p(r,t)-p_\infty(t)}{\rho} = \ddot{R}\frac{R^2}{r} + 2\dot{R}\left[\frac{R}{r} - \frac{R^4}{4r^4}\right] \tag{2.5}$$

where p_∞ is the pressure at infinity, r the radial distance from the bubble center for any point in the liquid domain, ρ the liquid density, R the bubble radius, and $\dot{R}$, $\ddot{R}$ the velocity and acceleration of the bubble interface respectively. On the interface $r = R$, and $p(r,t) = p_v$, and Eq. 2.5 gives

$$\rho\left[R\ddot{R} + \frac{3}{2}\dot{R}^2\right] = -(p_\infty - p_v) \tag{2.6}$$

Assuming that the pressure at infinity is known, this equation gives the temporal evolution of the radius R and consequently the pressure field in the liquid. However, in complex flows the pressure at infinity, $p_\infty(t)$, is ill-defined and the determination of the pressure driving the collapse is not straightforward as it is not only a function of space, but varies also in time. At the same time, the correct representation of the driving pressure is crucial for the computation of the initial potential energy contained in the collapsing structures, and consequently any potential impact on nearby surfaces.

For a bubble collapsing close to a solid wall, the driving pressure along the interface varies due to the effect of wall interaction [19]. Similarly, the presence of other bubbles in the vicinity, influence the pressure field around the interface. Considering the

flow around a hydrofoil where strong pressure gradients are present due to rapid velocity changes, the determination of the pressure field around those cavities becomes even more complex. Thus, it becomes clear that there is not a trivial way to determine the instantaneous driving pressure that triggers the collapse of those cavities. Therefore, a large uncertainty is introduced by the definition of $p_\infty(t)$, already before any consideration of the modeling of cavitating flows and cavitation erosion.

The pressure at infinity has been considered as the driving pressure, even for complex flows, however this typically leads to overprediction of the potential energy [20–22]. The presence of walls and other cavities in the domain hinders the pressure recovery and reduces the driving pressure. Using the far field pressure neglects any interaction with solid walls or other bubbles in the flow. At the same time any temporal effect on the driving pressure is also not considered.

The instantaneous pressure has also been used as an estimate for the pressure driving the collapse in complex flows [23]. Nevertheless, the driving pressure then needs to be computed at locations where phase transition occurs. At those locations, the density-pressure trajectory evolves very close to vapor pressure, and consequently any pressure difference from the instantaneous pressure should be close to zero, leading to low potential energy values. Therefore, using the instantaneous pressure to assess the driving pressure leads to under-prediction of the radiated energy and consequently the impact loads on the surface.

Arabnejad and Bensow [24] suggest a different and more delicate approach to compute the collapse driving pressure. They identify and simplify coherent cavitation structures to an isolated spherical bubble of equivalent volume. Then, the pressure driving the collapse can be determined by the Rayleigh-Plesset equation. This approach requires an additional set of kinematic parameters, that uniquely define the state of the collapse [25]. In this way, however, the exact shape of the collapsing structures and their orientation with regard to the surface cannot be reflected. Since both the cavity shape and orientation were found to be crucial for identifying the aggressiveness of a cavity collapse [26], a more generic approach is required, which nevertheless reflects all the significant aspects of the cavity dynamics with regard to the driving pressure.

In cyclic flows, the time-averaged pressure field $\overline{p}_t$, at time instant t, computed from the instantaneous pressure field in cavitating conditions, p, provides at least an approximation of the conditions which collapsing cavities experience on statistical average. However, this implies that the time-averaged pressure field has reached a sufficient level of convergence in time, which always requires many cycles. The use of a sliding window of size T_m, over which the instantaneous pressure field is averaged, can reduce significantly the computational time needed to compute the driving pressure field

$$\overline{p}_t = \frac{1}{T_m} \int_{t-T_m}^{t} p(t)\,dt \tag{2.7}$$

Nevertheless, the size of this moving window is important for the correct representation of the driving pressure, which varies now both in space and time. The appropriate size of the sliding window has been found to be at least equal to one period (one cavity cycle) of the cavitating flow. More details on this matter are discussed in chapter 4.

2.4. INSTANTANEOUS ENERGY BALANCE AND CAVITATION EROSION MODELING

Equation 2.2 shows the potential energy contained in a cavitating structure. When the structure is subjected to high ambient pressure it will start collapsing. The instantaneous energy balance during the collapse of a cavitating structure states that the change of potential energy is equal to the negative change of the kinetic energy at any time instant such that

$$\dot{E}_{pot,0} + \dot{E}_{kin} = 0 \tag{2.8}$$

Equation 2.8 reveals that during the collapse the potential energy is continuously feeding into collapse induced kinetic energy until the final stage of the collapse where we have the maximum kinetic energy concentrated at the collapse center. Then, part of the kinetic energy will convert into radiated acoustic energy. The novelty of this thesis lies within the energy balance and the energy cascade during the collapse. The erosion modeling accounts for the focusing of the potential energy, initially contained in the cavitation structures, into kinetic energy, and its transport towards the collapse center.

The generation of the collapse induced kinetic energy occurs at locations of negative change of potential energy. Since the exact distribution of the kinetic energy around the structure is not known, it is stored at the interface, and thereby is transported into the collapse center. At the final stage of the collapse, the energy is radiated to the domain. For relatively high ambient/driving pressures, almost all the energy stored at the collapse center is converted into shock wave energy. Finally, a fraction of this energy will be transferred to the surface depending on the distance and orientation from the collapse center.

For the generation and the transport of the collapse induced kinetic energy ε, an additional transport equation is solved during each time step [2]

$$\frac{\partial \varepsilon}{\partial t} + \mathbf{u}_i \cdot \nabla \varepsilon = -\varepsilon(\nabla \cdot \mathbf{u}_i) - \dot{e}_{rad}(t) \tag{2.9}$$

where $\mathbf{u}_i$ is the collapse induced velocity. The terms $\varepsilon(\nabla \cdot \mathbf{u}_i)$ and $\dot{e}_{rad}(t)$ of Eq. 2.9 represent the conversion of the potential energy into collapse induced kinetic energy and the conversion of the kinetic energy to radiated acoustic energy, respectively. The term $\mathbf{u}_i \cdot \nabla \varepsilon$ represents the conservative advective transport of ε. However, as mentioned, the distribution of the kinetic energy around the cavity is not known, and therefore, a model is used to store the energy at the interface as follows:

$$\frac{\partial \varepsilon}{\partial t} = (1-\beta)[\phi(\varepsilon) - \dot{e}_{pot,C}(t)] - \beta \frac{\varepsilon}{\delta t} \tag{2.10}$$

where $\phi(\varepsilon)$ is a model for the advective transport of the kinetic energy, and $\dot{e}_{pot,C}(t)$ is the reduction of potential energy. The parameter β is responsible for the conversion of the collapse induced kinetic energy into acoustic radiated energy, and it is defined as follows:

$$\beta = \begin{cases} 1, & if \quad p > p_\infty \quad and \quad \alpha = 0 \\ 0, & else \end{cases} \tag{2.11}$$

When $\beta = 0$, collapse induced kinetic energy is generated, stored at the interface, and focused towards the collapse center, while when $\beta = 1$ acoustic energy is released to the domain.

The complexity and delicacy in predicting the cavitation impact loads using the focusing approach is characterized by four key components in the model: the energy conservation in the computation of the material derivative of the vapor volume fraction associated with the kinetic energy generation, the modeling of the conservative transport of the collapse induced kinetic energy stored at the interface, the identification of the final collapse stage revealing the radiation sources, and finally the projection of the radiated energy to the surrounding surface as a fraction of the total shock wave energy released after the collapse.

As far as the kinematic features of the collapsing cavitating structures are concerned, e.g. the characteristic shedding frequency and the cavity collapse time, semi-empirical mass transfer models can give accurate predictions considering sufficient spatial and temporal resolution, as well as large enough mass transfer model coefficients. Thus, the presented erosion model, which is based on the kinematic evolution of the imploding cavitating structures, can work well in association with Unsteady RANS solvers, where the pure fluid phases are treated as incompressible. Moreover, the fact that there is no need to resolve fast propagating pressure waves allows for much larger time step sizes. On the other hand, the incompressibility of the pure phases, and the consequent infinite speed of sound, exhibits a non-convergent behavior of the collapse peak pressures indicating that cavitation erosion models based on the local pressure are not suitable for erosion risk prediction of cavitating flows within the presented numerical framework [16, 27].

Finally, it should be noted that the model demonstrated in this study, is discussing only the hydrodynamic aspects of erosion modeling. The mechanical response of the material is not addressed, although it is of similar importance for predictions of the actual erosion rate. The effect of the material behavior, which is highly non-linear, will depend on the number of shock impacts, and their intensity per unit time will determine if and when erosion will occur and how it will progress. However, within the scope of this study we only focus on the hydrodynamic loads, and the material response should be considered as a next step to complete the cavitation erosion analysis.

REFERENCES

[1] R. Fortes-Patella and J. L. Reboud, *A new approach to evaluate the cavitation erosion power,* Journal of Fluids Engineering **120**, 335 (1998).

[2] S. Schenke, T. Melissaris, and T. J. C. van Terwisga, *On the relevance of kinematics for cavitation implosion loads,* Phys. Fluids **31**, 052102 (2019).

[3] J. P. Franc and J. M. Michel, *Fundamentals of Cavitation* (Kluwer Academic Publishers, Dordrecht, 2004).

[4] H. Ganesh, *Bubbly Shock Propagation as a Cause of Sheet to Cloud Transition of Partial Cavitation and Stationary Cavitation Bubbles Forming on a Delta Wing Vortex.*, PhD Thesis, The University of Michigan (2015).

[5] H. Ganesh, S. A. Makiharju, and S. I. Ceccio, *Bubbly shock propagation as a mechanism for sheet-to-cloud transition of partial cavities,* Journal of Fluid Mechanics **802**, 37 (2016).

[6] S. Jahangir, *Experimental Investigation of Partial Cavitation*, PhD Thesis, Technical University of Delft, Delft, The Netherlands (2020).

[7] S. Joshi, J. P. Franc, G. Ghigliotti, and M. Fivel, *SPH modelling of a cavitation bubble collapse near an elasto-visco-plastic material,* Journal of the Mechanics and Physics of Solids **125**, 420 (2019).

[8] A. Vogel and W. Laterborn, *Acoustic transient generation by laser-produced cavitation bubbles near solid boundaries,* The Journal of the Acoustical Society of America **84**, 719 (1988).

[9] M. Cristofaro, W. Edelbouer, P. Koukouvinis, and M. Gavaises, *A numerical study on the effect of cavitation erosion in a diesel injector,* Applied Mathematical Modelling **78** (2020).

[10] E. Ghahramani, H. Ström, and R. Bensow, *Numerical simulation and analysis of multi-scale cavitating flows,* Journal of Fluid Mechanics **922** (2021).

[11] S. Schmidt, *A low Mach number consistent compressible approach for simulation of cavitating flows*, PhD Thesis, Technische Universität München (2015).

[12] N. Kyriazis, P. Koukouvinis, M. Gavaises, R. Pearson, and M. Fold, *Heating effects during bubble collapse using tabulated data,* in *Proceedings of the* 10^{th} *International Symposium on Cavitation* (Baltimore, Maryland, USA, 2018).

[13] Y. Delannoy and I. Kueny, *Two phase flow approach in unsteady cavitation modelling,* Cavitation and Multihase Flow Forum, ASMEFED **98** (1990).

[14] D. van der Heul, C. Vuik, and P. Wesseling, *Efficient computation of flow with cavitation by compressible pressure correction,* in *PECCOMAS* (Barcelona, Spain, 2000).

[15] A. Koop, H. Hoeijkmakers, G. Schnerr, and E. Foeth, *Desigh of twisted cavitating hydrofoil using a barotropic flow method,* in *Proceedings of the* 6^{th} *International Symposium on Cavitation* (Wageningen, The Netherlands, 2006).

[16] S. Schenke, *Cavitation implosion loads from energy balance considerations in numerical flow simulations*, PhD Thesis, Delft University of Technology (2020).

[17] G. H. Schnerr and J. Sauer, *Physical and numerical modeling of unsteady cavitation dynamics,* in *Fourth International Conference on Multiphase Flow* (New Orleans, USA, 2001).

[18] Lord Rayleigh, *On the pressure development in a liquid during the collpapse of a spherical cavity,* Phil. Mag. **34**, 94 (1917).

[19] M. S. Plesset and R. B. Chapman, *Collapse of an initially spherical vapour cavity in the neighbourhood of a solid boundary,* J. Fluid Mech. **47**, 283 (1971).

[20] C. Flageul, R. Fortes-Patella, and A. Archer, *Cavitation erosion prediction by numerical simulations,* in *Proceedings of the* 14^{th} *International Symposium on Transport Phenomena and Dynamics of Rotating Machinery* (Honolulu, HI, USA, 2012).

[21] C. Leclercq, A. Archer, R. Fortes-Patella, and F. R. F. Cerru, *Numerical cavitation intensity on a hydrofoil for 3d homogeneous unsteady viscous flows,* Int. J. Fluid Mach. Syst. **10**, 254 (2017).

[22] R. Fortes-Patella, G. Challier, J. L. Reboud, and A. Archer, *Energy balance in cavitation erosion: From bubble collapse to indentation of material surface,* Journal of Fluids Engineering **135**, 011303 (2013).

[23] Z. Li, M. Pourquie, and T. J. C. van Terwisga, *Assessment of cavitation erosion with a urans method,* Journal of Fluids Engineering **136** (2014).

[24] M. H. Arabnejad and R. Bensow, *A methodology to identify erosive collapse events in the incompressible simulation of cavitating flows,* in *Proceedings of the* 20^{th} *Numerical Towing Tank Symposium* (Wageningen, The Netherlands, 2017).

[25] G. Bark, N. Berchiche, and M. Grekula, *Application of principles for observation and analysis of eroding cavitation, EROCAV observation handbook*, 3rd ed. (Department of Shipping and Marine Technology, Chalmers University of Technology, Sweden, 2004).

[26] M. V. Rijsbergen, E.-J. Foeth, P. Fitzsimmons, and A. Boorsma, *High-speed video observations and acoustic-impact measurements on a naca 0015 foil,* in *Proceedings of the* 8^{th} *International Symposium on Cavitation* (Singapore, 2012) pp. 958–964.

[27] C. Eskilsson and R. E. Bensow, *Estimation of cavitation erosion intensity using cfd: Numerical comparison of three different methods,* in *Fourth International Symposium on Marine Propulsors* (Austin, Texas, USA, 2015).

3

On the Applicability of Cavitation Erosion Risk Models With a URANS Solver

In the maritime industry, cavitation erosion prediction becomes more and more critical, as the requirements for more efficient propellers increase. Model testing is yet the most typical way a propeller designer can, nowadays, get an estimation of the erosion risk on the propeller blades. However, cavitation erosion prediction using computational fluid dynamics (CFD) can possibly provide more information than a model test. In this chapter, we review erosion risk models that can be used in conjunction with a multiphase unsteady Reynolds-averaged Navier–Stokes (URANS) solver. Three different approaches have been evaluated, and we conclude that the energy balance approach, where it is assumed that the potential energy contained in a vapor structure is proportional to the volume of the structure, and the pressure difference between the surrounding pressure and the pressure within the structure, provides the best framework for erosion risk assessment. Based on this framework, the model used in this study is tested on the Delft Twist 11 hydrofoil, using a URANS method, and is validated against experimental observations. The predicted impact distribution agrees well with the damage pattern obtained from paint test. The model shows great potential for future use. Nevertheless, it should further be validated against full scale data, followed by an extended investigation on the effect of the driving pressure that leads to the collapse.

This chapter is based on: T. Melissaris, N. Bulten, T.J.C van Terwisga, *On the Applicability of Cavitation Erosion Risk Models With a URANS Solver*, Journal of Fluids Engineering **141** (2019).

3.1. INTRODUCTION

Cavitation is the creation and intense collapse of vapor pockets in a liquid when exposed to low pressures. These vapor structures occur at locations where the local pressure drops to such low values that the liquid evaporates. The collapse of the bubbly clouds in regions of pressure recovery can be very violent, leading to vigorous and rapid pressure wave emissions. In case of a collapse very close to the surface wall, a micro-jet is formed. The micro-jet pierces the side of the bubble which is closest to the wall, resulting in a high 'water hammer' pressure, felt as a pressure wave on the surface, followed by a stagnation pressure of lower magnitude, but longer duration [1]. If the impulsive pressure, which stems from either the pressure wave, originated from cloud collapse or the water hammer, or the impact of the micro-jet at the stagnation point, exceeds a certain threshold, then local damage is induced. That threshold depends strongly on the mechanical properties of the surface material.

In the maritime industry, propeller cavitation is often unavoidable, and therefore accepted. Cavitation could be avoided, but this comes at the cost of efficiency or extra capital investments. In certain applications (e.g. research and naval vessels), complete absence of cavitation is even favourable, but for merchant vessels, maximum efficiency is desired. Thus, it becomes essential to know when cavitation is not harmful in operation. Cavitation can be the origin of several negative effects such as noise, vibrations, structural damage, power and material loss. The later, cavitation erosion, might be responsible for severe damage on the propeller blades, considerably decreasing the propeller efficiency. Thus, the prediction of cavitation dynamics in the vicinity of a propeller becomes extremely important, in order to assess cavitation erosion risk on the propeller surface.

Although the first attempt to analyze a cavitation problem and to quantify the erosive potential of a single bubble, was made by Lord Rayleigh [2] in 1917, any further progress in actually quantifying the erosion process has been slow. He investigated bubble dynamics and solved the problem of the collapse of an empty cavity in a large mass of liquid, leading the way towards an extensive investigation on cavitation and bubble dynamics [3, 4]. Most of the findings on cavitation inception, formation of bubbles, formation of complex cavitation patterns, are reported and summarized by Plesset and Prosperetti [5] and Brennen [6]. They already knew that the high pressure peaks occurring during the implosion of a bubble, were partly responsible for the damage of propeller blades. However, the bending of trailing edges could not be caused by single collapse, but from collective collapses and interaction of many neighboring bubbles [7]. Momentum considerations were used for analysis of the collapse of a cluster, until Mørch [8] included the influence of the emitted pressure wave of each cavity to the cluster collapse, in the energy balance equation. Isselin *et al.* [9], and Philipp and Lauterborn [10], tried to elucidate the mechanism of cavitation erosion by investigating collective effects from consecutive bubble collapses. They showed that the destructive effect of cavitation is mainly caused by the collapse of bubbles in close vicinity of the solid boundary. However, they only observed the effects of single bubbles omitting any interaction between bubbles or collective collapses of bubbly clouds. Therefore, a complete description of the cavitation dynamics and the erosion process still remains obscure.

Recent research, within the EU CaFE project (see also http://cafe-project.eu), has led to a better understanding of the various types of collapsing cavities that lead to mate-

rial damage. However, there is still a lack of physical knowledge and of a detailed phenomenological description of the process leading to cavitation erosion. The notion that the aggressiveness of cavitation could be assessed through a consideration of energy conversion, was already acknowledged by Hammit [11] in 1963 and a potential energy approach was first proposed by Vogel and Laterborn [12]. Erosion will occur due to the concentration of mechanical energy on very small areas of the solid surface. This energy concentration results in high stress levels which can exceed the resistance of the material. However, which is the mechanism that contributes more to surface erosion, still remains unclear.

Plesset and Chapman [1] showed that the liquid jet can develop velocities high enough to explain cavitation damage. This approach was adopted by Dular *et al.* [13], proposing a cavitation erosion model based on experimental studies. He recently found that when the implosion is in the close vicinity of the wall, the most pronounced mechanism is the impact of the micro-jet. As we move further away from the wall the impact of the micro-jet diminishes and the collapses of microscopic bubbles during the rebound become more aggressive [14]. On the other hand, Fortes-Patella and Reboud [15], investigated various material samples submitted to different cavitation conditions, and they concluded that the pressure wave emission, that could be generated by spherical bubble and vortex collapses as well as by micro-jet formation, seemed to be the mechanism responsible for the damage. Furthermore, they developed an original approach to estimate the cavitation aggressiveness, based on energy balance between vapor bubble collapse, emitted pressure wave, and neighboring solid wall response [16].

Franc and Michel [17] claimed that both hydrodynamic mechanisms, the shock wave and the microjet, give rise to high pressure pulses, with the same order of magnitude as the yield strength of usual metals. However, in case of a collective collapse, which is typically characterized by cascades of implosions [10, 18], the emitted pressure waves of a particular bubble tend to enhance the collapse velocities of the neighboring bubbles, thus increasing the amplitude of their own pressure waves. Especially when these collapses are originated from vortical structures, the erosive potential can be enhanced, due to the formation of a foamy cloud triggering cascade mechanisms and the relatively long duration of the impact applied to the wall [17].

Bark *et al.* [19] also used an energy consideration to explain the risk of cavitation erosion. "The concentration or focusing of the collapse energy to a small domain of the solid surface is an obvious requirement for generation of cavitation erosion. A cavity can be associated with a potential energy", as has been already acknowledged [11, 12]. When the cavity collapses, the potential energy, contained initially in the bubble, will first be transformed into kinetic energy of the surrounding flow. When the minimum cavity radius is reached, the energy is transformed into potential energy and acoustic wave energy, which is felt as a pressure pulse in the surrounding liquid with the maximum value at the cavity interface. Thus, there is a focusing effect for the kinetic as well as the potential energy. The potential energy is then again transformed into kinetic energy during the rebound of the cavity [20].

To return to the main question, it should be noted that individual pits, early visible during the development of cavitation erosion, are typically of fairly small scale, from a few µm up to mm size. Larger scale damage, like deeper pits or extensive erosion, is certainly

generated by collective large scale collapsing cavities and cavitating vortices. "Vortex cavitation can be very erosive even though it is surrounded by a durable pressure lowering rotation. This rotation is however also the explanation for the high erosiveness. The rotation creates the high symmetry needed for a perfect focusing collapse towards a point" [19].

Considering all the above, van Terwisga *et al.* [21] claimed that the concentrated vorticity (from vortical structures originated from sheet cavitation), forms a mechanism to break up a monolithic cavity and to concentrate all the resulting micro-bubbles in space. The radiated shock-waves caused by an implosion of one micro-bubble, where there is a focusing of energy, is then hypothesized to be sufficient to initiate a synchronized implosion of the cloud of micro bubbles in the immediate vicinity. Thus, it is concluded that the most aggressive acoustic emission is originated from a collective micro bubble collapse, while cavitating vortices may increase the aggressiveness due to effective focusing of the acoustic power in space and time.

The first objective of this work is to review physical models for predicting cavitation erosion, following suggestions from the literature. Similar endeavors have been made in the past [21, 22], however, new numerical approaches have been proposed, and existing models have been further developed and tested within the last years. The complexity of the phenomenon, and the need to provide a reliable method to quantitatively predict (the risk of) cavitation erosion, renders the evaluation of such models a relevant task.

From an industrial point of view, where there is always a compromise between time and quality, the development of a quick and reliable method to assess cavitation erosion risk is required. Thus, the second objective of this paper is to evaluate the existing erosion models, and assess their applicability on an industrial/commercial pressure based Unsteady Reynolds Averaged Navier-Stokes (URANS) solver. To this end, we have conducted a detailed verification and validation study on the Delft Twist 11 hydrofoil in wetted and cavitating flow condition. We conclude that the energy balance approach proposed by Fortes-Patella *et al.* [23] is the most favorable method to estimate cavitation erosion risk for marine applications. The implemented erosion model, based on the previous work of Leclercq *et al.* [24] and Schenke and van Terwisga [25], is modified in such a way to reduce the computational cost. The numerical predictions are compared with experimental observations of material damage [26], showing a good correlation.

3.2. REVIEW OF CAVITATION EROSION RISK MODELS

Cavitation is being observed experimentally for more than half a century, however the need of including cavitating flow computations, already in the design phase, renders numerical simulations for cavitation prediction more imperative. Especially, the prediction of cavitation erosion, particularly on marine propellers, is quite a challenging task, and even observation in a cavitation tunnel does not give the required confidence, due to the difficulty either to observe such a process or to estimate scalabillity effects of such flows. Thus, the direct prediction of the erosion risk in full scale applications, using CFD, becomes very important.

Several attempts have been made in the past decades to predict cavitation erosion without using a model test. Kato *et al.* [27] proposed a scenario for quantitative prediction of the impact force distribution on the solid surface caused by cavitation. It uses

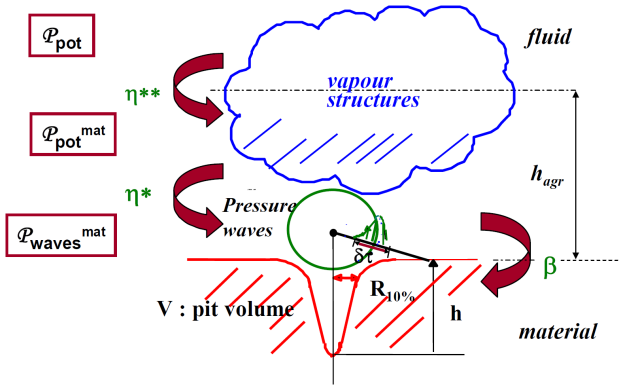

Figure 3.1: Energy balance approach showing the transition of the energy contained in the initial vapor cavity to the material surface [30]

several simplified empirical relations, which need further experimental and theoretical verification, rendering such a method questionable for propellers and rudders. Bark *et al.* [19] provided guidelines to assess erosiveness from visual observations. This model could easily be applied on rather large-scale cavities, at a scale which can be predicted be contemporary CFD methods, however, it is mainly based on the observation of rebound cavities and the estimation of their violence, thus not applicable for incompressible[1] solvers, where the simulation of a rebound cavity is impossible. van Terwisga *et al.* [21] encourage to combine this model with experimental observations and paint tests.

During the last decade, more detailed attempts have been made to describe the physical mechanisms for assessing the risk of cavitation erosion. Three erosion models have been proposed and are discussed in the following subsections: the energy balance approach by Fortes-Patella *et al.* [23], the erosion model by Dular and Coutier-Delgosha [28], and the collapse detector by Mihatsch *et al.* [29].

3.2.1. EROSION MODEL BY FORTES PATELLA ET. AL. (2004)

This model describes the physical mechanism of cavitation erosion based on the energy transfer through the shock wave emitted by the collapse of vapor structures (Fig. 3.1). The model consists of the four following stages:

1. The shedding vapor structures of the cavitating flow start to collapse;

2. The potential power, included in the vapor clouds, is converted into acoustic power through emitted pressure waves generated by the collapse. The pressure waves propagate towards the surface. It is suggested that those pressure waves are the main source contributing to the cavitation erosion;

3. The emitted pressure waves interact with the solid surface

[1] We should specify that with incompressible solvers we mean that they treat the pure phases as incompressible, because compressibility is considered when phase transition occurs.

4. The surface is exposed to material damage with a volume damage rate $\dot{V}_d$

The initial potential energy inside a vapor structure is defined as

$$E_{pot} = \Delta p \cdot V_v \tag{3.1}$$

where $\Delta p = (p_\infty - p_v)$, p_∞ is the surrounding pressure, p_v is the vapor pressure and V_v is the vapor volume. Then, the instantaneous potential power can be defined as the Lagrangian time derivative of the potential energy

$$P_{pot} = -\Delta p(DV_v/Dt) \tag{3.2}$$

where the pressure derivative has been ignored [30], as it is assumed to be an order of magnitude lower than the vapor volume derivative. The minus sign shows that a vapor structure is considered aggressive only when the relative variation of its vapor volume is negative (condensation), thus giving a positive potential power value. The aggressiveness intensity is characterized then as

$$P_{pot}^{mat} = \eta^{**} P_{pot} \tag{3.3}$$

where η^{**} is the energy transfer efficiency and is a function of the hydrodynamic characteristics of the main flow (the reference velocity of the flow V_{ref}, and the cavitation number σ), the distance, and the angle between the collapse center and the material surface. This efficiency depends on the type, unsteadiness and geometry of the cavitating flow. However, it should be mentioned here that, from the definition of the potential power, a lot of information regarding the flow characteristics and cavitation development is already included. Consequently, the distance and the angle between the accumulated energy at the collapse center and the material surface seem to be the most important influential factors.

When the vapor structures collapse, the emitted pressure waves apply a pressure wave power on the surface that is defined as

$$P_{waves}^{mat} = \eta^{*} P_{pot}^{mat} \tag{3.4}$$

where the collapse efficiency η^* characterizes the aggressiveness power of the vapor/gas implosion. It depends mainly on the initial vapor volume, which is a function of the initial bubble radius R_0, the initial gas pressure p_{g_0} within the bubble, and the surrounding pressure p_∞. The plastic deformation due to the pressure waves (during the incubation period) is characterized by the deformed volume V_{pit}. Therefore, the pressure wave power density is obtained as follows:

$$\frac{P_{waves}^{mat}}{\Delta S} = \beta \frac{\sum V_{pit}}{\Delta t \Delta S} = \beta V_d \tag{3.5}$$

where V_d is the volume damage rate, and β is a coefficient related to the surface material. The main advantage of this model is that it follows a physical energy balance process. However, the applicability and reliability of this model depends strongly on the assessment of the two efficiencies η^{**} and η^*, and the material parameter β.

Parameter β was found to be strongly dependent on the solid properties, and almost independent on the wave impact amplitudes [23]. However, the rate of the impulses impinging the material, the energy of the impulses, work hardening effects of the material, and changes in material mechanical properties may also affect the value of this parameter. Regarding the energy transfer efficiency η^{**} Flageul et. al. [30] proposed an empirical approximation for the distance to the solid h_{agr}, below which it is assumed that the vapor structures are close enough to be considered as aggressive. Based on Kato et. al [27] this distance, can be approximated as the 10% of the thickness of the sheet cavity. Nevertheless, it is not only the distance that determines the aggressiveness of the structures, but also the angle of the structures to the surface. Thus, Leclercq et. al. [24] used the solid angle approach to account for both the distance and the angle dependencies, to calculate the "instantaneous cavitation intensity" P_{pot}^{mat}.

A rather physical explanation of this "instantaneous cavitation intensity" could be the maximum aggressiveness of an initial vapor cloud, for a certain amount of potential energy within the cloud, and a specified collapse time. In other words, it is assumed that the whole potential energy is converted into a shock wave, neglecting any rebound effects and any heat transfer to the surrounding liquid.

3.2.2. EROSION MODEL BY DULAR AND DELGOSHA (2009)

This model is based on the micro-jet formation. Single bubbles, present near the solid surface, start to oscillate due to shock waves, traveling towards the surface, generated by the collapse of vapor clouds. Because of the oscillations of the single bubbles, a high-velocity liquid jet impact can occur, causing damage on the surface. It is stated that, the Eroded Surface (ES) is a result of repetition of the phenomenon mentioned above, considering only the incubation period. According to this erosion risk model the local velocity of the microjet is one of the most critical quantities for the prediction of cavitation erosion. The jet velocity is determined by Plesset and Chapman [1] as

$$u_{jet} = 8.97\gamma^2\sqrt{\frac{p-p_v}{\rho}} \tag{3.6}$$

where γ is the non-dimensional distance from the bubble center to the surface ($\gamma = H/R_0$, where H is the distance and R_0 is the bubble radius), p is the reference pressure, p_v is the vapor pressure and ρ is the liquid density. Based on the local velocity, the water hammer pressure can be expressed as

$$p_{hammer} \approx u_{jet}\rho_l c_l \tag{3.7}$$

where c_l is the speed of sound of pure liquid and ρ_l the liquid density. Assuming a perfectly rigid, solid surface, which behaves as a perfectly plastic solid, the critical velocity, for which the yield stress p_y is reached, can be expressed as derived by Lush [31]

$$u_{crit} \approx \sqrt{\frac{p_y}{\rho_l}\left(1-\left(1+\frac{p_y}{B}\right)^{\frac{-1}{n}}\right)} \tag{3.8}$$

where $B = 300MPa$ and $n = 7$ for liquid water.

While this hammer stress is definitely the most impressive impact, it is not clear whether it is the important damaging mechanism. Possibly, according to Plesset and Chapman

[1], it is not the water hammer pressure that makes the jet potentially aggressive, because the water hammer incidence time is relatively small. The duration is estimated to be no longer than the time for the impact signal to traverse the radius of the jet. Then, it would rather be the stagnation pressure, established right after the water hammer pressure, that is responsible for pit formation, because its duration is an order of magnitude larger, while its amplitude can be of the same order (jet velocities have been reported to be even higher than $1000 m/s$ [32, 33]). Nevertheless, this model does not consider the latter as a pressure pulse source.

To determine the erosion intensity from such an impact, Peters et. al. [34] proposed a dimensionless intensity coefficient $c_{intensity}$, which relates the local jet velocity u_{jet} to the critical velocity u_{crit}, as well as the water hammer pressure p_{hammer} to the pressure needed to reach the limit, before which deformation starts to occur. It is defined as follows:

$$c_{intensity} = \frac{u_{jet}}{u_{crit}} \approx \frac{p_{hammer}}{p_{plastic}} \tag{3.9}$$

This coefficient expresses the erosion intensity of a single micro jet impact on a face and it is calculated for every impact on a face of the desired surface. When there is no impact on a face the coefficient is equal to 0, while impacted faces have a value higher than 1, as the jet velocity in this case is higher than the critical velocity. Afterwards, all the intensity coefficients are integrated over the whole time interval for every face, and then they are normalized by the total sum of $c_{intensity}$ in the whole domain. Thus, the deformation coefficient c_{def} is defined as

$$c_{def} = \frac{\sum_t^T c_{intensity}}{\sum_n^N \left(\sum_t^T c_{intensity,t}\right)_n} \tag{3.10}$$

where t is the time step index, T the total calculation time, n the face index and N the total number of eroded faces. In the end, the value of the deformation coefficient c_{def} gives the fraction of the erosion on every face compared to the total predicted erosion.

It should be noted, that the physical process assumed to be responsible for cavitation erosion in this model, is based on the notion that damage is caused due to the impingement of the micro jet, associated with the implosion of the individual bubbles, while in this paper, it is hypothesized that the acoustic power, released from this mechanism is significantly smaller than the acoustic power, that is released from a synchronized collapse of a bubbly cloud collapse. Moreover, a disadvantage of the model is that it accounts only for the plastic deformation of the surface (during the incubation period). Consequently, this model cannot be used to assess the actual damage rate but only the erosion risk.

3.2.3. Collapse detector by Mihatsch (2011)

The concept of the "collapse detector" involves the derivation of a set of physical criteria to detect the collapse of isolated clouds and to evaluate the strength of the generated shock waves. The definition of the "collapse detector" is given as follows:

- Computational cells where the vapor volume content condenses completely during the last time step, are considered as "candidates". If the surrounding cells of a "candidate" contain liquid only, an isolated collapse is detected.

- Once a collapse is detected, the maximum pressure is generated at that instant in time, when the divergence of the velocity field changes its sign.
- The strength of the collapse is characterized by its maximum (negative) divergence and its maximum pressure.

The "collapse detector" offers two main advantages over just monitoring the maximum pressure. It automatically distinguishes the difference between the collapse maximum pressure and the high pressures due to stagnation points or wave interaction, and the number of collapse events, as well as their position, and their strength provide important information about a possible stress profile the material is exposed to. This information can be used to estimate erosion rates.

The main drawback of the "collapse detector" is the missing information of the collapse intensity on the material surface. To overcome this issue, Mihatsch et. al.[29] proposed an efficient projection method. The final pressure impact on the wall, p_{wall} is obtained, using the linear decay law, from the maximum pressure at the collapse center $p_{collapse}$, the distance of the collapse from the wall r_{wall}, and the cube root of the cell volume V_{cell}, where the collapse was detected

$$p_{wall} \sim \frac{\sqrt[3]{V_{cell}}}{r_{wall}} p_{collapse} \tag{3.11}$$

The "collapse detector" is designed for a density based compressible solver, where the pressure at the collapse center can reliably be estimated, given that sufficient temporal resolution has been applied, and any grid dependencies have been taken care of. In an incompressible flow, the prediction of maximum pressure is not assured and it is very sensitive to grid and time step resolution [35]. However, the number of the collapse events and their position can still provide very important information. Even though the collapse intensity may not be correctly predicted, multiple collapses around a specific area can indicate a high erosion risk. Furthermore, the detection of the "candidate" cell can be very useful for the reconstruction of the pressure driving the collapse. Thus, further investigation is needed, whether this model could be combined with other methods, suitable for pressure based incompressible solvers.

3.2.4. EVALUATION OF MODELS

The model by Dular and Delgoscha is based on the notion, that the damage is caused by the impingement of the liquid micro-jet, whereas in this paper we follow the hypothesis by Terwisga et. al. [21], that a synchronized bubble collapse can release much higher acoustic power, than the micro-jet from a single bubble. Furthermore, it is not obvious whether the water hammer pressure, which is considered as the damage mechanism in this model, is the dominant source of damage, when a liquid jet is formed. The stagnation pressure may contribute more to the surface material loss. Although its magnitude is somewhat lower, its duration is an order of magnitude larger.

The models by Mihatsch et. al. and Fortes Patella et. al., which are based on energy balance, are preferred for providing a more detailed physical basis. The model by Mihatsch et. al., however, requires a reliable prediction of the maximum pressure, originated by the collapse of vapor structures, which may not be reliably predicted by an in-

compressible pressure based solver. Thus, the energy balance approach by Fortes-Patella et. al. provides the best framework for erosion risk assessment using an incompressible pressure based URANS solver. The model used in this paper, described in section 3.4, has its basis on this approach.

3.3. NUMERICAL MODELING

3.3.1. GOVERNING EQUATIONS

The Reynolds Averaged Navier-Stokes (RANS) equations are solved using the commercial solver Star-CCM+, where each instantaneous quantity can be split into time-averaged and fluctuating components. The numerical simulations are based on FVM (Finite-Volume Method), and an incompressible segregated flow model is selected solving the integral conservation equations of mass and momentum in a sequential manner combined with the SIMPLE pressure-velocity coupling algorithm. For the time marching, a second-order implicit method is used, and for the convective terms, a second-order upwind scheme is adopted. From the basic principles of conservation of mass and momentum, the governing equations are written as follows:

$$\frac{\partial \rho}{\partial t} + \nabla \cdot (\rho \mathbf{u}) = 0 \tag{3.12}$$

$$\frac{\partial (\rho \mathbf{u})}{\partial t} + \nabla \cdot (\rho \mathbf{u}\mathbf{u}) = -\nabla p + \rho f + \nabla \cdot \tau \tag{3.13}$$

where $\mathbf{u}$ is the velocity tensor, ρ is the fluid density, p the pressure, ρf the exterior force density per unit mass and τ the viscous part of the stress tensor.

A homogeneous multiphase model is used, referred to as Volume of Fluid (VOF) in Star-CCM+, treating the fluid as a single continuum with two phases, assuming a no-slip condition between liquid and vapor phase, with varying properties in space according to its composition a_v. The vapor phase is transported in order to compute the vapor volume fraction. The liquid volume fraction is determined from the condition:

$$a_v + a_l = 1 \tag{3.14}$$

while density and viscosity are defined as:

$$\rho = a_v \rho_v + a_l \rho_l \qquad and \qquad \mu = a_v \mu_v + a_l \mu_l \tag{3.15}$$

respectively.

3.3.2. TURBULENCE MODELING

In this study the SST k-ω turbulence model, developed by Menter [36], is used (as result of previous study [37]. In order to fully resolve the boundary layer, the numerical mesh has been properly refined and a low-y+ wall treatment has been chosen. This approach effectively blends a k-ϵ model in the far field with a k-ω model near the wall. Reboud and Delannoy [38] showed the important role of the re-entrant jet on the cavity break-off cycle. However, the use of this turbulence model leads to very strong turbulent viscosity in the cavity wake hindering the re-entrant jet formation. It is stated by Reboud et al. [39],

that this effect, which is not representative of the real behaviour, has been analysed to be related to the hypothesis of homogeneous flow and its no-slip condition between the two phases. That no-slip condition behaves as an artificial increase of dissipation.

That problem has been treated by an empirical reduction of turbulence dissipative terms in the two-phase regions, by modifying the turbulent viscosity [39]

$$\mu_t = f(\rho) C_\omega \frac{k}{\omega} \tag{3.16}$$

$$f(\rho) = \rho_v + \frac{(\rho_m - \rho_v)^n}{(\rho_l - \rho_v)^{(n-1)}}; \qquad n \gg 1 \tag{3.17}$$

where ρ_v is the vapor density, ρ_l the liquid density and ρ_m the mixture density. For the constant n a recommended value $n = 10$ has been used. With this modification, the turbulent viscosity is modified in phase transition regions, according to the density change. Therefore, the numerical simulations are improved by taking into account the influence of the local compressibility effects of the vapor/liquid mixture on the turbulent structure, which where not considered before by the common two equation turbulence models for incompressible RANS methods.

3.3.3. CAVITATION MODELING

An additional conservation equation that describes the transport of vapor volume fraction α_v is solved

$$\frac{\partial \alpha_v}{\partial t} + \nabla \cdot (\alpha_v \mathbf{u}) = S_{\alpha_v} \tag{3.18}$$

In Eqn. 3.18, S_{α_v} represents the source of volume fraction of vapor. In order to account for bubble growth and collapse, a cavitation model should be introduced for the source term of the volume fraction of vapor. The cavitation model used in this study is the model proposed by Schnerr-Sauer [40] based on a simplified Rayleigh-Plesset equation, which neglects the influence of bubble growth acceleration, as well as viscous and surface tension effects:

$$\frac{dR}{dt} = sign(p_v - p) \frac{\sqrt{2 \mid p_v - p \mid}}{3\rho_l} \tag{3.19}$$

where p_v is the saturation pressure, p is the local pressure around the bubble and ρ_l is the fluid density. According to this rate, the source term in Eqn. 3.18 is defined as:

$$S_{\alpha_v} = \frac{4\pi R^2 n_0}{1 + (\frac{4}{3}\pi R^3) n_0} \frac{dR}{dt} \tag{3.20}$$

3.3.4. CAVITATION EROSION RISK ASSESSMENT

According to the approach of Fortes Patella et. al. [23], as described in section 2, pressure waves emitted during the collapses of vapor structures seem to be the main factor contributing to cavitation erosion. The potential energy of a cavity with volume V_v is given by Eqn. 3.1. It is interesting to note that, the model by Fortes-Patella et. al. (2004) defines the surrounding pressure (pressure driving the collapse) as the pressure at infinity, p_∞. This indicates, that the pressure driving the collapse is constant and equal to the pressure

at infinity. Here, the driving pressure term is further on referred to as p_d, denoting a general unknown pressure field driving the collapse, assuming that the pressure, surrounding the cloud cavities, differs from the pressure at infinity. Then, the instantaneous potential power, as defined in Eqn. 3.2, becomes

$$P_{pot} = (p_d - p_v) \cdot \frac{DV_v}{Dt} + \frac{Dp_d}{Dt} \cdot V_v \tag{3.21}$$

In Eqn. 3.21 both derivatives are considered, and they represent Lagrangian time derivatives. Therefore, the potential power density can be estimated in every cell from

$$\frac{P_{pot}}{V_{cell}} = (p_d - p_v) \cdot \frac{D\alpha_v}{Dt} + \frac{Dp_d}{Dt} \cdot \alpha_v \tag{3.22}$$

where $\alpha_v = V_v / V_{cell}$ is the void fraction. Furthermore, the void fraction is defined as $\alpha_v = (\rho - \rho_l)/(\rho_v - \rho_l)$, and from the local mass conservation $\partial\rho/\partial t + div(\rho u) = 0$ the potential power density becomes [24, 30]

$$\frac{P_{pot}}{V_{cell}} = (p_d - p_v) \cdot \frac{\rho}{\rho_l - \rho_v} div\mathbf{u} + \frac{\rho - \rho_l}{\rho_v - \rho_l} \left(\frac{\partial p_d}{\partial t} + \mathbf{u} \cdot \nabla p_d \right) \tag{3.23}$$

We assume that a change of energy in the domain, happens only when there is a change in the total vapor volume. Consequently, in this model, a vapor structure releases energy gradually as it condenses, and not instantaneously after its collapse. By looking the two terms of Eqn. 3.23 separately, only the first term describes volume change. The second term describes the change in ambient conditions that a bubble is experiencing for constant volume. As a cavity structure travels towards a positive/negative pressure gradient, its potential energy will change. However, it has no effect on the collapse energy balance, as long as it does not experience any volume change. Thus, the second term from Eqn. 3.23 should not be taken into account for the radiated energy. Furthermore, the effect of the pressure gradient on the energy release is depicted by the p_d term, as stated by Schenke and Terwisga[41]. Thus, the local impact rate $\dot{e}(t)$ is computed in every cell as follows:

$$\dot{e}(t) = -(p_d - p_v) \cdot \underbrace{\left(\frac{\partial \alpha}{\partial t} + u \cdot \nabla \alpha \right)}_{\frac{D\alpha}{Dt}} = -(p_d - p_v) \cdot \frac{\rho}{\rho_l - \rho_v} div\mathbf{u} \tag{3.24}$$

As it is shown in Eqn. 3.24, in a Eulerian reference frame, the local impact rate $\dot{e}(t)$ can be calculated either by the material derivative of the vapor volume fraction or the velocity divergence. To account only for condensation, $\frac{D\alpha}{Dt}$ (or $div\mathbf{u}$) should be negative, and a minus sign is needed to give a positive energy release. In both cases, an unknown error is introduced. The advective term $u \cdot \nabla\alpha$, and the velocity divergence term on the left hand side and the right hand side of Eqn. 3.24 respectively, cannot be computed directly, as after the discretization of the transport equation of the vapor volume, a combined term is computed, that includes the contribution of both terms. Thus, the divergence term cannot be separated from the advective term, and each one of them needs to be reconstructed. The reconstruction of these terms is responsible for the numerical error. Nevertheless, it is assumed that the advective term has a much smaller contribution to the

volume change than the divergence term, allowing us to compute the local impact rate $\dot{e}(t)$ from the partial derivative of the vapor volume $\frac{\partial \alpha}{\partial t}$

$$\dot{e}(t) = -(p_d - p_v) \cdot \frac{\partial \alpha}{\partial t} = -(p_d - p_v) \cdot \left(\frac{\rho}{\rho_l - \rho_v} div\mathbf{u} - u \cdot \nabla \alpha \right) \tag{3.25}$$

Assuming that each point source emits its potential energy as a radial wave of infinitely large propagation speed, Leclercq et. al. [24] define the potential power impact on the material surface $\dot{e}_S(t)$ using an algebraic approximation, which is based on the solid angle projection on a planar triangle. Schenke and Terwisga [25] proposed a continuous form of the energy impact rate on a surface location. In the present work, it is hypothesized that the vapor structures, which are in contact with the surface, are much more aggressive than any other structure, in further distance from the wall. This hypothesis is based on the work of Phillip and Lauterborn [10], where they demonstrated that the largest erosive force is caused by the collapse of bubbles in direct contact with the boundary. Thus, we assume that the impact from the structures in direct contact with the surface, is much higher than any impact from any other structure away from the surface. Therefore, it is not required to calculate the distance and the projection of any vapor structure, adding no further computational cost. The local impact power is evaluated only on the first prism layer, and the surface face value is obtained. The velocity in those cells is practically zero, thus the advective term, emerging on the right hand side of Eqn. 3.25 can be considered negligible, while the velocity divergence not necessarily, due to the finite volume formulation. This gives an extra credit to our assumption, that the condensation process is dominant, and the advective term has a much smaller contribution to the volume change. The local surface impact rate $\dot{e}_S(t)$ is then computed from the partial derivative of the vapor volume fraction $\frac{\partial \alpha}{\partial t}$, minimizing the numerical error. However, this needs further investigation.

The ambient pressure field, p_d, effectively driving the cavity collapse, introduces the largest uncertainty in the erosion risk assessment. The determination of this quantity is not straightforward for complex flow conditions. The local instantaneous cell pressure cannot be used as an estimate for the driving pressure, as the driving pressure needs to be computed at the same location where energy is radiated. There, the local pressure is almost equal to the vapor pressure, leading to a driving pressure difference $p_d - p_v$ close to zero. This is also depicted by the density-pressure trajectory, which should be very close to vapor pressure during phase change. On top of that, the driving pressure is practically never exactly constant in space [41]. In this study, the time averaged pressure field is computed, from the instantaneous pressure field p_i in cavitating flow conditions, assuming this field to be the ambient pressure field driving the cavity collapses. This field is steady, and it is computed in the whole domain before the erosion risk assessment. In this way, we can at least get a rough estimate of the conditions that collapsing cavities experience on statistical average [25, 37].

To address the cavitation erosion risk on the surface (since the local surface impact rate $\dot{e}_S(t)$ is known) , two aggressiveness indicators are used as proposed by Schenke and Terwisga [25]:

$$\langle \dot{e}_S \rangle_{e_S} = \left(\frac{1}{e_S} \int_0^t \dot{e}_S^{n+1} dt \right)^{1/n} \tag{3.26}$$

and

$$\langle \dot{e}_S \rangle_f = \left(\frac{1}{T} \int_0^t \dot{e}_S^{n+1} dt \right)^{1/(n+1)} \tag{3.27}$$

where

$$e_S = \int_0^t \dot{e}_S dt \tag{3.28}$$

The indicator $\langle \dot{e}_S \rangle_{e_S}$ averages the local energy impact rate over the surface accumulated energy e_S, amplifying the local extreme events, and being independent from the impact frequency. On the other hand, the indicator $\langle \dot{e}_S \rangle_f$ is normalized by the total impact time T. It is proportional to the frequency of the impact, showing converging behavior as the impact time $T \to \infty$ [25]. The parameter n is used to emphasize the peak events. The indicators work as a generalized mean value (also known as power mean or Hölder mean). Each mean value lies between the smallest and the largest impacts, and it gets closer to the largest impacts, as the n parameter increases, converging to the maximum peak value as $n \to \infty$.

To allow a fair qualitative comparison between the indicators for different values of the n parameter, we further normalize each indicator by the maximum aggressiveness indication on the surface, for each parameter n

$$\langle \dot{e}_S \rangle'_{e_S} = \frac{\left(\frac{1}{e_S} \int_0^t \dot{e}_S^{n+1} dt \right)^{1/n}}{max\left(\langle \dot{e}_S \rangle_{e_{S,n}} \right)} \tag{3.29}$$

and

$$\langle \dot{e}_S \rangle'_f = \frac{\left(\frac{1}{T} \int_0^t \dot{e}_S^{n+1} dt \right)^{1/(n+1)}}{max\left(\langle \dot{e}_S \rangle_{f,n} \right)} \tag{3.30}$$

By using this feature scaling, we bring each indicator into the range [0,1]. Thus, we can easier identify the areas with high erosion risk and better analyze the whole impact distribution on the surface.

3.4. TEST CASE

The simulated hydrofoil is the Delft Twist 11 hydrofoil (Fig. 3.2). The section of the foil is a NACA 0009 hydrofoil with an angle of incidence that changes along the spanwise direction

$$a(\overline{y}) = a_{max}(2 \mid \overline{y} - 1 \mid^3 - 3(\overline{y} - 1)^2 + 1) + a_{wall} \tag{3.31}$$

where $a_{max} = 11$deg the maximum angle of attack at the mid span, $\overline{y}$ is non-dimensionalised with the chord length c and varies over the spanwidth ($0 \leq \overline{y} \leq 2$) with $\overline{y} = 0$ at the wall. The chord length and the spanwise length are $150mm$ and $300mm$ respectively. The twisted design and the larger angle of attack in the middle area cause the cavitation to mainly develop near the mid-span.

The hydrofoil is simulated in wetted flow ($u_{in} = 6.75m/s$, $P_{out} = 97kPa$) and cavitating flow ($u_{in} = 6.97m/s$, $\sigma = 1.07$) in -2 degrees angle of incidence and water temperature 24°C. A no-slip condition is applied on the foil and slip condition on the walls, as no cavitation development is expected near the tunnel walls. A symmetry plane is used at the

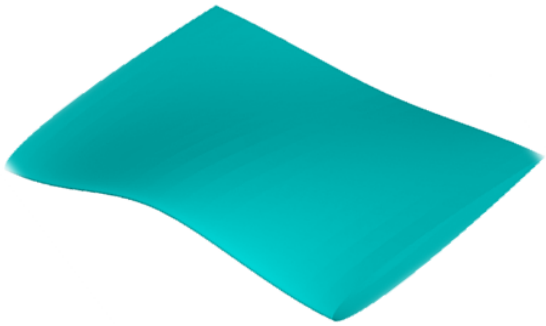

Figure 3.2: Geometry of the Delft Twist 11 hydrofoil

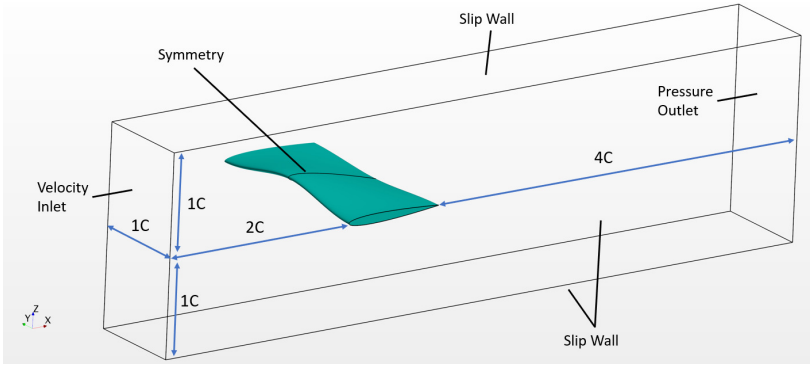

Figure 3.3: Description of the computational domain and the boundary conditions

mid-span to reduce the computational cost. Figure 3.3 shows the computational domain and the imposed boundary conditions.

For the grid generation, trimmed hexahedral cells are used with local refinements and prism layers along the wall, with such first cell distance so the average y+ value is well below 1 to resolve the viscous sublayer. Several refinement levels are applied (Fig. 3.4). To ensure the geometrical similarity on the meshes for the assessment of numerical uncertainty, the following approach was used for the prism layer mesh, proposed by Crepier [42]:

$$S_n = S_0 \frac{1 - r_1^{1/n}}{1 - r_1} \qquad and \qquad r_n = r_1^{1/n} \tag{3.32}$$

where S_0, r_1 the first cell size and the growth ratio of the initial coarse grid respectively and S_n, r_n the first cell size and the growth ratio of the grid refinement n ($n = 1$ for the coarse grid).

The analysis for the erosion risk assessment is carried out under different flow conditions, and a slightly smaller foil geometry, so that we are in line with the experiment by Cao et. al. [26]. The inflow is $14 m/s$, at 0° angle of incidence at the wall and 11° at the

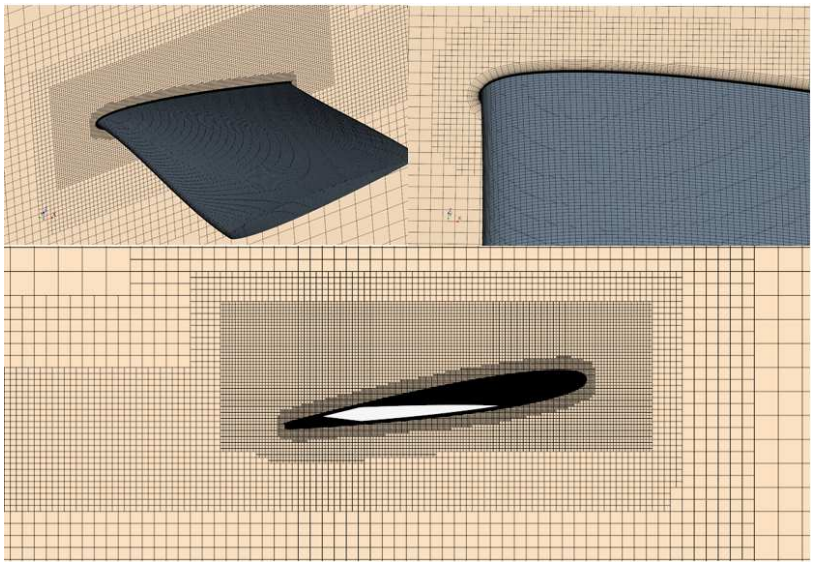

Figure 3.4: Grid refinement levels around the foil

mid-chord, and a cavitation number $\sigma = 1.2$, resulting in an ambient pressure of about $120kPa$. The chord length and the spanwise length are $112.5mm$ and $225mm$ respectively. The identified erosion regions, after the three-hour paint test, are compared with our predicted impact distributions, obtained with the two aggressiveness indicators.

3.5. RESULTS

A verification and validation study is conducted in wetted and cavitating flow. An extensive grid and time-step size sensitivity study is presented in the following section (section 3.5.1), showing an impression of the uncertainty estimates. The results are validated against experimental data. Finally, the cavitation erosion risk is assessed and compared with the obtained impact distribution from paint test [26] (section 3.5.2).

3.5.1. VERIFICATION AND VALIDATION

WETTED FLOW

The results for the lift coefficient and the pressure distribution in wetted flow are presented and compared with experimental data. The Validation & Verification tool, developed by MARIN[2], has been used to assess the numerical uncertainty. The analysis is based on the procedure given by Eca and Hoekstra [43]. Tab. 3.1 shows the lift force, for different grid densities. The deviation from the experimental value ($L_{exp} = 455N$) is less than 4% for all the grids.

Figure 3.5 shows the convergence of the lift force with the grid refinement ratio $\frac{h_i}{h_1}$ (where h_i and h_1 the typical cell size of each grid and the finest grid respectively), and

[2]http://www.refresco.org/verification-validation/utilitiesvv-tools/

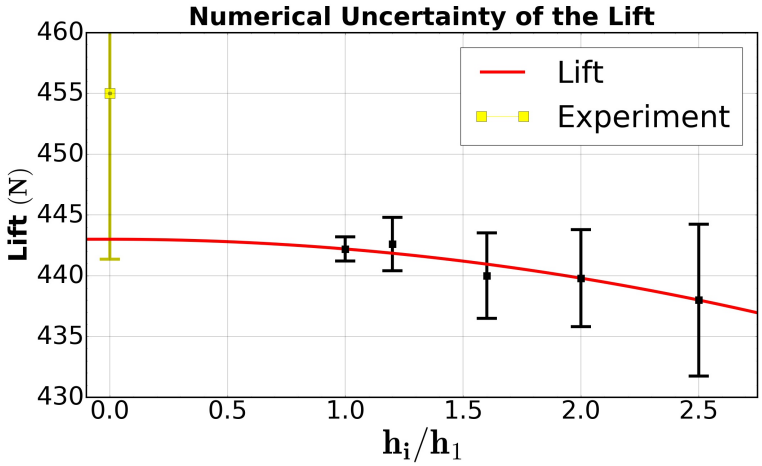

Figure 3.5: Convergence of the lift force with the grid refinement ratio. Impression of the numerical uncertainty estimates.

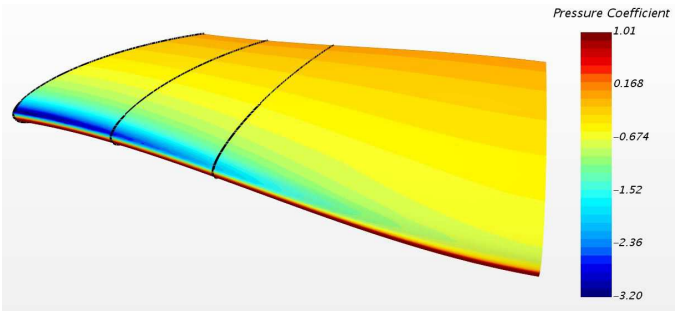

Figure 3.6: The different planes where the pressure distributions are compared with experimental data

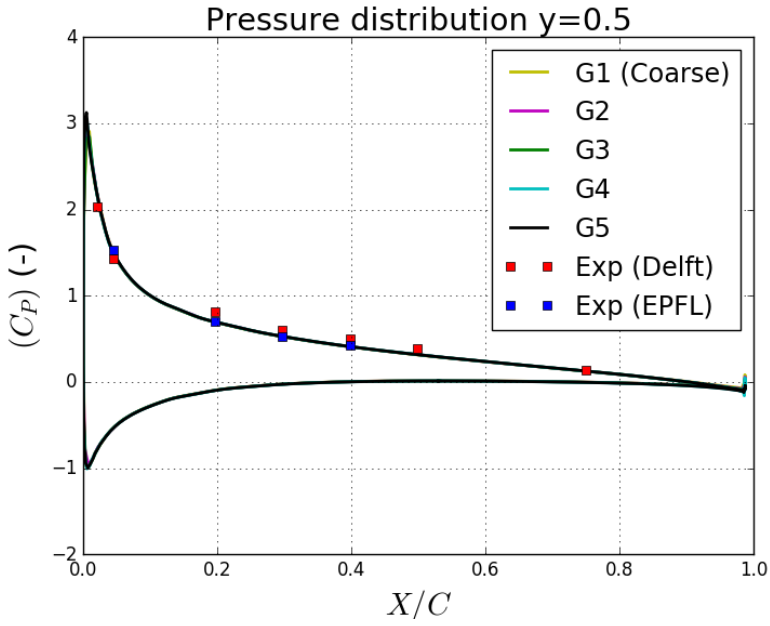

Figure 3.7: Pressure distribution at the 50% of the span

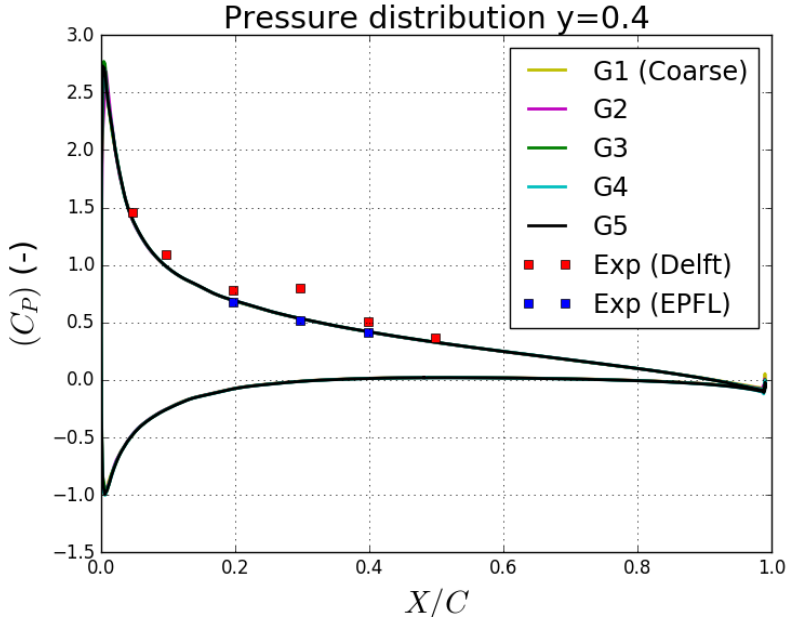

Figure 3.8: Pressure distribution at the 40% of the span

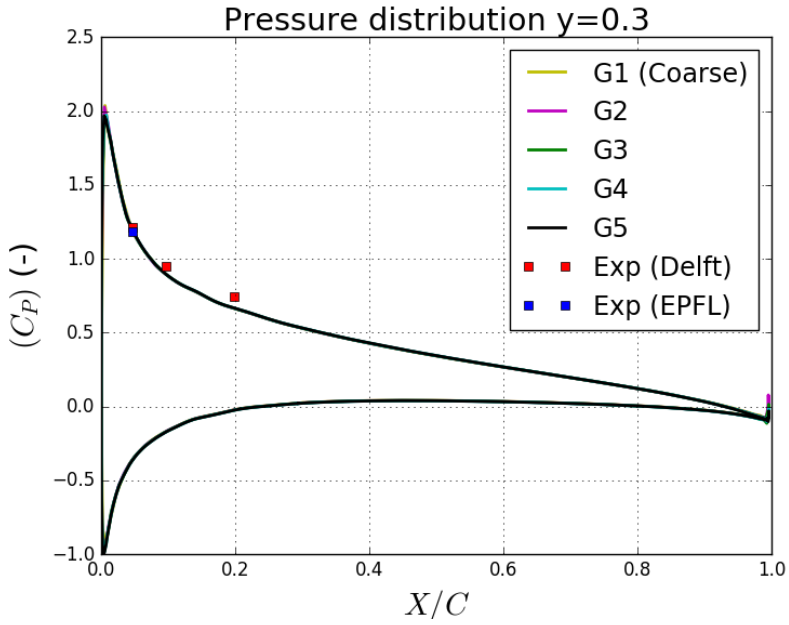

Figure 3.9: Pressure distribution at the 30% of the span

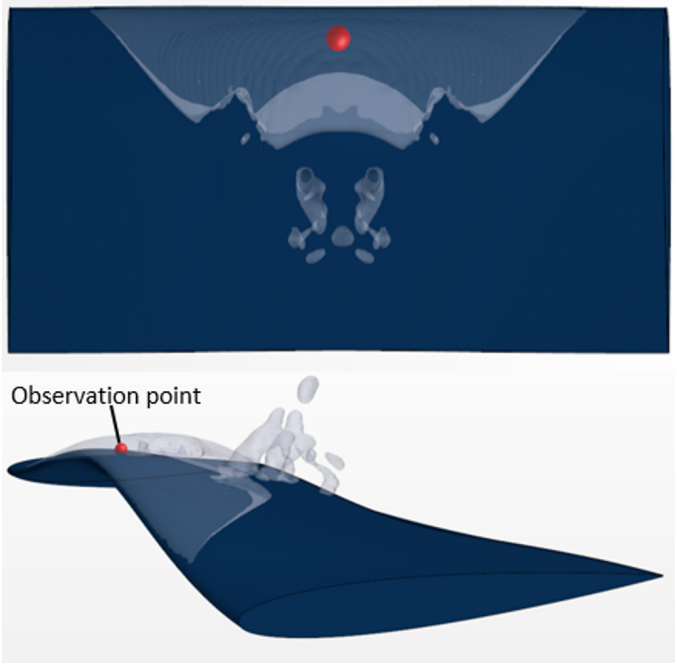

Figure 3.10: Observation point P1, close to the surface

Table 3.1: Number of cells, grid refinement ratio, average Y+ value, lift force and its numerical uncertainty for each grid

Grid	# Cells (10^6)	hi/h1	$\overline{y+}$	Lift (N)	U %
G1	0.59	2.5	0.79	438	1.41
G2	1.05	2	0.63	439.8	0.9
G3	2.07	1.6	0.49	440	0.79
G4	4.17	1.2	0.37	442.6	0.5
G5	7.08	1	0.34	442.2	0.23

the uncertainty estimates. The corresponding numerical uncertainty is indicated by an interval that contains the exact solution with 95% coverage. The observed order of convergence is equal to the theoretical one ($P = 2$), resulting in a low uncertainty for all grids (1.4% for the coarsest grid and 0.2% for the finest grid). The difference between the computed lift force and the measurements is higher than the numerical uncertainty in any of the cases. Nevertheless, the experimental uncertainty has been reported to be significantly high [44]. By assuming an uncertainty as low as 3%, the results for each grid density is within the acceptable range (Fig.3.5).

The pressure distribution is also calculated in three different planes along the chord of the foil and is compared with experimental data. Two experimental datasets are available, from two different cavitation tunnels. The first dataset has been obtained at the Delft University of Technology, and the second one at the École Polytechnique Fédérale de Lausanne (EPFL). The test section of the cavitation tunnel in Delft is twice as big as the test section in Lausanne. The dimensions of our numerical "tunnel" are identical to the ones of the Delft cavitation tunnel, with only difference an extension downstream of the foil, to avoid interaction of the flow with the outlet boundary. Fig. 3.6 shows the planes where the pressure distribution is measured, and Fig. 3.7-3.9 show the comparison between the different grid densities and the experimental results at each plane. A small sensitivity to the grid density is observed for the pressure at the leading and trailing edge, although it is negligible. A very good agreement is obtained with the EPFL measurements. The Delft measurements show somewhat higher pressure in the area between the 10% of the chord and the mid-chord. However, the difference is small enough to assume that the numerical results lie within the experimental uncertainty.

CAVITATING FLOW

The hydrofoil is tested in cavitating flow, for 4 different meshes (G1-G4 from Tab. 3.1) and 5 different time-step sizes. The time-step size is chosen by selecting the number of time-steps during a collapse. The collapse time of a shedded cloud can be calculated from the analytical solution of the Rayleigh-Plesset equation by just estimating the radius of the cloud

$$T_C^2 = \frac{(\xi^2 R_0 \rho)}{p} \tag{3.33}$$

where $\xi = 0.915$ is the Rayleigh factor, ρ the liquid density, p the far-field pressure and R_0 the bubbly cloud radius. By estimating the collapse time, we can determine in advance

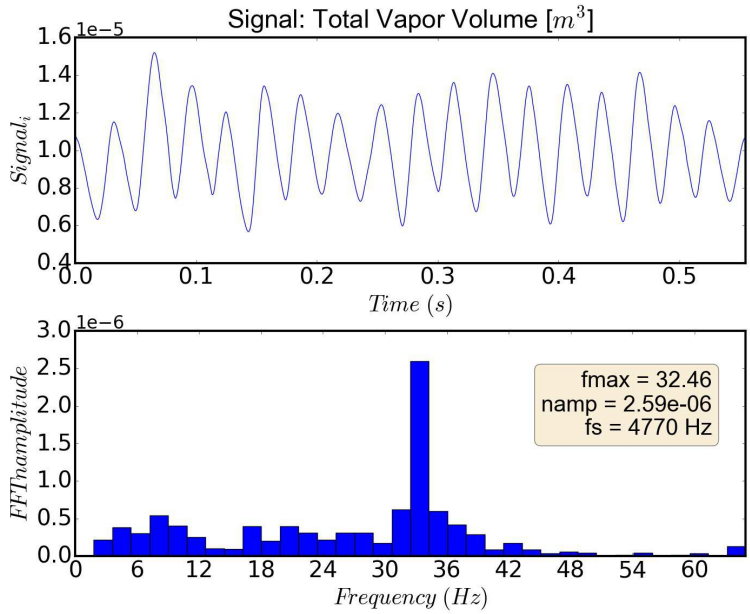

Figure 3.11: Time history of the total vapor volume (top), and its spectral analysis (bottom)

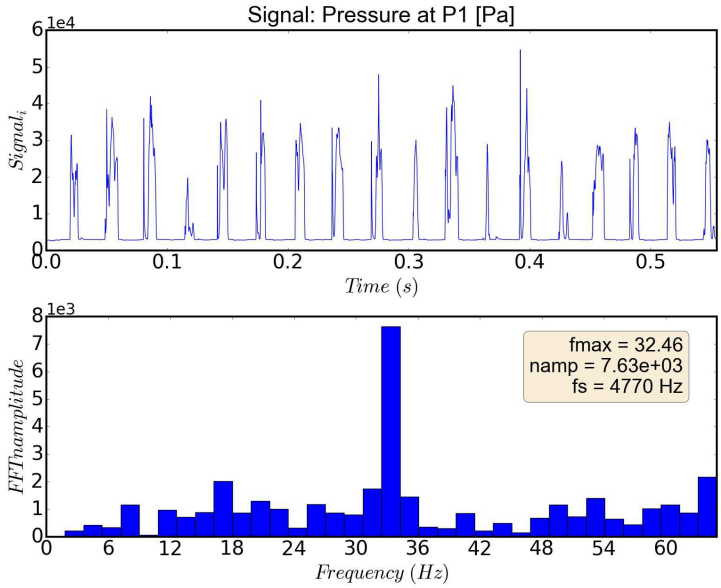

Figure 3.12: Time history of the pressure at the observation point P1 (top), and its spectral analysis (bottom)

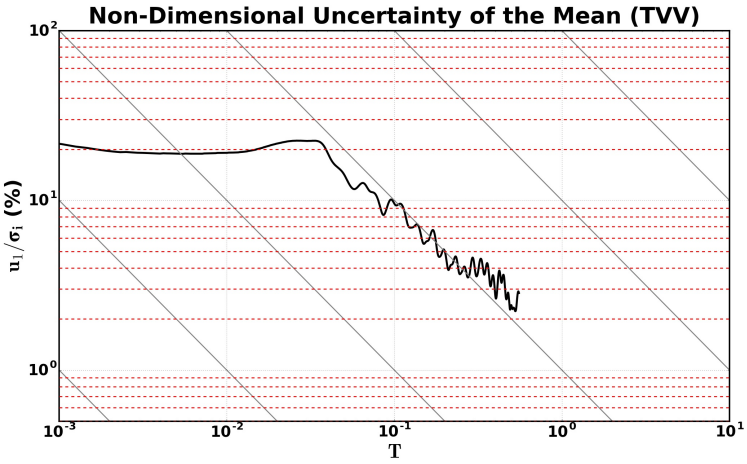

Figure 3.13: TST results for the total vapor volume, after removing a section at the beginning

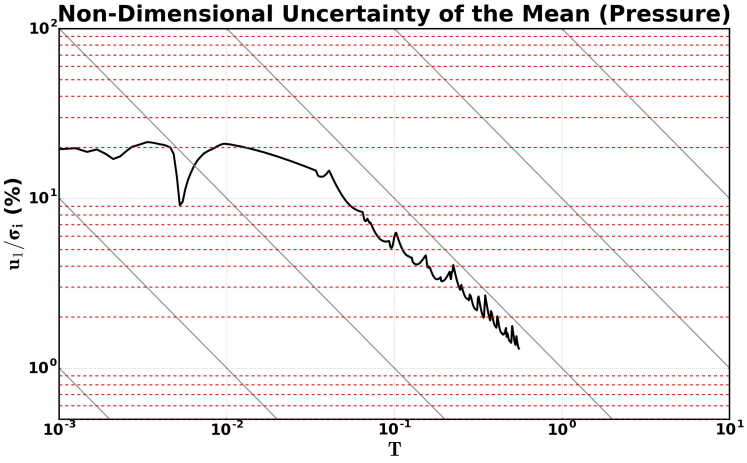

Figure 3.14: TST results for the pressure signal at the observation point P1, after removing a section at the beginning

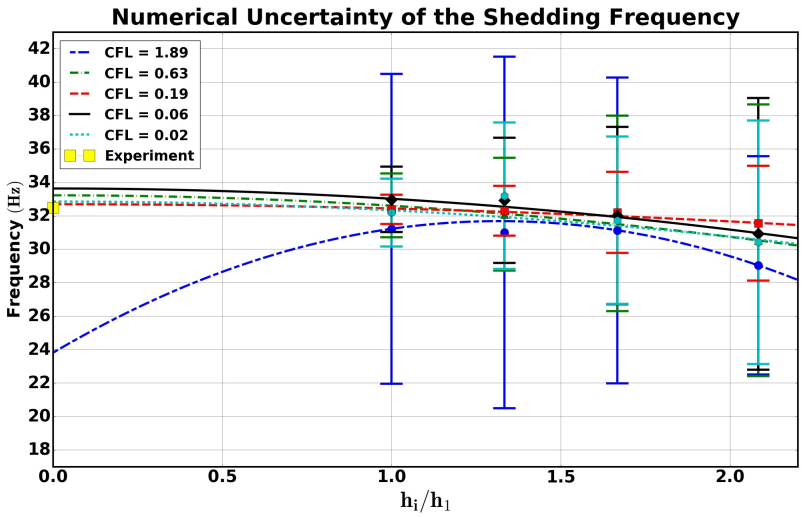

Figure 3.15: Convergence of the shedding frequency with the grid refinement ratio. Impression of the numerical uncertainty estimates for different reference courant numbers.

the number of time-steps during the collapse and therefore the time-step size for each computation. The number of time-steps is selected for the coarsest grid, assuming an average cloud radius of 1 mm. This number is chosen arbitrarily, as it is just an initial indication. We just consider a radius, that is much smaller than the size of the largest structures observed in the experiment. The final time-step size is determined by the uncertainty assessment. For the rest, the time-step size is computed so that a reference Courant Number remains constant. The reference Courant Number is defined as

$$CFL_{ref} = \frac{u_{in}\Delta t}{\Delta x} \tag{3.34}$$

where u_{in} is the inflow velocity, Δt is the time-step and Δx is the length of the smallest typical cell in x-direction.

The shedding frequency is derived from a Fast Fourier Analysis (FFT) of the total vapor volume history (Fig. 3.11), and the pressure signal (Fig. 3.12) on the observation point P1 shown in Fig. 3.10. To make sure that both signals are stationary, and to quantify the statistical uncertainty, the Transient Scanning Technique (TST) has been used [45, 46]. The TST is a practical tool, developed within MARIN, to verify whether the mean value is constant or not, by locating trends in signals, at the beginning or at the end of the series. For CFD simulations, we only have to make sure that the end solution does not depend on the start solution anymore. There are two methods to estimate the statistical uncertainty, the autocovariance method and the segment method (for more information see [45]). Both methods provide an estimate for the standard deviation of the mean s_m, called u_1, the standard uncertainty of the mean. In this study we use the autocovariance

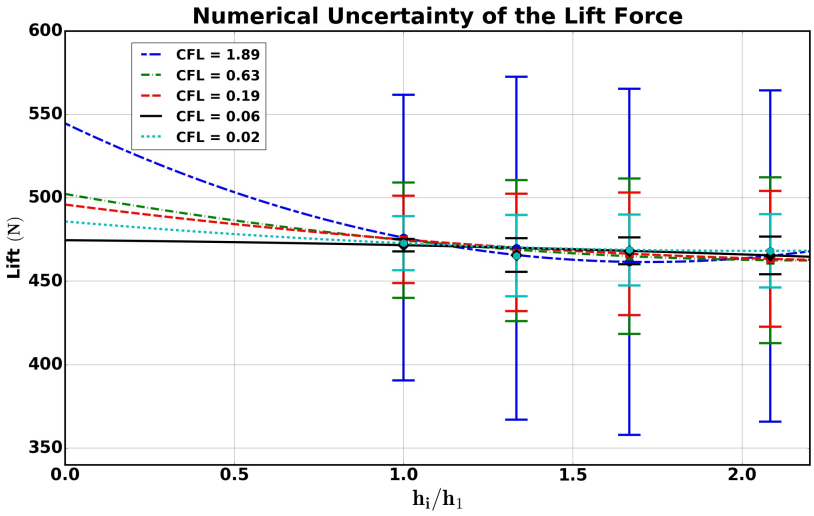

Figure 3.16: Convergence of the lift force with the grid refinement ratio. Impression of the numerical uncertainty estimates for different reference courant numbers.

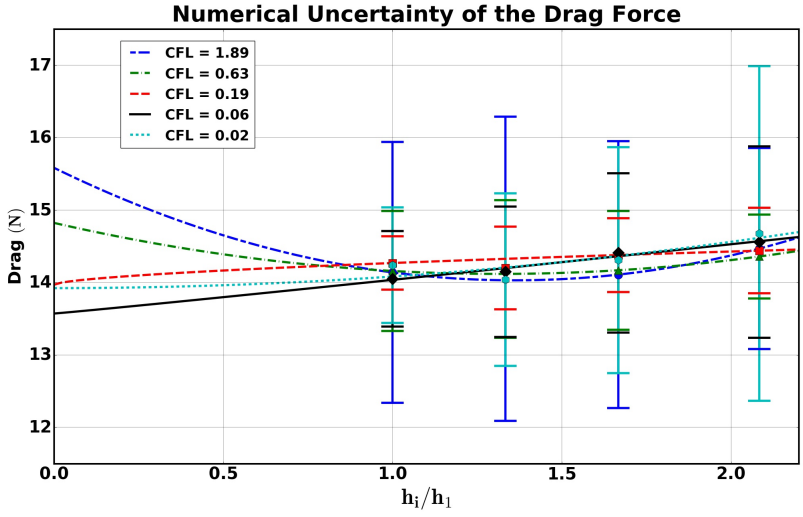

Figure 3.17: Convergence of the drag force with the grid refinement ratio. Impression of the numerical uncertainty estimates for different reference courant numbers.

Table 3.2: Comparison between the computed shedding frequency and the experimental frequency, as well as the frequency obtained from other numerical studies

Reference	Shedding Frequency
Foeth (Experiment) [47]	32.55 Hz
I. Oprea [48]	31 Hz
S. Muzaferija [49]	32 Hz
Vaz et. al. [44]	32.5 Hz
Current study	≈ 32.46 Hz

method, therefore, u_1 is calculated as follows:

$$u_1 = \sqrt{\frac{1}{T}\int_0^T \left(1 - \frac{\tau}{T}\right) C_{xx,biased}(\tau) d\tau} \tag{3.35}$$

where $C_{xx,biased}(\tau)$ is the biased estimator for the autocovariance [45]. Using the TST based on cumulative u_1 calculated from the end of the signal, we can identify any start-up effect. For the signal to be stationary, u_1 should decay with the inverse of T, without showing any sudden rise ("hockey stick" [46]). Fig. 3.13 and Fig. 3.14 show the cumulative u_1, non-dimensionalized with the standard deviation of the process σ_i, in function with the section size T, for the total vapor volume, and the pressure signal on the observation point P1 respectively. A statistical uncertainty lower than 3% has been reached for the total vapor volume, and lower than 1.5% for the pressure signal.

The numerical uncertainty is assessed in the same way as for the wetted flow condition. The results are shown in Fig. 3.15-3.17, where the convergence of the shedding frequency, the lift and the drag force with respect to the grid refinement ratio h_i/h_1 is indicated. For the shedding frequency, although some data points fairly deviate from the least square fit (scatter), especially for G3 (h_i = 1.33), the order of convergence reaches the theoretical one for CFL_{ref} below 1, giving an estimate of the exact solution between 32 and 34 Hz. An uncertainty of around 6% is achieved for CFL_{ref} below 1, apart from CFL_{ref} = 0.19, where the uncertainty drops below 3%. A good agreement is achieved with the experimentally obtained frequency, as well as other numerical studies (Tab. 3.2).

For the lift force, the order of convergence is not approaching the theoretical one. The same for the drag force, apart from the smallest time-step size. There are two main reasons for that. First, the coarse mesh (G1) might be too coarse that should have been excluded from the fit. In that case, an even finer mesh should be used. Second, the grids are not totally geometrically similar, increasing the chance of scatter in the results. However, the uncertainty is even lower than the one for the shedding frequency. For the lift force the discretization error is below 4% for CFL_{ref} = 0.02, and even below 1% for CFL_{ref} = 0.06. For the drag force, the uncertainty is around 6% for CFL_{ref} below 1, except for CFL_{ref} = 0.19, where the uncertainty is less than 3%.

Furthermore, the time averaged pressure distribution at the mid span (Fig. 3.18) is also compared with experimental measurements. The results are insensitive to grid and time step resolution. They agree well with the pressure data from EPFL, but they deviate

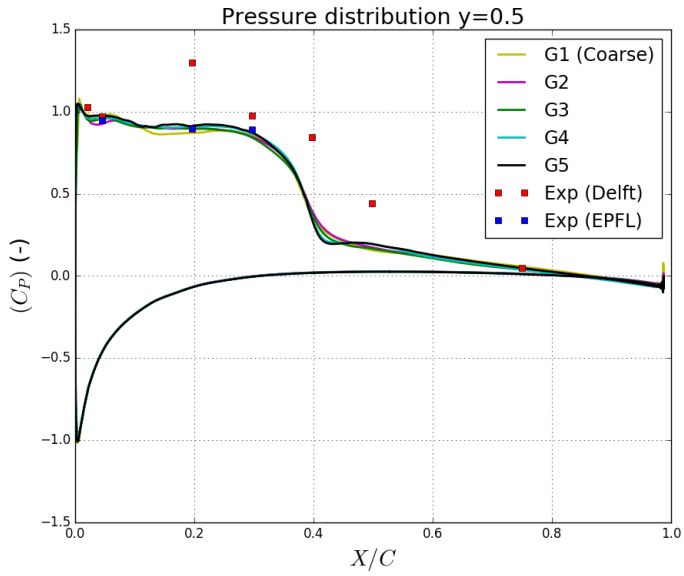

Figure 3.18: Time averaged pressure distribution at the midspan for different grid densities. Comparison with experimental measurements.

from the data from TU Delft, underestimating the length of the sheet cavity (Fig. 3.18). The qualitative comparison between the shedding cycle from the PIV imaging and the computations, visualized as an isosurface of $a_v = 0.01$ (see Fig. 3.19), shows similar behaviour. Although a good agreement with the shedding frequency is obtained, we observe a slightly smaller sheet cavity length. Nevertheless, both the experimental and numerical observations are instantaneous snapshots of one shedding cycle, while the shedding process is a random process with variable vapor volume in each cycle.

3.5.2. CAVITATION EROSION RISK

From the grid and time-step sensitivity study in the previous section, the finest grid (Grid 4 in Tab. 3.1) is used for the erosion risk prediction and the chosen time-step corresponds to $CFL_{ref} = 0.19$ ($dt = 6.1e-06s$). First, we estimate cavitation aggressiveness, on the foil surface, for five different inflow velocities at the same cavitation number. The surface potential power density $P_{pot}/\Delta S$ is computed, for each velocity, as the total accumulated energy on the surface E_S, divided by the sample time T and the surface area ΔS. Flow aggressiveness potential power density increases approximately as $P_{pot} \sim u_{in}^{3.2}$ showing a similar trend with experiments [16], as well as other numerical studies [24, 50].

The time averaged pressure field $\overline{p_t}$ is computed from the local instantaneous pressure field p_i, under cavitating flow conditions, assuming this field to be the ambient pressure field driving the collapses. Figure 3.21 shows the evolution of both signals in time, at the observation point P1. After $\overline{p_t}$ has converged in each volume cell, a distinct pressure recovery region is distinct (Fig. 3.22), compared to the instantaneous pressure field (Fig.

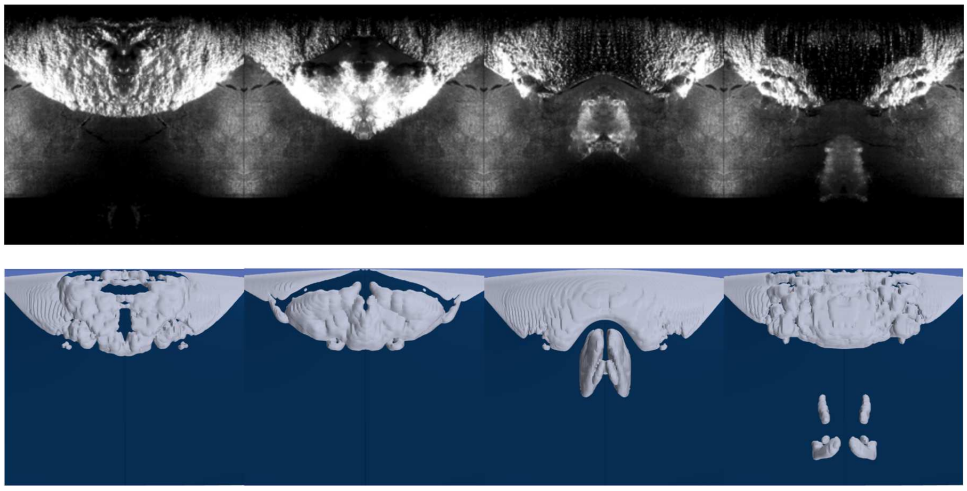

Figure 3.19: Qualitative comparison between the PIV imaging and the simulated shedding cycle, visualized as an isosurface of $a_v = 0.01$.

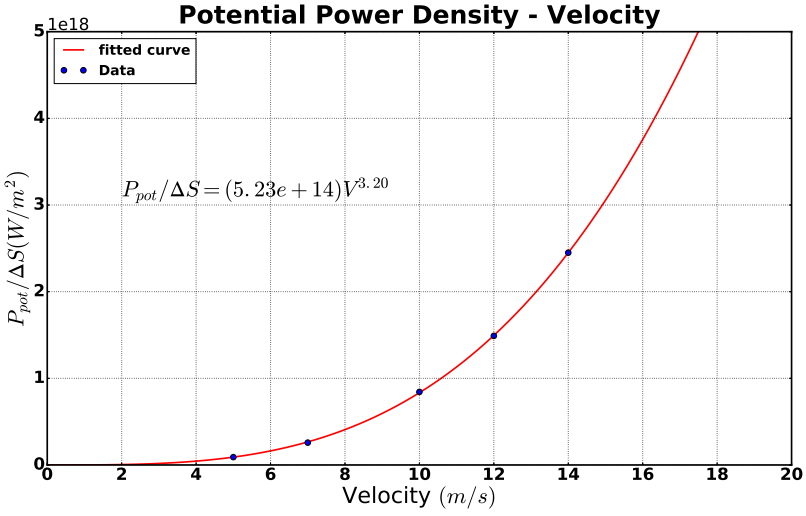

Figure 3.20: Flow aggressiveness potential power density, as a function of the flow velocity

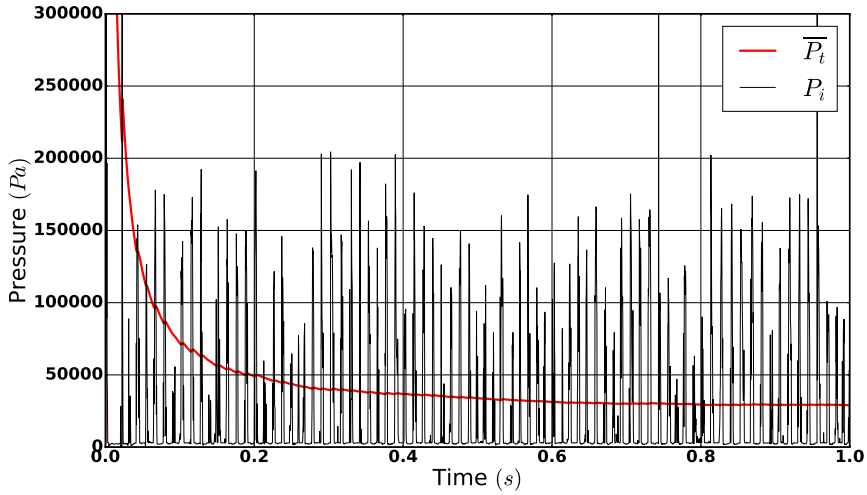

Figure 3.21: Pressure Signal and the time averaged pressure evolution at the observation point in Fig. 3.10

3.23).

Figure 3.24 depicts the distribution of the accumulated surface energy e_s, when (a) the instantaneous pressure p_i or (b) the time averaged pressure $\overline{p_t}$ is used as the driving pressure. When the instantaneous pressure field is driving the collapses, we would expect that the energy accumulated on the surface is negligible, as the instantaneous pressure in areas where phase transition occurs should be equal to vapor pressure (see also sec. 3.3.4). However, as a matter of fact, the driving pressure difference $p_d - p_v$ is not close to zero, resulting in accumulation of collapse energy close to the leading edge. Similar trend has been found by Li and Terwisga [51], where they also used the instantaneous local pressure as driving pressure, and inevitably predicted high impact rates close to the leading edge. Nevertheless, the non-zero driving pressure difference may be considered as a numerical artifact, due to the cavitation modeling approach. It strongly depends on the mass transfer source term and the evolution of the density-pressure trajectory. The closer it gets to the vapor pressure during phase change, the smaller the driving pressure difference, and therefore the accumulated surface energy. On the other hand, when we account for the effect of spatial pressure recovery, large impact rates emerge towards the trailing edge region (Fig. 3.24 (b)).

The rapidness of the local impacts is assessed by the two aggressiveness indicators $\langle \dot{e}_S \rangle_f$ and $\langle \dot{e}_S \rangle_{e_S}$ given by Eqn. 3.30. Both indicators have been tested for different n values (see Fig. 3.25). Indicator $\langle \dot{e}_S \rangle_f$ seems to be more sensitive to the n parameter, showing different impact distributions for different n values. Low n, results in large impact rates at the leading edge, which are getting lower as the n increases, resulting in larger predicted impact rates towards the trailing edge, with similar magnitude. Indicator $\langle \dot{e}_S \rangle_{e_S}$ is less sensitive to the n constant, showing similar impact distributions for different n values, however with larger magnitude for higher n values. Qualitatively, both indicators show

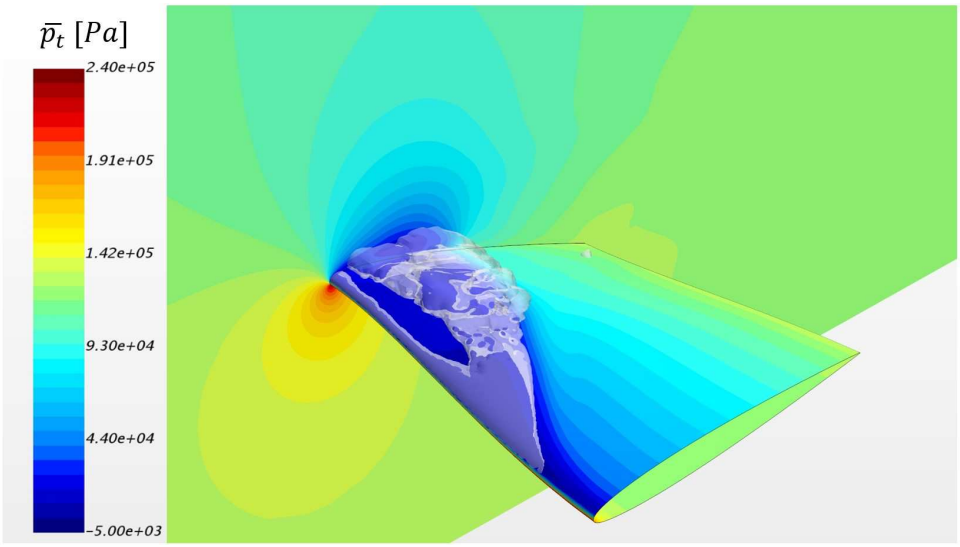

Figure 3.22: Time averaged pressure field $\overline{p_t}$ after it has converged in each volume cell, showing a distinct pressure recovery region

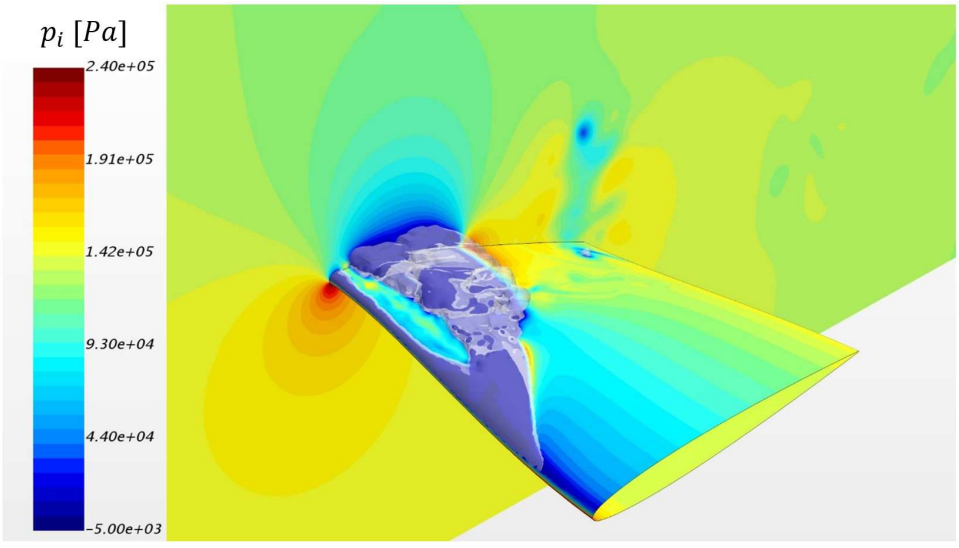

Figure 3.23: Instantaneous pressure field p_i for a random instant of time

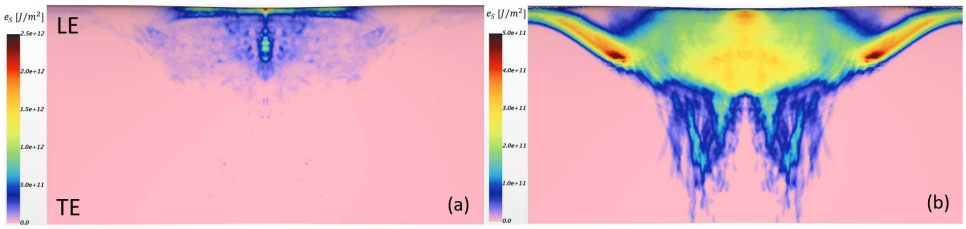

Figure 3.24: Accumulated energy on the surface (a) for the instantaneous pressure field p_i or (b) the time averaged pressure field $\overline{p_t}$

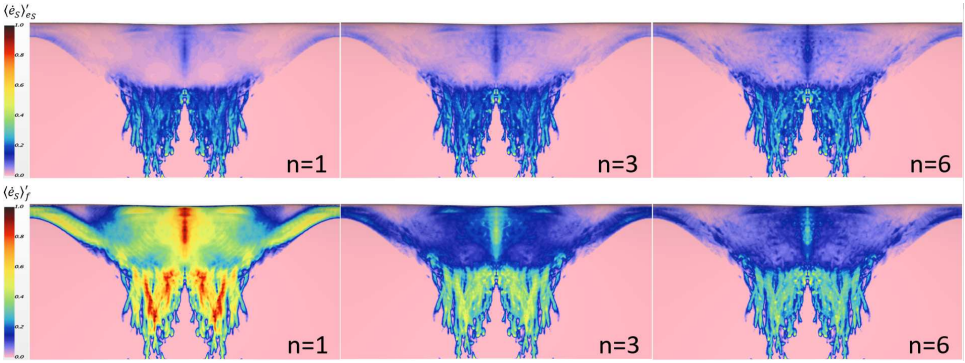

Figure 3.25: Surface impact distribution for different values of the parameter n, for each aggressiveness indicator $\langle \dot{e}_S \rangle'_{e_S}$ (top) and $\langle \dot{e}_S \rangle'_f$ (bottom)

similar aggressiveness distribution for high n values. The high erosion risk regions on the surface show a good qualitative agreement with the damage pattern obtained by Cao [26] in Fig. 3.26. High erosion risk was predicted in all three regions, identified from experimental paint tests.

3.6. CONCLUSION

Cavitation erosion can cause severe damage to the propeller blades, and gives opposite design trends to fuel efficiency, rendering cavitation erosion risk assessment imperative, already in the design stage. Making an early stage propeller erosion assessment requires

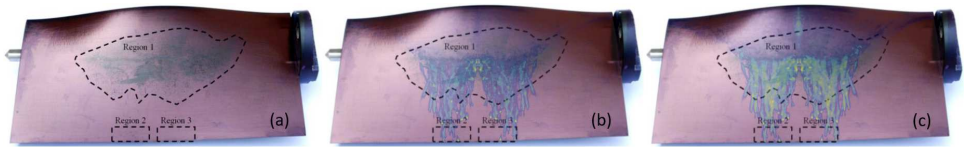

Figure 3.26: Comparison between the surface impact distributions obtained from (a) three hours of paint test, (b) the indicator $\langle \dot{e}_S \rangle'_{e_S}$ and (c) the indicator $\langle \dot{e}_S \rangle'_f$. The CFD solution, n=6 for both indicators, has been plotted on the actual surface to compare the eroded regions with the paint test.

balance between sufficient numerical resolution and computational effort. In this study, the shock wave emission, originated by the collapse of cloudy vapor structures, is considered as the most aggressive mechanism for cavitation erosion. Therefore, a validation and verification study has been conducted on the ability of a URANS solver, treating the pure phases as incompressible, to predict those cavity structures and the consequent energy transfer to the surface of the Delft Twist 11 hydrofoil. The following conclusions are drawn:

- In wetted flow, the prediction of the lift force and the pressure distribution on the foil is in good agreement with the experimental measurements. The numerical uncertainty for the generated lift is lower than 1% for all mesh densities (apart from the coarsest grid).

- In the cavitating conditions, the shedding frequency converges with the grid refinement ratio, according to the theoretical order of convergence, and agrees well with the experimental frequency. The numerical uncertainty is somewhat higher than in wetted flow, however is less than 3% in the best case ($CFL_{ref} = 0.19$). The lift generated force does not converge with the grid refinement ratio, thus a finer mesh should be used for the uncertainty analysis. The same holds for the drag force, apart from the smallest time-step size, which follows the theoretical order of convergence. Nevertheless, the uncertainty estimates are quite low for the finer meshes (3% for the drag and even lower than 1% for the lift force).

- The flow aggressiveness in cavitating flow conditions has been estimated, following the energy balance approach proposed by Fortes Patella [16], and further elaborated by Flageul et. al. [30], Leclercq et. al. [24] and Schenke [25]. We found that the cavitation aggressiveness potential power increases as $u_{in}^{3.2}$, being in line with experimental [16] and other numerical results [24, 50].

- The effect of the pressure field driving the collapse has been investigated. Accounting for special pressure recovery, by time averaging the local pressure field, strongly affects the distribution of the accumulated energy on the surface, originated by the initial potential energy in the cavities. Next to that, the rapidness of the collapse event has been evaluated with two aggressiveness indicators. A parameter n is used to emphasize the peak events with higher amplitude. The indicator $\langle \dot{e}_S \rangle_f$, normalized by the total impact time, seems to be more sensitive to the n parameter. However, both indicators give similar impact distributions, when a high n value ($n = 6$), in combination with the time averaged driving pressure field are used. The distributions agree well with the erosion pattern obtained from the paint test [26], indicating high erosion risk in all three identified regions.

3.7. DISCUSSION

As a first assessment, our main hypothesis that the vapor structures, which are in contact with the surface, are much more aggressive than any other structure away from the surface (based on [10]), is initially confirmed. Our numerical model is able to predict high erosion risk in all three locations obtained from the paint test. However, some high risk

was predicted also in the area in between of those regions, where no paint was removed in the experiment. This might be explained by the fact that in our model, energy is released instantaneously throughout the whole condensation process and not at the moment the cavity has collapsed. Thus, during the advection of the horseshoe cavity downstream, an impact is continuously computed, while the cavity condenses, leaving a footprint on the surface, before its final collapse close to the trailing edge. Apart from that, the water temperature during the experiment has not been reported, so the cavitating flow conditions might not be identical. Furthermore, it should be noted that the damage pattern from the paint test was obtained after three hours, while the simulation time is only $0.7s$, probably not enough to obtain a fully converged impact distribution.

The contribution of vapor structures in further distance from the wall to the surface impact distribution, requires additional investigation in order to further confirm our main hypothesis. Moreover, the determination of the pressure effectively driving the collapse, still remains an issue and requires further research as well. We have shown that any change in the driving pressure term p_d, might have a considerable effect on the impact distribution. Therefore, more insight should be gained on the selection of the driving pressure. Yet, any attempt to estimate cavitation aggressiveness, can only be related to a risk, as the material response has been left out of consideration in this paper.

REFERENCES

[1] M. S. Plesset and R. B. Chapman, *Collapse of an initially spherical vapour cavity in the neighbourhood of a solid boundary,* J. Fluid Mech. **47**, 283 (1970).

[2] Lord Rayleigh, *On the pressure development in a liquid during the collpapse of a spherical cavity,* Phil. Mag. **34**, 94 (1917).

[3] R. Hickling and M. S. Plesset, *Collapse and rebound of a spherical bubble in water,* The Physics of Fluids **7** (1964).

[4] M. S. Plesset and D. Hsieh, *Theory of gas bubble dynamics in oscillating pressure fields,* The Physics of Fluids **3** (1977).

[5] M. S. Plesset and A. Prosperetti, *Bubble dynamics and cavitation,* Ann. Rev. Fluid Mech **9**, 145 (1917).

[6] C. E. Brennen, *Cavitation and Bubble Dynamics* (Oxford University Press, New York, 1995).

[7] L. van Wijngaarden, *On the collective collapse of a large number of gas bubbles in water,* , Netherlands Ship Model Basin, Wageningen, latest ed. (1966).

[8] K. A. Mørch, *Energy considerations on the collapse of cavity clusters,* Tech. Rep. (Technical University of Denmark, Lyngby, Denmark, 1982).

[9] J.-C. Isselin, A.-P. Aloncle, and M. Autric, *On laser induced single bubble near a solid boundary: Contribution to the understanding of erosion phenomena,* Journal of Applied Physics **84** (1998).

[10] A. Philipp and W. Lauterborn, *Cavitation erosion by single laser-produced bubbles,* J. Fluid Mech. **361**, 75 (1998).

[11] F. G. Hammit, *Observations on cavitation damage in a flowing system,* J. Basic Eng **85**, 347 (1963).

[12] A. Vogel and W. Laterborn, *Acoustic transient generation by laser-produced cavitation bubbles near solid boundaries,* The Journal of the Acoustical Society of America **84**, 719 (1988).

[13] M. Dular, B. Stoffel, and B. Sirok, *Development of a cavitation erosion model,* Wear **261**, 642 (2006).

[14] M. Dular, T. Pozar, J. Zevnik, and R. Petkovsek, *High speed observation of damage created by a collapse of a single cavitation bubble,* Wear **418–419**, 13 (2019).

[15] R. Fortes-Patella and J. L. Reboud, *A new approach to evaluate the cavitation erosion power,* Journal of Fluids Engineering **120**, 335 (1998).

[16] R. Fortes-Patella, G. Challier, J. L. Reboud, and A. Archer, *Energy balance in cavitation erosion: From bubble collapse to indentation of material surface,* Journal of Fluids Engineering **135**, 011303 (2013).

[17] J. P. Franc and J. M. Michel, *Fundamentals of Cavitation* (Kluwer Academic Publishers, Dordrecht, 2004).

[18] Y. Tomita and A. Shima, *Mechanisms of impulsive pressure generation and damage pit formation by bubble collapse,* J. Fluid Mech. **169**, 535 (1986).

[19] G. Bark, N. Berchiche, and M. Grekula, *Application of principles for observation and analysis of eroding cavitation, EROCAV observation handbook*, 3rd ed. (Department of Shipping and Marine Technology, Chalmers University of Technology, Sweden, 2004).

[20] M. Tinguely, D. Obreschkow, P. Kobel, N. Dorsaz, A. de Bosset, and M. Farhat, *Energy partition at the collapse of spherical cavitation bubbles,* Phys. Rev. E **86** (2013).

[21] T. J. C. van Terwisga, P. A. Fitzsimmons, Z. Li, and E. J. Foeth, *Cavitation erosion - a review of physical mechanism and erosion risk models,* in *Proceedings of the* 7^{th} *International Symposium on Cavitation* (Michigan, USA, 2009).

[22] C. Eskilsson and R. E. Bensow, *Estimation of cavitation erosion intensity using cfd: Numerical comparison of three different methods,* in *Fourth International Symposium on Marine Propulsors* (Austin, Texas, USA).

[23] R. Fortes-Patella, J.-L. Reboud, and L. Briancon-Marjollet, *A phenomenological and numerical model for scaling the flow agressiveness in cavitation erosion,* in *EROCAV Workshop* (Val de Reuil, 2004).

[24] C. Leclercq, A. Archer, R. Fortes-Patella, and F. R. F. Cerru, *Numerical cavitation intensity on a hydrofoil for 3d homogeneous unsteady viscous flows,* Int. J. Fluid Mach. Syst. **10**, 254 (2017).

[25] S. Schenke and T. J. C. van Terwisga, *Erosive aggressiveness of collapsing cavitating structures,* in *Proceedings of the* 10^{th} *International Symposium on Cavitation* (Baltimore, USA, 2018).

[26] Y. T. Cao, X. X. Peng, K. Yan, L. H. Xu, and L. W. Shu, *A qualitative study on the relationship between cavitation structure and erosion region around a 3d twisted hydrofoil by painting method,* in *Fifth International Symposium on Marine Propulsors* (Espoo, Finland, 2017).

[27] H. Kato, A. Konno, M. Maeda, and H. Yamaguchi, *Possibility of quantitative prediction of cavitation erosion without model test,* Journal of Fluids Engineering **118**, 582 (1996).

[28] M. Dular and O. Coutier-Delgosha, *Numerical modelling of cavitation erosion,* Int. J. Numer. Meth. Fluids **61**, 1388 (2009).

[29] M. S. Mihatsch, S. J. Schmidt, M. Thalhamer, and N. A. Adams, *Numerical prediction of erosive collapse events in unsteady compressible cavitating flows,* in *Proceedings of IV International Conference on Computational Methods in Marine Engineering* (Lisbon, Portugal, 2011).

[30] C. Flageul, R. Fortes-Patella, and A. Archer, *Cavitation erosion prediction by numerical simulations,* in *Proceedings of the* 14^{th} *International Symposium on Transport Phenomena and Dynamics of Rotating Machinery* (Honolulu, HI, USA, 2012).

[31] P. Lush, *Impact of a liquid mass on a perfectly plastic solid,* J. Fluid Mech. **135**, 373 (1983).

[32] E.Lauer, X.Y.Hu, S.Hickel, and N.A.Adams, *Numerical modelling and investigation of symmetric and asymmetric cavitation bubble dynamics,* Computers and Fluids **69**, 1 (2012).

[33] G. L. Chahine, J.-P. Franc, and A. Karimi, eds., *Cavitation and cavitation erosion: Computational and experimental approaches,* in *Advanced Experimental and Numerical Techniques for Cavitation Erosion Prediction*, Vol. 106 (Springer, Dordrecht, The Netherlands, 2014) Chap. 1–7, pp. 3–180, 1^{st} ed.

[34] A. Peters, H. Sagar, U. Lantermann, and O. el Moctar, *Numerical modelling and prediction of cavitation erosion,* Wear **338-339**, 189 (2015).

[35] S. Schenke and T. J. C. van Terwisga, *Numerical prediction of vortex dynamics in inviscid sheet cavitation,* in *Proceedings of the* 20^{th} *Numerical Towing Tank Symposium* (Wageningen, the Netherlands, 2017).

[36] F. Menter, *Two-equation eddy-viscosity turbulence modeling for engineering applications,* AIAA Journal **32**, 1598 (1994).

[37] T. Melissaris, N. Bulten, and T. J. C. van Terwisga, *A numerical study on the shedding frequency of sheet cavitation,* in *Proceedings of VII International Conference on Computational Methods in Marine Engineering* (Nantes, France, 2017).

[38] J.-L. Reboud and Y. Delannoy, *Two-phase flow modelling of unsteady cavitation,* in *Proceedings of the* 2^{nd} *International Symposium on Cavitation* (Tokyo, Japan, 1994).

[39] J.-L. Reboud, B. Stutz, and O. Coutier, *Two-phase flow structure of cavitation: experiment and modelling of unsteady effects,* in *Proceedings of the* 3^{rd} *International Symposium on Cavitation* (Grenoble, France, 1998).

[40] G. H. Schnerr and J. Sauer, *Physical and numerical modeling of unsteady cavitation dynamics,* in *In Fourth International Conference on Multiphase Flow* (New Orleans, USA, 2001).

[41] S. Schenke and T. J. C. van Terwisga, *An energy conservative method to predict the erosive aggressiveness of collapsing cavitating structures and cavitating flows from numerical simulations,* Journal of Multiphase Flow **111**, 200 (2019).

[42] P. Crepier, *Ship resistance prediction: verification and validation exercise on unstructured grids,* in *Proceedings of VII International Conference on Computational Methods in Marine Engineering* (Nantes, France, 2017).

[43] L. Eca and M. Hoekstra, *A procedure for the estimation of the numerical uncertainty of CFD calculations based on grid refinement studies,* Journal of Computational Physics **262**, 104 (2014).

[44] G. Vaz, T. Lloyds, and A. Gnanasundaram, *Improved modelling of sheet cavitation dynamics on delft twist11 hydrofoil,* in *Proceedings of VII International Conference on Computational Methods in Marine Engineering* (Nantes, France, 2017).

[45] J. Brouwer, J. Tukker, and M. van Rijsbergen, *Uncertainty analysis of finite length signals,* in *The* 3^{rd} *International Conference on Advanced Model Measurement Technologies for the Maritime Industry* (Istanbul, Turkey, 2015).

[46] J. Brouwer, J. Tukker, and M. van Rijsbergen, *Uncertainty analysis and stationarity test of finite length time series signals,* in *The* 4^{th} *International Conference on Advanced Model Measurement Technologies for the Maritime Industry* (Gdansk, Poland, 2013).

[47] E.-J. Foeth, *The structure of three-dimensional sheet cavitation,* PhD Thesis, Delft University of Technology, Delft, the Netherlands (2008).

[48] A. Oprea, *Prediction of Tip Vortex Cavitation for Ship Propellers,* PhD Thesis, University of Twente, Enschede, The Netherlands (2013).

[49] S. Muzaferija, D. Papoulias, and M. Peric, *VOF simulations of hydrodynamic cavitation using the asymptotic and classical rayleigh-plesset models,* in *Proceedings of Fifth International Symposium on Marine Propellers* (Espoo, Finland, 2017).

[50] J.-B. Carrat, R. Fortes-Patella, and J.-P. Franc, *Assessment of cavitating flow aggressiveness on a hydrofoil: Experimental and numerical approaches,* in *Proceedings of the ASME 2017 Fluids Engineering Summer Meeting* (Waikoloa, Hawaii, USA, 2017).

[51] Z. Li and T. van Terwisga, *Assessment of cavitation erosion with a URANS method,* Journal of Fluids Engineering **136** (2014).

4

On the Accuracy of Predicting Cavitation Impact Loads on Marine Propellers

Predicting the cavitation impact loads on a propeller surface using numerical tools becomes essential, as the request for more efficient designs, stretched to the limit, is increasing. One of the possible design limits is governed by cavitation erosion. The accuracy of estimating such loads, using a URANS approach, is investigated in this study. In this chapter, we follow the energy balance approach by Schenke and van Terwisga [1], Schenke et al. *[2], where we take account of the focusing of the potential energy into the collapse center before it is converted into shock wave energy. The local surface impact power is then estimated following different considerations for the vapor destruction rate. We show that when the vapor volume destruction rate is estimated using the mass transfer source term, then all the energy is conserved and the total energy balance is satisfied. The model is verified on a single cavitating bubble collapse, and it is further validated on a model propeller test case. The obtained surface impact distribution agrees well with the experimental paint test results, illustrating the potential for practical use of our fully conservative method to predict cavitation impact loads on propeller blades.*

This chapter is based on: T. Melissaris, S. Schenke, N. Bulten, T.J.C. van Terwisga, *On the accuracy of predicting cavitation impact loads on marine propellers*, WEAR 456-457 (2020), http://dx.doi.org/10.1016/j.wear.2020.203393.

4.1. INTRODUCTION

Cavitation is the formation of vapor bubbles of a flowing liquid in regions where the liquid accelerates such that the local pressure of the liquid drops below its vapor pressure. The collapse of these cavities in pressure recovery regions, often leads to vibration and damage of mechanical components, for instance bearings, fuel injectors, impellers, pumps, propellers and rudders. Propeller cavitation might have a big impact on the whole operation of a ship and its environment. Hull vibrations, thrust breakdown, propeller erosion, and underwater radiated noise are the main threats. Cavitation erosion when experienced, normally leads to significant repair and maintenance costs, and even safety issues. Thus, there is a clear need for more efficient designs. Stringent regulations on the fuel efficiency of ships and their propulsion units, make things even more urgent, and designs should be stretched to the limits. For a propeller design this means taking away the margins against unwanted cavitation phenomena as much as possible in favor of higher propulsive efficiency. Most often the performance of propulsion systems is sub-optimal because countermeasures are needed to prevent erosion. Hence, the challenge for modern designs is to find the right balance between efficiency and the allowable level of cavitation. Evaluation of different designs requires objective numerical tools and methods, capable of providing accurate and reliable prediction of cavitation implosion loads, to secure the selection of the best design.

The history of cavitation research dates back to the mid-eighteenth century, when Euler discussed the possibility of a phenomenon, which influences the performance of a water wheel. The first to introduce the phenomenon as it is known today, was Reynolds in 1850's, by discussing the effect it had on the performance of a screw propelled steamer. However, the first observer of cavitation was Parsons, whose ship, Turbinia, suffered from severe thrust breakdown due to cavitation, in 1894. Since then, a lot of knowledge has been gained on cavitation dynamics on propellers, however the underlying physics behind the mechanisms of cavitation erosion due to the implosion of cavitating structures in the vicinity of the propeller surface, remain yet unclear. And even though cavitation dynamics and cavitation behavior on marine propellers are being extensively investigated, for more than a century experimentally [3], and over 20 years numerically, cavitation erosion prediction is still a major challenge.

The assessment of cavitation erosion risk on marine propellers from numerical simulations had not been studied thoroughly, until recently. The lack of physical understanding on how the cavitation implosion loads correlate with the material properties, increases the complexity of such simulations. Besides, a good estimation of the dynamics and the aggressiveness of cavitation impact loads requires extremely high resolution in space and time, as these flow phenomena act on extremely small scales (from mm down to μm and from μs to ns [4]). These are cardinal reasons why research was first focused mainly on the hydrodynamic aspects of cavitation erosion, and primarily on the dynamics of large scale cavitating structures.

In one of the first attempts to estimate the cavitation erosion risk numerically on marine propellers, Hasuike *et al.* [5] investigated the risk of cavitation erosion in four differently loaded propellers operating in a wake flow. They used the erosion indices proposed by Nohmi *et al.* [6] to estimate the aggressiveness of the cavitation impact loads. However, it is not very clear how these indices are derived and they also seem quite empir-

ical. Ponkratov and Caldas [7] and Ponkratov [8], tried to predict the cavitation erosion risk on a ship scale rudder and propeller, respectively. To estimate the cavitation erosion aggressiveness, they used several numerical functions, developed by the Lloyd's Register Technical Investigation Department (LR TID). Unfortunately, the formulation of these functions was not reported. Usta *et al.* [9] and Usta and Korkut [10] estimated the erosion aggressiveness using different indicators, as found in the literature. All the indicators are based on the potential energy hypothesis [11, 12], which states that the initial potential energy of a cavitating structure is proportional to its volume and the pressure difference driving the collapse. One of the indicators they used was the Erosion Intensity Function by Li *et al.* [13]. However, in all the indicators, an artificial threshold needs to be defined for the erosive cavitation impact loads. All of the aforementioned attempts to estimate the cavitation erosion risk on the propeller blades are more or less based on the potential energy hypothesis. None of the attempts was able to ensure energy conservation, while they all ignore the spatial and temporal focusing of the potential energy, which actually takes place during a cavity collapse.

Another philosophy applies the microjet erosion model [14, 15], as elaborated by Peters *et al.* [16], considering only collapses of single bubbles near the blade surface. In a previous work [17], we have discussed in detail the importance of the water hammer originating from a microjet impingement, and the pressure wave originated from the collapse of a cavity, with respect to erosion. We hypothesized that the impact load due to a collective cloud collapse, may be much more powerful than the one from a microjet, formed on a single bubble collapsing close to the surface. A more detailed comparison, can be found in Joshi *et al.* [18], who simulated a single bubble collapse close to a wall, using SPH. They focused on the relation between the shock at the moment of the jet impact, and the shock wave from the eventual collapse of the bubble. The authors also modeled the material plastic deformation. They concluded that, although the water hammer can produce twice the maximum plastic deformation compared to a shock wave from the collapse, the volume of material that is plastically deformed, is miniscule. Basically, a collapse shock wave can plastify almost 800 times larger volume, and hence, the erosion rate will be higher. Considering that both the collapse shock and the microjet impact are eventually fed by the initial potential energy content, and the fact that reliable prediction of a microjet formation and its water hammer would require extremely high resolution in time and space, an energy balance consideration, based on the initial potential energy contained in cavitating structures, is believed to be more successful on a macroscopic scale.

In the present study, an energy conservative method is used to predict the cavitation erosion aggressiveness on a surface. This method is based on the potential energy hypothesis, but it allows for the spacial and temporal focusing of the potential energy during the collapse of cavitating structures. First, the initial potential energy is converted into kinetic energy in the surrounding liquid, and focused in space before the conversion to shock wave energy, and eventually to local surface impact power takes place, at the final stage to the collapse. The model is first applied to a single cavitation bubble, collapsing under ambient pressure of 1 bar, in order to investigate the source of different numerical errors made on the estimation of the radiated power during the collapse. Then, the flow around the KCD-193 model propeller is investigated and the erosion risk on the blades

is assessed. The propeller perfomance under cavitating conditions is compared with the experimental observations and measurements, whereas the identified high erosion risk areas are compared with paint test results.

Previous studies [1, 17] have shown, that the overall energy balance can be satisfied if and only if the numerical errors, involved in the reconstruction of the radiated energy, are minimized. In simple cases, where condensation can be separated from evaporation (for instance a single bubble or a bubbly cloud collapse initially at rest), those numerical errors can easily be eliminated. However, in complex flows where it is impossible to isolate a cavity collapse (flow over a hydrofoil, propeller blade etc.) the errors made on the reconstruction of the radiated energy cannot easily be avoided, resulting in eventual violation of the energy balance. Thus, it is imminent to investigate different possible approaches to reconstruct the radiated energy in such a way that all the initial potential energy is conserved.

4.2. Numerical Modeling

4.2.1. Governing Equations

The Unsteady Reynolds Averaged Navier-Stokes (URANS) equations for momentum and mass continuity to be solved, are given by

$$\frac{\partial(\rho\mathbf{u})}{\partial t} + \nabla\cdot(\rho\mathbf{u}\mathbf{u}) = -\nabla p + \rho f + \nabla\cdot\tau \tag{4.1}$$

$$\frac{\partial\rho}{\partial t} + \nabla\cdot(\rho\mathbf{u}) = 0 \tag{4.2}$$

where $\mathbf{u}$ is the velocity tensor, ρ is the fluid density, p the pressure, f the external force per unit mass and τ the viscous part of the stress tensor. The finite volume method is employed to discetize the continuous governing equations, and a segregated approach is adopted, where the flow equations are solved in a SIMPLE like manner to achieve pressure-velocity coupling. A second-order implicit method, and a second-order upwind scheme are used for the time marching and the convective terms respectively.

The SST k-ω turbulence model is employed with a low-y^+ wall treatment similarly to previous studies [17, 19, 20]. The empirical reduction of turbulence dissipative terms in the two-phase regions has been applied, by modifying the turbulent eddy viscosity[21]

$$\mu = f(\rho)C_\omega\frac{k}{\omega} \tag{4.3}$$

$$f(\rho) = \rho_v + \frac{(\rho-\rho_v)^n}{(\rho_l-\rho_v)^{(n-1)}}; \qquad n \gg 1 \tag{4.4}$$

where ρ_v is the vapor density, ρ_l the liquid density and ρ the mixture density. For the constant n the recommended value $n = 10$ has been used.

4.2.2. Cavitation Modeling

In Eq. 4.1 and 4.2, the fluid density ρ and the turbulent eddy viscosity μ are given by the linear mixture relations

$$\rho = a_v\rho_v + (1-a_v)\rho_l \qquad and \qquad \mu = a_v\mu_v + (1-a_v)\mu_l \tag{4.5}$$

respectively, where $0 < a_v < 1$ is the vapor fraction. A homogeneous multiphase mixture model is employed to achieve phase transition, and to track the interfaces between the two phases. The pure liquid ($a_v = 0$) and vapor ($a_v = 1$) phases are modeled as incompressible. The mixture regime is also incompressible, however, compressible behaviour can be mimicked during phase transition.

An additional conservation equation that describes the transport of vapor volume fraction α_v is solved

$$\frac{\partial \alpha_v}{\partial t} + \nabla \cdot (\alpha_v \mathbf{u}) = S_{\alpha_v} \tag{4.6}$$

In Eq. 4.6, S_{α_v} represents the mass transfer source term. In order to account for bubble growth and collapse, a cavitation model should be introduced. The Schnerr-Sauer [22] cavitation model is used in this study, based on a simplified Rayleigh-Plesset equation, which neglects the influence of bubble growth acceleration, as well as viscous and surface tension effects. Within the control volume, the vapor phase is assumed to be present in the form of bubbles. Each bubble has the same radius R_b. The number density of seeds is defined as n_0, which corresponds to the number of bubbles per unit volume [23]. Therefore the mass transfer source term becomes

$$S_{\alpha_v} = \frac{4\pi R_b^2 n_0}{1 + \left(\frac{4}{3}\pi R_b^3\right) n_0} \frac{dR_b}{dt} \tag{4.7}$$

where the bubble radius R_b can be expressed as:

$$R_b = \left(\frac{\alpha_v}{n_0 \frac{4}{3}\pi (1 - \alpha_v)} \right)^{1/3} \tag{4.8}$$

The seed density n_0 and the seed diameter $D_0 = 2R_0$ are user specified, and the latter provides a lower limit R_{min} for the bubble size. Finally the bubble radius change rate $\frac{dR_b}{dt}$ is estimated using the inertia controlled growth model

$$\frac{dR}{dt} = \begin{cases} -C_{c,SF} \sqrt{\frac{2}{3} \frac{p - p_v}{\rho_l}}, & if \quad p > p_v \\ C_{v,SF} \sqrt{\frac{2}{3} \frac{p_v - p}{\rho_l}}, & if \quad p < p_v \end{cases} \tag{4.9}$$

where p_v is the saturation pressure, p is the local pressure around the bubble and ρ_l is the fluid density. $C_{c,SF}$ and $C_{v,SF}$ are scaling factors to adjust the source term magnitude for the condensation and the evaporation process, respectively. They work similarly to the condensation and evaporation coefficients found in other cavitation models [24–26].

In mass transfer models, compressibility is mimicked only in regions subjected to phase transition. Frikha *et al.* [27] and Morgut and Nobile [28] have shown that such models are at least able to correctly reflect the inertia driven kinematics of cavitating flows. Additionally, Koukouvinis and Gavaises [29] and Schenke and van Terwisga [30]

have pointed out that the equilibrium assumption for a barotropic flow can theoretically be mimicked by the mass transfer model, if the finite transfer rate tended to infinity. This transfer rate is controlled by the mass transfer model coefficients, which in this case are the scaling factors $C_{c,SF}$ and $C_{v,SF}$. These factors should be set as such, that the transfer rate is forced towards infinity, and thus a sharp transition is achieved from liquid to vapor phase and vice versa. Given that, the mass transfer source term always provide enough capacity to establish the equilibrium flow condition, where the time scale of phase transition is not important within the advective time scale of the flow. The density-pressure trajectory then remains close to vapor pressure during phase transition and the behavior of more realistic thermodynamic models is mimicked. Thus, in strong inertia driven flows, mass transfer models, and fully compressible models, can give very similar results as far as the inertial dynamics of cavitating flows are concerned. However, a fully compressible flow model still behaves differently in many aspects, such as wave propagation, and compressibility of pure phases and mixture.

4.3. Cavitation Erosion Modeling

The increased demand for the prediction of cavitation erosion has paved the way for the development of computational tools that can give a numerical estimation of high erosion risk areas. Model testing of the propeller cavitation behavior in a depressurized towing tank is nowadays the most typical way a propeller designer can get an assessment of the erosion risk on the propeller blades. However, assessing the cavitation intensity through optical observation requires a high degree of experience, and thus remains rather subjective. Besides, it does not provide more detailed information than high fidelity numerical simulations. Recent work shows that cavitation erosion risk assessment with numerical methods has a great potential, and it is expected to become integrated into the design process in the near future [1, 2, 17, 19]. The presented method to estimate the cavitation erosion risk, has been developed within the European project “CaFE”, as proposed by Schenke *et al.* [2].

4.3.1. Energy Balance

In previous studies [1, 17, 20], we assumed that the potential energy within the vapor structures is instantaneously radiated in the domain, during the condensation process. However, it has been shown that the initial potential energy is partitioned into different forms of energy during the collapse, while the total energy is conserved [2, 31, 32]. When the vapor structure enters a pressure recovery region, then the potential energy is converted gradually into kinetic energy till the final moment of the collapse, where the initial potential energy is fully converted into kinetic energy [2]. At the final stage of the collapse, Tinguely *et al.* [32] showed that the initial potential bubble energy $E_{pot,0}$ is eventually partitioned into shock wave energy E_{SW}, dissipative thermal energy ΔU and rebound energy E_{reb}, such that

$$E_{SW} = E_{pot,0} - E_{reb} - \Delta U \tag{4.10}$$

The dissipative thermal energy has been shown to be negligible, as thermal processes typically absorb negligible energy fractions [33]. The rebound energy depends strongly on the initial gas content and the pressure driving the collapse. As we assume that the

cavitating structures are completely filled with vapor and there is no non-condensable gas in the flow, the rebound energy depends only on the driving pressure, and thus it becomes relevant only for low ambient pressures, significantly lower than 1 bar [32]. Therefore we can assume that the initial potential energy in the structure is first feeding into kinetic energy E_{kin} until it has fully collapsed and the kinetic energy is completely converted into shock wave energy E_{SW}.

4.3.2. POTENTIAL ENERGY IN COLLAPSING CAVITATING STRUCTURES

Following the notion by Hammit [11], Vogel and Lauterborn [12] proposed that the potential energy of a cavity is equal to the work done by the driving pressure difference $p_d - p_v$ on its vapor volume V_v

$$E_{pot} = (p_d - p_v) \cdot V_v \tag{4.11}$$

where p_d is the ambient pressure driving the collapse and p_v the vapor pressure. The instantaneous change of volume specific potential energy then can be estimated in every cell at location x from the material derivative of $E_{pot}(t,x)$, written as

$$\dot{e}_{pot} = \frac{DE_{pot}/Dt}{V_{cell}} = \underbrace{(p_d - p_v) \cdot \left(\frac{\partial \alpha_v}{\partial t} + \mathbf{u_i} \cdot \nabla \alpha_v \right)}_{\text{collapse induced energy flux}} + \underbrace{\left(\frac{\partial p_d}{\partial t} + \mathbf{u_a} \cdot \nabla p_d \right) \cdot \alpha_v}_{\text{inertial energy flux}} \tag{4.12}$$

$$where \quad \frac{D}{Dt} := \frac{\partial}{\partial t} + \mathbf{u} \cdot \nabla. \quad and \quad \alpha_v = \frac{V_v}{V_{cell}}$$

Considering the change of potential energy in time in the domain, the potential energy is going to convert into kinetic energy. However, each term of Equation (4.12) will contribute in a different way. It is crucial, at this point, to distinguish two different sources of kinetic energy. The first term on the r.h.s. of Equation (4.12) includes a change in cavity volume. This will result in a collapse induced energy flux, and part of the initial potential energy in the bubble will convert into collapse induced kinetic energy, distributed to the liquid around the cavity interface. That is the kinetic energy which is responsible for the relative motion of the cavity interface with respect to the cavity (collapse) center, with velocity u_i, proportional to the pressure difference between the ambient driving pressure p_d and the vapor pressure p_v.

The second term on the r.h.s. of Equation (4.12) is activated only when the driving pressure is time dependent in the Lagrangian frame of reference, and it represents a change in pressure. Following the cavity in time, it can experience a change in driving pressure in two ways. One is when the cavity is subjected to a steady state driving pressure gradient. In this case, the change of driving pressure can only be seen by following the cavity in space, hence in the Lagrangian reference frame. Due to the pressure gradient, part of the initial potential will convert into inertial kinetic energy. This change of potential energy can only contribute to the acceleration or deceleration of the cavity as a rigid body (or deformable body if we assume that the shape of the cavity can change, but without changing its volume). The cavity interface is then forced to move along with the center of the cavity with velocity u_a. The second way that the cavity can experience a change in driving pressure is if the driving pressure somehow changes in the entire control volume in time. This effect can be seen in the Eulerian reference frame as well. As the

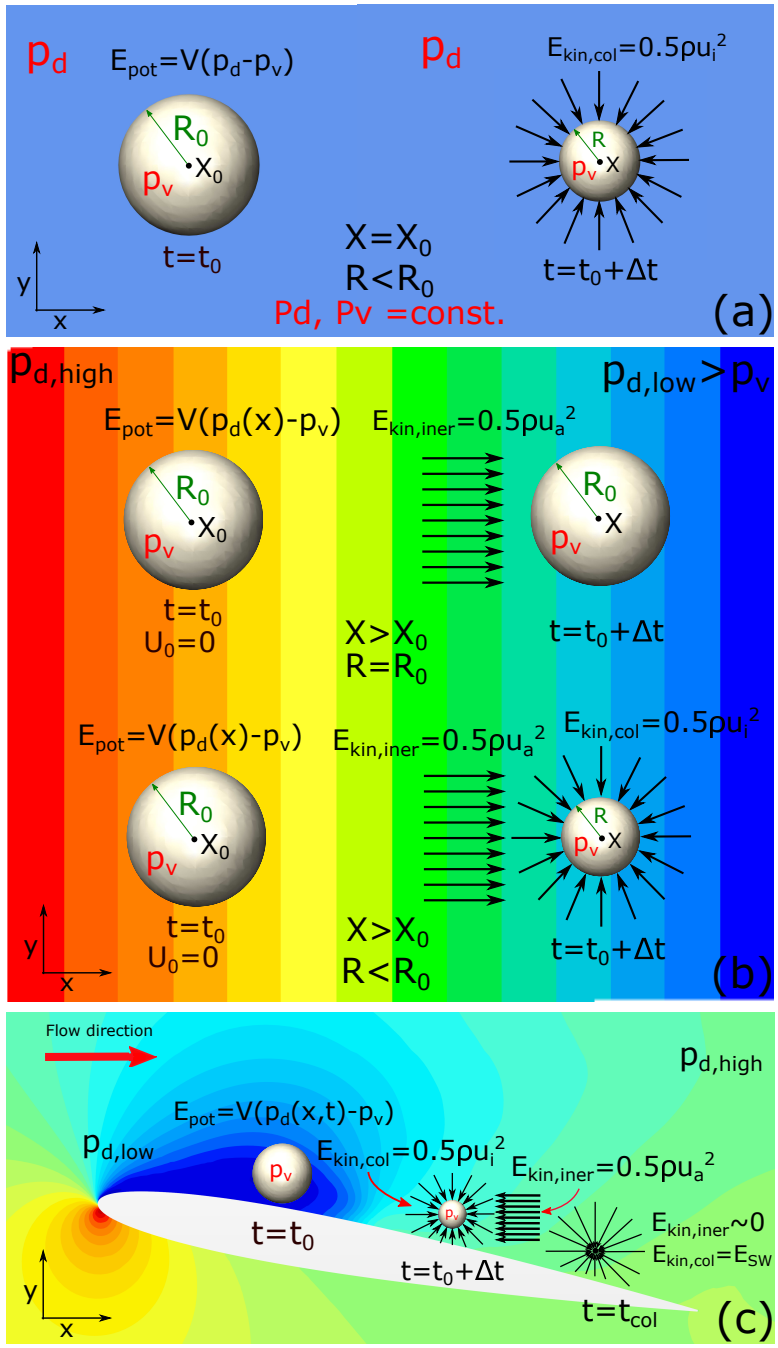

Figure 4.1: Examples of potential energy feeding into kinetic energy for a single cavitation bubble under constant driving pressure (a), under a negative pressure gradient (b), and under an adverse pressure gradient (flow over a hydrofoil, c)

pressure is uniform everywhere, and the driving pressure gradient is zero, there will be no change in the inertial kinetic energy. However, there will be a change in the potential energy of the cavity. This effect appears in the first term on the r.h.s. of Equation (4.12) by expanding the driving pressure p_d in time using a first order Taylor series approximation in the Lagrangian reference frame, as shown by Schenke and van Terwisga [1].

Figure 4.1 illustrates the contribution of each term on the r.h.s. of Equation (4.12) by depicting three conditions with changing potential energy. In the first example, Fig. 4.1a, a cavitation bubble is collapsing under steady driving pressure. Therefore the second term on the r.h.s. of Equation (4.12) is zero. In this case, the collapse center does not move during the collapse, and the liquid around the cavity interface cannot accelerate without volume change. Thus, the bubble will start shrinking with collapse induced velocity u_i, and all the potential energy contained in the bubble will convert into collapse induced kinetic energy $E_{kin,col}$.

In the second example, Fig. 4.1b, the cavitation bubble is subjected to a negative pressure gradient in the x-direction. We assume that the volume of the bubble remains constant during this process. Then, the first term on the r.h.s. of Equation (4.12) is zero. Consequently, all the potential energy initially contained in the bubble will convert into "inertial" kinetic energy $E_{kin,iner}$, which will accelerate the bubble towards the positive x direction. In a Langrangian frame of reference (following the bubble motion), the bubble will experience a time dependent driving pressure. In the Eulerian reference frame this is translated as a partial time derivative term $\frac{\partial p_d}{\partial t}$, and an advective term $\boldsymbol{u} \cdot \nabla p_d$ (see second term on the r.h.s. of Equation (4.12)). In this specific case, the driving pressure field is constant in time but not in space. This means that the partial derivative of pressure is zero, and the pressure gradient ∇p_d is the only responsible for the bubble motion with advective velocity u_a. If the bubble volume is free to change its volume, the first term on the r.h.s. of Equation (4.12) is not zero anymore. Then, the bubble will start shrinking, and eventually collapse, as the liquid pressure is always higher than the vapor pressure p_v. However, the bubble will collapse at a location x different than the initial location of the bubble x_0.

In the last example, Fig. 4.1c, the flow around a hydrofoil is investigated. We assume that a cavitation bubble is shed from the sheet cavity on the suction side. The bubble reaches its maximum volume (and hence potential energy) the time instant $t = t_0$. As the bubble is advected due to the main flow towards the trailing edge, it experiences an adverse pressure gradient. Since the pressure is higher than the vapor pressure p_v, the bubble will start to collapse. At the same time, due to the positive pressure gradient, the fluid force is opposed to the bubble motion, resulting in a deceleration of the bubble. At a time instant $t = t_0 + \Delta t$, part of the initial potential energy has been converted into collapse induced kinetic energy $E_{kin,col}$, responsible for the bubble volume change, while another part has been converted into "inertial" kinetic energy $E_{kin,iner}$, responsible for the deceleration of the bubble. At the final stage of the collapse, the "inertial" kinetic energy will be minimum, while the collapse induced kinetic energy will be maximum, which will eventually feed into acoustic energy. Thus, only the first term on the r.h.s. of Equation (4.12) is contributing to the radiated energy from the collapse of the bubble, and consequently to the surface accumulated energy.

Then, the volume specific potential energy reduction rate in every cell is given by

$$\dot{e}_{pot} = (p_d - p_v) \cdot \left(\frac{D\alpha_v}{Dt} \right)^- \tag{4.13}$$

where $\left(\frac{D\alpha_v}{Dt}\right)^-$ denotes specific volume change due to condensation. In Equation 4.13, the unknowns are the material derivative of α_v, and the driving pressure p_d. The material derivative of α_v is proportional to the velocity divergence $\nabla \cdot \mathbf{u}$ and the mass transfer source term S_{α_v} according to Equation 4.6. Furthermore, the void fraction is defined as $\alpha_v = \frac{\rho - \rho_l}{\rho_v - \rho_l}$, and from the local mass conservation $\frac{\partial \rho}{\partial t} + \nabla \cdot (\rho u) = 0$ we deduce [34]:

$$\frac{D\alpha_v}{Dt} = \left(\frac{\partial \alpha_v}{\partial t} + u \cdot \nabla \alpha_v \right) = \frac{\rho}{\rho_l - \rho_v} \nabla \cdot \mathbf{u} = \frac{\rho}{\rho_l} S_{\alpha_v} \tag{4.14}$$

Thus, we end up with the following three formulations for the material derivative of α_v:

$$\frac{D\alpha_v}{Dt} = \begin{cases} \frac{\partial \alpha_v}{\partial t} + \mathbf{u} \cdot \nabla \alpha_v & \text{(4.15a)} \\ \frac{\rho}{\rho_l - \rho_v} \nabla \cdot \mathbf{u} & \text{(4.15b)} \\ \frac{\rho}{\rho_l} S_{\alpha_v} & \text{(4.15c)} \end{cases}$$

All the considerations above, should theoretically give the same volume change rate. Nevertheless, each formulation introduces a different numerical error. For instance, the advective term $\mathbf{u} \cdot \nabla \alpha_v$ in Equation 4.15a, and the velocity divergence term $\nabla \cdot \mathbf{u}$ in Equation 4.15b, are discretized as one term in the transport equation of the vapor fraction, and thus, they cannot be computed separately from the solver. Nonetheless, a combined term is computed, that includes the contribution of both terms. Consequently, each one of them needs to be reconstructed. The velocity divergence term $\nabla \cdot \mathbf{u}$ can easily be reconstructed directly from the face fluxes. However, the reconstruction of this term introduces a non-negligible numerical error. One possible reason is that the face fluxes of $\mathbf{u}$ are the result of an interpolation from the cell centers due to the collocated grid arrangement.

On the other hand, the advective term $\mathbf{u} \cdot \nabla \alpha_v$ involves the reconstruction of $\nabla \alpha_v$. As we use a homogeneous multi-phase method to model the different phases in the flow, the cells at the interface consist of a homogeneous mixture of liquid and vapor. In cases where a sharp interface is pursued (e.g. a single bubble or a cloud of separated bubbles) the derivatives of α_v with respect to space are not defined, due to the sudden jump in vapor fraction from 0 to 1, and therefore, this term cannot be reconstructed. In case of a cloudy mixture (with unresolved sub-grid bubbles) the interface is more diffused and the advective term $\mathbf{u} \cdot \nabla \alpha_v$ can be computed. However, the accuracy of reconstructed gradients on unstructured meshes depends strongly on grid quality and grid effects (e.g. mesh stretching, curvature, skewness), and therefore a (sometimes significant) numerical error is introduced.

Furthermore, the mass transfer source term, on the r.h.s. of Equation 4.15c, is obtained from the instantaneous pressure p and the vapor fraction α_v. Thereby, it is a direct

outcome of the solution at each time step. In that case, the introduced error is equal to the iterative error during each time step. The source of the aforementioned errors and their magnitude are investigated in Section 4.4.

Finally, the volume specific potential energy reduction rate can be estimated, accordingly, by the following three considerations

$$\dot{e}_{pot,C}(t,\boldsymbol{x}_{cell}) = (p_d - p_v)\cdot \begin{cases} \min\left[\dfrac{\partial \alpha_v}{\partial t}, 0\right] & \text{(4.16a)} \\ \min\left[\dfrac{\rho}{\rho_l - \rho_v}\nabla\cdot\mathbf{u}, 0\right] & \text{(4.16b)} \\ \min\left[\dfrac{\rho}{\rho_l} S_{\alpha_v}, 0\right] & \text{(4.16c)} \end{cases}$$

where only the volume change due to condensation is considered in each case, and it is indicated by the subscript C. In Equation 4.16a, the advective term has been omitted, since either it cannot be reconstructed, when a sharp interface is achieved, or its error cannot be estimated, and thus we introduce an additional modeling error. For simplicity, from now on, we will refer to Equations 4.16a, 4.16c and 4.16c, as "partial derivative", "divergence" and "source term", respectively.

The unsteady term of Eq. 4.15a, $\dfrac{\partial \alpha_v}{\partial t}$, represents the rate of change of α_v in time, and it can be accurately predicted assuming a sufficient temporal discetization. In Eq. 4.14, moving the advective term to the right hand side gives

$$\frac{\partial \alpha_v}{\partial t} = \frac{\rho}{\rho_l - \rho_v}\nabla\cdot\mathbf{u} - \mathbf{u}\cdot\nabla\alpha_v \tag{4.17}$$

As long as only condensation takes place (for instance a single cavitation bubble collapsing under ambient pressure higher than its vapor pressure, while far from the bubble the liquid is assumed at rest), the advective term $\mathbf{u}\cdot\nabla\alpha_v$ is zero, and thus, the partial derivative of α_v will be equal to the material derivative of α_v. Similarly, in cases where we know a priori that the advective term is negligible compared to the velocity divergence term (see r.h.s of Eq. 4.17), then the rate of vapor reduction can be approximated by the partial time derivative of α_v.

4.3.3. EFFECTIVE DRIVING PRESSURE

The second unknown in Equation 4.13 is the pressure driving the collapse p_d. The determination of this quantity is not straightforward for complex flows, and it introduces the largest uncertainty in the prediction of the cavitation impact loads on a surface. For an isolated single cavitation bubble, collapsing in an infinite liquid volume, without the effect of gravity, the pressure effectively driving the collapse is just the pressure at infinity, which will result in a spherical collapse. Nevertheless, when the bubble is collapsing close to a wall (or close to another bubble), the driving pressure across its interface will vary due to the interaction with the wall (or the other bubble), as there is no space for the pressure to recover to ambient pressure. Similarly, in a flow around a lifting body, a hydrofoil or a propeller for instance, the interaction between the cavities formed on the blade or the

hydrofoil surface, and their interaction with the wall, should be taken into account, as the pressure recovery gradients along the surface are considered important for the cavitation dynamics.

Unfortunately, the determination of the driving pressure in such complex flows is not an easy task. The local instantaneous pressure p could not be used to estimate the driving pressure, because it would imply that the pressure at the cavity interface is higher than the vapor pressure, in order to obtain a non-zero driving pressure difference $p_d - p_v$, at locations where energy is radiated. However, looking at the density pressure trajectory, it remains very close to vapor pressure during phase change, thus the corresponding pressure difference would physically be nearly zero, in case the local cell pressure is used as a measure for the driving pressure. Therefore, a different way to estimate the driving pressure should be found.

In previous studies [1, 17, 19], the time-averaged pressure field at time instant t, $\overline{p}_t$, computed from the instantaneous pressure field in cavitating conditions p, was assumed to be the ambient pressure field driving the cavity collapses. In this way, a rough estimate of the conditions that collapsing cavities experience on statistical average can be achieved. However, this implies that the time-averaged pressure field is sufficiently converged (almost constant in time), which always requires several cycles. In the present study, we investigate the influence of several more instantaneous pressure field definitions, computed by averaging the instantaneous pressure field over a moving time window of size T_m

$$\overline{p}_t = \frac{1}{T_m} \int_{t-T_m}^{t} p(t)\, dt \tag{4.18}$$

Computing the moving average requires to store all the values within the chosen time window of the pressure signal in a buffer at each time step, for every cell of the computational domain. Depending on the size of the window, the amount of data can easily exceed the available random-access memory (RAM) limit [35]. Therefore, we apply the method by Welford [36] to approximate the moving average of the pressure field at time instant t, $\overline{p}_t$, over a sliding window T_m at each computational cell

$$\overline{p}_t = \overline{p}_{t-1} + \frac{p_t - \overline{p}_{t-1}}{n} \quad \xLeftrightarrow{n=T_m/\Delta t} \quad \overline{p}_t = \overline{p}_{t-1} + \left(p_t - \overline{p}_{t-1}\right) \frac{\Delta t}{T_m} \tag{4.19}$$

where n is the number of time steps within the sliding window, and Δt the time step size.

4.3.4. RADIATED ENERGY AND SURFACE IMPACT POWER

Let us consider the potential energy released instantaneously at each time step and each location where condensation takes place. Then, the instantaneous radiated power is given directly by the reduction rate of the volume specific potential energy:

$$\dot{e}_{rad}(t, \boldsymbol{x}_{cell}) = -\dot{e}_{pot,C}(t, \boldsymbol{x}_{cell}) \tag{4.20}$$

where the minus (-) sign is a consequence of the energy conservation. However, in order to follow the energy consideration, as discussed in Section 4.3.2), the potential energy should somehow be stored as kinetic energy around the cavities, focused towards the collapse center, and eventually converted into radiated (acoustic) energy, at the final stage of

the collapse, giving a more physical representation of the collapsing process of cavitating structures.

To account for the conversion of the potential energy into kinetic energy, and the focusing of the kinetic energy into the collapse center, a novel approach is employed, as introduced by Schenke *et al.* [2]. In this "focusing" model the reduction of the potential energy due to condensation is absorbed by an accumulated kinetic energy field $\varepsilon(t, \boldsymbol{x}_{cell})$, until a criterion for the conversion of the kinetic energy into acoustic energy is met. This process is described by an additional transport equation:

$$\frac{\partial \varepsilon}{\partial t} + \nabla \cdot (\varepsilon \mathbf{u}_i) = -\dot{e}_{rad}(t) \tag{4.21}$$

and by applying the product rule, Eq. 4.21 becomes

$$\frac{\partial \varepsilon}{\partial t} + \mathbf{u}_i \cdot \nabla \varepsilon = -\varepsilon(\nabla \cdot \mathbf{u}_i) - \dot{e}_{rad}(t) \tag{4.22}$$

where $\mathbf{u}_i$ is the collapse induced velocity, and ε is the consequent kinetic energy induced by the volume reduction of the cavitating structures in the flow. Practically, this collapse induced kinetic energy is induced from locations of negative velocity divergence only, or in general, only from locations where condensation takes place. The sum of the two terms on the left hand side of Eq. 4.22, i.e, the unsteady term and the advection, is the material derivative of ε that gives the rate of change of ε following a fluid particle. In particular, the term $\mathbf{u}_i \cdot \nabla \varepsilon$ represents the conservative advective transport of the collapse induced kinetic energy, and it is responsible for its spatial distribution around the cavitating structure as the kinetic energy is focusing towards the collapse center. However, the exact spatial distribution of $\varepsilon(t, \boldsymbol{x}_{cell})$ is unknown, and consequently, a modeling assumption is required for the conservative transport of the accumulated kinetic energy $\mathbf{u}_i \cdot \nabla \varepsilon$.

Furthermore, the two source terms on the right hand side, represent the kinetic energy source (or creation of kinetic energy), and the radiation source (or reduction of kinetic energy), respectively. The kinetic energy source is directly connected to the reduction of potential energy. When the volume specific potential energy is reducing at any location x_{cell}, as a result of condensation, then the kinetic energy source term is activated. On the other hand, the kinetic energy source term remains zero, when an increase of potential energy, associated with cavity growth, takes place. Consequently, the kinetic energy source term $\varepsilon(\nabla \cdot \mathbf{u}_i)$ can be modeled by the volume specific potential energy reduction rate, discussed in Section 4.3.2.

The radiation source term, $\dot{e}_{rad}(t)$, is activated only when a certain criterion is met. To physically represent a cavity collapse, most of the energy, initially contained as potential energy in the structure, should be released at the final stage of the collapse. To chose a suitable criterion, we should take a close look to what happens as we approach the final stage of the collapse. The pressure in the mixture regime cannot be much higher than the vapor pressure, and therefore, a high amplitude pressure wave can only form in the liquid phase. Besides, the absorbed kinetic energy should accumulate on the low pressure side, and propagate inwards, towards the collapse center. Considering these assumptions, we derive the following criterion for β:

$$\beta = \begin{cases} 1, & if \quad p > p_\infty \quad and \quad \alpha = 0 \\ 0, & else \end{cases} \tag{4.23}$$

According to Equation 4.23, the parameter β is defined such that $\beta = 1$ at locations where the vapor has completely disappeared and the local pressure is higher than the pressure at infinity. Considering also the fact that the value of β is of interest only at locations where the potential energy has been converted into collapse induced kinetic energy, then we can isolate all the locations where a collapse of a vapor structure has taken place. Consequently, a volume cell, where there is some collapse induced kinetic energy focused, is a candidate to radiate energy, if and only if its vapor volume has fully condensed and if a pressure wave is emitted.

Then Eq. 4.22 can be replaced by the following modeling assumption:

$$\frac{\partial \varepsilon}{\partial t} = (1-\beta)[\phi(\varepsilon) - \dot{e}_{pot,C}(t)] - \beta \frac{\varepsilon}{\delta t} \tag{4.24}$$

The term $\phi(\varepsilon)$ is a model for the unknown conservative advective transport of the kinetic energy $\mathbf{u}_i \cdot \nabla\varepsilon$ in Eq. (4.22). The term $\dot{e}_{pot,C}(t)$ represents the source term for the reduction of potential energy, and consequently the generation of kinetic energy $\varepsilon(\nabla \cdot \mathbf{u}_i)$ in Eq. (4.22). Hence, $\phi(\varepsilon) - \dot{e}_{pot,C}(t)$ serves for the kinetic energy flux. The term $\beta \frac{\varepsilon}{\delta t}$ is a model for the radiation source term $\dot{e}_{rad}(t)$ in Eq. (4.22). The energy radiation is modeled as a discrete event, because all the focused energy is released within the time interval δt, which means that the energy content of the radiated wave is conserved, while the exact wave shape across the wave front is not captured. Finally, the term $(1-\beta)$ in Eq. (4.24) has been added to make sure that at locations where volume specific energy is radiated, there is no production of kinetic energy, and therefore the overall energy balance is satisfied.

The advective transport term $\phi(\varepsilon)$ in Eq. (4.24) is given by [2]

$$\phi(\varepsilon) = \dot{e}_{pot,C} k - \frac{\varepsilon}{\delta t} \mathfrak{P}_u(\nabla\varepsilon) \tag{4.25}$$

where k is assumed constant in space and is defined such that

$$k = \frac{\int_V \frac{\varepsilon}{\delta t} \mathfrak{P}_u(\nabla\varepsilon) dV}{\int_V \dot{e}_{pot,C}(t) dV} \tag{4.26}$$

and $\mathfrak{P}_u(\nabla\varepsilon)$ is the normalized projection of $\nabla\varepsilon$ on the local flow velocity vector $\mathbf{u}$

$$\mathfrak{P}_u(\nabla\varepsilon) = \max\left[\frac{\mathbf{u}}{\|\mathbf{u}\|} \cdot \frac{\nabla\varepsilon}{\|\nabla\varepsilon\|}, 0\right] \tag{4.27}$$

In Eq. 4.25, the first term on the right hand side is associated with the production of collapse induced kinetic energy, and it is proportional to the reduction rate of potential energy. The second term is related to the transport of the kinetic energy, and it is based on the assumption that the flow around the interface of the collapsing cavity is directed towards the center, thus aligned with $\nabla\varepsilon$, considering that ε is stored at the cavity interface. To get the collapse induced kinetic energy at each time step δt, we explicitly forward the solution in time using a first order Taylor expansion, which gives

$$\varepsilon|_{t+\delta t} = \varepsilon|_t + \frac{\partial \varepsilon}{\partial t}\Big|_t \delta t = (1-\beta|_t)\Big[\dot{e}_{pot,C}\delta t(k-1) - \varepsilon(\mathfrak{P}_u(\nabla\varepsilon) - 1)\Big]\Big|_t \tag{4.28}$$

and the volume specific radiated power is given by

$$\dot{e}_{rad}|_{t+\delta t} = \frac{1}{\delta t}(\beta\varepsilon)|_t \tag{4.29}$$

Knowing the radiated volume specific power at each cell in the domain, and assuming that each point source x_{cell} emits its converted potential energy as a radial wave with an infinitely large propagation speed, the instantaneous surface specific impact power $\dot{e}_S(t, x_S)$, at some surface location x_S is given by Schenke and van Terwisga [1] as

$$\dot{e}_S(t, \mathbf{x}_S) = \frac{1}{4\pi}\int_V \dot{e}_{rad}(t, \mathbf{x}_{cell})\left[\frac{(\mathbf{x}_{cell} - \mathbf{x}_S)\cdot\mathbf{n}}{\|\mathbf{x}_{cell} - \mathbf{x}_S\|^3}\right] dV \tag{4.30}$$

where $\mathbf{n}$ is the surface normal vector at the impact location.

Finally, cases where the cavity collapse rate goes from negative to zero before the cavity is fully collapsed, and the condensation process stops, or it is even reversed and evaporation takes place, are not considered in this model. In such cases, the kinetic energy accumulated at the cavity interface should be dissipated or even converted back to potential energy, which cannot be handle by the model as described in this section. However, such cases are assumed to occur quite rarely when the cavities undergo high pressure differences.

4.4. SINGLE CAVITATION BUBBLE COLLAPSE

A verification study is conducted on a single cavitation bubble collapse, considering an inviscid flow. This study serves for verification of the cavitation and erosion model. First, an idealized spherical bubble is simulated in an infinite liquid. The sensitivity of the collapse time to the condensation scaling factor $C_{c,SF}$, the time step size Δt, and the grid size has been investigated. The obtained converged solution is then compared to the analytical solution of the Rayleigh-Plesset equation [37]. Then, the focusing model is applied to verify that the potential energy is stored at the interface as kinetic energy, until the final stage of the collapse, when it is radiated to the domain as acoustic energy. Subsequently, we apply an inflow velocity at the one boundary, parallel to the x-axis, so that the flow around the bubble is advected downstream during the collapse. This configuration serves for identification of the numerical error sources on the prediction of the total radiated energy E_{rad}.

As mentioned in Section 4.3.2 we consider three alternative methods to estimate the change in potential energy during condensation. The volume reduction rate can be estimated by using the partial derivative of the vapor fraction, the velocity divergence, or the cavitation mass transfer source term. In the case where the flow is initially at rest, the total volume change can be accurately predicted by the volume integration of the partial derivative of the vapor fraction $\int_v(\frac{\partial\alpha}{\partial t})dV$, as the advective term $\mathbf{u}\cdot\nabla\alpha_v$ is zero then. However, it is interesting to see how this term behaves when there is large advection in the flow, and how it compares with the other two considerations for the prediction of the volume change.

Finally, we let the bubble collapse close to an infinite flat surface to verify that half of the energy is accumulated on the surface and the total energy is conserved [1].

Table 4.1: Description of the different generated grids, where the number of cells per diameter, the total number of cells, and the volume off-set from the theoretical bubble volume is demonstrated

Grid	# Cells/Diameter	# Cells Total	Volume off-set
Grid 1	2	3,200	2.58%
Grid 2	6	14,384	0.86%
Grid 3	10	43,840	0.52%
Grid 4	14	84,504	0.37%
Grid 5	18	177,752	0.29%
Grid 6	22	282,640	0.24%

4.4.1. ISOLATED BUBBLE COLLAPSE

SENSITIVITY STUDY

The collapse of an isolated single cavitation bubble with a radius of $R_b = 3.84mm$ has been simulated. Six different meshes are used for the sensitivity studies. Table 4.1 shows the number of cells per diameter, the total amount of cells and the volume off-set from the theoretical bubble volume. For all grids, apart from the coarsest grid (Grid 1), the volumeoff-set is less than 1%. Figure 4.2 shows the domain size and the grid refinement around the bubble in Grid 5. The domain boundaries are located 250 radii away from the bubble center.

A pressure outlet boundary condition has been applied to all boundaries with $p_\infty = 1bar$, while the vapor pressure inside the bubble is equal to $p_v = 2340Pa$ (see Figure 4.3). The pressure field in the rest of the domain is initialized such that it satisfies the Laplace equation $\nabla \cdot \nabla p$ outside the bubble surface. An initialization algorithm has been used to compute the Laplacian pressure field and the vapor volume fraction at each cell for each grid. The initial vapor fraction field is such, that all the cells entirely located inside the bubble are assigned a vapor fraction of $\alpha_v = 1$, while those entirely located outside the bubble are assigned a vapor fraction of $\alpha_v = 0$. To determine the vapor fraction of the cells at the interface, a sample algorithm has been used. The algorithm divides every cell that is cut by the bubble interface in 100^3 subcells and determines the amount of the subcells that are entirely inside the interface, assigning a percentage of vapor to each cut cell. The initial vapor fraction field for the second coarsest (Grid 2) and second finest (Grid 5) mesh is depicted in Figure 4.4, where the better representation of the bubble interface (red line) can be seen as we refine the mesh around the bubble. The bubble interface is shown as an iso-line of $\alpha_v = 0.5$.

The sensitivity of the collapse time to the condensation scaling factor $C_{c,SF}$ (see Eq. 4.9), and the temporal and spatial resolution has been investigated. Figure 4.5 shows the evolution of the dimensionless vapor volume for different values of the condensation scaling factor $C_{c,SF}$, and a fixed time step size $\Delta t = 1 \times 10^{-6}$, in grid 3. For very small values, a significant delay of the collapse time is observed, while for $C_{c,SF} \geq 1$ the solution becomes independent of the coefficient value. However, this behavior can only be achieved if the temporal and spatial resolution are sufficient. Figure 4.6 depicts the evolution of the dimensionless vapor volume in time, for a constant condensation scaling

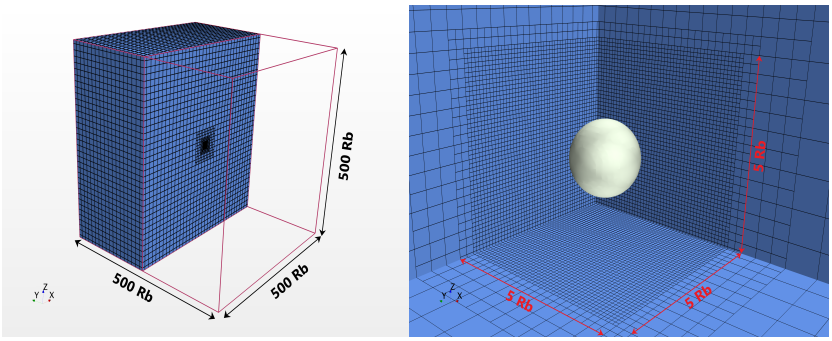

Figure 4.2: Dimensions of the domain and the refinement box around the bubble in Grid 5

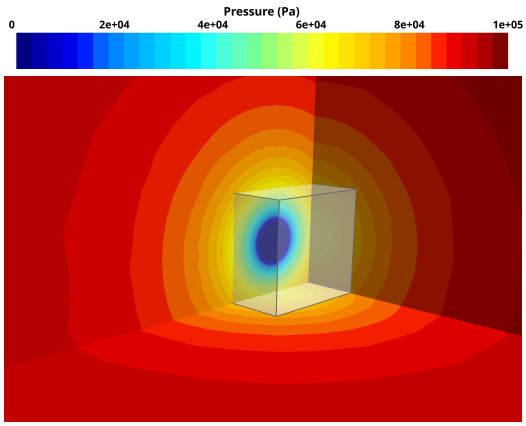

Figure 4.3: Evolution of pressure within and around the bubble in Grid 5. The size of the refinement area is shown.

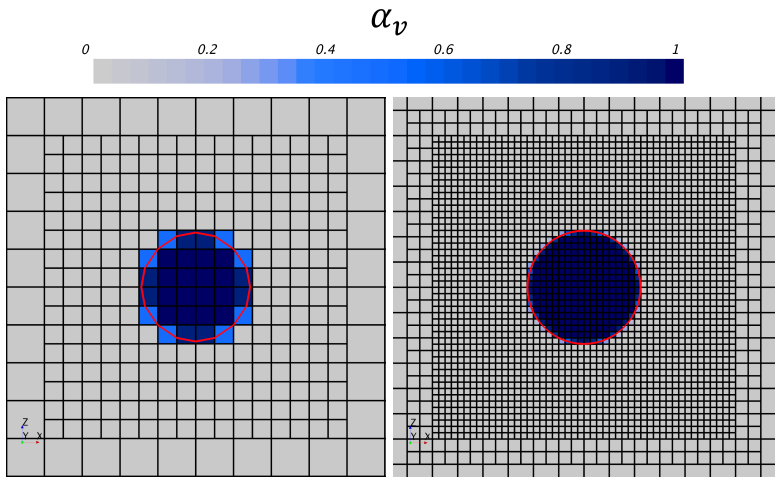

Figure 4.4: Initial field of the vapor fraction α_v for the second coarsest (Grid 2) and second finest (Grid 5) mesh. The bubble interface is shown as an iso-line of $\alpha_v = 0.5$.

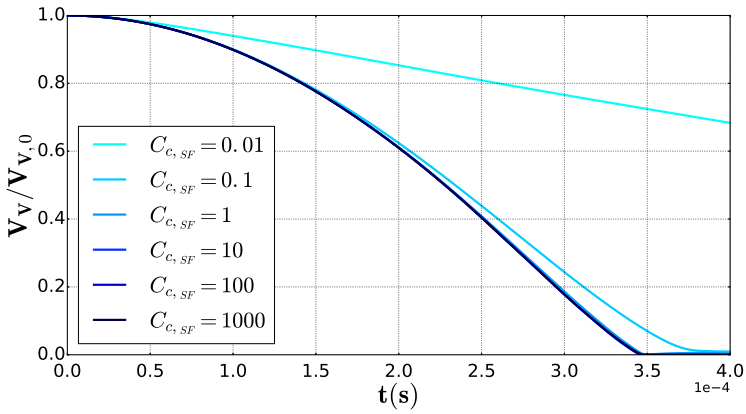

Figure 4.5: Evolution of the dimensionless vapor volume, normalized by the initial vapor volume, over time for $\Delta t = 1 \times 10^{-6}$ in grid 3, and a systematic variation of the condensation mass transfer coefficient C_c

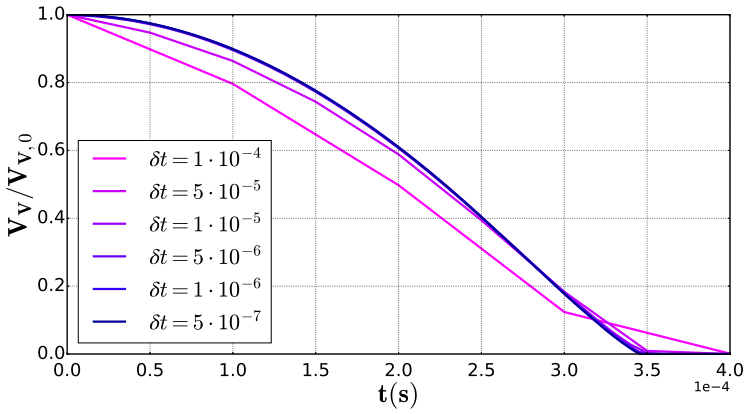

Figure 4.6: Evolution of the dimensionless vapor volume, normalized by the initial vapor volume, over time for $C_{SF} = 10$ in grid 3, and a systematic variation of the timestep size Δt

factor $C_{c,SF} = 10$, and a systematic variation of the time step size Δt in grid 3. Surprisingly, the collapse time is not very sensitive to the temporal resolution, as already with a time step size of $\Delta t = 1 \times 10^{-5}$, a time step size independent solution is achieved. In other words, we need no more than 40 time steps during the collapse, in order to obtain a time step size independent solution. The sensitivity of the grid size is depicted in Figure 4.7 for 6 different grid sizes. It shows the evolution of the dimensionless vapor volume for $C_{c,SF} = 10$ and $\Delta t = 1 \times 10^{-6}$, and how they compare to the Rayleigh-Plesset equation. As we move to a grid density higher than grid 2, the collapse time does not show high sensitivity. Looking more thoroughly at the predicted collapse time, grid 5 gives a fully converged and grid size independent solution, which deviates less than 1% from the collapse time obtained from the Rayleigh-Plesset equation.

ENERGY CONSIDERATION

As discussed in Section 4.3.1, in this study we assume that the initial potential energy $E_{pot,0}$, contained in the vapor structures, is continuously feeding into kinetic energy E_{kin}, during the condensation process, until eventually it is fully converted into radiated energy E_{rad}, at the final stage of the collapse. In this Section, we compare the energy focusing approach, with the original consideration that energy is continuously released in the domain, and the potential energy is instantaneously converted into radiated energy (see Eq. (4.3.4)). Figure 4.8 shows the evolution of the radiated energy, normalized by the initial potential energy, in time for the non-focusing and the focusing approach. In the non-focusing approach, the instantaneous potential power is computed using the three different considerations, as explained in section 4.3.2. The volume integrated rate of vapor reduction is predicted (see Eq. 16) using the partial derivative (red), the velocity divergence (green), and the cavitation mass transfer source term (blue dotted). While the total energy in the domain is conserved, when the partial derivative and the source term are considered for the prediction of the instantaneous power, with the velocity divergence, part of the energy is being lost and only 63% of the total energy is finally being released.

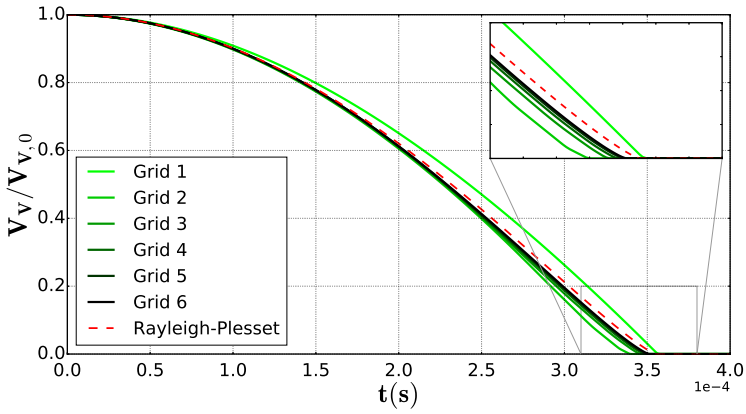

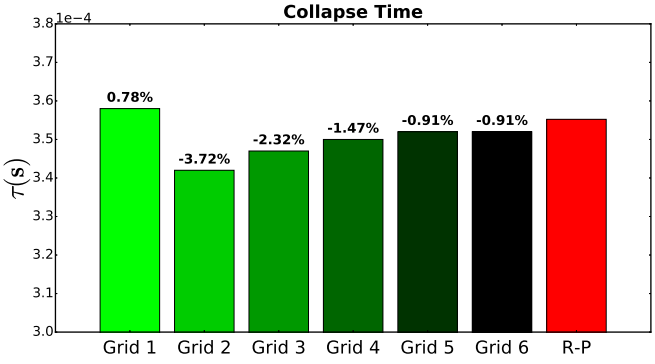

Figure 4.7: Evolution of the dimensionless vapor volume, normalized by the initial vapor volume, over time for $C_{SF} = 10$, $\Delta t = 1 \times 10^{-6}$, and a systematic variation of the mesh density

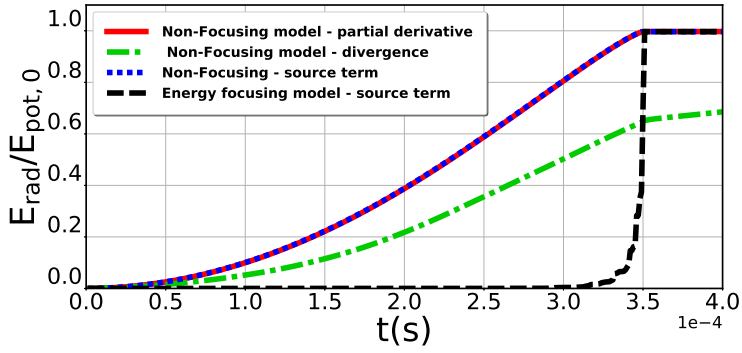

Figure 4.8: Total radiated energy, normalized by the initial potential energy, with the non-focusing and the energy focusing model. For the non-focusing model, the volume integrated rate of vapor reduction is predicted using the partial derivative (red), the velocity divergence (green), and the mass transfer source term (blue). For the energy focusing model, the volume integrated rate of vapor reduction is predicted using the mass transfer source term only (black).

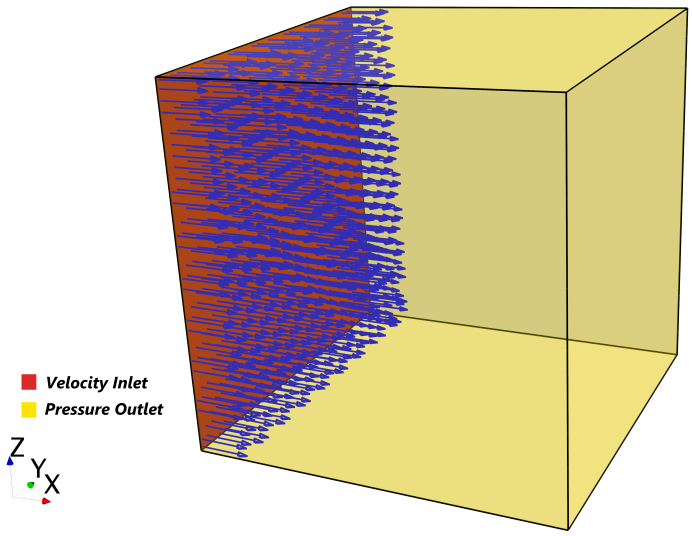

Figure 4.9: Boundary conditions when a non-zero inflow velocity is applied to the domain. A velocity inlet boundary condition is assigned to the left boundary, and a flow advection is forced in positive x direction.

The source of this error is the divergence term $\nabla \cdot \mathbf{u}$. The velocity divergence cannot be computed directly from the solver, as has been demonstrated in a previous study [17], and as a result it needs to be reconstructed. The reconstruction of the velocity divergence introduces a numerical error, which results in the error shown here. In this particular test case, this error could be eliminated by correcting the velocity divergence field by a constant factor c, determined at each time step as reported by Schenke and van Terwisga [1], as the vapor volume change is subjected only to the condensation process during the cavity collapse, and there is no advection in the flow. However, in most of the cases the condensation process cannot be estimated from the total volume change and this correction is not possible.

The focusing approach has only been applied in the case where the mass transfer source term is used to predict the vapor volume reduction rate. It is demonstrated that the potential energy, initially contained in the bubble, is successfully converted into kinetic energy during the condensation process, until we approach the final stage of the collapse where all the energy is radiated radially to the domain and the total energy is conserved. We could also use the partial derivative, however, this would hold for that particular case only, due to the fact that the flow is at rest and no advection takes place. The partial derivative term includes an advective contribution, which in this case is negligible. Nevertheless, in case we would have a non-zero advective velocity, then the predicted total energy would not be conserved. This can be shown by applying an inflow velocity in positive x direction, as shown in Figure 4.9.

Now, the computed partial derivative of the vapor volume includes an advective contribution which cannot be neglected. The error made in the energy conservation is getting

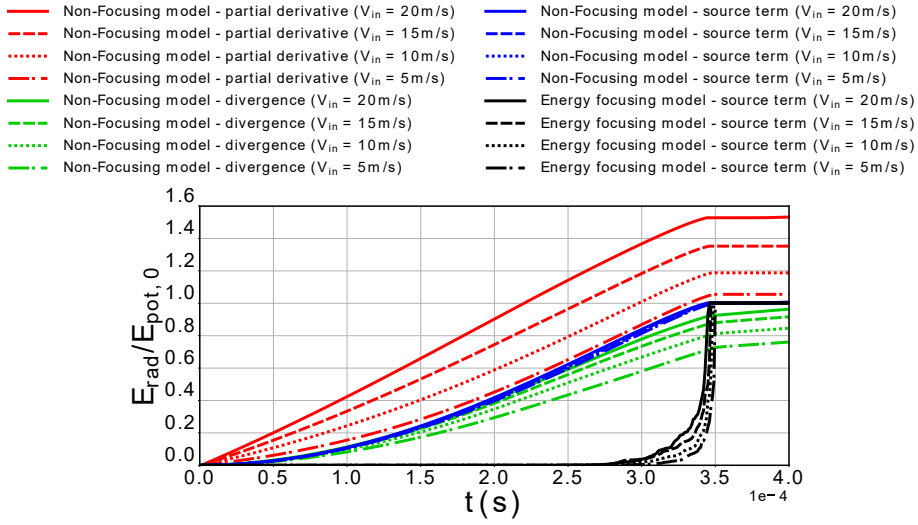

Figure 4.10: Total radiated energy, normalized by the initial potential energy, with the non-focusing and the energy focusing approach for a systematic variation of the inlet flow velocity. For the non-focusing model, the volume integrated rate of vapor reduction is predicted using the partial derivative (red), the velocity divergence (green), and the mass transfer source term (blue), while for the energy focusing model the the volume integrated rate of vapor reduction is predicted only using the mass transfer source term.

more dominant with increasing the inflow velocity, as illustrated in Figure 4.10. The total energy released in the domain after the bubble has collapsed is overpredicted, while with the material derivative consideration is still underpredicted. However, in the latter case, the magnitude of the error is diminishing as the flow velocity increases. Finally, when the volume integrated rate of vapor reduction is predicted from the mass transfer source term, all the energy is fully conserved, regardless of the magnitude of the flow velocity.

4.4.2. COLLAPSE NEAR AN INFINITE FLAT SURFACE

The collapse of the same spherical cavitation bubble close to an infinite flat wall has been simulated (see Figure 4.11). The bottom boundary has been placed close to the bubble at a distance $H = 5mm$ ($\gamma = \frac{H}{R_b} = 1.3$) from the bubble center, and a slip wall boundary condition has been assigned. In the previous section, 4.4.1, we showed that all the initial potential energy is released and converted into shock wave energy during the collapse, such that the total energy is conserved. Since we do not consider the energy absorbed by the liquid jet mechanism, usually observed for a bubble collapsing close to a wall, it can be argued that half of this energy should be distributed to the lower surface of infinite dimensions, assuming a spherical wave propagation. Figure 4.12 shows the total accumulated surface energy over time, normalized by the initial potential energy, obtained from the non-focusing cavitation intensity model, and the energy focusing approach. The surface energy is estimated at twelve time instants during the collapse. Similar to Figure 4.8, the total energy is conserved when the volume integrated rate of vapor reduction is predicted from the partial derivative or the mass transfer source term, as half of the initial

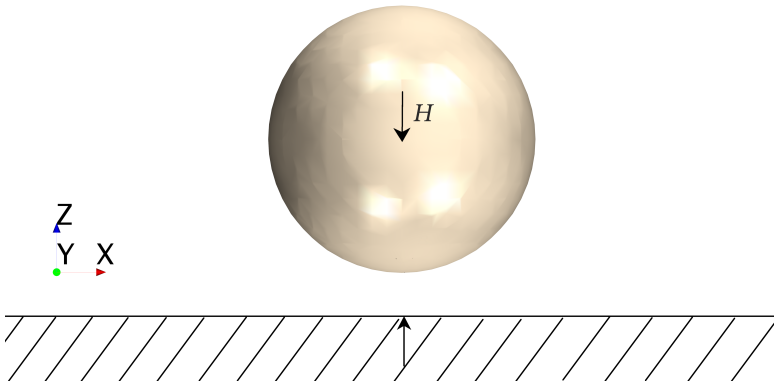

Figure 4.11: Representation of the bubble interface for an iso-surface of $\alpha_v = 0.5$ in Grid 5, at a distance $H = 5mm$ ($\gamma = \frac{H}{R_b} = 1.3$) from an infinite flat surface

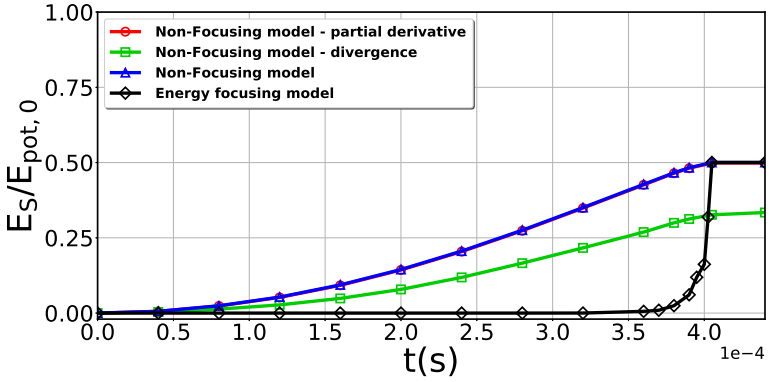

Figure 4.12: Total accumulated surface energy over time, normalized by the initial potential energy, with and without focusing. For the non-focusing model, the volume integrated rate of vapor reduction is predicted using the partial derivative (red-circle), the velocity divergence (green-square), and the mass transfer source term (blue-triangle). The latter is also used to predict the accumulated surface energy with the energy focusing model (black-diamond).

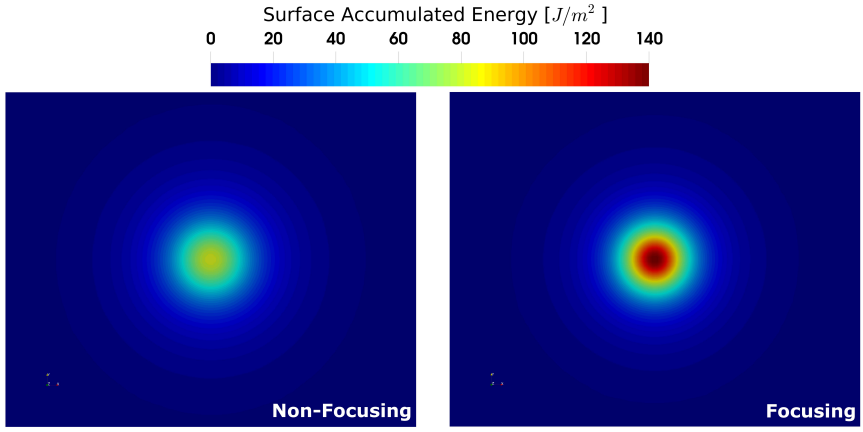

Figure 4.13: Distribution of the accumulated surface specific energy for the non-focusing model (left) and the focusing model (right).

potential energy is transmitted to the surface. When the volume change is predicted from the velocity divergence term, part of the energy is lost, due to numerical error in the reconstruction of the velocity divergence, however the final energy, distributed on the flat surface, is still half of that in the case of the bubble collapse in an infinite liquid.

The accumulated specific energy on the surface can be estimated for the two different approaches, which should give an indication of the cavitation erosion intensity of the impact. Figure 4.13 depicts the distribution of the accumulated surface specific energy, after the bubble has collapsed. In both cases, there is a distinct axisymmetric footprint with a clear peak value in the center. However, the magnitude of the maximum specific energy in the middle, is higher in the focusing approach. This can be explained by the fact that in this approach the potential energy is continuously focused into the collapse center, therefore right before the collapse, all the energy is concentrated at a single point, and is released all at once, giving a footprint with high intensity towards the middle. While with the non-focusing approach, the energy is continuously being released in the domain, such that the energy remained in the cavity right before the collapse is less than in the focusing approach. This results in an accumulated surface energy, which smears out throughout the collapse, and the energy is continuously distributed over a larger area.

4.5. PROPELLER TEST CASE

4.5.1. CASE DESCRIPTION

The cavitation erosion intensity is estimated on the King's College-D (KCD)-193 model propeller. This propeller has been tested at the Emerson Cavitation Tunnel of Newcastle University. Experimental paint test has been conducted on the propeller blades [38]. A 2D wake screen was used, located $0.4572m$ ($1.5D$) from the propeller centre, to create a non-uniform inflow to the propeller, and test the propeller performance under more realistic conditions. The propeller geometry, and the velocity and turbulence intensity measurements at the 2D wake screen plane, were provided by the University of Strath-

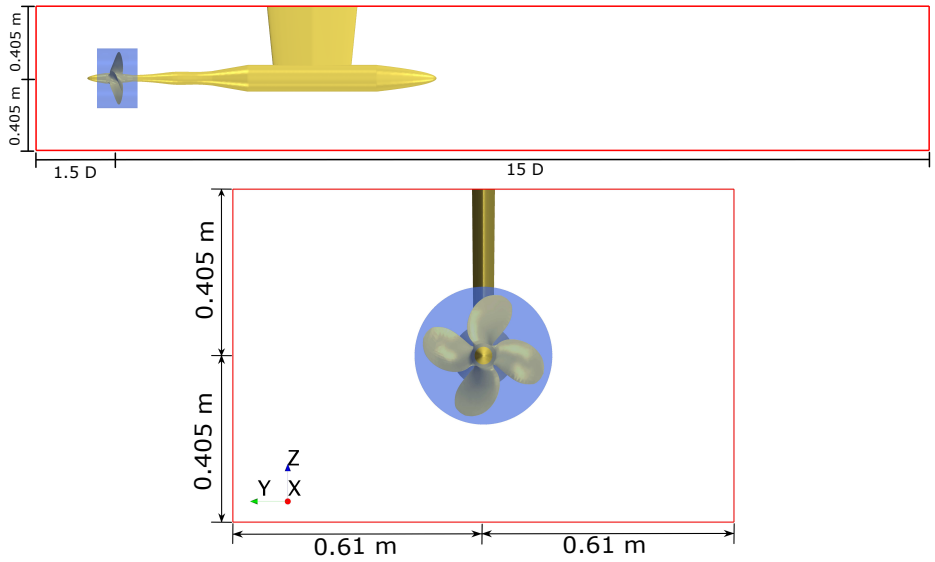

Figure 4.14: Computational domain with the tunnel cross section being $1.22m \times 0.81m$, and the propeller center being $1.5D$ from the velocity inlet and $15D$ from the pressure outlet. The size of the rotating region (light blue) is also shown.

Table 4.2: Propeller Characteristics

Propeller Diameter	$0.3048m$
P/D	1
Blade Area Ratio	0.65
Number of Blades	4

clyde, Glasgow [9].

Table 4.2 shows the propeller characteristics. The propeller was tested in atmospheric condition (see Table 4.3). Fig. 4.14 shows the propeller geometry within the computational domain. The dimensions of the tunnel cross section and the position of the propeller are identical with the experimental set-up by Mantzaris *et al.* [38]. The location of the inlet boundary is located 1.5 diameters from the propeller center, where the non-uniform inflow velocity is specified only in the x-direction. The size of the rotating domain (light blue) is chosen such, that the interfaces are not located in areas, where high pressure gradients occur. The propeller rigid motion is simulated using a sliding mesh approach. In Fig. 4.15 the velocity distribution in the inlet is shown, and in a plane just in front of the propeller hubcap. The flow is slightly accelerated by the propeller motion, before entering the rotating domain, however, the character of the non-uniform overall flow is maintained. A pressure boundary condition, with a constant ambient pressure, is applied 15 diameters downstream, while the top, bottom and the side boundaries are

Table 4.3: Flow Characteristics

Condition	p_{ref} (kPa)	n (RPM)	V_{in} (m/s)	J	σ	$Re_{0.7\%R}$
Atmospheric	116.72	1500	3	0.393	3.88	2.45×10^6

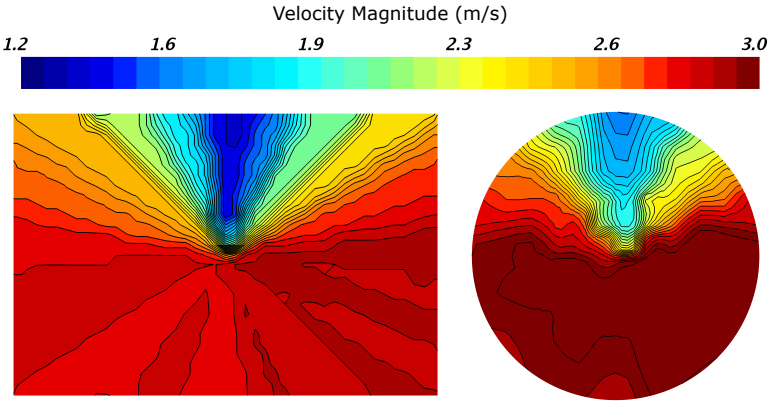

Figure 4.15: Velocity distribution in the inlet (left) and in a plane just in front of the propeller hubcap (right)

set to slip wall condition, as they are assumed to not interfere with the propeller motion. The Reynolds number at 70% of the radius R is of the order of 10^6 (see Table 4.3), which is higher than the critical Reynolds numbers for transition from laminar to turbulent flow (typically $10^5 < Re < 10^6$). Besides, the non-uniform inflow reduces even more the risk of regions with laminar flow, and the flow over the whole blade can be considered, more or less, fully turbulent.

For the grid generation, trimmed hexahedral cells are used with local refinements and prism layers along the wall to resolve the viscous sub-layer. First a coarse grid, with a refinement at the propeller leading and trailing edge, is generated to roughly estimate the amount of vapor on the propeller blades. Then, an additional refinement is applied on one of the blades to assess the cavitation intensity on the surface, in order to follow the guidelines for the spatial resolution, as proposed in Section 4.4. First, the size of the cavitating structures needs to be estimated, so that the required grid resolution and time step size can be determined. In Fig. 4.16, a 2D section of the developed cavity is shown, approximately at the location on the blade, where the maximum amount of paint was removed during the paint test. The width of the cavity in the x-direction is estimated to be around $1.2cm$. The corresponding Rayleigh collapse time is found to be $\tau \simeq 4.27 \times 10^{-4} s$.

In Section 4.4 we showed that approximately 18 cells per diameter, and about 40 time steps, are required to get a grid and time step size independent solution for the single bubble collapse test case. For a cavity with diameter $D = 1.2cm$, this translates to a minimum cell size of $c \simeq 0.667mm$, and a time step size of $\Delta t = 1.28 \times 10^{-5}$ or a rotation rate of $0.115deg$ per time step. Eventually, the minimum cell size of the current domain is selected, $c \simeq 0.45mm$, which corresponds to approximately 27 cells over the cavity width,

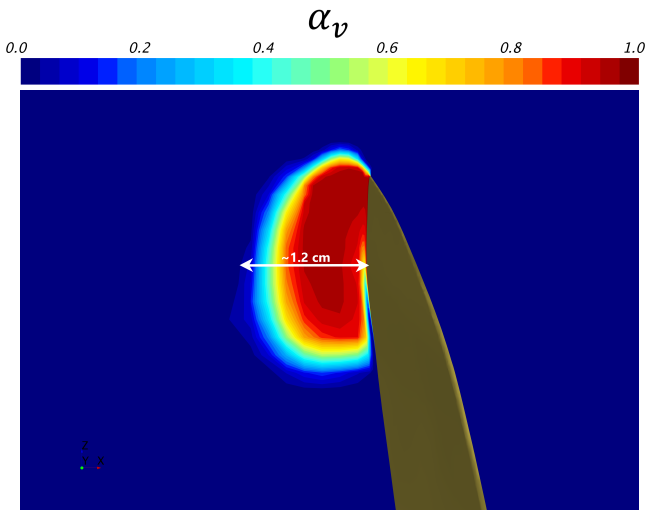

Figure 4.16: Volume fraction of vapor α_v at an arbitrary cross section, showing the maximum width of the developed cavity on the propeller blade over one revolution. The location of the cross section is located approximately where the maximum amount of paint was removed from the blade during the paint test.

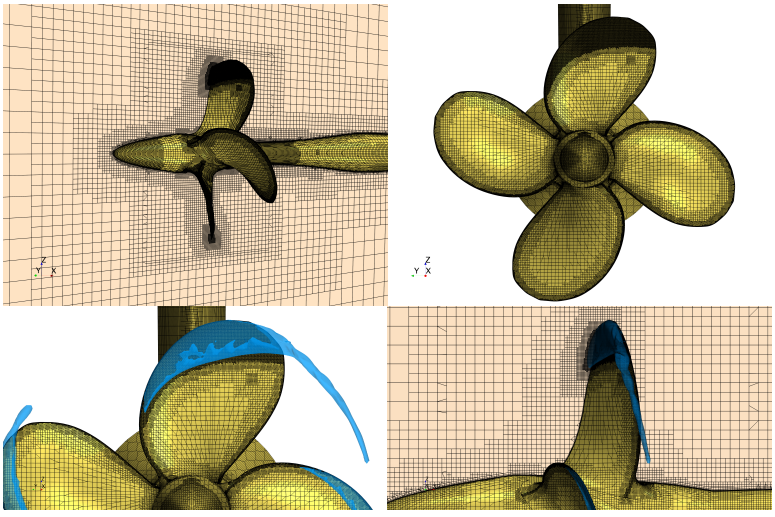

Figure 4.17: Computational mesh around the propeller and the vapor cavity on the refined blade at its top position. The vapor volume is represented by an iso-surface of $\alpha_v = 0.01$.

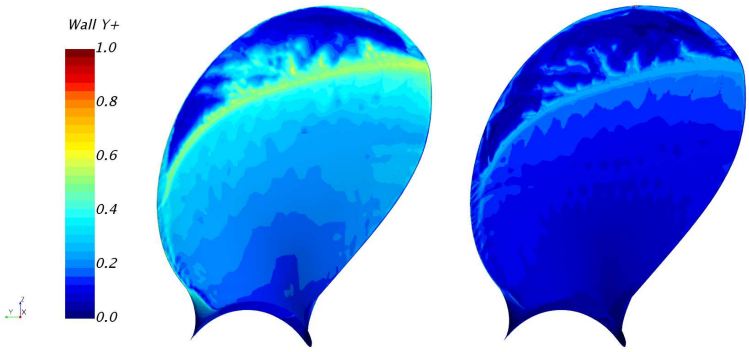

Figure 4.18: Wall y^+ values on the refined blade for Grid 1 (left) and Grid 3 (right). The blade is depicted at its top position.

and a time step size of $\Delta t = 1.11 \times 10^{-5}$, or a rotation rate of $0.1 deg$ per time step. Then, the refinement is applied at locations where the maximum value of α_v over one rotation is not zero, and only on one blade to reduce the computational cost. This results in a refinement region that covers the whole cavity in the vicinity of the blade surface, at any time instant, during a full rotation. Fig. 4.17 shows the mesh refinement and the cavity size when the refined blade is located at the top position (0^o). Three finer grids have been generated to assess the temporal and spatial discretization error. In order to keep the different grids as geometrically similar as possible, special attention has been paid to the generation of the prism layers close to the blade surface (for details see Melissaris *et al.* [17], Crepier [39]). Eca *et al.* [40] have shown that for the SST k-ω turbulence model at high Reynolds number, wall y^+ equal to 1 is not sufficient to obtain low numerical uncertainties, and y^+ values as low as 0.1 (or at least below 0.5) are required to obtain numerical uncertainties similar to other turbulence models. Thus, average wall y^+ values at the refined blade are kept lower than 0.25 for all grids. Table 4.4 shows, for each grid, the number of computational cells in the whole domain, as well as on the refined blade, and the number of prism layers, and the average wall y^+ values on the refined blade. Finally, Fig. 4.18 shows the wall y^+ distribution on the refined blade, for the coarsest (Grid 1) and the second finest grid (Grid 3). Clearly, the y^+ values drop as we go to finer grids and more prism layers, even below 0.1 for the finest grid (Grid 4, see Table 4.4).

Finally, the condensation and evaporation coefficients, $C_{c,SF}$ and $C_{v,SF}$, are selected based on the results from the single bubble collapse test case (Section 4.4). Coefficient values equal or larger than one gave solutions, which were independent of these coefficient values. However, in the propeller test case, we observed that vales higher than one introduce some numerical instabilities to the solver, and thus the default value of one was chosen for both coefficients for all cases.

4.5.2. RESULTS

PROPELLER PERFORMANCE AND NUMERICAL UNCERTAINTY

The propeller performance is predicted and compared with experimental measurements as reported in Usta *et al.* [9]. Propeller thrust and torque are computed for the refined

Table 4.4: Description of the four different generated grids and propeller thrust an torque results for each grid. Comparison with experimental measurements

Grid	# Cells Total	# Cells on refined blade	# Prism Layers	average y^+ on refined blade
Grid 1	3.64 M	43.3 k	10	0.24
Grid 2	6.86 M	78.7 k	15	0.15
Grid 3	10.1 M	112.6 k	20	0.11
Grid 4	17.55 M	165.2 k	25	0.09

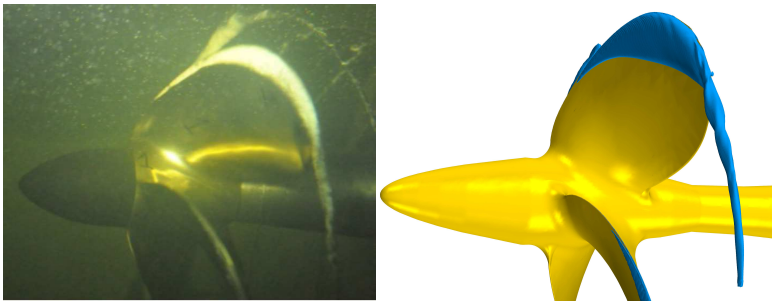

Figure 4.19: Qualitative comparison between the experimental observation [38] and the cavitation development on the blade, where the mesh refinement is applied, visualized as an isosurface of $\alpha_v = 0.01$

blade, and then multiplied by the number of blades. The numerical uncertainty is assessed following the procedure by Eca and Hoekstra [41], using the Validation & Verification tool, developed by MARIN [1]. In Fig. 4.19 the cavitation development on the propeller blades is compared with the experimental observation. Because of the non-uniform inflow, the vapor volume varies at different blade positions, and unfortunately, due to the limited documentation of the vapor volume development during the cavitation test, it is hard to compare between the experiment and the simulated cavity. However, qualitatively, the cavitation extent seems comparable.

First the temporal discretization error is estimated. Table 4.5 shows the propeller thrust and torque for the coarsest grid (Grid 1), and different time step sizes, and how they compare with the experiment. The convergence of the propeller thrust and torque with respect to the rotation rate, is depicted in Fig. 4.20 and Fig. 4.21 respectively. The corresponding numerical uncertainty is indicated by an interval that contains the exact solution with 95% coverage. Propeller thrust and torque are not very sensitive to the time step size. The deviation between the computed thrust and torque, and the experimental values is less than 2% even for the highest time step size, while the numerical uncertainty is estimated less than 0.5% for all time step sizes.

The grid discretization error is also assessed for each grid. Table 4.6 compares the propeller performance for each grid, and Fig. 4.22 and 4.23 depict the convergence of

[1] http://www.refresco.org/verification-validation/utilitiesvv-tools/

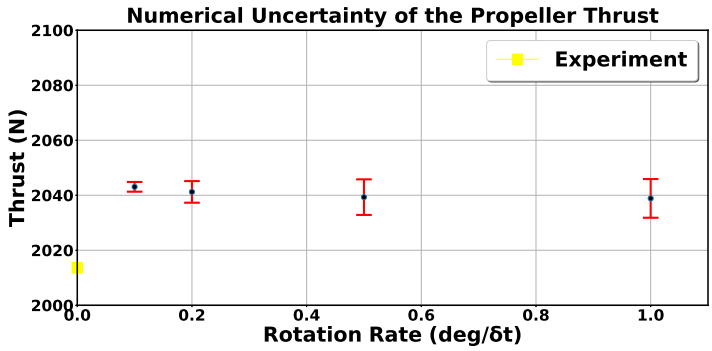

Figure 4.20: Convergence of the propeller thrust with the time step size. Impression of the numerical uncertainty estimate, and comparison with the experimental measurement.

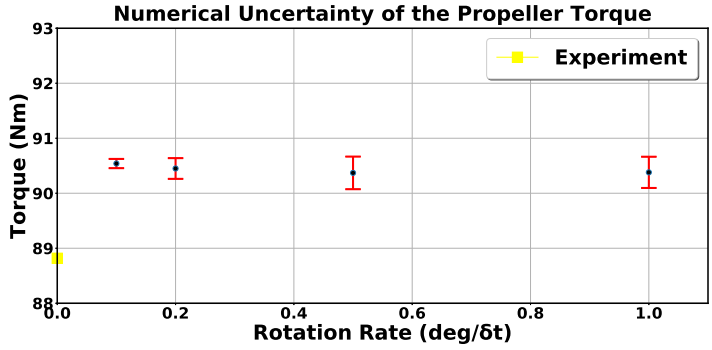

Figure 4.21: Convergence of the propeller torque with the time step size. Impression of the numerical uncertainty estimate, and comparison with the experimental measurement.

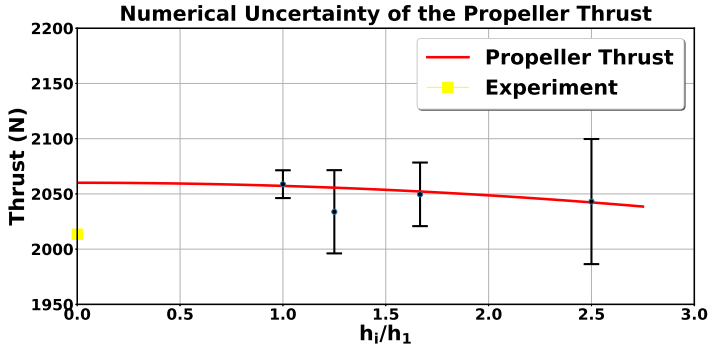

Figure 4.22: Convergence of the propeller thrust with the refinement ratio h_i/h_1. Impression of the numerical uncertainty estimate, and comparison with the experimental measurement.

Table 4.5: Propeller performance for the coarsest grid (Grid 1) and four different time-step sizes, and comparison with experimental measurements

Time step ($deg/\Delta t$)	Thrust (N)	Deviation from Experiment	Torque (N)	Deviation from Experiment
1	2038.9	1.26%	90.38	1.75%
0.5	2039.3	1.28%	90.37	1.75%
0.2	2041.2	1.37%	90.45	1.84%
0.1	2043.1	1.47%	90.54	1.94%

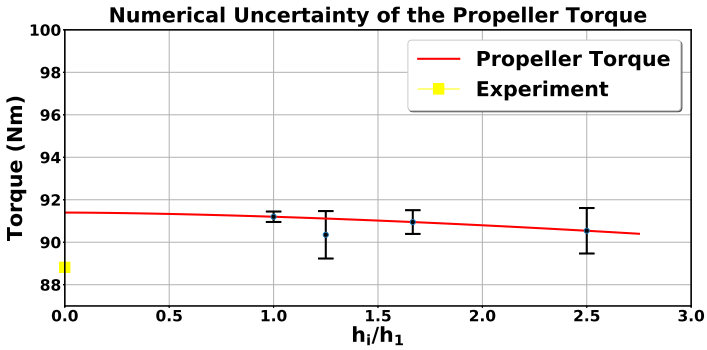

Figure 4.23: Convergence of the propeller torque with the refinement ratio h_i/h_1. Impression of the numerical uncertainty estimate, and comparison with the experimental measurement.

propeller thrust and torque with respect to the refinement ratio h_i/h_1, and the corresponding numerical estimates. Here, h_i is the typical cell size of the i_{th} grid, and h_1 the typical cell size of the finest grid. Propeller thrust is slightly more sensitive to the grid density. The observed order of convergence is equal to the theoretical one ($P = 2$), and the numerical uncertainty is below 3% for all grids, while it drops below 1% only for the finest grid, probably because the average wall y^+ is below 0.1 only for Grid 4. On the other hand, propeller torque is not that sensitive to the grid size. The observed order of convergence is close to the theoretical one ($P = 1.61$), and the numerical uncertainty is very low for each grid (about 1% for Grid 1 and 0.3% for Grid 4).

EROSION RISK ASSESSMENT

The cavitation intensity on the propeller blades is estimated by determining the local surface impact power $\dot{e}_S(t, \boldsymbol{x}_S)$, according to Eq. 4.30. First, an investigation on the effect of the pressure field effectively driving the collapses has been conducted. The accumulated volume specific potential energy in the domain is estimated using the mass transfer source term and different driving pressure fields. The driving pressure fields are obtained by averaging in time the local cell pressure p over different time windows. Fig. 4.24, demonstrates the influence of the different driving pressure fields, as computed for different sliding windows, on the total potential energy. The total accumulated potential energy

Table 4.6: Propeller performance for the four generated grids, and comparison with experimental measurements

Grid density h_i/h_1	Thrust (N)	Deviation from Experiment	Torque (Nm)	Deviation from Experiment
2.5 (Grid 1)	2043.1	1.47%	90.54	1.94%
1.67 (Grid 2)	2049.6	1.79%	90.95	2.40%
1.25 (Grid 3)	2033.8	1.01%	90.35	1.73%
1 (Grid 4)	2058.8	2.25%	91.20	2.68%

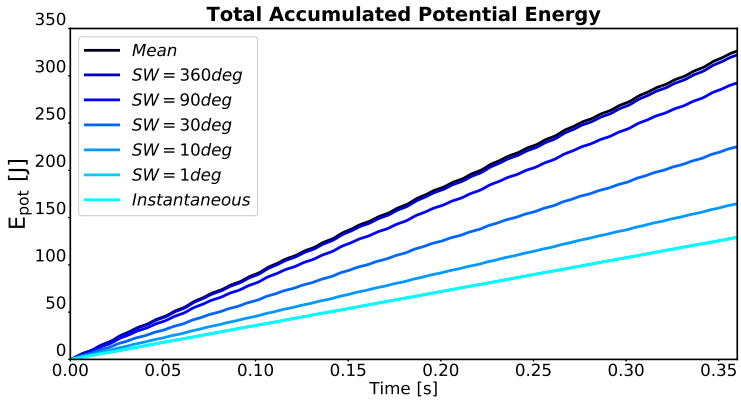

Figure 4.24: Total accumulated volume specific potential energy in the domain for different driving pressure fields. The driving pressure fields are obtained from a moving average of the instantaneous pressure field over different sliding windows (SW).

obtained from the instantaneous pressure field, is compared with the one obtained from pressure fields averaged over a time window of 1 deg, 10 deg, 30 deg, 90 deg, 360 deg, and eventually, the pressure field obtained from a time averaging over the total sample time. We observe, that when the chosen time window is smaller than one full propeller rotation, the predicted energy is quite sensitive to the window size. As the time window decreases, the predicted energy is approaching what we obtain when the instantaneous pressure is used as driving pressure. Thereby, high amplitude pressure peaks are expected by the periodic cavity collapses and thus, we cannot account for pressure recovery gradients, as typically present along lifting bodies. As the time window is getting larger, so does the total accumulated volume specific potential energy. Eventually, when a time window of one whole revolution is used, the predicted energy is almost identical to the one obtained with a time window of the total sample time. Thus, a time averaged pressure field over one rotation, or one shedding cycle, is considered sufficient for an estimate of the effective driving pressure field.

Afterwards, the distributions of the accumulated surface specific energy on the refined blade, obtained by the non-focusing and the energy focusing model, after eight

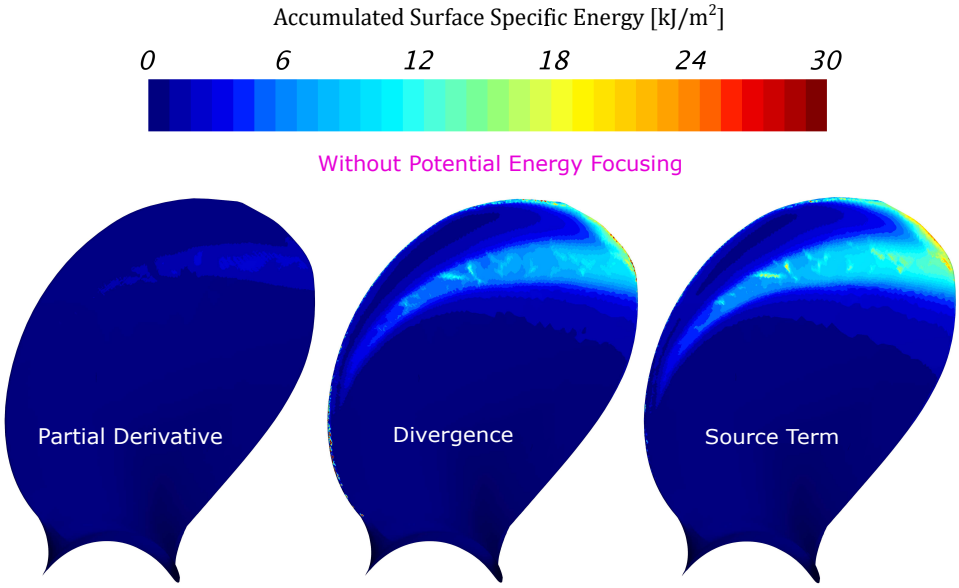

Figure 4.25: Surface specific accumulated energy on the refined propeller blade, obtained from the non-focusing model after eight propeller revolutions, where the vapor volume reduction rate has been estimated using the partial derivative (left), the divergence (middle), and the source term (right)

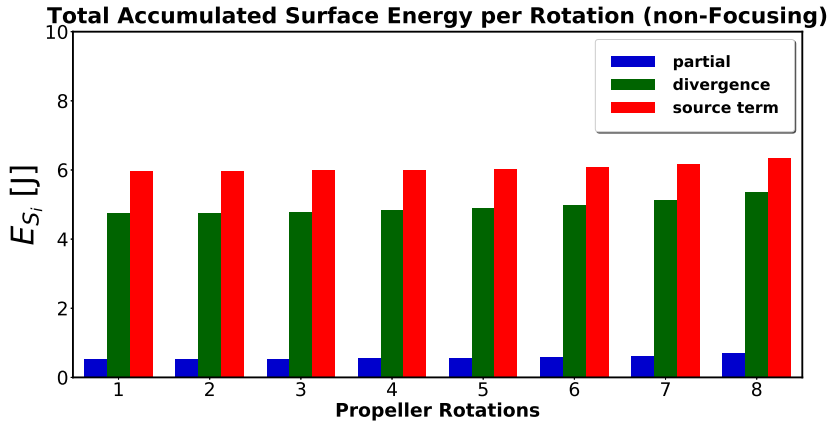

Figure 4.26: Surface integrated accumulated energy per rotation on the refined blade, in J, obtained by the non-focusing model over 8 propeller revolutions, using the partial derivative (blue), the divergence (green), and the source term (red)

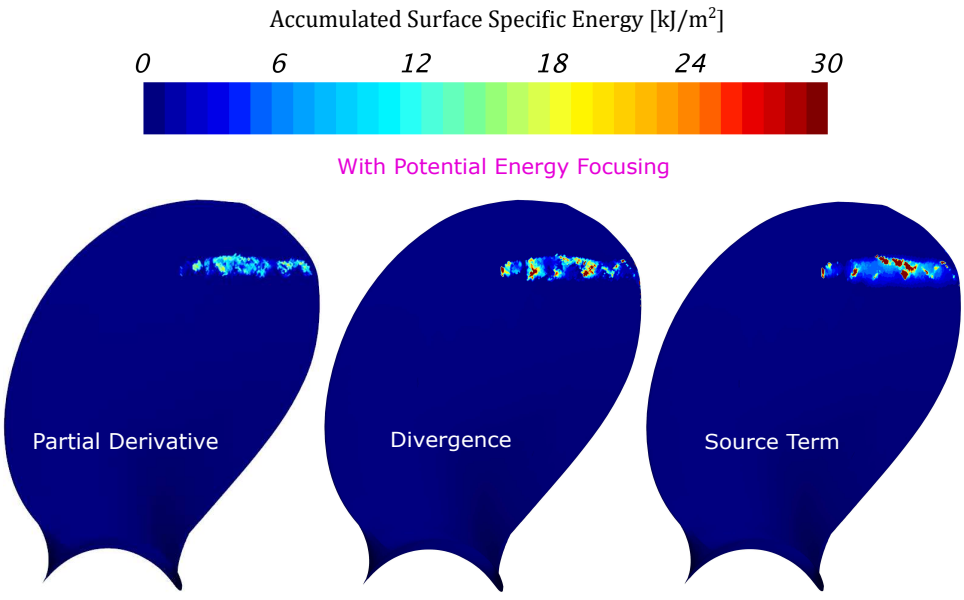

Figure 4.27: Surface specific accumulated energy on the refined propeller blade, obtained from the energy focusing model after eight propeller revolutions, where the vapor volume reduction rate has been estimated using the partial derivative (left), the divergence (middle), and the source term (right)

propeller revolutions, using the three different considerations for the vapor volume reduction rate are compared. Fig. 4.25 depicts the distributions of the non-focusing model. It is obvious that there is a huge discrepancy between the distribution obtained with the partial derivative and the one obtained with the source term. This is explained by the fact that the partial derivative of α in Eq. 4.15a includes an advective term. As the flow accelerates in higher radii, the advective term contributes more and more to the radiated energy, and as a consequence, it deviates from the radiated energy obtained with the source term. The higher the velocities occuring around the blade, the larger the error. Similarly, the distribution obtained with the divergence, still shows a discrepancy from the one obtained with the source term, although quite smaller. The reason for that is that the numerical error involved in the reconstruction of the radiated energy using Eq. 4.15b is getting smaller as the flow velocities get larger, and the inertia in the flow increases.

To further analyze the errors made in the reconstruction of the radiated energy in a more quantitative manner, the total accumulated surface energy per rotation E_{S_i} is obtained by the surface integral of the accumulated surface specific energy at the end of each rotation i

$$E_{S_i} = \int_A e_{S_i} dA \qquad for \quad i = 1,2,...8 \tag{4.31}$$

and it is depicted in Fig. 4.26. The total accumulated energy obtained by the partial derivative of α is almost an order of magnitude smaller than the other two, while the accumulated energy obtained by the divergence term is about 20% smaller than the one obtained by the mass transfer source term.

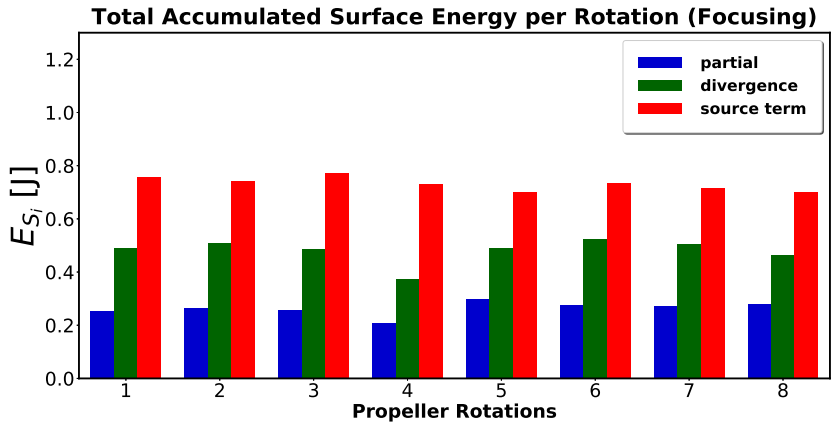

Figure 4.28: Surface integrated accumulated energy per rotation on the refined blade, in J, obtained by the energy focusing model over 8 propeller revolutions, using the partial derivative (blue), the divergence (green), and the source term (red)

Now, comparing the impact distribution between the non-focusing model, where the potential energy is radiated instantaneously, Fig. 4.25, and the energy focusing model, Fig. 4.27, the energy appears to be accumulated in a much larger area, with the non-focusing model. Any dynamics of the sheet cavity, result in energy transfer to the surface, thus leaving a footprint, which extends almost over the whole blade along the cavity trailing edge. On the other hand, the surface impacts are much more scattered, and shifted towards the trailing edge, when the energy focusing approach is applied. In addition to that, these localized events are expected to be more aggressive, as big amounts of energy are concentrated into very small areas of the blade surface.

Looking at the total accumulated energy per rotation as obtained by the energy focusing model for the three different energy reconstruction methods (see Fig. 4.28), one can notice that the error magnitudes are different than the ones with the non-focusing model. The accumulated energy obtained by the partial derivative is higher than before, while the one obtained by the velocity divergence is smaller, which shows that the errors involved in these two energy reconstruction methods are highly dependent on the flow characteristics. As shown in the single bubble collapse test case, when the inertia in the main flow increases, the error involved in the reconstruction of the radiated energy using the partial derivative of α and the velocity divergence are getting larger and smaller respectively. The total inertia in the flow depends on the flow velocity and the collapse induced velocity. While the collapse induced velocity is the highest at the final stage of a collapse, the flow velocity is almost zero as the collapsing cavities are decelerated by the adverse pressure gradient. Thus, the total inertia at locations where we approach the final stage of a collapse is lower than locations with higher flow velocity but low collapse induced velocity. Since with the energy focusing model, the radiated energy is reconstructed only at locations of the final stage of the collapse the errors involved in the reconstruction of the radiated energy using the partial derivative will be smaller and the ones using the velocity divergence will be larger. All in all, we see a similar behavior as in the single bubble

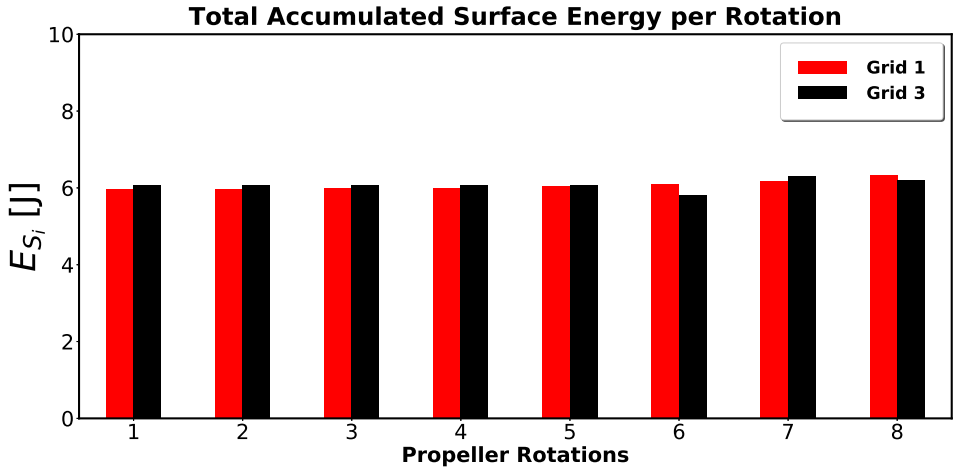

Figure 4.29: Surface integrated accumulated energy per rotation on the refined blade, in J, obtained by the non-focusing model over 8 propeller revolutions.

collapse in Section 4.4, and the radiated energy reconstruction errors obtained from the partial derivative of α and the velocity divergence are strongly dependent on the inertia of the flow.

Figures 4.29 and 4.30 show the surface integrated accumulated energy per rotation for eight propeller revolutions for the two grids, using the non-focusing and the energy focusing model respectively. The radiated energy on the blade is rather insensitive to the grid density, for both models. Similar energy content is predicted on the blade surface during each revolution for both grids. These results are well in line with the findings in Section 4.4, and the resolution of the coarsest grid is already sufficient to obtain a grid independent solution for the amount of accumulated energy on the blade. However, the total surface accumulated energy obtained from the energy focusing model is about an order of magnitude less than the one obtained from the non-focusing model. When no potential energy focusing is considered, the energy is radiated instantaneously, when there is a reduction of vapor volume. On the other hand, with the energy focusing model, energy is radiated only from structures that actually reach a final collapse stage, resulting in less accumulated energy on the surface.

Furthermore, some small variations are observed between the propeller revolutions. These variations are partly related to cloud cavitation and system instabilities. One can show from the localized Euler equations at the cavity closure that the stagnation point is highly unstable, even for a globally steady cavity flow [4]. The instability affects the re-entrant jet and the whole closure region, leading to irregular break-up patterns. It appears that the re-entrant jet and cloud cavitation instability preferably occurs in short cavities with pronounced adverse pressure gradients, whereas system instability mostly effects long cavities with weak adverse pressure gradients. Long cavities can be very sensitive to variations in the incoming flow, which is the case for a propeller operating in a non-uniform inflow. These 3-D aspects of cloud shedding are referred to as being intrin-

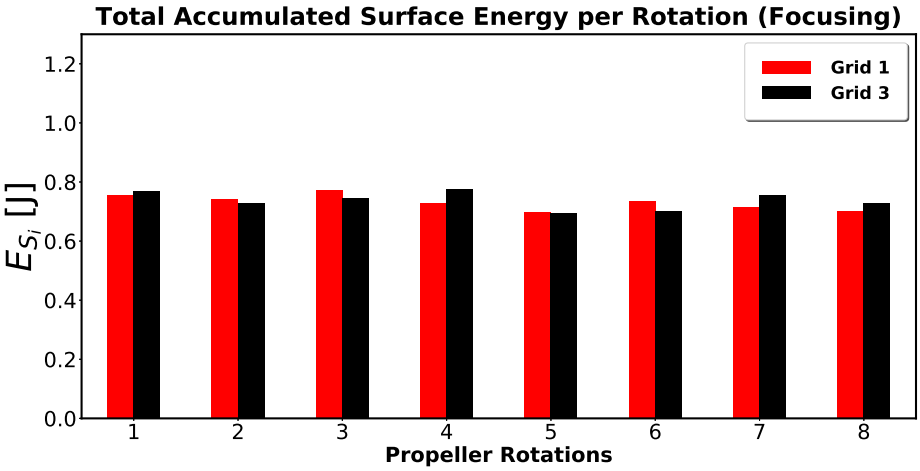

Figure 4.30: Surface integrated accumulated energy per rotation on the refined blade, in *J*, obtained by the energy focusing model over 8 propeller revolutions

sic instabilities or often referred to as self-excited instabilities [4], and it has been shown that they are essentially inertia controlled, and developed naturally, separated from instabilities due to turbulence [42]. In a RANS modeling, most of those instabilities are restrained due to the increase of eddy viscosity at the mixture interface. However, employing the correction to suppress the eddy viscosity at the interface, we allow for partial cavity shedding and therefore we introduce intrinsic instabilities. The other part of these variations at each propeller revolution is related to modeling and iterative convergence errors. Therefore, more than one propeller rotations are necessary in order to obtain a reliable estimate for the average accumulated surface energy. Still, these discrepancies are rather small, and already after the first revolution we get a good idea of the amount of the accumulated energy on the blade.

Comparing the accumulated energy distribution on the blade obtained by the non-focusing model for Grid 1 and Grid 3 after 8 propeller rotations (Fig. 4.31), they look quite similar. On the other hand, when we compare the distributions obtained by the energy focusing model, some differences are rather noticeable. While for the coarse grid (Grid 1) most of the energy is radiated towards the blade trailing edge, for the fine grid (Grid 3) some part of the initial potential energy is distributed closer to the leading edge. This is because small scale properties are typically dependent on the chosen resolution in unsteady solution of cavitating flows [42], and thus with the finer grid we resolve more vapor structures in the domain than in the coarse grid. To generate the coarse grid, we estimated the width of the sheet cavity close to the trailing edge, at the area where the maximum paint removal was observed during the paint test. Therefore, the grid resolution in areas closer to the leading edge, where the width of the sheet cavity is thinner, is perhaps not sufficient to resolve any possible collapse, but only bigger structures that are shed towards the trailing edge. However, the finer grid probably provides this resolution to resolve some of the smaller structures closer to the leading edge. On top of that,

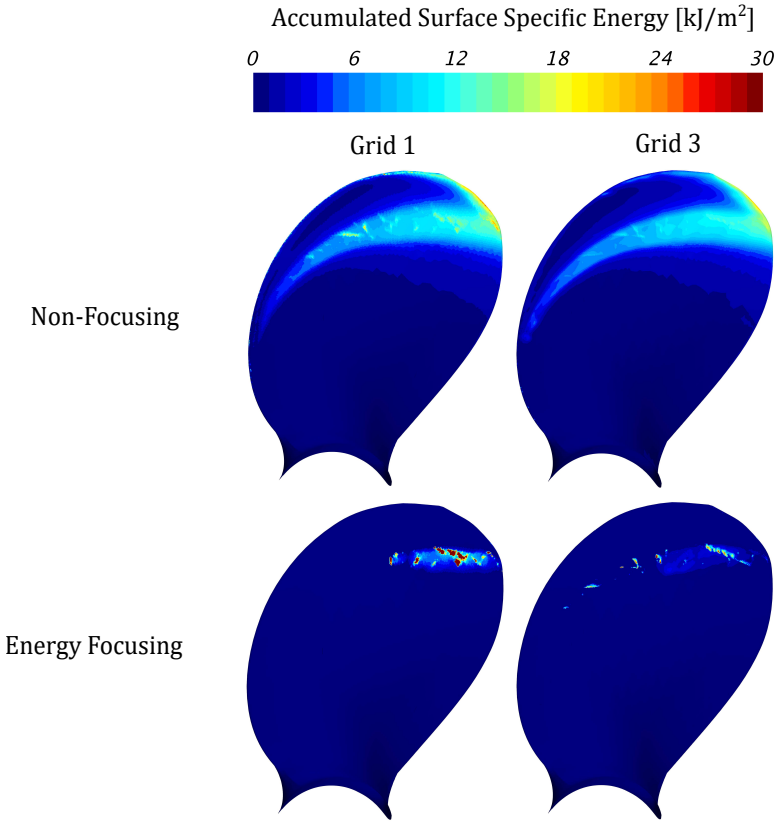

Figure 4.31: Surface specific accumulated energy on the refined propeller blade, obtained by the non-focusing (top) and the energy focusing model (bottom) for Grid 1 (left) and Grid 4 (right) after 8 propeller rotations

due to the smaller cell size in the finer grid, the energy at the final stage of the collapse is focused on a much smaller area, and therefore the radiated energy is more localized to smaller surface areas. That explains why for the coarse grid the high energy density areas are broader than for the fine grid. However, the total energy on the blade for both grids is similar, since large scale properties such as shedding frequencies and characteristic void fraction distributions, regarding the basic shape of the sheet and cloud cavities, seem to be less dependent on the grid density.

Furthermore, we compare the distributions of the accumulated surface specific energy on the refined blade, obtained by the energy focusing model for the coarse and the fine grid (Grid 1 and Grid 3 respectively), with the one obtained from the paint test (see Fig. 4.32). Although the impacted areas are not as extensive as in the test, this is reasonable since the erosion pattern on the blade was obtained after half an hour of testing, and thousands of propeller revolutions, while we assessed the impact distribution after only $0.32s$ and 8 revolutions. Due to the intrinsic instabilities of the partial cavity dynamics and the modeling/numerical instabilities we introduce, the location of the final collapse

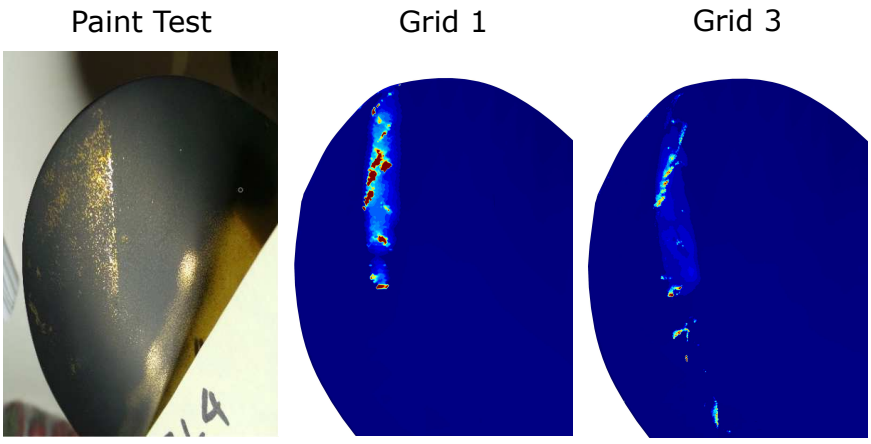

Figure 4.32: Comparison between the experimental paint test (left) and the surface specific accumulated energy on the refined blade, obtained by the energy focusing model, after 8 propeller revolution, with the coarse (middle) and the finer grid (right)

of shed cavities of smaller scale, will vary between different propeller revolutions and, thus much more time is needed to get a fully converged impact distribution on the blade, especially for the finest grid, where more small scale structures are resolved. However, in both grids, high energy density is obtained in blade areas, where paint was removed during the test, and the main impact areas are captured. Finally, it is important to mention that areas with high energy density are not necessarily areas with the highest erosion risk. As we have indicated in previous studies on hydrofoils [1, 17], the impact power is of much higher importance. Surface areas with similar high energy content can be observed either by repetitive low amplitude events, or by extreme events of lower frequency. While in both cases the energy content might be comparable, in an extreme event large amount of energy is released, and distributed to the surface, during a small period of time, which might render such an event more aggressive. Such analysis of the rapidness of the cavity collapses could be done using aggressiveness indicators (see Schenke and van Terwisga [1], Melissaris *et al.* [17], Schenke *et al.* [35]), however that is beyond the scope of this paper.

4.6. CONCLUSION

A novel methodology, developed within the European project "CaFE", by Schenke *et al.* [2], has been used in this study to predict cavitation implosion loads on a surface. This model takes into consideration the time accurate energy balance during a cavity collapse. While the cavity starts to condense, the initial potential energy is continuously feeding into kinetic energy, around the cavity interface. At the final stage of collapse, all the potential energy has been converted into kinetic energy, and has been focused into the collapse center. That is the point, when all the energy is released in the domain as shock wave energy.

The model has been verified on a single cavitating bubble collapsing in an infinite

fluid and close to a wall, where an investigation on the numerical errors involved in the reconstruction of the radiated energy has been conducted. The vapor volume reduction rate is predicted using three different considerations. One involves the partial derivative of the vapor fraction α_v, the second involves the velocity divergence, and the last one involves the mass transfer model source term. The model is further applied to the KCD 193 model propeller test case, that was tested in the Newcastle cavitation tunnel behind a 2D wake screen. From these studies, we draw the following conclusions:

- When the vapor volume reduction rate is estimated using the cavitation model mass transfer source term, then the numerical error, involved in the reconstruction of the radiated energy, is minimal. All the energy is then conserved and the total energy balance is fully satisfied. The error (modeling or numerical) in the other two considerations depends strongly on the inertia of the flow. They could provide a good estimate of the surface accumulated energy in specific cases, however one should be aware of their sensitivity to the flow conditions.

- The temporal and spatial discretization errors have been assessed for the propeller performance. Propeller thrust and torque are rather insensitive to the time step size and low uncertainty estimates are obtained (below 0.5%). Propeller thrust is more sensitive to the grid density than torque. However, the uncertainty of the propeller thrust is below 3% for all grids, and it drops below 1% for the finest grid. The uncertainty of the propeller torque is rather low for all grids (about 1% or lower).

- The moving time average of the instantaneous pressure field over a time window equal to one shedding cycle (or one revolution) or higher, is considered sufficient for an estimate of the effective driving pressure field. It has been shown that when the sliding window is equal to one shedding cycle or higher, the difference on the total accumulated potential energy in the domain is negligible. Nevertheless, as long as the driving pressure distribution is not exactly known, some uncertainties regarding the potential energy content remain.

- The total accumulated surface energy on the refined blade was found to be insensitive to the grid density for the non-focusing and the energy focusing model. Comparable amount of energy was obtained for the coarse and the fine grid (Grid 1 and Grid 3) during each propeller revolution. However, the total surface accumulated energy obtained from the energy focusing model is about an order of magnitude less than the one obtained from the non-focusing model. In the latter, each volume variation results in radiated energy, leading to over-prediction of the surface accumulated energy.

- When the potential energy focusing is considered some discrepancies are observed on the impact distribution between the coarse and the fine grid, which are related to the grid resolution. The finer mesh resolves smaller scale structures, and provides sufficient resolution for thinner parts of the sheet cavity, while the energy at the final stage of the collapse is focused to a much smaller area. Therefore, the events are more localized, and the energy scattering is increased, so does the time

to get a fully converged impact distribution on the blade. Yet, the impact distribution obtained by the energy focusing model agrees well with the high erosion risk areas, as indicated from the paint test, for both grids, and high energy density is observed in the areas of maximum paint removal. The basic cavity dynamics (shape of sheet and cloud cavities) are well captured even with the coarser grid, while, in the finer grid some part of the energy is distributed closer to the leading edge, however it does not necessarily indicate that the erosion risk in those areas is high, as the rapidness/aggressiveness of the collapsing events has not been taken into account.

- Finally, the capabilities of our fully energy conservative model to predict the implosion loads of large scale cavitating structures on propeller blades illustrates its potential for engineering applications. Nonetheless, a good estimate of the size of the collapsing cavitating structures to be resolved is a prerequisite for this model, in order to apply the required grid and temporal resolution, as proposed in this study.

REFERENCES

[1] S. Schenke and T. J. C. van Terwisga, *An energy conservative method to predict the erosive aggressiveness of collapsing cavitating structures and cavitating flows from numerical simulations,* Journal of Multiphase Flow **111**, 200 (2019).

[2] S. Schenke, T. Melissaris, and T. J. C. van Terwisga, *On the relevance of kinematics for cavitation implosion loads,* Phys. Fluids **31**, 052102 (2019).

[3] E. A. Weitendorf, *On the history of propeller cavitation and cavitation tunnels,* in *Proceedings of the* 4^{th} *International Symposium on Cavitation* (California Institute of Technology, Pasadena, USA, 2001).

[4] J. P. Franc and J. M. Michel, *Fundamentals of Cavitation* (Kluwer Academic Publishers, Dordrecht, 2004).

[5] N. Hasuike, S. Yamasaki, and J. Ando, *Numerical study on cavitation erosion risk of marine propellers operating in wake flow,* in *Proceedings of the* 7^{th} *International Symposium on Cavitation* (Michigan, USA, 2009).

[6] N. Nohmi, Y. Iga, and T. Ikohagi, *Numerical prediction method of cavitation erosion,* in *Proceedings of the FEDSM 2008* (Jacksonville, Florida, USA, 2008).

[7] D. Ponkratov and A. Caldas, *Prediction of cavitation erosion by detached eddy simulation (DES) and its validation against model and ship scale results,* in *Proceedings of the* 4^{th} *International Symposium on Marine Propulsors* (Austin, Texas, USA, 2015).

[8] D. Ponkratov, *Des prediction of cavitation erosion and its validation for a ship scale propeller,* J. Phys. Conf. Ser. **656** (2015).

[9] O. Usta, B. Aktas, M. Maasch, O. Turan, M. Atlar, and E. Korkut, *A study on the numerical prediction of cavitation erosion for propellers,* in *Proceedings of the* 5^{th} *International Symposium on Marine Propulsors* (Espoo, Finland, 2017).

[10] O. Usta and E. Korkut, *Prediction of cavitation development and cavitation erosion on hydrofoils and propellers by detached eddy simulation,* Ocean Engineering **191** (2019).

[11] F. G. Hammit, *Observations on cavitation damage in a flowing system,* J. Basic Eng **85**, 347 (1963).

[12] A. Vogel and W. Lauterborn, *Acoustic transient generation by laser-produced cavitation bubbles near solid boundaries,* The Journal of the Acoustical Society of America **84**, 719 (1988).

[13] Z. Li, M. Pourquie, and T. J. C. van Terwisga, *Assessment of cavitation erosion with a URANS method,* Journal of Fluids Engineering **136** (2014).

[14] M. Dular, B. Stoffel, and B. Sirok, *Development of a cavitation erosion model,* Wear **261**, 642 (2006).

[15] M. Dular and O. Coutier-Delgosha, *Numerical modelling of cavitation erosion,* Int. J. Numer. Meth. Fluids **61**, 1388 (2009).

[16] A. Peters, U. Lantermann, and O. el Moctar, *Numerical prediction of cavitation erosion on a ship propeller in model- and full-scale,* Wear **408-409**, 1 (2018).

[17] T. Melissaris, N. Bulten, and T. J. C. van Terwisga, *On the applicability of cavitation erosion risk models with a urans solver,* Journal of Fluids Engineering **141** (2019).

[18] S. Joshi, J. P. Franc, G. Ghigliotti, and M. Fivel, *Sph modelling of a cavitation bubble collapse near an elasto-visco-plastic material,* Journal of the Mechanics and Physics of Solids **125**, 420 (2018).

[19] T. Melissaris, N. Bulten, and T. J. C. van Terwisga, *On cavitation aggressiveness and cavitation erosion on marine propellers using a urans method,* in *Proceedings of the* 10^{th} *International Symposium on Cavitation* (Baltimore, USA, 2018) see also URL https://cav2018.jhu.edu.

[20] T. Melissaris, N. Bulten, and T. J. C. van Terwisga, *A numerical study on the shedding frequency of sheet cavitation,* in *Proceedings of VII International Conference on Computational Methods in Marine Engineering* (Nantes, France, 2017).

[21] J.-L. Reboud, B. Stutz, and O. Coutier, *Two-phase flow structure of cavitation: experiment and modelling of unsteady effects,* in *Proceedings of the* 3^{rd} *International Symposium on Cavitation* (Grenoble, France, 1998).

[22] G. H. Schnerr and J. Sauer, *Physical and numerical modeling of unsteady cavitation dynamics,* in *In Fourth International Conference on Multiphase Flow* (New Orleans, USA, 2001).

[23] STAR-CCM+, *User Guide* (2018).

[24] C. L. Merkle, J. Z. Feng, and P. E. O. Buelow, *Computational modeling of the dynamics of sheet cavitation,* in *Proceedings of the* 3^{rd} *International Symposium on Cavitation* (Grenoble, France, 1998).

[25] R. F. Kunz, D. A. Boger, and D. R. Stinebring, *A preconditioned navier-stokes method for two-phase flows with application to cavitation prediction,* Computers & Fluids **29**, 849 (2000).

[26] A. K. Singhal, M. M. Athavale, H. Li, and Y. Jiang, *Mathematical basis and validation of the full cavitation model,* Journal of Fluids Engineering **124**, 617 (2002).

[27] S. Frikha, O. Coutier-Delgosha, and J. Astolfi, *Influence of the cavitation model on the simulation of cloud cavitation on 2d foil section,* Int. J. Rotating Mach. **2008** (2009).

[28] M. Morgut and E. Nobile, *Influence of the mass transfer model on the numerical prediction of the cavitating flow around a marine propeller,* in *Proceedings of the* 2^{nd} *International Symposium on Marine Propulsors* (Hamburg, Germany, 2011).

[29] P. Koukouvinis and M. Gavaises, *Simulation of throttle flow with two phase and single phase homogenous equilibrium model,* J. Phys. Conf. Ser. 656 (2015).

[30] S. Schenke and T. J. C. van Terwisga, *Finite mass transfer effects in cavitation modelling,* in *Proceedings of* 19^{th} *Numerical Towing Tank Symposium* (St Pierre d'Oléron, France, 2016).

[31] D. Obreschkow, P. Kobel, N. Dorsaz, A. de Bosset, C.Nicollier, and M. Farhat, *Cavitation bubble dynamics inside liquid drops in microgravity,* Phys. Rev. Letters **97** (2006).

[32] M. Tinguely, D. Obreschkow, P. Kobel, N. Dorsaz, A. de Bosset, and M. Farhat, *Energy partition at the collapse of spherical cavitation bubbles,* Phys. Rev. E **86** (2013).

[33] I. Akhatov, O. Lindau, A. Topolnikov, R. Mettin, N. Vakhitova, and W. Lauterborn, *Collapse and rebound of a laser-induced cavitation bubble,* Phys. Fluids **13**, 2805 (2001).

[34] C. Flageul, R. Fortes-Patella, and A. Archer, *Cavitation erosion prediction by numerical simulations,* in *Proceedings of the* 14^{th} *International Symposium on Transport Phenomena and Dynamics of Rotating Machinery* (Honolulu, HI, USA, 2012).

[35] S. Schenke, T. Melissaris, and T. J. C. van Terwisga, *On the relation between the potential cavity energy and the acoustic power signature caused by periodic vapor cavity collapses,* in *Proceedings of the* 6^{th} *International Symposium on Marine Propulsors* (Rome, Italy, 2019).

[36] B. P. Welford, *Note on a method for calculating corrected sums of squares and products,* Technometrics **4**, 419 (1962).

[37] Lord Rayleigh, *On the pressure development in a liquid during the collpapse of a spherical cavity,* Phil. Mag. **34**, 94 (1917).

[38] A. Mantzaris, B. Aktas, P. Fitzsimmons, and M. Atlar, *Establishment and verification of reproducible method for coating propeller blades for erosive cavitation detection,* in *Forth International Conference on Advance Model Measurement Technologies for the Maritime Industry* (Istanbul, Turkey, 2015).

[39] P. Crepier, *Ship resistance prediction: verification and validation exercise on unstructured grids,* in *Proceedings of VII International Conference on Computational Methods in Marine Engineering* (Nantes, France, 2017) nantes, France.

[40] L. Eca, F. S. Pereira, and G. Vaz, *Viscous flow simulations at high reynolds numbers without wall functions: Is y+ 1 enough for the near-wall cells?* Comput Fluids **170**, 157 (2018).

[41] L. Eca and M. Hoekstra, *A procedure for the estimation of the numerical uncertainty of cfd calculations based on grid refinement studies,* Journal of Computational Physics **262**, 104 (2014).

[42] S. J. Schmidt, M. Thalhamer, and G. H. Schnerr, *Inertia controlled instability and small scale structures of sheet and cloud cavitation,* in *Proceedings of the* 7^{th} *International Symposium on Cavitation* (Michigan, USA, 2009).

5

CAVITATION EROSION RISK PREDICTION ON A FULL-SCALE STEERABLE THRUSTER

Propeller cavitation erosion prediction at an early design stage is becoming more and more important since it is one of the key constraints in the search for maximum propeller efficiency. Despite the experience from model tests, cavitation erosion research on actual ship scale is very limited. In this chapter, an attempt is made to assess the erosion risk on the blades of a full-scale steerable thruster of a tug boat. Pressure side cavitation was detected on board for three different propeller designs. For the first time, a cavitation erosion analysis is performed on ship-scale, using a rigorous potential energy approach, which accounts for the focusing of the potential energy at the collapse center during the cavity collapse. A full sensitivity study has been performed for the blade surface accumulated energy. The erosion model shows the erosion risk for different propeller designs applied on the vessel, and different operating conditions, by looking at the surface specific energy on the blade. The erosion analysis shows locations of high erosion risk that show a good resemblance with the actual damage locations on the real blades.

This chapter is based on: T. Melissaris, S. Schenke, N. Bulten, T.J.C. van Terwisga, *Cavitation erosion risk assessments on a full-scale steerable thruster*, Ocean Engineering **251** (2020) 111019.

5.1. INTRODUCTION

Cavitation is characterized by the sudden growth and intense collapse of vapor structures in a liquid due to large pressure variations. Vaporization of a liquid occurs when its pressure drops below the vapor pressure, while when these vapor structures enter a pressure recovery region they collapse. The intensity of their collapse depends strongly on the pressure difference they are subjected to, and the collapse may be so violent that can result in undesired nuisance such as noise, vibrations, and erosion damage. While noise and vibrations are most of the times acceptable until a certain level, cavitation erosion should be avoided, since severe erosion on mechanical components such as propellers, pumps, valves etc. has a significant impact on their efficiency and structural integrity.

Efficient propeller designs cavitate and there is a trade-off between hydrodynamic efficiency and cavitation [1, 2]. Therefore cavitation on the propeller blades is most of the times unavoidable. However, there is a limit until a propeller can cavitate without eroding (or eroding with a very small erosion rate), resulting in the maximum hydrodynamic efficiency. This limit is hard to predict and identify. Cavitation observations in a towing tank using high speed cameras are conducted conventionally to get an impression of the erosiveness of the cavitating structures on the blades in model-scale. Although, such observations can give important information about the shape of the cavity, and possible locations of collapses, it is hard to quantify the intensity and violence of a collapse, while the influence of scale effects is also not considered. Furthermore, propeller designers are using potential flow codes to optimize any propeller design. The majority of those potential flow models, cannot represent the break-up of cavities, and certainly not the dynamics of their collapse. These aspects lead to the necessity of a numerical tool which can simulate the growth and collapse of such cavitating structures on the blade and assess the intensity and aggressiveness of their collapse, as well as the surface impact distribution, with sufficient accuracy.

Although cavitation dynamics have been thoroughly investigated during the last decades, cavitation erosion prediction on marine propellers still remains a challenging topic. And while there are several studies in model scale, investigations on full scale propellers are very limited. In one of the first attempts to predict cavitation erosion on ship scale, Ponkratov and Caldas [3] and Ponkratov [4], estimated cavitation aggressiveness on the rudder and the propeller, respectively. The results showed good correlation with the actual eroded areas. They used erosion functions developed by the Lloyd's Register Technical Investigation Department (LR TID), however these functions have not been reported in the studies. Peters *et al.* [5] used the micro-jet hypothesis to predict cavitation erosion on a ship propeller, both in model and full scale. The simulations were compared to experimental data, demonstrating a good qualitative prediction of the cavitation erosion on the propeller.

The limited research on ship scale propeller erosion prediction emphasizes the difficulty of performing such simulations, as well as the necessity of a more reliable and quantitative approach. In this study, an attempt exactly towards this step is made, where a more quantitative prediction of the cavitation erosion risk on the propeller blades is pursued. We compute the cavitation impact loads on the blades of a full-scale steerable thruster propeller. The erosion risk is represented by the surface specific energy distribution on the blade area, originated from the implosion of the cavitating structures. An

energy balance approach is employed [6–8], where we allow for the focusing of the potential energy, contained in the cavitating structures, into the collapse center, before it is radiated in a shock wave.

At the moment of a cavity collapse, energy is emitted isotropically in the domain. The computation of the exact amount of the radiated energy that will reach any surface in the vicinity, involves the concept of the solid angle. A solid angle is a 3D angular volume that is defined analogously to the definition of a plane angle in two dimensions [9]. In this study, a fully continuous reconstruction of the solid angle is used. For unstructured meshes, the analytical computation of the solid angle is not straightforward, and a discreet approximation is often used instead. For sources very close to the surface, this approximation leads to solid angles significantly larger than the exact solid angle, leading to substantial errors in the computation of the surface accumulated energy. To minimize these errors, the solid angle is bounded to its maximum value.

Finally, to assess the reliability of the model on full scale simulations, an extensive verification study has been performed, based on propeller designs which have been in real operation. The results of the CFD simulations are validated against the actual eroded areas on the used azimuth-thruster propeller blades.

5.2. NUMERICAL MODELING

5.2.1. GOVERNING EQUATIONS AND CAVITATION MODELING

The Reynolds Averaged Navier-Stokes (RANS) equations for momentum and mass continuity are solved, given by

$$\frac{\partial(\rho\mathbf{u})}{\partial t} + \nabla\cdot(\rho\mathbf{u}\mathbf{u}) = -\nabla p + \rho f + \nabla\cdot\tau \tag{5.1}$$

$$\frac{\partial\rho}{\partial t} + \nabla\cdot(\rho\mathbf{u}) = 0 \tag{5.2}$$

where $\mathbf{u}$ is the velocity tensor, ρ is the fluid density, p the pressure, f the external force per unit mass and τ the viscous part of the stress tensor. The density and the turbulent viscosity of the cavitating flow is given by the mixture relations

$$\rho = a_v\rho_v + (1-a_v)\rho_l \qquad and \qquad \mu = a_v\mu_v + (1-a_v)\mu_l \tag{5.3}$$

respectively, where $0 < a_v < 1$ is the vapor fraction. The phase transition is modeled using a homogeneous multiphase mixture model. A single set of momentum equations is solved for the mixture. An additional transport equation is solved to determine the volume fraction of each phase in each computational cell

$$\frac{\partial\alpha_v}{\partial t} + \nabla\cdot(\alpha_v\mathbf{u}) = S_{\alpha_v} \tag{5.4}$$

where S_{α_v} is the mass transfer source term, modeled by the Schnerr-Sauer cavitation model. For further details see Melissaris *et al.* [10, 11].

The k-ω SST turbulence model by Menter [12] is used to model the Reynolds Stress term. A finite-volume discretization technique with cell centered collocated variables is employed to solve the equations. The governing equations are solved sequentially in a

segregated manner. The mass conservation is ensured by a pressure correction equation based on the SIMPLE (**S**emi-**I**mplicit **M**ethod for **P**ressure-**L**inked **E**quations) algorithm [13]. To avoid the artificial increase of eddy viscosity at the mixture regime, an empirical reduction of turbulent dissipative terms is applied, by modifying the turbulent eddy viscosity (see Melissaris *et al.* [10])

5.2.2. CAVITATION EROSION MODELING

Cavitation erosion is modeled considering an energy transfer from the collapsing cavitating structures to the impacted surface. The approach is based on the potential energy hypothesis [14, 15] where the potential energy, initially contained in the vapor cavities, is proportional to the pressure difference driving the cavity collapse $p_d - p_v$, and the cavity vapor volume V_v. During the collapse, the initial potential energy can be partitioned into different forms of energy, and the instantaneous energy balance is considered [16, 17]. The initial potential energy is first converted into kinetic energy, before it is radiated in the domain as acoustic (shock wave) energy. For strong inertia driven flows (about 1 bar driving pressure difference $p_d - p_v$ or higher), and in the absence of non-condensible gas within the cavitating structures, any thermal effects and cavity rebounds respectively, may be neglected [17]. Thus, at the final stage of the collapse, all the initial potential energy has been converted into shock wave energy:

$$E_{SW} = E_{pot,0} - E_{reb} - \Delta U \quad \xLeftrightarrow{E_{reb}\approx 0,\ \Delta U \approx 0} \quad E_{SW} \approx E_{pot,0} \tag{5.5}$$

In every computational cell, the instantaneous volume specific change of potential energy is given by

$$\dot{e}_{pot} = \frac{DE_{pot}/Dt}{V_{cell}} = (p_d - p_v) \cdot \frac{D\alpha_v}{Dt} + \frac{Dp_d}{Dt} \cdot \alpha_v \tag{5.6}$$

In Eq. 5.6 only the first term on the r.h.s. can directly feed into collapse induced kinetic energy, as it represents the change of potential energy due to condensation or evaporation. The second term describes any change of potential energy due to changes of the ambient pressure, however this change can only contribute to inertial motion of the cavities, and it does not involve any change in the vapor volume and subsequently to the collapse induced velocity field around the cavities (see [11, 18]).

Combining Eq. 5.3, 5.4 and 5.6, and considering only condensation, the volume specific potential energy reduction rate becomes

$$\dot{e}_{pot,C}(t, \mathbf{x}_{cell}) = (p_d - p_v) \cdot min\left[\frac{\rho}{\rho_l} S_{\alpha_v}, 0\right] \tag{5.7}$$

In Eq. 5.7 the condensation rate is computed from the cavitation mass transfer model source term S_{α_v}, as in previous work it has been shown that the error made in the reconstruction of the material derivative of the vapor volume, $D\alpha_v/Dt$, is then minimized (see Melissaris *et al.* [11]). The driving pressure field p_d, is computed by time-averaging the instantaneous pressure field in cavitating conditions, p, over one shedding period of the cavity cycle (or higher) [11, 19]. To avoid exceeding random-access memory (RAM) limits, the method applied by Welford [20] is used to approximate the moving average of the

instantaneous pressure field, $\overline{p}_t$, at time instant t, at each computational cell:

$$\overline{p}_t = \overline{p}_{t-1} + \left(p_t - \overline{p}_{t-1}\right)\frac{\Delta t}{T_m} \tag{5.8}$$

where Δt is the time step size, and T_m the sliding window, equal to the cavity shedding period (or higher).

To account for energy partition during the condensation process, a transport equation is implemented for the collapse induced kinetic energy ε, which is given by [18]

$$\frac{\partial \varepsilon}{\partial t} + \mathbf{u}_i \cdot \nabla \varepsilon = -\varepsilon(\nabla \cdot \mathbf{u}_i) - \dot{e}_{rad}(t) \tag{5.9}$$

where $\mathbf{u}_i$ is the collapse induced velocity. The terms $\varepsilon(\nabla \cdot \mathbf{u}_i)$ and $\dot{e}_{rad}(t)$ of Eq. 5.9 represent the conversion of the potential energy into collapse induced kinetic energy and the conversion of the kinetic energy to radiated acoustic energy, respectively. The term $\mathbf{u}_i \cdot \nabla \varepsilon$ represents the conservative advective transport of ε, however the distribution of the collapse induced kinetic energy during the cavity collapse is not known, and therefore a modeling assumption is introduced. In previous work [11, 18, 21], we have shown that the collapse induced kinetic energy transport (Eq. 5.9) can be modeled as

$$\frac{\partial \varepsilon}{\partial t} = (1-\beta)[\phi(\varepsilon) - \dot{e}_{pot,C}(t)] - \beta\frac{\varepsilon}{\delta t} \tag{5.10}$$

where $\phi(\varepsilon)$ is a model for the advective transport of the kinetic energy, and $\dot{e}_{pot,C}(t)$ is the reduction of potential energy. The parameter β is responsible for the conversion of the collapse induced kinetic energy into acoustic radiated energy, and it is defined as follows:

$$\beta = \begin{cases} 1, & if \quad p > p_\infty \quad and \quad \alpha = 0 \\ 0, & else \end{cases} \tag{5.11}$$

When $\beta = 0$, then potential cavity energy is being converted into collpase induced kinetic energy, while when $\beta = 1$ the kinetic energy, focused at the cavity collapse center, is released as shock wave energy.

The conservative transport of the induced kinetic energy, $\phi(\varepsilon)$, can be decomposed into a production and a reduction term, such that

$$\int_V \left[\phi(\varepsilon)^+ + \phi(\varepsilon)^-\right] dV = 0 \tag{5.12}$$

The production and reduction terms are defined as

$$\phi(\varepsilon)^+ = -k\dot{e}_{pot,C}(t,\mathbf{x}_{cell}), \quad where \quad k = \begin{cases} \dfrac{\int_V \phi(\varepsilon)^- dV}{\int_V \dot{e}_{pot,C}(t) dV}, & \text{for} \quad \dot{e}_{pot,C} < 0 \\ 0, & \text{elsewhere} \end{cases} \tag{5.13}$$

and

$$\phi(\varepsilon)^- = -\frac{\varepsilon}{\delta t}\mathfrak{P}_u(\nabla \varepsilon) \tag{5.14}$$

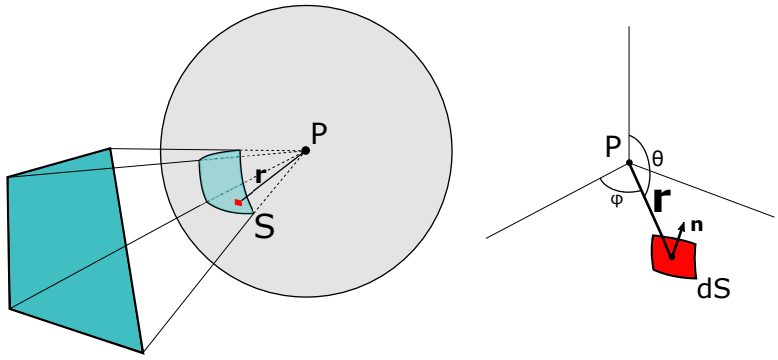

Figure 5.1: Representation of the solid angle for an arbitrary oriented surface subtended to a point P. The solid angle of that surface is equal to the solid angle of its projection S to the unit sphere with center P, and radius r.

, respectively. In Eq. 5.13 and 5.14, $\mathfrak{P}_u(\nabla\varepsilon)$ is the normalized projection of $\nabla\varepsilon$ on the local flow velocity vector $\mathbf{u}$

$$\mathfrak{P}_u(\nabla\varepsilon) = \max\left[\frac{\mathbf{u}}{\|\mathbf{u}\|}\cdot\frac{\nabla\varepsilon}{\|\nabla\varepsilon\|}, 0\right] \tag{5.15}$$

Then, the transport equation of ε given by Eq. 5.10 becomes

$$\frac{\partial\varepsilon}{\partial t} = (1-\beta)\left[\dot{e}_{pot,C}(k-1) - \frac{\varepsilon}{\delta t}(\mathfrak{P}_u(\nabla\varepsilon))\right] - \beta\dot{e}_{rad} \tag{5.16}$$

Forwarding the solution in time gives the collapse induced kinetic energy at each time step Δt

$$\varepsilon|_{t+\delta t} = \varepsilon|_t + \frac{\partial\varepsilon}{\partial t}\Big|_t \delta t = (1-\beta|_t)\left[\dot{e}_{pot,C}\delta t(k-1) - \varepsilon(\mathfrak{P}_u(\nabla\varepsilon)-1)\right]\Big|_t \tag{5.17}$$

and the volume specific radiated power is given by

$$\dot{e}_{rad}|_{t+\delta t} = \frac{1}{\delta t}(\beta\varepsilon)|_t \tag{5.18}$$

A more detailed description and implementation of the model can be found in Schenke [18], and Melissaris *et al.* [11].

5.2.3. SURFACE IMPACT POWER

When a cavitating structure has fully collapsed, it is assumed that all the initial potential energy contained in the structure has been converted into shock wave energy. This energy is emitted from the source (collapse point) isotropically. The energy is radiated instantaneously to any surrounding surface, which means that the propagation speed is infinite. The simplifying assumption of infinite wave propagation speed is justified by the fact the advective velocities are typically orders of magnitude smaller than the sound speed in a nearly incompressible medium such as water. The fraction of energy which passes through any surface is simply the solid angle Ω subtended by this surface at the source point, divided by the total solid angle [22]. In such way, we quantify the distance

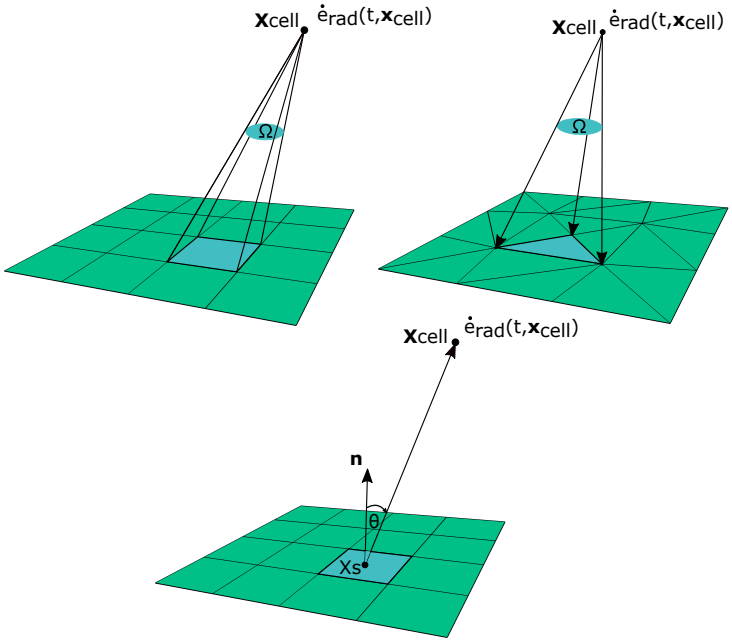

Figure 5.2: Solid angle for a rectangular (top left) and triangular surface (top right), and a surface face center (bottom) subtended to a radiation source at a volume cell center $\mathbf{x}_{cell}$

and angle dependencies. For a closed convex surface, $\Omega = 4\pi$, and thus, the impact power on a surface location $\mathbf{x}_S$ at time instant t is given by

$$\dot{e}_S(t,\mathbf{x}_S) = \frac{\Omega}{4\pi}\dot{e}_{rad}(t,\mathbf{x}_{cell}) \tag{5.19}$$

where $\dot{e}_{rad}(t,\mathbf{x}_{cell})$ is the radiated power at a volume cell center $\mathbf{x}_{Cell}$. By definition, the solid angle for an arbitrary oriented surface subtended at a point P is equal to the solid angle of the projection of the surface to the unit sphere with center P (see Fig. 5.1), and it is given by

$$\Omega = \iint_S \frac{\hat{r}\cdot\mathbf{n}}{\|\mathbf{r}\|^2}dS = \iint_S \frac{\mathbf{r}\cdot\mathbf{n}}{\|\mathbf{r}\|^3}dS = \iint_S sin\theta d\theta d\phi \tag{5.20}$$

where for an infinitesimal area dS, $\mathbf{r}$ is the position vector with respect to P, and $\mathbf{n}$ the unit normal vector. θ and ϕ are the polar and azimuthal angle in spherical coordinates respectively.

Using Eq. 5.20 Gotoh and Yagi [23] were able to derive analytically the solid angle subtended by a rectangle to an arbitrary point. In a similar way, Oosterom and Strackee [24] used an analytic exact expression of the solid angle for a plane triangle, which was used by Leclercq *et al.* [25] to deduce the rate of impact energy applied on the surface (see Fig. 5.2). However, both cases require to discretize the surface into rectangular and triangular elements of finite size respectively. For complicated geometries, where unstructured grids are predominantly used, this is not always straightforward. In this respect, Schenke

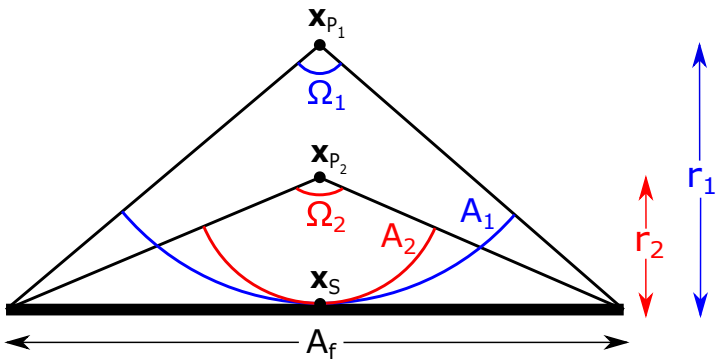

Figure 5.3: Solid Angles of a flat surface subtended to the points $\mathbf{x}_{P_1}$ and $\mathbf{x}_{P_2}$, where r_1 and r_2 are the distances of $\mathbf{x}_{P_1}$ and $\mathbf{x}_{P_2}$ from the face center $\mathbf{x}_S$, respectively, with $r_1 > r_2$

et al. [21] proposed a fully continuous form of the solid angle, that represents the impact at a surface point location. Then, a discrete formulation of the solid angle Ω_d for any surface location $\mathbf{x}_S$ subtended to a volume cell center $\mathbf{x}_{cell}$ is given by

$$\Omega_d = \frac{(\mathbf{x}_{cell} - \mathbf{x}_S) \cdot \mathbf{n}}{\|\mathbf{x}_{cell} - \mathbf{x}_S\|^3} A \approx \frac{(\mathbf{x}_{cell} - \mathbf{x}_S) \cdot \mathbf{n}}{\|\mathbf{x}_{cell} - \mathbf{x}_S\|^3} A_f \tag{5.21}$$

In Eq. 5.21, A is the area of the projection of the surface face to a sphere with center $\mathbf{x}_{cell}$ and radius $\|\mathbf{x}_{cell} - \mathbf{x}_S\|$. Since this projected area is not known, and for arbitrary surfaces is hard to compute, we can substitute the projected area with the face area A_f. This leads to an approximation of the discrete solid angle Ω_d, which can be applied however, to any surface subtended to any arbitrary point.

However, the error involved in the discrete approximation of the solid angle, can be significant for large solid angles, as it strongly depends on the location of the point source and its distance from the surface face, as illustrated in Fig. 5.3. The solid angle Ω_1 of a flat surface with face area A_f subtended to a point $\mathbf{x}_{P_1}$ with position vector pointing in the same direction as the surface normal vector, is equal to

$$\Omega_1 = \frac{(\mathbf{x}_{P_1} - \mathbf{x}_S) \cdot \mathbf{n}}{\|\mathbf{x}_{P_1} - \mathbf{x}_S\|^3} A_1 = \frac{A_1}{r_1^2} \tag{5.22}$$

where A_1 the area of the surface projection to a sphere with radius r_1, and the error made in the discrete approximation of the solid angle is represented by the ratio A_1/A_f. The further from 1 the ratio, the larger the error. When the source is closer to the surface ($r_2 < r_1$), the solid angle increases ($\Omega_2 > \Omega_1$), while the projected area decreases ($A_2 < A_1$). Thus, for larger solid angles, the error increases. When the source is extremely close to the surface the discrete approximation of the solid angle can lead to solid angles orders of magnitude larger than the maximum solid angle ($\Omega_{max} = 2\pi$ for a flat surface subtended to a point). One way to minimize the margin of error is to bound the solid angle to always be smaller or equal to 2π such that

$$\Omega_d = min\left[\left(\frac{(\mathbf{x}_{cell} - \mathbf{x}_S) \cdot \mathbf{n}}{\|\mathbf{x}_{cell} - \mathbf{x}_S\|^3} A_f\right), 2\pi\right] \tag{5.23}$$

Table 5.1: Operating conditions reported responsible for high cavitation erosion risk on the propeller blades

Condition	% of time	Power $[kW]$	Vessel Speed $[kn]$	Propeller revs $[RPM]$	Draught $[m]$
Ballast Min Load	1%	1000 (33%)	7	217.7	4.5
Minimum Towing	48%	1000 (33%)	0	217.7	5.2
Dynamic Positioning	7%	600 (20%)	0	217.7	5.2

If the approximation error still remains significant, the surface face could further be discretized into smaller equal segments, and then the discrete solid angle could be computed for each segment, resulting in an error reduction proportional to the ratio of the initial face area over the new face area. If the surface face is known a priori to be rectangular or triangular, then the exact analytical solution for the solid angle can be used.

Now, considering all the emission sources, the impact power per unit surface at any location $\mathbf{x}_S$ is given by

$$\dot{e}_S(t,\mathbf{x}_S) = \frac{1}{4\pi A_f}\int_V \Omega_d\, \dot{e}_{rad}(t,\mathbf{x}_{cell})dV \tag{5.24}$$

and the accumulated surface specific energy e_S at any location $\mathbf{x}_S$ and after some sample time T is given by

$$e_S(T,\mathbf{x}_S) = \int_0^T \dot{e}_S(t,\mathbf{x}_S)dt \tag{5.25}$$

Finally, integrating over the surface gives the total accumulated surface energy after some sample time T

$$E_S(T) = \int_S e_S(T,\mathbf{x}_S)dS \tag{5.26}$$

5.3. TEST CASE DESCRIPTION

A Tug boat is a type of vessel that maneuvers other vessels by pushing or pulling. As a result, these type of vessels operate at low speeds for long periods of time. The test case considered in this study is a tug boat equipped with two steerable propulsion thrusters. The thrusters operate at constant rotation rate, and the propeller thrust (and therefore various vessel speeds) for different conditions is achieved by adjusting the propeller pitch. The original propeller design of the thrusters, first mounted on the ship, experienced extensive pressure side cavitation at certain conditions, leading to severe cavitation erosion on the blades. The first attempt to improve the propeller design was followed by a reduced amount of pressure side cavitation on the blades at the same critical conditions. Nevertheless, the propeller blades still suffered from cavitation erosion, even though the actual erosion rate was observed to be lower. Finally, a third propeller was designed, which showed the least amount of pressure side cavitation at the critical conditions, and the erosion rate on the blades was minimized. Table 5.1 shows the critical operating conditions, and the three different propeller designs are depicted in Figure 5.4.

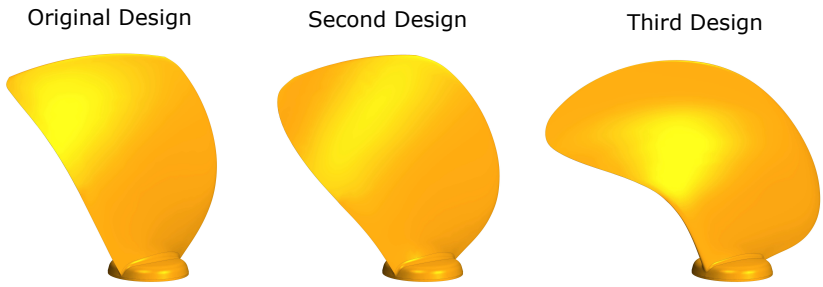

Figure 5.4: Original propeller design (left), and first (middle) and second (right) redesigns

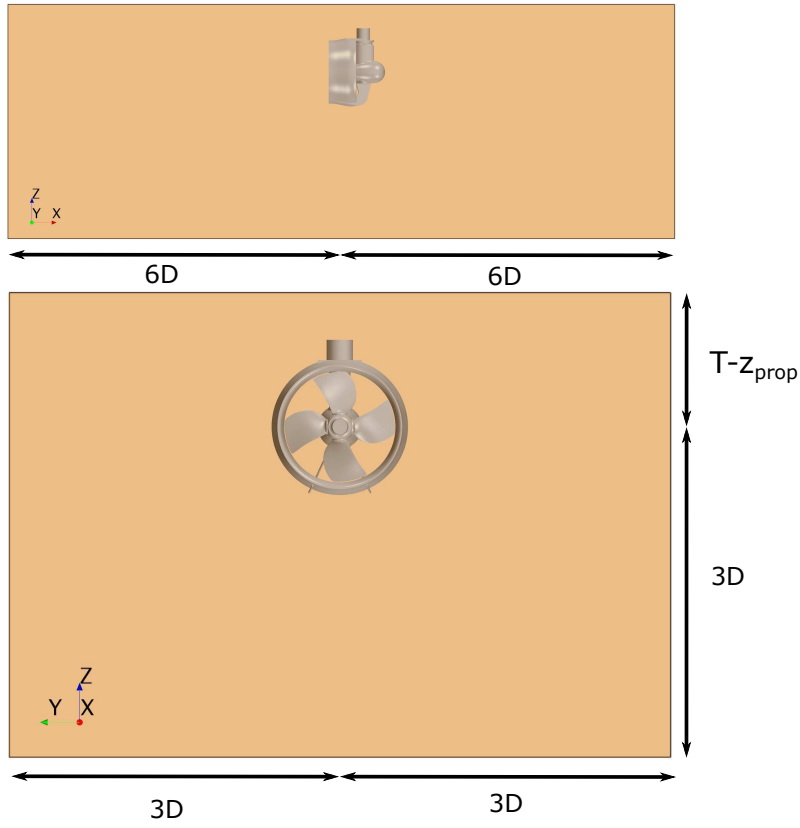

Figure 5.5: Representations of the computational domain D2, and the location of the thruster unit. The propeller is rotating in clockwise direction seen from the aft.

To reduce the computational cost, the flow towards the thruster unit is simulated without including the ship hull, since it is assumed that the unit itself is mainly responsible for the non-uniform inflow to the propeller. Figure 5.5 shows the computational

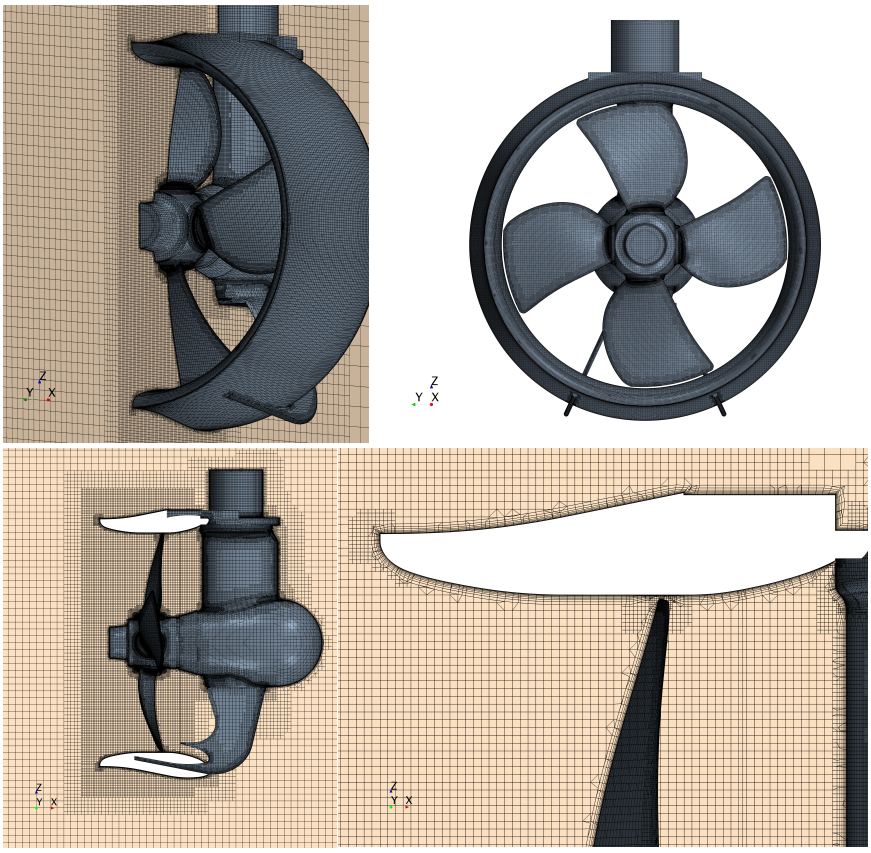

Figure 5.6: The finest (Grid 3) mesh around the Nozzle and Propeller

domain. The top boundary is located at the waterline level, which is at distance $T - z_{prop}$ from the propeller center, where T is the draught of the vessel, and z_{prop} the z coordinate of the propeller center from the baseline. A symmetry plane is applied on the top boundary. The (velocity) inlet and the (pressure) outlet are located 6 diameters from the propeller center, while the side (slip) walls and the bottom boundary (symmetry plane) are 3 diameters away from the propeller center.

5.4. POWER PREDICTION

To simulate the performance of the thruster, the generated mesh consists of trimmed hexahedral cells with local refinements and prism layers along the wall boundaries. Wall functions are used to model the near wall region, applying 8 prism layers, and a first cell distance resulting in wall y^+ values so that $30 < y^+ < 300$. A moving mesh with sliding interfaces is employed to simulate the propeller motion. The moving grid area is determined by a second domain around the propeller geometry (spin domain). A representation of the mesh around the propulsion thruster is depicted in Figure 5.6. The com-

Table 5.2: Delivered power for three different outer domain sizes for Grid 3 for the original blade, pitch deflection -11 deg at the ballast minimum load condition

Outer Domain	Power [kW]	Deviation from D1
D1	940.4	1.40%
D2	931.6	0.49%
D3	927.1	-

putational results can sometimes be highly dependent on the size of this spin domain, especially for nozzle propellers, due to the restrictions on the size imposed by the geometry itself. Thus, a sensitivity study needs to be conducted, apart from the time step and grid size investigation.

5.4.1. SENSITIVITY STUDY

A verification study is conducted to investigate the sensitivities related to the outer domain size, the spin domain size, the time step size, and the grid density. Three domain sizes have been used to assess the influence of the boundaries to the solution. Apart from the medium domain size, D2, shown in Fig. 5.5, two more have been tested, one with dimensions two time smaller, D1, and one with dimensions 5 time larger, D3. Of course, the distance from the free surface remains the same for all three domains. Table 5.2 presents the difference in power predictions for the three domain sizes. Delivered power is 1.4% higher for the smallest domain compared to the largest one, while for the medium domain size the difference is less than 0.5%. In order to reduce the number of cells and therefore CPU time, the medium domain size has been selected for all the calculations.

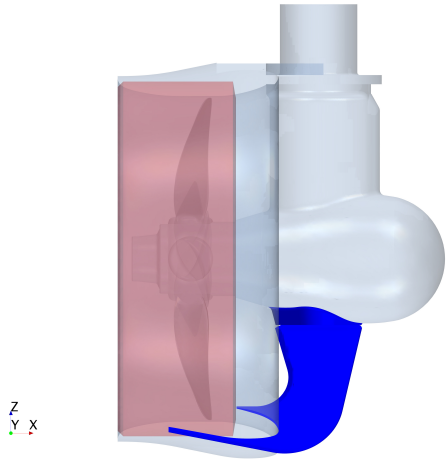

Figure 5.7: Geometrical restriction on the size of the spin domain, where it extends until the connection between the thruster pod and the inner part of the nozzle

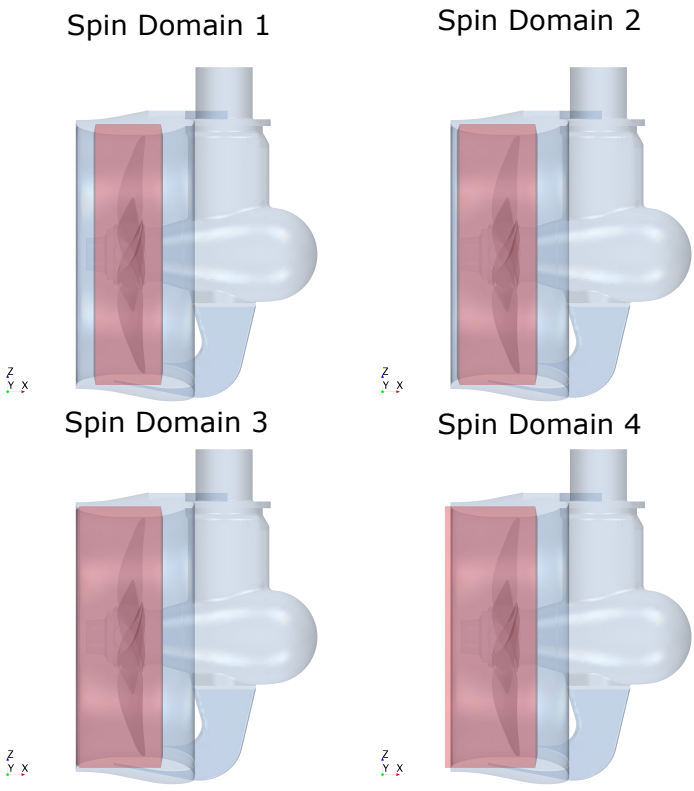

Figure 5.8: Spin Domain Size

The size of the spin domain is determined by the location of the interface at the inflow and the outflow of the moving mesh. The interfaces should be located at areas with low velocity and pressure gradients. However, very often geometrical restrictions impose certain limits to the size of the spin domain and the location of the interfaces. In this particular case, the location of the inflow interface is limited by the connections between the pod and the nozzle. Thus, the inflow interface is positioned as far from the propeller blades as possible, but cannot extend further than the connections at the inner part of the nozzle (see Fig. 5.7). On the other hand, the location of the outflow interface is not limited by any geometrical part, and thus the optimum size has been investigated.

Four different spin domain sizes are tested, as shown in Figure 5.8. The first spin domain is the smallest and it includes the blade, the hub and part of the hubcap. The second spin domain includes the whole hubcap, the third spin domain is extended until the trailing edge of the nozzle, and the fourth spin domain is extended even further away than the nozzle trailing edge. Table 5.3 shows the thruster power output for each spin domain size. When the spin domain is extended until the nozzle trailing edge or further, then the delivered power P_d is independent of the domain size.

The delivered power P_d is calculated for the finest grid (Grid 3) and four different time step sizes 1,2,4 and 8 deg per time step (see Table 5.4). The results seem to be time step

Table 5.3: Delivered power for different spin domain sizes for Grid 3 for the original blade, pitch deflection -11 deg at the ballast minimum load condition

Spin Domain	Power [kW]	Deviation from SD4
SD1	940.4	0.94%
SD2	933.7	0.21%
SD3	931.6	0.01%
SD4	931.7	-

Table 5.4: Delivered power for different time step sizes for Grid 3 for the original blade, pitch deflection -11 deg at the ballast minimum load condition

Rotation rate	Power [kW]	Deviation from 1 deg/Δt
8 deg/Δt	931.3	-0.03%
4 deg/Δt	930.1	-0.17%
2 deg/Δt	929.6	-0.22%
1 deg/Δt	931.6	-

independent even for the highest time step size (8 deg per time step). Furthermore, table 5.5 shows the delivered power P_d, as calculated for three different grid densities, and for a time step size of 1 deg per time step. Since wall functions are used to model the near wall region, the same prism layer mesh has been used for all grids, to keep the same $y+$ values for a more fair comparison. It has been shown that even the coarsest grid is sufficiently fine, as far as the delivered power P_d is concerned. The deviation of the delivered power is of the same order as the deviation due to different time step size. Finally, it should be noted that for the presented ranges of time step size, grid resolution and spin domain size, the spin domain size has the largest influence on the delivered power.

5.4.2. PITCH DEFLECTION

Since each propeller is operating at constant rotation rate, the right pitch deflection needs to be calculated in order to match the propeller thrust and delivered power for each condition. The delivered power is determined by computing the propeller torque for three pitch deflections, and then interpolating to the pitch deflection value resulting in 1 MW power absorption. This procedure is applied for all three blade designs. The eventual pitch deflection for each operating condition and each design is depicted in Table 5.6.

5.5. PROPELLER CAVITATION EROSION RISK ASSESSMENT

The erosion model described in Section 5.2 is employed to compute the impact distribution on the propeller blades. To better resolve the cavity dynamics, a finer grid is needed, than the one used for the delivered power prediction. Therefore, an additional refinement is applied on the volume cells where the vapor volume fraction is non-zero over one full

Table 5.5: Delivered power for different grid densities, for the original blade, pitch deflection -11 deg, and time step size 1 deg/Δt, at the ballast minimum load condition

	# Cells (10^6)	h_i/h_3	Power [kW]	Deviation from Grid 3
Grid 1	5.26 M	1.5625	926.1	-0.59%
Grid 2	6.53 M	1.25	932.1	0.05%
Grid 3	9.06 M	1	931.6	-

Table 5.6: Propeller pitch deflection for each blade design and each operating condition

Condition	Power (kW)	Pitch Deflection (deg)		
		1st Design	2nd Design	3rd Design
BML	1000	-10.41	-5.90	-
MT	1000	-12.35	-8.09	-
DP	600	-17.68	-12.71	-13.61

revolution. Only the volume around one blade is refined to reduce the computational cost.

First, a coarser mesh is applied to estimate the maximum vapor fraction in each cell over one propeller revolution. Based on that, a refinement is applied on one of the blades, at each location where the maximum vapor fraction is non-zero. The grid and time step size follows the best practice guidelines as proposed in previous work (see [11]), thus approximately 20 cells along the smallest dimension of the vapor cavity, at its maximum size, and 40 time steps during the collapse, based on the Rayleigh-Plesset collapse time. For a cavity with diameter $D \approx 45$ mm (see Fig. 5.9), this translates to a minimum cell size of $c \approx 2.25$ mm, and a time step size of $\Delta t = 6.13 \times 10^{-4}$ s or a rotation rate of 0.085 deg per time step. Table 5.7 shows the eventual number of cells per cavity width, when the cavity is at its maximum size, for each grid, excluding the number of the prism layers close to the wall. A wall resolved approach is used to better control the grid similarity for different grid densities. The wall y^+ values on the blade are well below 0.1 even for the coarsest grid (see Fig. 5.10). The developed vapor volume on the original blade is depicted in Fig. 5.11, for the ballast minimum load condition, indicating the cavity size and dynamics. The shed cavity shown at 330 deg blade position has already collapsed at top blade position, while the width of the main sheet cavity has been significantly reduced. Furthermore, a representation of the mesh, after applying the refinement, is shown in Fig. 5.12.

A convergence criterion, r, is employed to ensure the iterative convergence during each time step. The criterion is satisfied when the deviation between the maximum and the minimum value of the total vapor volume fraction, α_v, over the last n iterations, di-

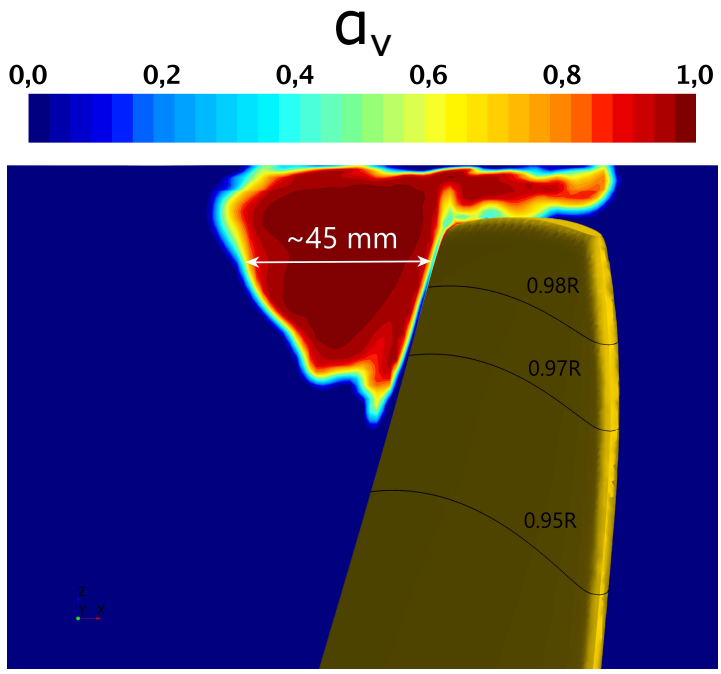

Figure 5.9: Maximum vapor volume fraction over one full propeller revolution. The cross section is showing the approximate maximum size of the shed cavity.

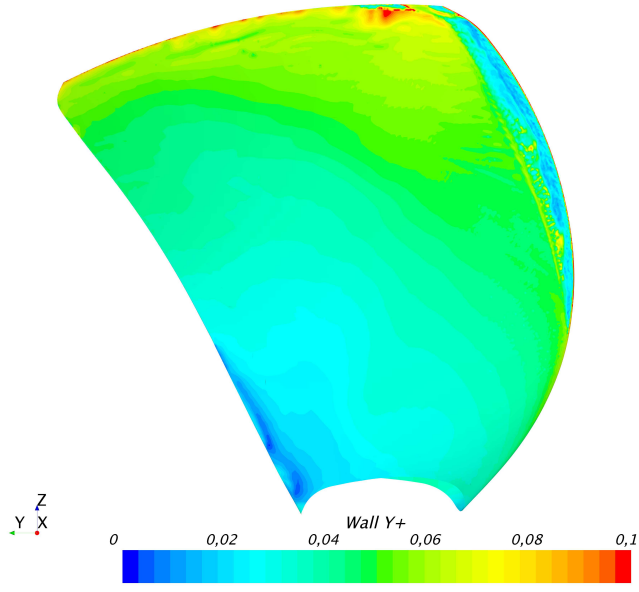

Figure 5.10: Wall y+ distribution on the blade for Grid 2

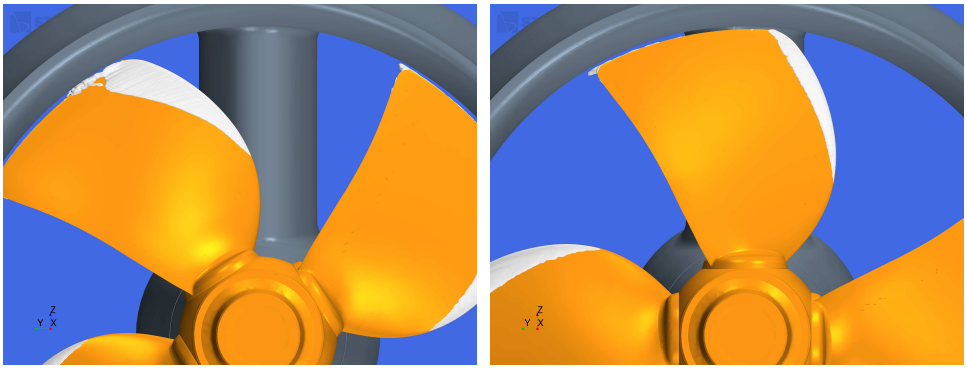

Figure 5.11: Total vapor volume on the original blade at 330 deg (left) and top (right) position, in ballast minimum load condition

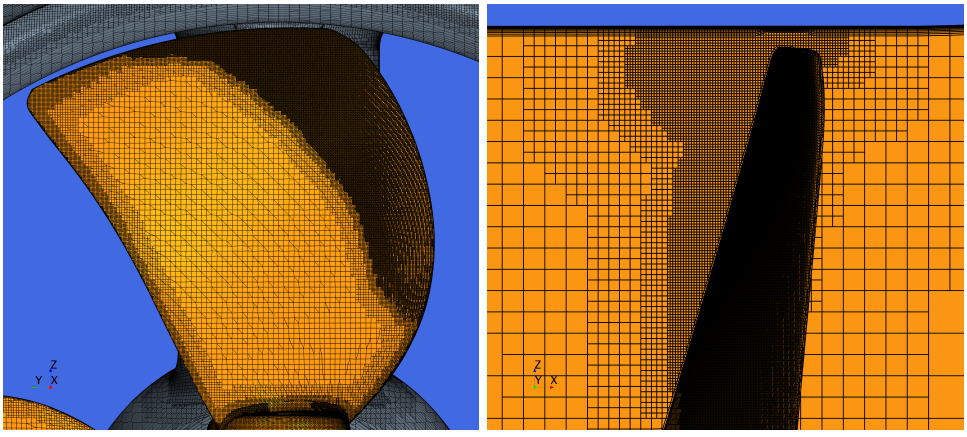

Figure 5.12: Mesh representation of the refined blade for the original blade, showing the additional refinement to capture the cavity dynamics

Table 5.7: Mesh information for three different grids, showing the total number of volume cells, surface cells on the refined blade, prism layers, and cells per cavity width along the maximum cavity size

Grid	# cells total	# cells on refined blade	# prism layers	# cells per width at maximum cavity size
Grid 1	7.37 M	102.9 k	13	19
Grid 2	11.03 M	142.8 k	16	24
Grid 3	18.70 M	232.0 k	20	30

vided by the average of α_v over the last n iterations is lower than 10^{-6}:

$$r = \frac{|\, max\{\alpha_v\}_{j=i-n+1}^{i} - min\{\alpha_v\}_{j=i-n+1}^{i} \,|}{\frac{1}{n}\sum_{j=i-n+1}^{i} \alpha_{v_j}} < 10^{-6} \tag{5.27}$$

where $i >= 5$ the iteration number during the time step. In all simulations, a value $n = 5$ is set, which always results in a reduction of the residual of the vapor volume transport equation at least below 10^{-6}.

5.5.1. ORIGINAL DESIGN

SENSITIVITY STUDY

A sensitivity study is conducted for the original blade at the ballast condition, so that a time step and grid size independent solution is obtained for the cavity impact distribution on the blade (blade impact distribution). First, the blade impact distribution is computed for Grid 2 and rotation rates, 0.1, 0.08 and 0.06 deg per time step. Fig. 5.13, depicts the total accumulated surface energy on the blade per rotation, without energy focusing, for 5 propeller revolutions, and three different time step sizes. A very small decrease in the surface impact energy is observed for smaller time step sizes, as a result of the shift in collapse locations. Large time step sizes could lead to delayed collapse times, which affect the locations where energy will be radiated. For a cavity to collapse at a different location means different driving pressure. When there is a delay in collapse, the collapsing cavity is more likely to be advected towards stronger pressure gradients, resulting in a more violent collapse, and higher amount of radiated energy. Therefore, we should always expect higher magnitude of radiated energy for large time step size.

Different collapse locations also affect the projection of the radiated energy, since the distance and orientation from the surface changes. If the energy is radiated above an infinite and flat surface, the overall amount of surface energy should be independent of the collapse location. However, the propeller blade has a finite and curved surface, and therefore the total amount of surface impact energy should depend on the collapse location. For the non-focusing approach this effect is not that pronounced, since the energy is continuously being radiated during negative volume change, and the shift in locations where energy is radiated is not that big.

On the other hand, the sensitivity is higher when energy focusing is applied (see Fig. 5.14), and the amount of energy projected onto the blade surface is more sensitive to

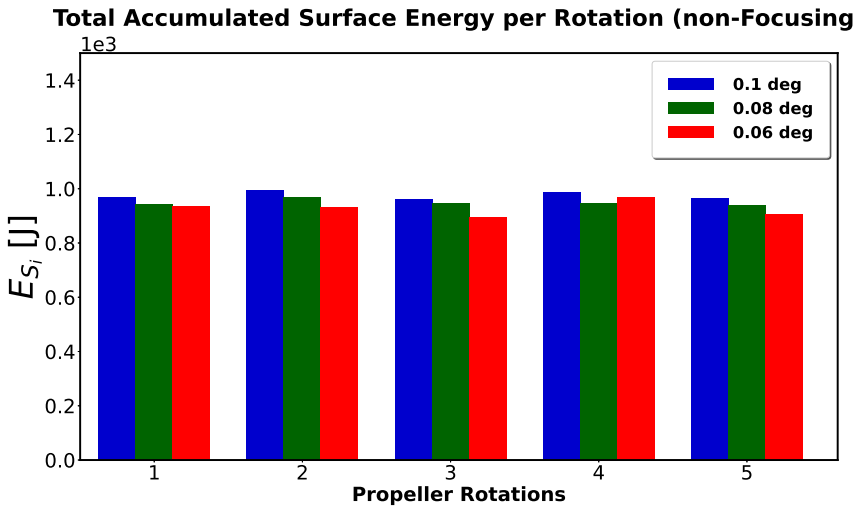

Figure 5.13: Total accumulated surface energy per propeller rotation on Grid 2, for five consecutive revolutions, for three different time step sizes, using the non-focusing model

5

the location of the final collapse. In the focusing approach, the entire collapse energy is radiated from a very confined volume, the collapse center. Consequently, the shift in the location of radiation sources can be very large, and therefore a much larger impact on the surface energy distribution should be anticipated.

Furthermore, since the time step sizes have been selected so that we can resolve the larger structures that are shed from the sheet cavity, the sensitivity on the surface accumulated energy should be larger at locations of smaller collapsing cavities, which are not fully resolved. For instance, even the smallest time step size might not be sufficient to resolve the small cavities that are shed at the trailing edge of the sheet cavity, leading to a larger overall sensitivity of the total accumulated energy on the blade. Achieving an absolute time step size independent solution with energy focusing might require extremely smaller time step sizes, and consequently a compromise needs to be made between accuracy and computational effort. Since our main goal here is to mainly resolve the larger scales and the collapse of the bigger cavities during each propeller revolution, a time step size lower than 0.1 deg per time step is considered sufficient.

Finally, we also observe some deviation between the total surface impact energy for each time step and different propeller revolutions. Nevertheless, those differences are mainly related to system instabilities of cloud cavitation, and in particular the instability of the stagnation point at the closure of the sheet cavity [11, 26].

Now, looking at the impact distribution on the blade surface, for the non-focusing approach, and different grid densities, a grid independent solution is achieved for the different meshes, as shown in Fig. 5.15. The time step size is modified for each mesh based on the refinement ratio h_i/h_3 (see Table 5.5). On the other hand, when the kinetic energy focusing is applied, the accumulated energy on the blade is more sensitive to the grid resolution. Insufficient spatial resolution can lead to early collapse of cavitating struc-

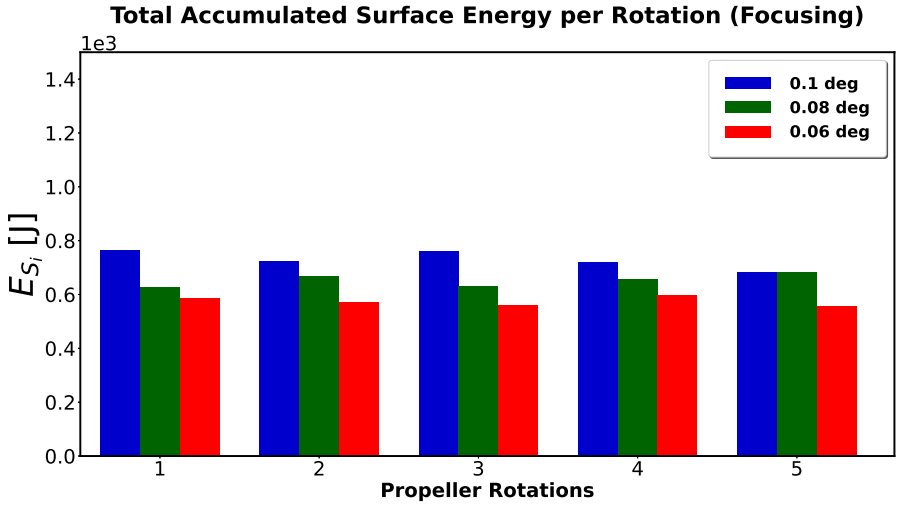

Figure 5.14: Total accumulated surface energy per propeller rotation on Grid 2, for five consecutive revolutions, for three different time step sizes, using the focusing model

tures, leading to the opposite effect than insufficient time step size. The final stage of the collapse takes place at locations, which either are further away from the surface, or experience weaker pressure gradients and consequently smaller amounts of energy are radiated. For the original propeller design, and the ballast condition a higher accumulated surface energy is predicted for finer grids (Grid 2 and 3) as shown in Fig. 5.16.

The impact distributions on the refined blade, after five propeller revolutions, for each grid, are illustrated and compared in Fig. 5.17. The high energy density areas are mainly located close to the tip, and towards the mid-chord region. Although the same impact locations are predicted for all grids, the magnitude of the accumulated surface specific energy is slightly under-predicted with the coarser mesh, both with and without energy focusing. In addition, small differences are observed on the energy distribution close to the tip, between Grid 2 and 3, however, these differences are probably related to the higher grid resolution, since the total accumulated energy is similar. As the grid resolution increases, more details are captured in the flow, and a higher amount of secondary flow is resolved. That results in accurately resolving the collapse of smaller and smaller structures, and therefore some small deviations in the impact distributions are expected.

Finally, comparing the distributions with and without energy focusing, we notice that the radiated energy is accumulated in larger areas on the blade, if we do not apply the energy focusing model. Since energy is radiated instantaneously, as the cavity volume is decreasing, the energy is continuously being distributed, leaving a footprint along the sheet cavity trailing edge. On the other hand, the energy is more scattered and localized with the energy focusing model. The energy is focused into smaller volumes, towards the collapse center, and thus, at the final stage of the collapse, the radiated energy is accumulated in smaller areas on the blade, especially when the collapse center is close to the surface. For implosions at larger distances, the energy impact distribution can be very

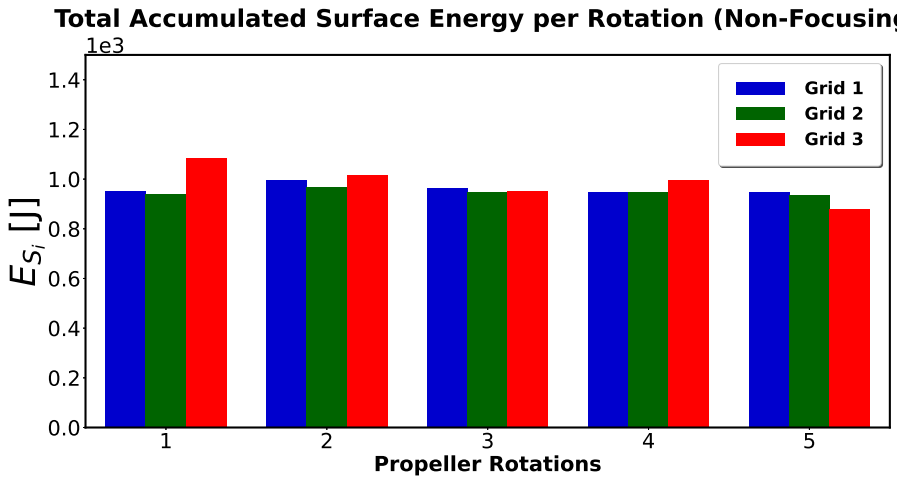

Figure 5.15: Total accumulated surface energy per propeller rotation, for five consecutive revolutions, for three different grid densities, using the non-focusing model

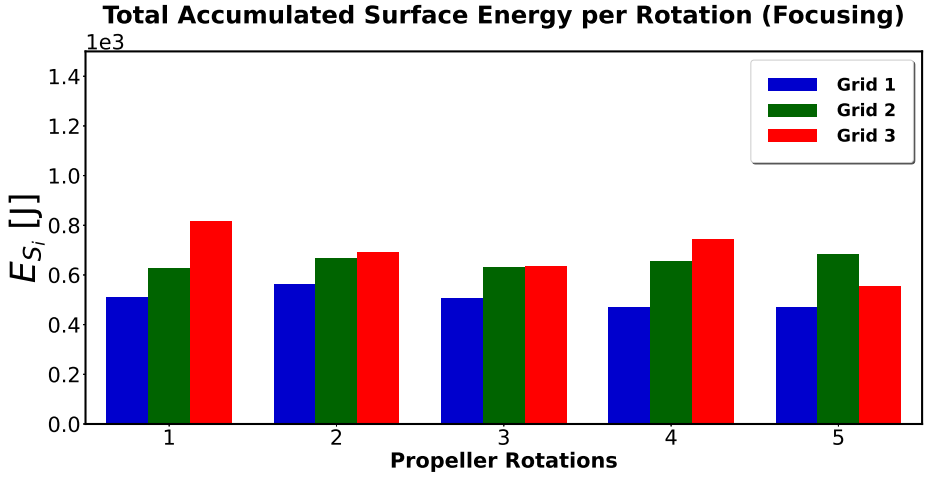

Figure 5.16: Total accumulated surface energy per propeller rotation, for five consecutive revolutions, for three different grid densities, using the focusing model

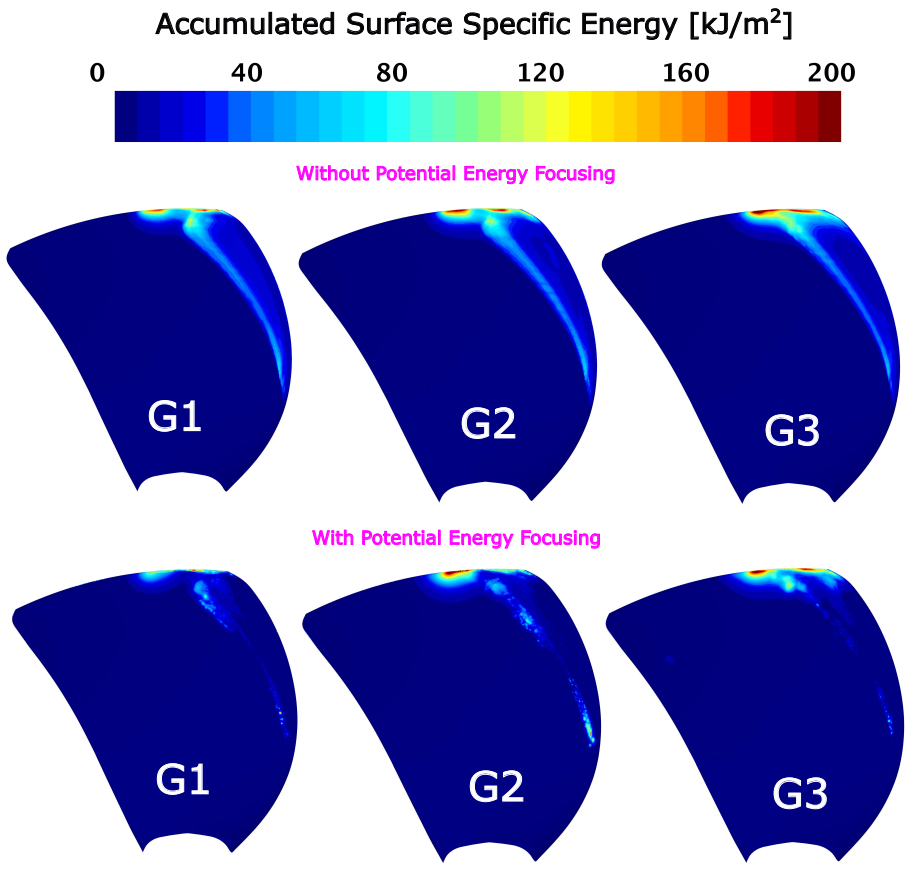

Figure 5.17: Surface specific accumulated energy on the refined propeller blade, obtained from the non-focusing and the focusing model after five propeller revolutions, for Grid 1 (left), Grid 2 (middle), and Grid 3 (right)

similar with both methods.

OTHER OPERATING CONDITIONS

A representation of the developed vapor volume on the original blade, when it is at the top position, is depicted in Fig. 5.18 for the minimum towing, and dynamic positioning condition. The total accumulated surface energy per propeller rotation for all three operating conditions for Grid 2 and a time step size of 0.08 deg per time step is shown in Fig. 5.19 and 5.20, without and with energy focusing respectively. In minimum towing condition, the cavity dynamics are very similar to the ballast minimum load condition, showing a slight increase in the vapor volume and consequently in the accumulated surface energy. On the other hand, in dynamic positioning, the unit clearly experiences a much higher amount of cavitation, resulting in a much larger amount of accumulated energy on the surface (about 2-2.5 times larger). It is important to note that, since the amount of vapor in both the minimum towing condition and dynamic positioning is larger than the ballast min load condition, a grid resolution as fine as in Grid 2 and a rotation rate of 0.8 deg per

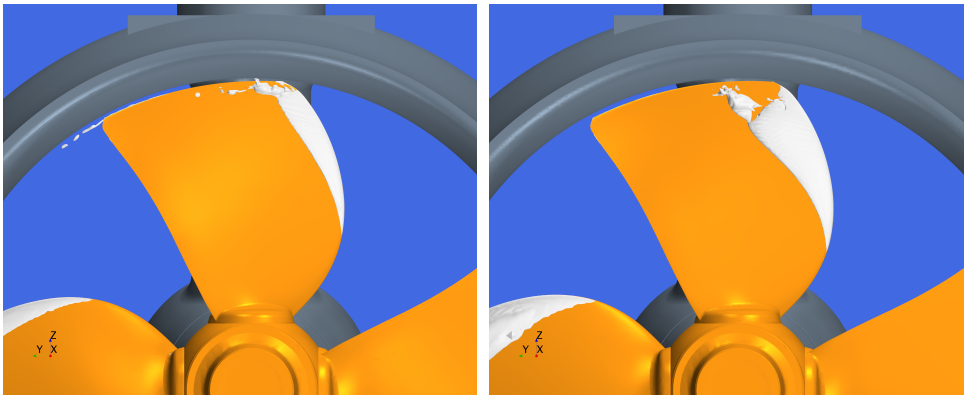

Figure 5.18: Total vapor volume when the blade is at the top position, for minimum towing (left), and dynamic positioning condition (right)

time step (as derived by the sensitivity study in Section 5.5.1) are sufficient to resolve the cavities of at least the same size as in the ballast minimum load condition.

Comparing the total accumulated surface energy between the non-focusing and focusing model, it is again observed that a larger amount of surface energy is predicted when there is no energy focusing. That is because of the instantaneous release of energy in case of a negative volume change. Thus, cavities that are subjected to negative volume change, but either never collapse or collapse far away from the surface, will leave a substantial energy footprint on the surface, while that will not occur when energy focusing is applied. That becomes even more obvious when looking at the distribution of the surface specific energy on the original blade after 5 propeller revolutions, without (Fig. 5.21) and with energy focusing (Fig. 5.22). The non-focusing model is predicting larger amount of surface energy both at the trailing edge of the developed sheet cavity, and at the location of the main impact originated from the cloudy structures shed from the sheet cavity.

Furthermore, the energy distributions for the ballast and the towing condition are very similar, as it was already indicated by the total accumulated surface energy. However, in the ballast condition, most of the surface energy is accumulated closer to the tip and more towards the mid-chord, which is probably related to the difference in inflow speed, resulting in slightly different angles of attack of the incoming flow. In dynamic positioning the accumulated energy on the blade is clearly much larger, and it is distributed over a larger blade area.

Looking at the energy distribution for each condition, it is easy to distinguish the amount of the accumulated energy, however, it is not trivial to identify whether higher energy content means also higher risk for erosion. To get a better impression of the flow aggressiveness and the extent of the impacted area, a more quantative analysis of the damage in the impacted areas is needed. Figures 5.23 and 5.24 give the surface specific energy over the percentage of the impacted blade area. Such a plot shows the amount of energy distributed over a certain amount of area on the blade. These representations give a better insight into the erosion risk of the impacted areas on the blade. Areas with high surface specific energy have an increased probability to experience erosion and ma-

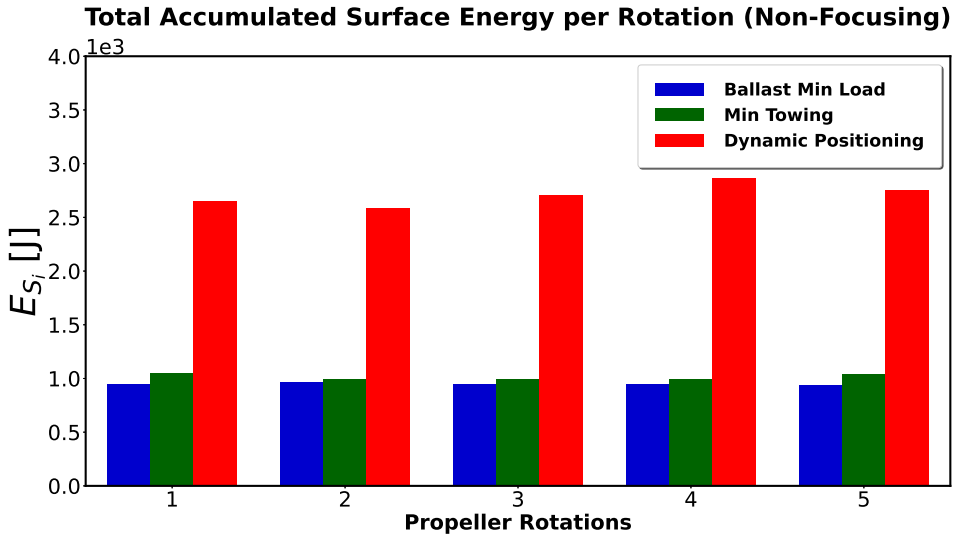

Figure 5.19: Total accumulated surface energy per propeller rotation, for five consecutive revolutions, for ballast minimum load (blue), minimum towing (green), and dynamic positioning condition (red), using the non-focusing model

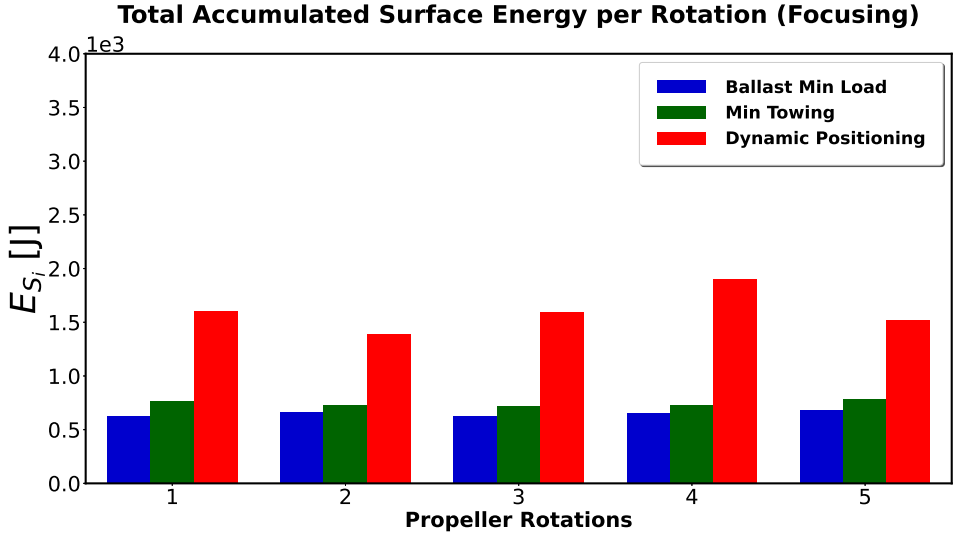

Figure 5.20: Total accumulated surface energy per propeller rotation, for five consecutive revolutions, for ballast minimum load (blue), minimum towing (green), and dynamic positioning condition (red), using the focusing model

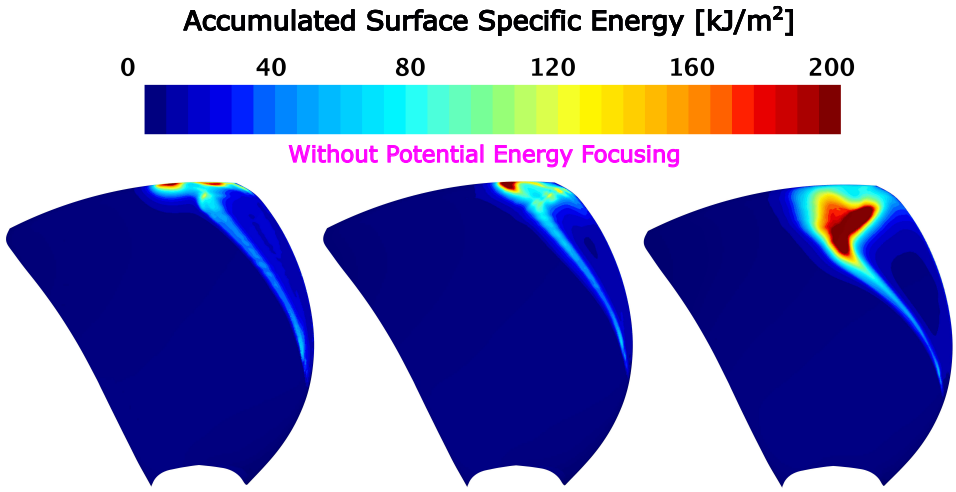

Figure 5.21: Surface specific accumulated energy on the refined propeller blade, obtained from the non-focusing model after five propeller revolutions, for ballast minimum load (left), minimum towing (middle), and dynamic positioning condition (right)

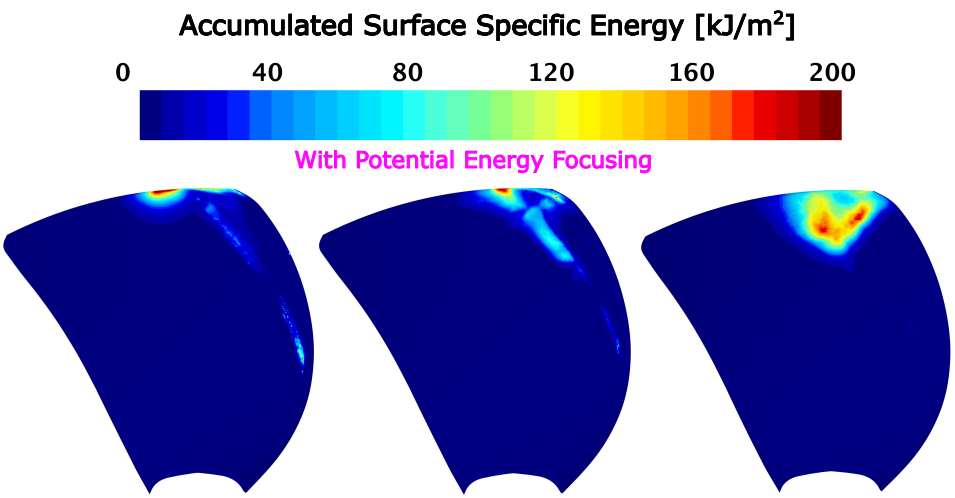

Figure 5.22: Surface specific accumulated energy on the refined propeller blade, obtained from the focusing model after five propeller revolutions, for ballast minimum load (left), minimum towing (middle), and dynamic positioning condition (right)

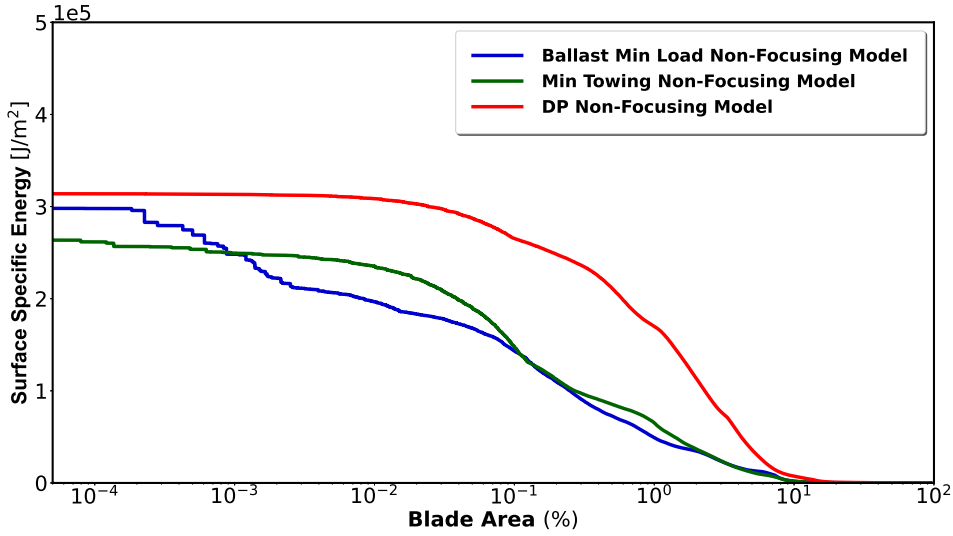

Figure 5.23: Surface specific energy over the blade area, showing the extent and the percentage of the impacted blade area, after five propeller revolutions, for the non-focusing model

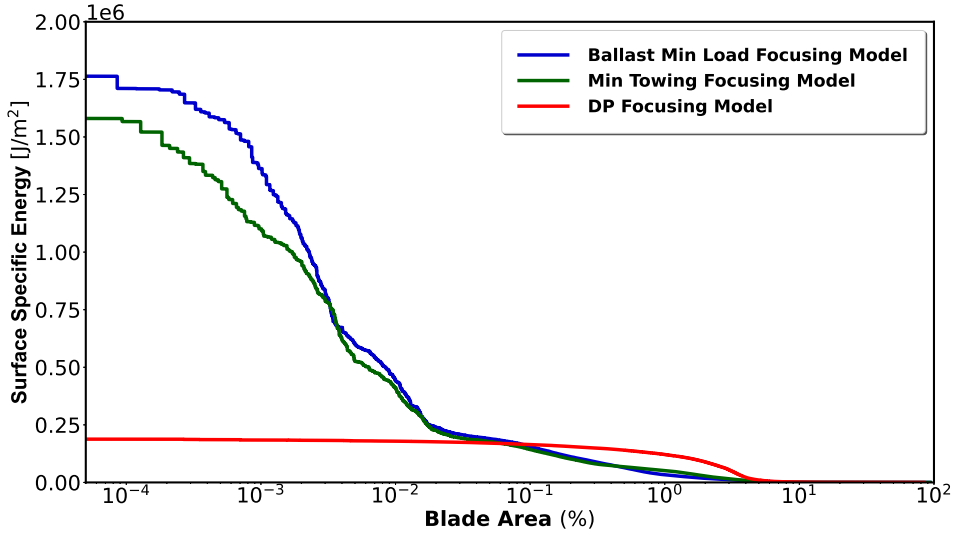

Figure 5.24: Surface specific energy over the blade area, showing the extent and the percentage of the impacted blade area, when the energy focusing approach is employed

terial loss. Based on such analysis, a more quantitative comparison is possible between the different conditions, as well as the different propeller designs.

Comparing Fig. 5.23 and Fig. 5.24 it is noteworthy that the energy is evenly distributed for all three conditions if the non-focusing model is used, while more extreme events can be identified with the energy focusing approach. That is only the case for the ballast and towing condition, since in DP the energy remains evenly distributed over a larger area even with the focusing model (see Fig. 5.24). This possibly indicates that the collapse of the main cloudy structures shed from the developed sheet cavity, during each cycle, collapse further away from the surface resulting in a surface impact of larger area and lower magnitude. That leads to an energy impact distribution similar to the one obtained from the non-focusing model.

Looking at the magnitude of the surface specific energy, obtained from the focusing model, the cavity dynamics during the ballast condition seem to be the most aggressive ones, indicating slightly higher erosion risk than the towing condition. On the contrary, in dynamic positioning, even though the total accumulated energy is much larger than in the other two conditions, the energy is evenly distributed over a much larger area, indicating a much lower erosion risk. Nevertheless, when we compare the energy distribution obtained by CFD, with the actual erosion on the original blade (see Fig. 5.25), we can clearly see that the actual erosion on the real blade is a result of the combined impacts originated form all three operating conditions.

Based on the CFD analysis, in the ballast and minimum towing condition, the highest erosion risk area is close to the tip. Indeed, looking at the actual erosion on the real blade, severe erosion is identified close to the tip, matching well with the CFD locations. On the other hand, the eroded area on the real blade extends to lower radii, while very little energy was found from the computations at lower radii for these two conditions. Therefore, it is concluded that erosion is also likely to occur when the vessel is operating in DP. Even though a low magnitude of surface specific energy is predicted for this condition, and the energy is evenly distributed over a large area of the blade, this amount of energy still seems to be sufficient to cause erosion.

One of the long lasting debates about cavitation erosion is whether common erosion on the blades occurs due to extreme events of low frequency or due to repetitive events of lower magnitude, but of higher frequency. The implosion loads reproduced during the ballast and towing condition can be characterized as extreme events due to their high energy content, which is distributed over smaller areas. The location of the implosion might differ from cycle to cycle, and therefore the frequency of the impact on each fixed location of the blade is lower than the BPF. On the other hand, the impact exerted by the implosion loads during dynamic positioning, can be considered as repetitive events of lower amplitude. In this case the frequency of the impact at a fixed location can be much higher since the energy is evenly distributed over a larger area. From the actual erosion on the real blade, it seems that both cases are qualified to cause erosion and material loss. So, in the case where the frequency of an implosion at a fixed location is high enough, it seems that it can cause erosion even though the exerted stress at that location does not exceed the material yield stress (similar to fatigue). This can further be explained by the work hardening of the material, which is causing a surface deterioration and even embrittlement and therefore makes the material more vulnerable to erosion damage [1].

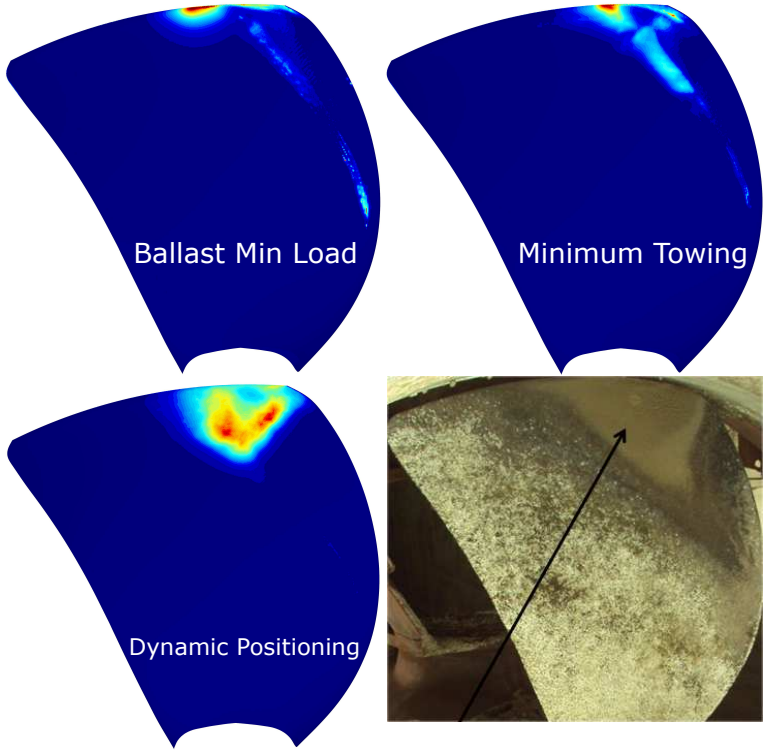

Figure 5.25: Comparison of the erosion risk predicted by CFD with the focusing model for the three operating conditions and the real erosion on the original blade

Finally, there is still the possibility that the implosion loads exerted on the surface during dynamic positioning condition are still exceeding the material yield strength, causing plastic deformation. In such a case, the implosion loads during the other two conditions, should be even higher, resulting in more severe erosion close to the tip. Looking at the actual blade, the erosion at the tip seems slightly more severe than in lower radii, however it is not as obvious, and makes it difficult to explain such big differences in the magnitude of the implosion loads.

5.5.2. FIRST RE-DESIGN

Since extensive erosion occured on the original blade, a new propeller design was made to mitigate pressure side cavitation erosion, without compromising in performance and thruster efficiency. Indeed, in ballast minimum load and minimum towing condition, propeller cavitation on pressure side was significantly reduced, showing no potential of cavitation erosion. However, a serious amount of cavitation was predicted in dynamic positioning (see Fig. 5.26), and therefore the erosion model was applied to estimate the erosion risk on the first re-design.

In a similar way as for the original design, a new volume refinement is applied around

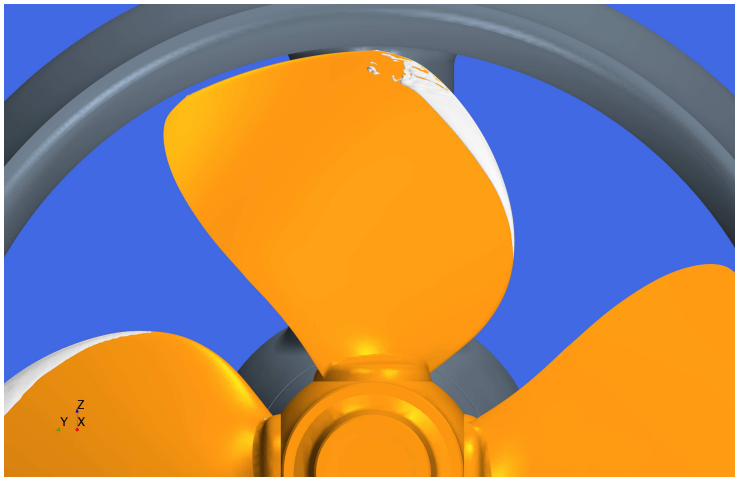

Figure 5.26: Representation of the total vapor volume on the refined blade of the first redesign, in dynamic positioning

one of the blades, on the cells where the vapor volume is non-zero over one full revolution. For a cavity with a maximum width $D \approx 20$ mm (see Fig. 5.27), a minimum cell size of $c \approx 1$ mm, and a time step size of $\Delta t = 2.32 \times 10^{-}5$ are suggested by previous studies [11]. This is translated to about 20 cells over the maximum cavity width. Based on the results of the original design, a slightly finer grid is required (24 cells per cavity width were used in Grid 2). Therefore, a minimum cell size of $c \approx 0.8$ mm, and a time step size of $\Delta t = 1.86 \times 10^{-}5$ are eventually used, resulting in 25 cells per cavity width (excluding the prism layer cells). Figure 5.28 depicts the mesh representation on the refined blade.

The total accumulated surface energy on the refined blade, when the vessel is operating in dynamic positioning, is compared between the original design and the first redesign, without (Fig. 5.29) and with (Fig 5.30) energy focusing, for a simulation time of 5 propeller revolutions. First, the total accumulated surface energy for the original design shows higher deviation during each revolution. These differences come mainly from the intrinsic instabilities of the partial cavity [26]. The larger amount of vapor and the stronger dynamics in DP are strengthening the instabilities, causing larger deviations between each propeller revolution.

Furthermore, The accumulated energy on the original blade is much larger than the accumulated energy on the re-design, especially when energy focusing is used. This is caused by the much larger vapor volume we observe at the same condition as for the original blade. We notice the same, when looking at the surface impact distribution (see Fig. 5.31). A much larger area is impacted on the original blade, while the accumulated energy and the impacted area are much smaller on the first re-design. However, as already mentioned, this does not necessarily mean that the risk for erosion on the original blade is higher than on the re-design.

To get a better insight into the high erosion risk areas, we should have a look at the surface specific energy. Fig 5.32 presents the magnitude of the surface specific energy over

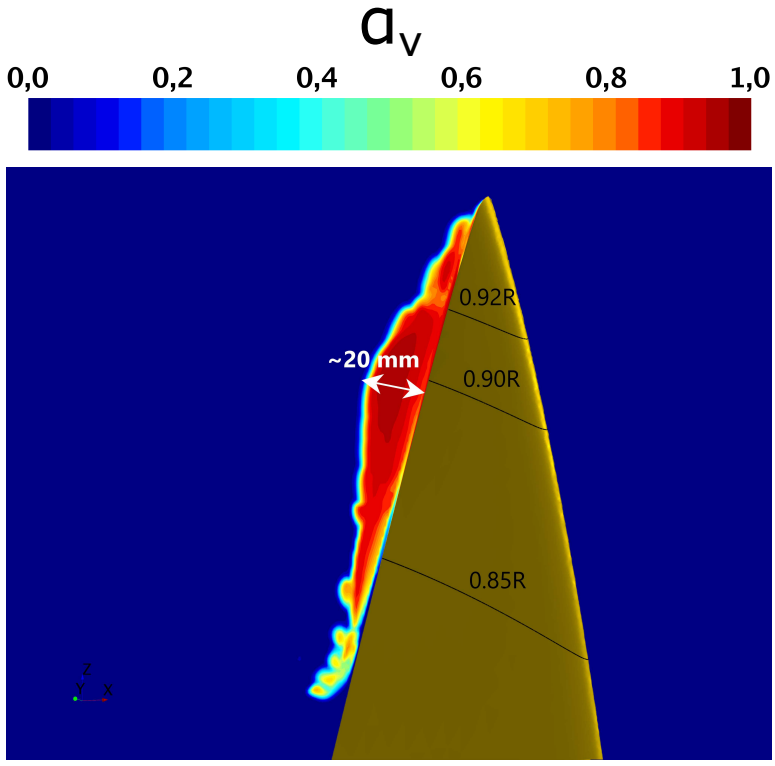

Figure 5.27: Maximum vapor volume fraction over one full propeller revolution. The cross-section is showing the approximate maximum size of the shed cavity.

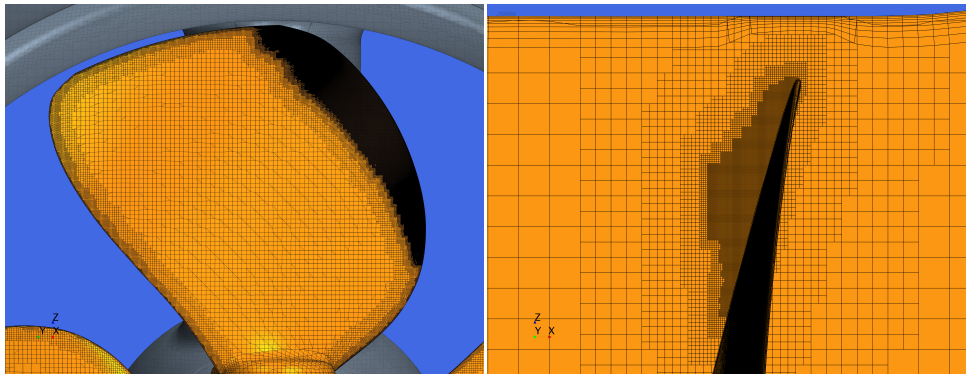

Figure 5.28: Mesh representation on the refined blade for the first redesign, showing the additional refinement to capture the cavity dynamics

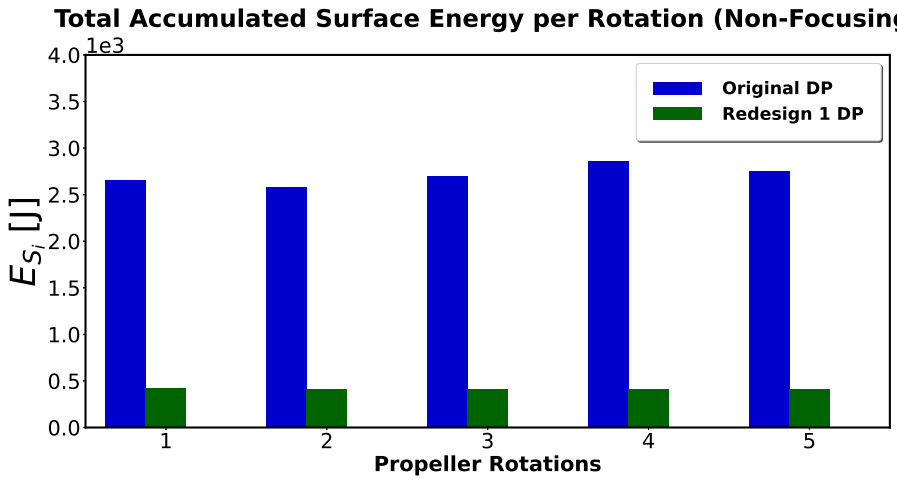

Figure 5.29: Total accumulated surface energy per propeller rotation for five consecutive revolutions, for the original blade and the first re-design, in dynamic positioning, using the non-focusing model

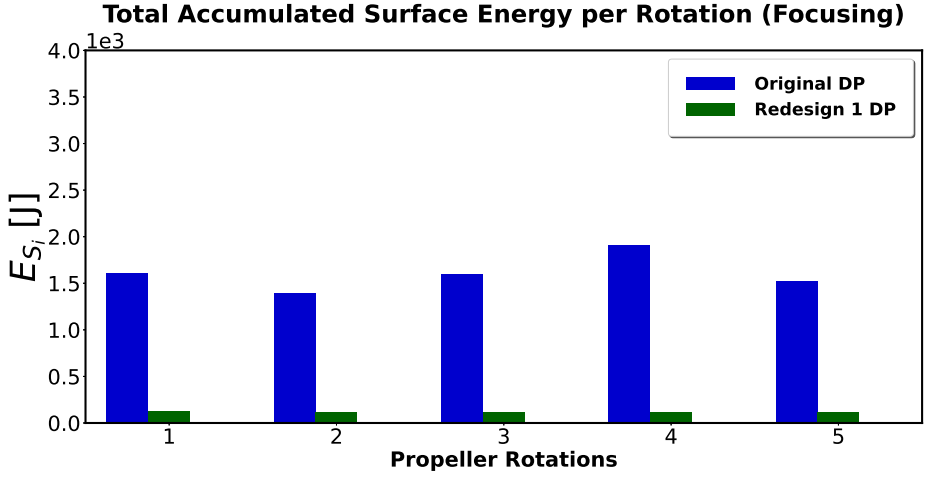

Figure 5.30: Total accumulated surface energy per propeller rotation for five consecutive revolutions, for the original blade and the first re-design, in dynamic positioning, using the energy focusing model

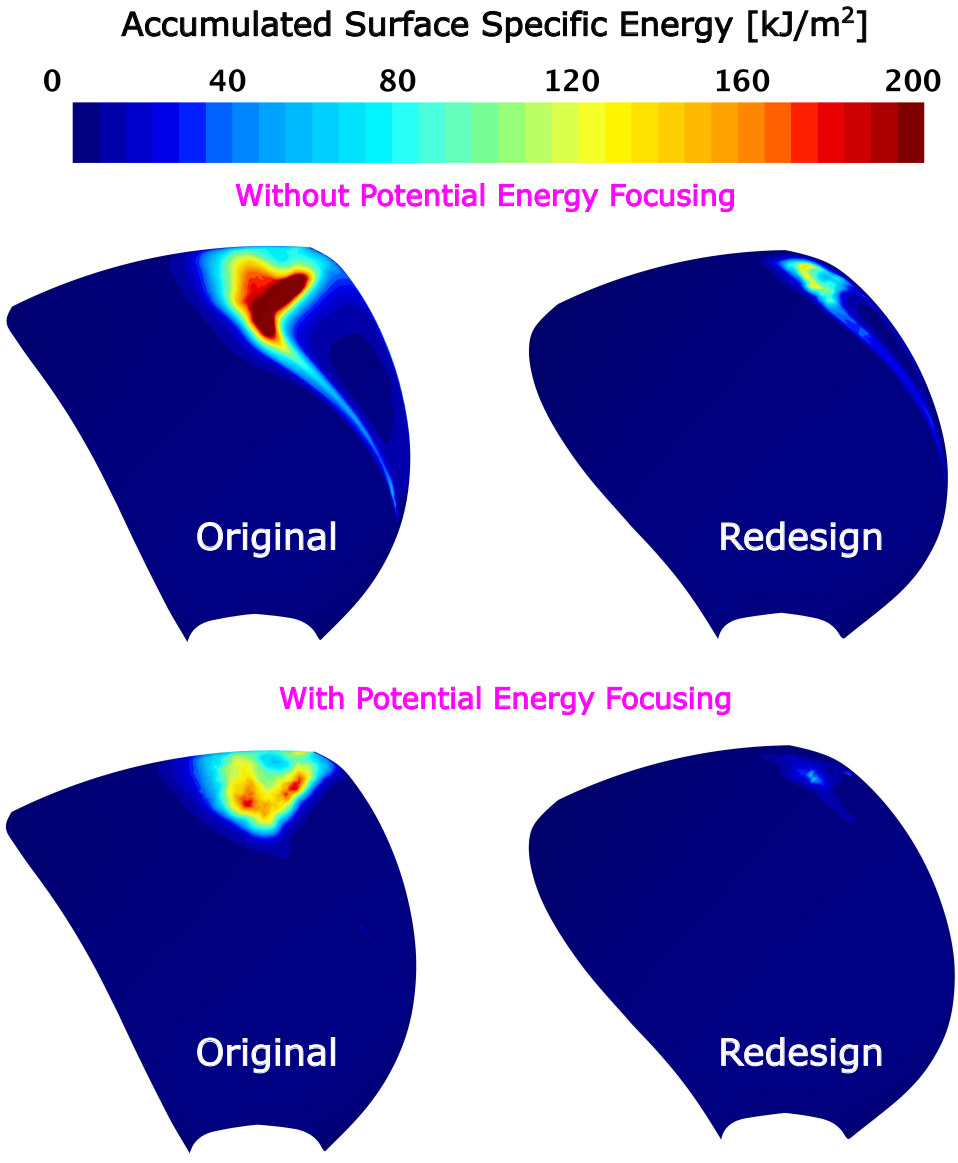

Figure 5.31: Surface specific accumulated energy on the refined propeller blade of the original propeller (left) and the first re-design (right), obtained from the non-focusing (top) and the focusing model (bottom) after five propeller revolutions

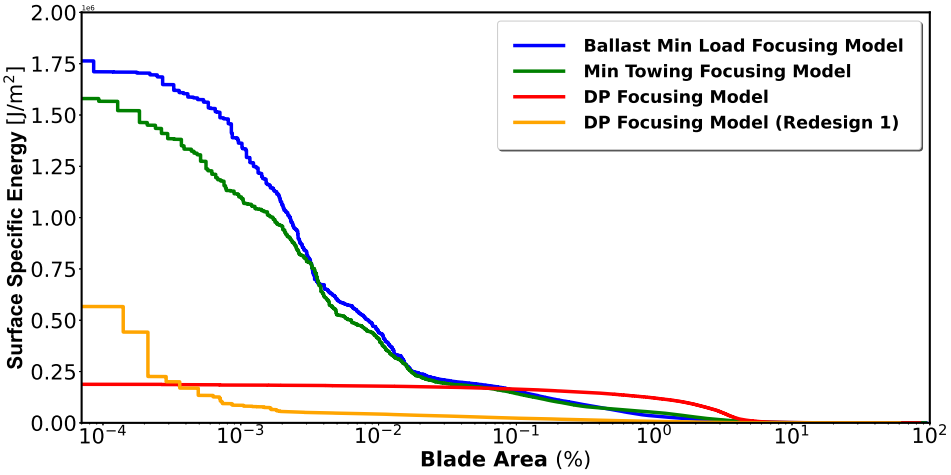

Figure 5.32: Surface specific energy over the blade area, showing the extent and the percentage of the impacted blade area, for the original blade in all three operating conditions, and the first re-design in dynamic positioning, after five propeller revolutions, using the energy focusing model

Figure 5.33: Comparison of the erosion risk predicted by CFD with the focusing model for the first re-design in dynamic positioning, and the real erosion on the actual re-design

Figure 5.34: Representation of the vapor volume on the blades of the second re-design, in dynamic positioning (left), and the actual damage on the real blade (right)

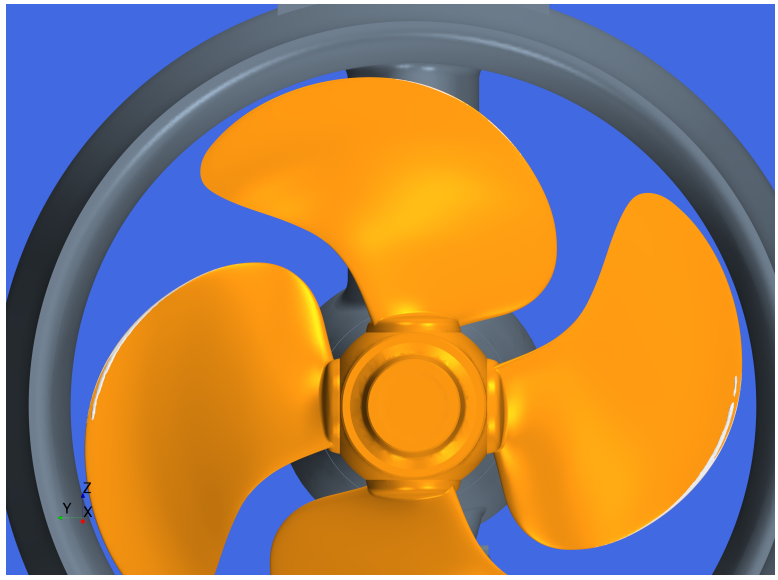

Figure 5.35: Representation of the vapor volume on the blades of the second re-design, at 7 knots, with incoming flow at 15 deg angle to emulate the flow behind the ship hull

the percentage of area, on which the energy is distributed, when energy focusing is applied. Comparing the impacted area between the original design and the first re-design, in the dynamic positioning condition, we see that a much larger area is impacted on the original blade. On the other hand, there is a small area on the blade of the re-design where more energy is accumulated. This indicates a higher risk of erosion for the re-design, even though the vapor volume is much smaller. This numerical finding is confirmed by the actual damage on the real blade of the re-design. Figure 5.33 shows that severe erosion occurs at the location where high surface specific energy is predicted. Looking only at the surface impact distribution, we could consider a very low risk of erosion. However, the high surface specific energy indicates a high risk of erosion, which corresponds well with the actual damage location. The difference in affected surface area may be explained by the lack of statistics on the surface impact in the simulations.

5.5.3. SECOND RE-DESIGN

Cavitation analysis on the second re-design, in all three operating conditions, showed very little cavitation on the pressure side. Even in dynamic positioning, only a small amount of cavitation is predicted at the leading edge. Looking at the actual erosion on the real blade (see Fig. 5.34), cavitation erosion occurred further away from the leading edge, indicating more extensive cavitation on the blades than what we could expect from the simulations. Therefore, we can hypothesize that, especially in this case, including the ship hull will have a significant impact on the propeller wakefield, resulting in a different inflow compared to the one used in the simulations. The presence of the hull results in a highly inclined flow towards the upcoming blade, leading to higher angles of attack, and consequently more cavitation dynamics.

Indeed, Fig. 5.35 shows the vapor volume on the second redesign at an inclined inflow of 15 degrees, 7 knots speed, and a pitch deflection similar to the one in dynamic positioning. Clearly, a larger amount of vapor volume is simulated, and especially on the upcoming blade. A vary thin sheet cavity is observed, which is shed to smaller structures, that possibly collapse at locations close to the actual damage on the real blade. Therefore, it is possible to simulate larger amount of vapor volume on the blade, but at an operating condition different than the ones reported as critical for cavitation erosion in Table 5.6.

Finally, water quality and roughness can play a major role in cavitation inception and cavity dynamics. In all the simulations performed, a perfect liquid and water quality is assumed, while all surfaces are perfectly smooth, possibly influencing the cavitation development and the impact distribution to some extent.

5.6. CONCLUSION

A novel erosion model has been used for the first time to predict propeller cavitation erosion on ship scale. An erosion risk assessment has been performed on a full scale steerable thruster in open water configuration, in three different operating conditions, and three different propeller designs.

To compute the fraction of radiated energy (originating form the collapse of cavitating structures) on the impacted surface, a fully continuous form of the solid angle is used. The exact solid angle of a surface element, i.e. a surface face, depends on the face topology

and requires specific algebraic formulas. If the topology of the surface face is unknown or if the topology is known, but the exact surface angle involves algebraic expressions that are difficult to evaluate, one might employ an approximation of the solid angle that only depends on the surface area of the face, its normal vector, and the distance vector between face center and the point of wave radiation. This approximation often leads to significant errors for sources located very close to the surface. Bounding the solid angle to the maximum solid angle for such cases, reduces the approximation error to its minimum.

A sensitivity study has been performed on the magnitude of the total accumulated surface energy on the propeller blade, during each propeller revolution. When energy focusing is applied, the grid and time step sensitivity is larger than without energy focusing, due to the larger influence of the shift in the collapse location on the projected surface energy. However, 24 cells per initial cavity width, and a time step size that corresponds to at least 40 steps per cavity collapse time are considered sufficient to resolve at least the larger structures that are shed from the developed sheet cavity on the pressure side of the blade (the collapse time can be estimated from the Rayleigh-Plesset collapse time of a spherical cavity with diameter equal to the maximum width of the sheet cavity on the blade).

When the blade impact distribution is assessed without energy focusing, the predicted accumulated surface energy is much higher than the one predicted with energy focusing, while it extends over a larger surface area, even larger than the actual impacted area on the real blade. At the same time, the surface specific energy is lower, leading to smaller magnitudes of the maximum loads on the surface. Due to the continuous release of energy at any moment there is a negative volume change, the non-focusing approach fails to predict the right amount of radiated energy at the right locations. Consequently, energy focusing is essential for an accurate prediction of the instantaneous impact loads and their distribution on the blades.

The capability of the erosion model to estimate the implosion loads and their potential damage on the blade surface is demonstrated for different conditions and different designs. The surface specific energy distribution provides good information about the erosion risk over the blade area, where large amounts of accumulated energy indicate a high risk for erosion. Comparison of the computed blade impact distribution with the actual damage on the blade, showed, for two propeller designs, a very good agreement between the high erosion risk areas, as predicted by the energy focusing model, and the actual damage location. A third propeller design showed less cavitation at the critical operating conditions than what the actual erosion indicates. This is hypothesized to be due to the difference in the wakefield with and without the hull. Highly inclined flow, as if the unit was operating behind the hull, showed, at certain condition, an increase in the vapor volume on the blades.

Finally, we show that the energy focusing model is suitable for identifying different cavitation aggressiveness levels, based on the operating condition and the blade design. Based on the analysis of the surface specific energy, the highest erosion risk was found on the original blade, in ballast minimum load, and minimum towing condition. A very slight amount of cavitation was found on the blades of the first re-design, and therefore no erosion risk for these two conditions. On the other hand, in dynamic positioning, the

surface specific energy on the first re-design indicated higher risk than on the original blade. Insufficient cavitation was found on the second re-design, for the given operating conditions, to allow for erosion risk assessment. This lack of predicted cavitation dynamics is credited to the neglect of the presence of the hull.

REFERENCES

[1] J. Carlton, *Marine Propellers and Propulsion* (Butterworth-Heinemann, Kidlington, Oxford, 2019).

[2] G. L. Chahine, J.-P. Franc, and A. Karimi, eds., *Cavitation and cavitation erosion: Computational and experimental approaches,* in *Advanced Experimental and Numerical Techniques for Cavitation Erosion Prediction*, Vol. 106 (Springer, Dordrecht, The Netherlands, 2014) Chap. 1–7, pp. 3–180, 1^{st} ed.

[3] D. Ponkratov and A. Caldas, *Prediction of cavitation erosion by detached eddy simulation (des) and its validation against model and ship scale results,* in *Proceedings of the* 4^{th} *International Symposium on Marine Propulsors* (Austin, Texas, USA, 2015).

[4] D. Ponkratov, *Des prediction of cavitation erosion and its validation for a ship scale propeller,* J. Phys. Conf. Ser. **656** (2015).

[5] A. Peters, U. Lantermann, and O. el Moctar, *Numerical prediction of cavitation erosion on a ship propeller in model- and full-scale,* Wear **408-409**, 1 (2018).

[6] R. Fortes-Patella and J. L. Reboud, *A new approach to evaluate the cavitation erosion power,* Journal of Fluids Engineering **120**, 335 (1998).

[7] C. Flageul, R. Fortes-Patella, and A. Archer, *Cavitation erosion prediction by numerical simulations,* in *Proceedings of the* 14^{th} *International Symposium on Transport Phenomena and Dynamics of Rotating Machinery* (Honolulu, HI, USA, 2012).

[8] R. Fortes-Patella, G. Challier, J. L. Reboud, and A. Archer, *Energy balance in cavitation erosion: From bubble collapse to indentation of material surface,* Journal of Fluids Engineering **135**, 011303 (2013).

[9] A. V. Arecchi, T. Messadi, and R. J. Koshel, *Field Guide to Illumination* (SPIE Press, Bellingham, WA, 2007).

[10] T. Melissaris, N. Bulten, and T. J. C. van Terwisga, *On the applicability of cavitation erosion risk models with a urans solver,* Journal of Fluids Engineering **141** (2019).

[11] T. Melissaris, S. Schenke, N. Bulten, and T. J. C. van Terwisga, *On the accuracy of predicting cavitation impact loads on marine propellers,* WEAR **456–457** (2020), https://doi.org/10.1016/j.wear.2020.203393.

[12] F. Menter, *Two-equation eddy-viscosity turbulence modeling for engineering applications,* AIAA Journal **32**, 1598 (1994).

[13] S. V. Patankar, *Numerical Heat Transfer and Fluid Flow* (Hemisphere Publishing Corporation, New York, 1980).

[14] F. G. Hammit, *Observations on cavitation damage in a flowing system,* J. Basic Eng **85**, 347 (1963).

[15] A. Vogel and W. Lauterborn, *Acoustic transient generation by laser-produced cavitation bubbles near solid boundaries,* The Journal of the Acoustical Society of America **84**, 719 (1988).

[16] D. Obreschkow, P. Kobel, N. Dorsaz, A. de Bosset, C.Nicollier, and M. Farhat, *Cavitation bubble dynamics inside liquid drops in microgravity,* Phys. Rev. Letters **97** (2006).

[17] M. Tinguely, D. Obreschkow, P. Kobel, N. Dorsaz, A. de Bosset, and M. Farhat, *Energy partition at the collapse of spherical cavitation bubbles,* Phys. Rev. E **86** (2013).

[18] S. Schenke, *Cavitation Implosion Loads from Energy Banalnce Considerations in Numerical Flow Simulations*, PhD Thesis, Delft University of Technology, Delft, The Netherlands (2020).

[19] S. Schenke, T. Melissaris, and T. J. C. van Terwisga, *On the relation between the potential cavity energy and the acoustic power signature caused by periodic vapor cavity collapses,* in *Proceedings of the* 6^{th} *International Symposium on Marine Propulsors* (Rome, Italy, 2019).

[20] B. P. Welford, *Note on a method for calculating corrected sums of squares and products,* Technometrics **4**, 419 (1962).

[21] S. Schenke, T. Melissaris, and T. J. C. van Terwisga, *On the relevance of kinematics for cavitation implosion loads,* Phys. Fluids **31**, 052102 (2019).

[22] G. Rowlands, *Solid angle calculations,* International Journal of Applied Radiation and Isotopes **10**, 86 (1961).

[23] H. Gotoh and H. Yagi, *Solid angle subtended by a rectangular slit,* Nucl. Instr. and Meth. **96**, 485 (1971).

[24] A. V. Oosterom and J. Strackee, *The solid angle of a plane triangle,* IEEE Transactions on Biomedical Engineering **2**, 125 (1983).

[25] C. Leclercq, A. Archer, R. F. Patella, and F. Cerru, *Numerical cavitation intensity on a hydrofoil for 3d homogeneous unsteady viscous flows,* International Journal of Fluid Machinery and Systems **10** (2017).

[26] J. P. Franc and J. M. Michel, *Fundamentals of Cavitation* (Kluwer Academic Publishers, Dordrecht, 2004).

6

Cavitation Erosion Risk Assessment for a Marine Propeller Behind a Ro-Ro Container Vessel

In the previous sections, we predicted the risk of cavitation erosion on propellers in an open water set-up, both in model and full-scale. In this chapter, we focus on assessing the cavitation development and the risk of erosion on the blades of propellers operating behind a Ro-Ro container vessel. The presence of the hull contributes to the non-uniformity of the inflow. The consequent variation in velocities and angles of attack leads to amplification of the cavitation dynamics, especially when the blade passes through the top position. Two designs are investigated that experience cavitation erosion on the pressure side. A statistical filter is used to attenuate low amplitude implosion loads, and identify the extreme events on the blade. The results show a very good correlation with the position of the actual erosion damage on the real propeller blades.

Parts of this chapter will be submitted to the special topic in *Physics of Fluids* on Cavitation

6.1. INTRODUCTION

The continuous restrictions on propeller noise and overall emissions, together with the increase in oil prices, enhance the need for maximum efficiency and optimum designs. As cavitation and cavitation erosion is one of the major constraints in propeller design, one of the key factors to achieve optimum designs is to understand, predict and resolve cavitation dynamics and cavitation nuisance. When in behind condition, propeller cavitation and dynamics depend strongly on the inflow coming from the hull. Köksal *et al.* [1] showed that flow non-uniformity is one of the most dominant factors in cavitation and cavitation erosion intensity, compared to other factors, for instance the cavitation number. That said, a good representation of the wakefield and the inflow towards the propeller seems very crucial for cavitating flow and erosion risk predictions.

Research on cavitation erosion on marine propellers is very limited. Even though studies performed during the EROCAV project indicated that there is a clear need for improved methods for cavitation erosion prediction, and that experiments are and will be the only reasonable way to make such predictions [2], prediction of cavitation erosion with CFD is becoming more popular recently. However, especially on full-scale, only a few attempts for erosion prediction on propellers or rudders can be found in the literature [3–5]. The generated pressures forming at the final stage of the collapse at extremely small scales require very high resolution both in space and time, rendering such simulations computationally inefficient. Furthermore, the lack of an appealing erosion model, that could easily be used with incompressible URANS solvers, that could increase computational efficiency, makes full-scale erosion simulations less attractive. Incompressible solvers fail to predict the peak pressures produced during the final stage of the collapse. Therefore an alternative model may be used that could estimate cavitation implosion loads in a quantitative manner.

The consideration of the erosive potential of cavitating structures from an energy balance point of view [6, 7], led the way for erosion models that use the potential energy contained within the cavitating structures as basis for the analysis of the surface impacts[8–11]. Moreover, the observation that a visual analysis of cavitation could give more insight into the hydrodynamic process of the global development of erosive cavities by Bark *et al.* [12], illustrated that an erosion model based on the kinematics of the collapsing cavities could work ideally with pressure based incompressible solvers. The key factor for such a model is the energy conservation as well as the overall and the instantaneous energy balance during the collapse.

As presented in Section 4 and 5, a novel energy conservative model that accounts for the temporal and spatial energy focusing towards the collapse center is employed, that is able to predict the cavitation implosion loads in a quantitative manner [13–15]. The erosion risk on the propeller blades in behind condition is simulated to ensure that the non-uniformity of the flow is well considered. Two propeller designs have been assessed to illustrate the capabilities of the model to distinguish different erosive potential levels originating from the violent collapse of the developed cavities on the blades. The estimated loads and the energy distribution on the blades have been compared to the actual damage on the real blades, highlighting the effectiveness of the presented model and its potential for commercial use already at an early design stage, towards the main goal of higher propulsive efficiency. Such a numerical model could potentially replace model

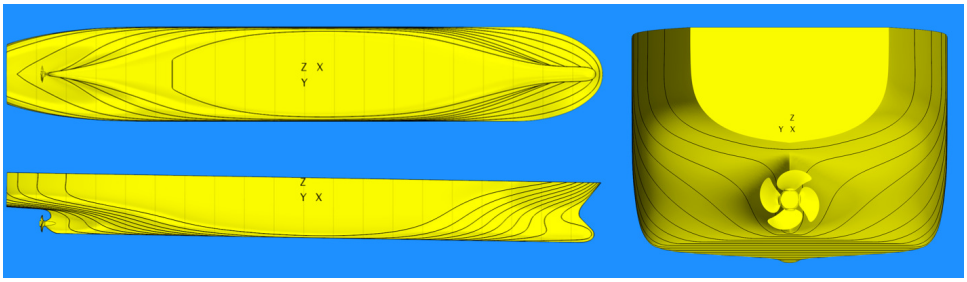

Figure 6.1: Hull Geometry.

Table 6.1: Main particulars of the ship

Length Between Perpendiculars	165.0 m
Length Overall	181.9 m
Length at Waterline	173.3 m
Beam	28.8 m
Draught	9.99 m
Draught at aft PP	8.50 m
MCR	15630 kW
Engine rate of revs	517 RPM
Design Ship Speed	19 knots

scale cavitation observations in the future.

6.2. CASE DESCRIPTION

Pressure side cavitation erosion on the blades behind a Ro-Ro container vessel is investigated. Table 6.1 shows the main characteristics of the ship depicted in Fig. 6.1. This ship was one of the test cases studied during the EROCAV project [2]. Two propeller designs were mounted on this ship (Design 1 and 2, see Fig. 6.2). First the ship operated with Design 1, which experienced severe pressure side cavitation erosion. Then, Design 2 was taken from a sister ship and was mounted on the vessel. Full scale observations were performed only on this design, as part of the EROCAV project. Table 6.2 shows the particulars of the two designs.

The vessel has mainly been operating in the design speed of 19 knots (11450 kW Power), when both engines are engaged, however, it may also sail with one engine at a lower speed of 13.5 knots and lower power (5930 kW). Based on the operation with Design 1, and from the observations with Design 2 mounted on the ship, both designs suffer from cavitation erosion on the pressure side. Additionally, calculations were made for both designs and both conditions using the lifting surface program MPUF-3A (Mid-chord cavity detachment - Propeller Unsteady Flow). MPUF-3A solves the potential flow around the propeller using the Vortex Lattice Method (VLM). From the results it appeared that Design 1 exhibits

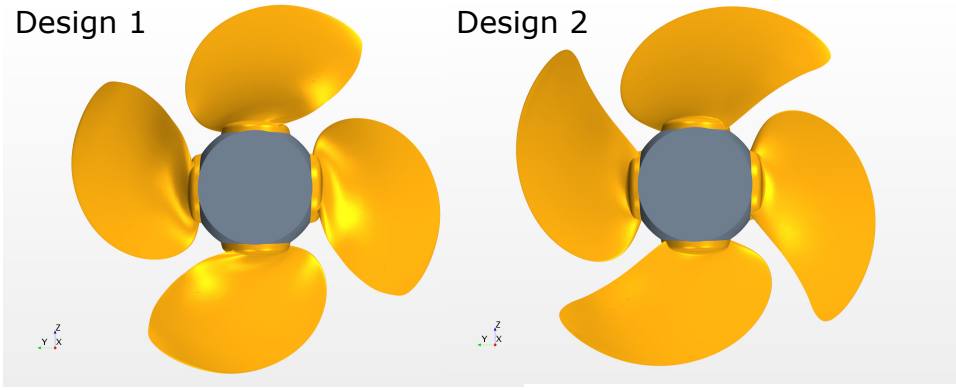

Figure 6.2: Propeller Designs

Table 6.2: Main particulars of the propellers

	Design 1	Design 2
Diameter	5.6 m	5.6 m
Number of blades	4	4
Expanded blade area ratio	0.638	0.665
Pitch diameter ratio (0.7R)	0.897	0.890
Hub diameter ratio	0.340	0.340
Direction of rotation	Left handed	Left handed
Propeller rate of revs	134 RPM	134 RPM

much more pressure side cavitation as well as higher erosion risk than Design 2. While the calculations showed sufficient pressure side cavitation for both ship speeds (13.5 and 19 knots) for Design 1, very little cavitation was predicted on Design 2 at 19 knots.

Figure 6.3 illustrates the erosion damage on the actual blades of Design 1 and 2. Based on these snapshots, Design 2 shows more severe damage on the pressure side. However, the operation time after which these snapshots where captured is unknown, and based on the observations during the ship trials, Design 1 is expected to have larger amount of cavitation on the pressure side as well as higher erosion risk on the blades, which is in line with the MPUF-3A calculations. It should also be noted that the depicted erosion pattern on Design 1 is probably due to a combination of operating conditions, since it exhibits pressure side cavitation during a wider range of speeds. On the other hand, Design 2 was taken from a sister vessel, which is more likely that she has sailed for longer periods at a relatively lower power (probably at only one of the two engines). Therefore, the erosion damage on Design 2 is most likely originated from the low speed condition (13.5 knots). In this study, both designs have been simulated at the low speed condition.

Figure 6.3: Actual erosion on the blades for Design 1 (left) and Design 2 (right). The exact period over which each propeller design had been operated to get the depicted erosion damage is unknown.

6.3. NUMERICAL SET-UP

6.3.1. WETTED FLOW

The Unsteady Reynolds-Averaged Navier Stokes (U-RANS) equations are solved for the fluid motion, using the commercial solver StarCCM+ 13.04.

$$\frac{\partial(\rho\mathbf{u})}{\partial t} + \nabla\cdot(\rho\mathbf{u}\mathbf{u}) = -\nabla p + \rho f + \nabla\cdot\tau \tag{6.1}$$

$$\frac{\partial\rho}{\partial t} + \nabla\cdot(\rho\mathbf{u}) = 0 \tag{6.2}$$

where $\mathbf{u}$ is the velocity tensor, ρ is the fluid density, p the pressure, f the external force per unit mass and τ the viscous part of the stress tensor. A segregated approach is adopted solving the conservation equations of mass and momentum in a sequential manner combined with the SIMPLE algorithm for pressure-velocity coupling. Second-order implicit time marching is employed together with a second-order upwind convection scheme.

The free surface is modeled using a homogeneous multiphase model, referred to as Volume of Fluid (VoF) in StarCCM+. The fluid is treated as a single continuum with different phases. At the interface the two phases share the same velocity (no-slip condition). The density and the turbulent viscosity at the interface is given by the mixture relations

$$\rho = (1-a)\rho_{air} + a\rho_l \qquad and \qquad \mu = (1-a)\mu_{air} + a\mu_l \tag{6.3}$$

respectively, where $0 < a < 1$ is the liquid volume fraction. An additional transport equation is solved to determine the liquid volume fraction in each computational cell

$$\frac{\partial\alpha}{\partial t} + \nabla\cdot(\alpha\mathbf{u}) = 0 \tag{6.4}$$

High Resolution Interface Capturing Scheme (HRIC) is employed for the discretization of the convective term in Eq. 6.4 [16] to minimize numerical diffusion, and increase the sharpness of the interface. Based on Normalized Variable Diagram (NVD) [17], the

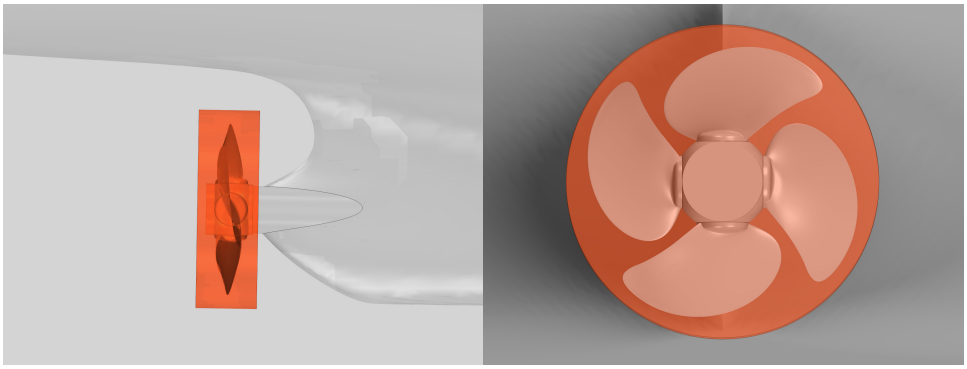

Figure 6.4: Representation of the size of the rotating domain

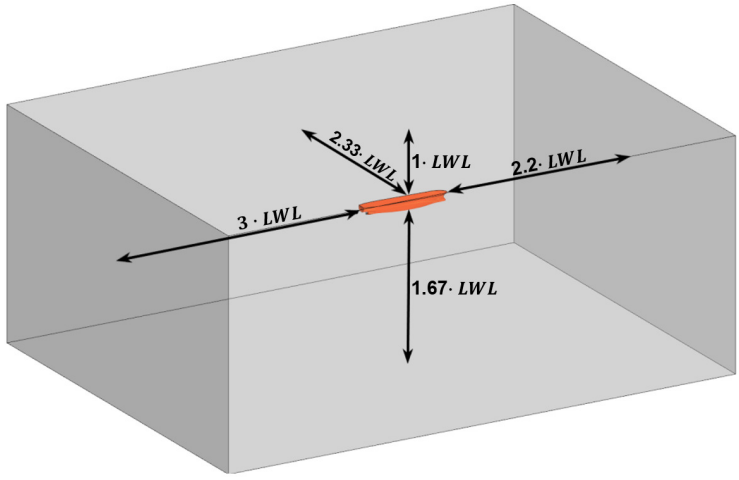

Figure 6.5: Dimensions of the numerical domain

HRIC scheme simplifies the dependence on the CFL condition, while using an increased order of accuracy [18]. The k-ω SST turbulence model is used to close the RANS equations, and to model the Reynolds Stress term [19], together with an empirical model to reduce the turbulent dissipative terms [20], to avoid any artificial increase of the eddy viscosity at the interface (see Melissaris *et al.* [21]).

The propeller motion is simulated by creating a rotating region that surrounds the propeller. A non-conformal interface (sliding interface) is used to couple the rotating with the static region at each timestep. A representation of the size of the rotating region is shown in Fig 6.4, while Fig 6.5 shows the dimensions of the static domain used for the self-propulsion simulations.

The mesh consists of trimmed hexahedral cells with a number of local refinements for the bow, the stern, the free surface, and the wake of the vessel, as shown in Fig. 6.6. A target wall y+ value of $30<y^+<300$ is aimed for the hull, while in the propeller higher

Table 6.3: Description of the different generated grids for the wetted flow self-propulsion simulations, showing the smallest cell size of each grid h_i, and the number of cells on the static and the rotating region

Grid	h_i	h_i/h_4	# cells in Rot. Region	# cells in Static Region
Grid 1	0.00661	1.875	2.55 M	1.80 M
Grid 2	0.00529	1.5	3.76 M	2.59 M
Grid 3	0.00441	1.25	4.95 M	4.20 M
Grid 4	0.00353	1	5.77 M	6.66 M

values are expected due to the higher velocities, especially close to the tip. Wall y^+ values up to 2000 are acceptable in the propeller surface. Four sets of grids were generated to assess the mesh sensitivity. Table 6.3 shows the grid densities and the number of cells in the rotating and the static region for each set of grids.

6.3.2. CAVITATING FLOW

The low Froude number (Fr=0.164) and the low wave resistance at low ship speeds (U=13.5kn) allows for neglecting the free surface waves in order to increase computational efficiency in the cavitating flow simulations. This is done by replacing the free surface by a symmetry boundary condition at the free surface level. In that case, the air phase is neglected and it replaced by the vapor phase in the solver, so that the mixture relations become

$$\rho = a_v \rho_v + (1 - a_v)\rho_l \qquad and \qquad \mu = a_v \mu_v + (1 - a_v)\mu_l \tag{6.5}$$

respectively, where $0 < a_v < 1$ is now the vapor volume fraction. An additional source term is added on the r.h.s. of Equation 6.4 to model the mass transfer between liquid and vapor

$$\frac{\partial \alpha_v}{\partial t} + \nabla \cdot (\alpha_v \mathbf{u}) = S_{\alpha_v} \tag{6.6}$$

where S_{α_v} is the mass transfer source term as defined by the Schnerr-Sauer cavitation model [22]. The pure phases are treated as incompressible and compressibility is mimicked only in the mixture regime. The high ambient pressures ($\approx$ 1 bar) result in an inertia driven flow and the mass transfer model can give realistic predictions as long as the density-pressure trajectories are steep enough. The steepness of the density-pressure trajectory is controlled by the evaporation and condensation coefficients of the mass transfer source term [13, 14], that should be large enough (equal or larger than 1) to enforce a quick transition form vapor to liquid phase and vice versa. In this study, both coefficients are set equal to 1, which even though is at the limit, it gave the best convergence behavior.

6.3.3. CAVITATION EROSION MODELING

The cavitation implosion loads are predicted using the energy balance approach presented in Sections 4 and 5, where the initial cavity potential energy is proportional to the cavity volume and the difference between the driving pressure, p_d, and the pressure within the cavity, p_v. During the collapse, the potential energy is converted into kinetic

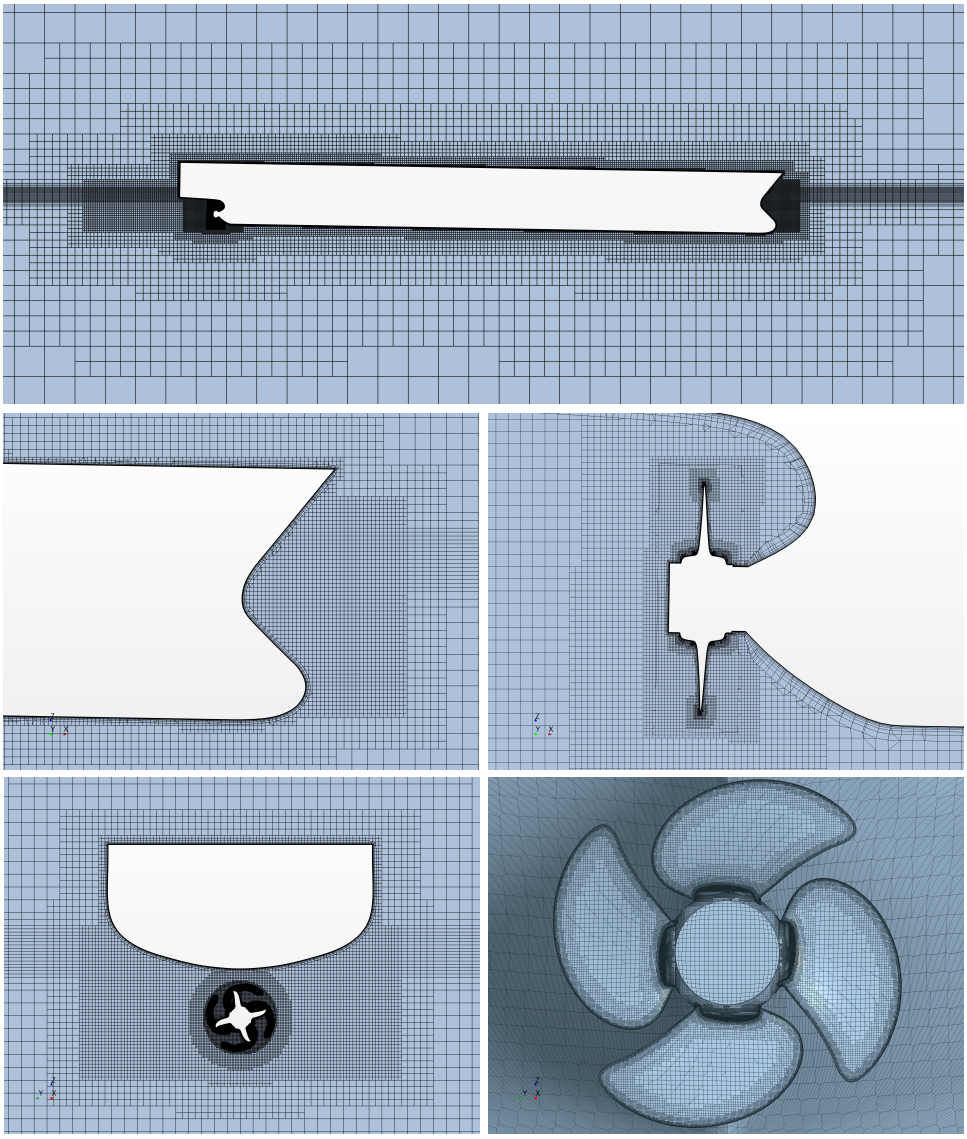

Figure 6.6: Representation of the mesh of Grid 3 and the refinements on the bow, stern, free surface, and the wake of the hull

energy, while it is being focused into the collapse center. At the final stage of the collapse it is assumed that all the kinetic energy is converted into acoustic radiated energy, justified by the relatively high driving pressures and the absence of non-condensible gas in the flow [23].

The change of potential energy in each volume cell with volume, V_{cell}, is computed by the material derivative of the potential energy, E_{pot}, such that

$$\dot{e}_{pot} = \frac{DE_{pot}/Dt}{V_{cell}} = (p_d - p_v) \cdot \frac{D\alpha_v}{Dt} \tag{6.7}$$

where the material derivative of the driving pressure has been omitted, as it does not contribute to energy radiation from the imploding cavities [13, 14]. The material derivative of the vapor volume fraction a_v is computed from the mass transfer source term, while only condensation is considered

$$\dot{e}_{pot,C}(t,\mathbf{x}_{cell}) = (p_d - p_v) \cdot min\left[\frac{\rho}{\rho_l} S_{\alpha_v}, 0\right] \tag{6.8}$$

The surface accumulated energy is predicted with and without energy focusing to illustrate once more the capabilities of the energy focusing approach. In the case where no focusing is applied, then the radiated power, $\dot{e}_{rad}$ is directly coupled to the negative change of potential energy during condensation from Eq. 6.8. On the other hand, when energy focusing is applied the radiated energy is derived as

$$e_{rad}|_{t+\delta t} = \frac{1}{\delta t}(\beta\varepsilon)|_t \tag{6.9}$$

where ε is the collapse induced kinetic energy as computed from Eq. 5.17 and β the collapse parameter, which is 1 when a final collapse stage has reached, and 0 otherwise (see Eq. 5.11).

Considering all the emission sources, the impact power per unit surface at any location $\mathbf{x}_S$ is given by

$$\dot{e}_S(t,\mathbf{x}_S) = \frac{1}{4\pi A_f} \int_V \Omega_d \, \dot{e}_{rad}(t,\mathbf{x}_{cell}) dV \tag{6.10}$$

where

$$\Omega_d = min\left[\left(\frac{(\mathbf{x}_{cell} - \mathbf{x}_S) \cdot \mathbf{n}}{\|\mathbf{x}_{cell} - \mathbf{x}_S\|^3} A_f\right), 2\pi\right] \tag{6.11}$$

is the discrete solid angle, and A_f is the face area.

Since the energy radiation in the present study is done in a discrete way at each time step, and the exact energy distribution is unknown, a statistical approach is applied to distinguish between extreme events and repetitive events of low amplitude. The identification of the extreme events is based on the idea to amplify the surface impact power by an intensity component n [13], which is achieved by the power or Hölder mean, given by

$$M_{\{n\}}(\dot{e}_S) = \left(\frac{1}{T}\int_T (\dot{e}_S(t,\mathbf{x}_S))^n \, dt\right)^{\frac{1}{n}} \tag{6.12}$$

As the intensity parameter n increases, the power mean approaches the amplitude of the input signal $\dot{e}_S$. Eq. 6.12 requires that the energy projection to the surface takes place

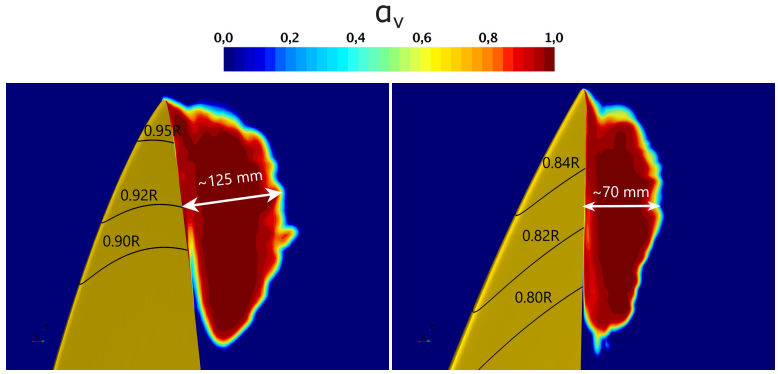

Figure 6.7: Representation of the vapor volume at an arbitrary radial section, showing the approximate maximum size of the developed sheet cavity, before it starts to shed, over one revolution for Design 1 (left) and Design 2 (right)

during each time step. Since the surface projection is computationally not very efficient, the intensity component n is applied in a modified way, so that the energy projection can be performed at any time instant, for instance at the end of each propeller revolution. That gives

$$M_{\{n\}}(\dot{e}_S(\mathbf{x}_S)) = \left(\frac{1}{TV}\int_T\int_V (\dot{e}_S(t,\mathbf{x}_S))^n \, dV\,dt\right)^{\frac{1}{n}} \tag{6.13}$$

and since the solid angle Ω_d is not time dependent, the time and volume integrals can be interchanged, so that the volume integration is performed only once at the end of the time integration

$$M_{\{n\}}(\dot{e}_S) = \left(\frac{1}{TV}\frac{1}{4\pi A_f}\int_V \Omega_d^n \int_T (\dot{e}_{rad})^n \, dt\,dv\right)^{\frac{1}{n}} \tag{6.14}$$

The amplified impact power from Eq. 6.14 is used to construct a filter that attenuates the contribution of low amplitude events, so that extreme events can be identified. Similar to the normalization of the erosion indicators in Sec. 3.3.4, and following the work by Schenke [13], the filter $F_{\{n\}}$ is derived by normalizing the amplified impact power distribution by its maximum value, such that

$$F_{\{n\}} = \frac{M_{\{n\}}(\dot{e}_S)}{max\left[M_{\{n\}}(\dot{e}_S)\right]}, \quad where \quad F_{\{n\}} \in [0,1] \tag{6.15}$$

Then, the filtered surface energy distribution is given by

$$e_{S_{\{n\}}} = e_S F_{\{n\}}, \quad where \quad e_S = \int_0^T \dot{e}_S(t,\mathbf{x}_S)dt \tag{6.16}$$

The filtering procedure is done after each propeller revolution. Finally, the filtered average impacted power after a certain amount of revolutions can be computed by

$$\dot{e}_{S_{\{n\}}} = \frac{e_{S_{\{n\}}}}{iT_i} \tag{6.17}$$

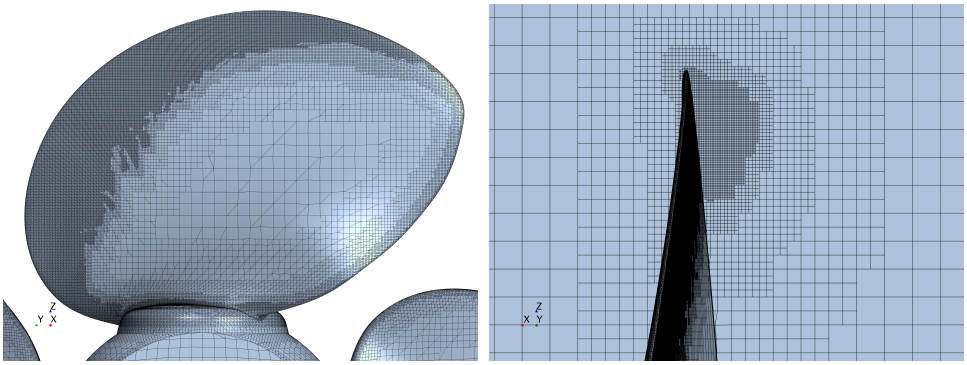

Figure 6.8: Representation of the mesh on the refined blade of Design 1

where i is the number of propeller revolutions, and T_i is the time for each revolution.

The best practice guidelines from the erosion risk analysis on the KCD model propeller (Chapter 4) and the full-scale steerable thruster (Chapter 5) are used to estimate the implosion loads on the two designs. As in each test case, a volume refinement is applied around one of the blades, and on the volume cells where the vapor volume has a non-zero value over one full revolution. Based on the guidelines, approximately $20-25$ cells (excluding the prism layer cells) along the smallest dimension of the vapor cavity, when its is at its maximum size, are used, as well as about 40 time steps during the collapse, based on the Rayleigh-Plesset collapse time [24]. Figure 6.7 shows the approximate maximum size of the developed sheet cavity, before it starts to shed, for Design 1 and 2, respectively. Regarding Design 1, for a cavity with diameter $D \approx 125$ mm, this translates to a minimum cell size of $c \approx 5$ mm, and a time step size of $\Delta t = 1.45 \times 10^{-4}$ s or a rotation rate of 0.12 deg per time step. To keep the cell size of the refinement a perfect multiple of the background mesh, eventually, a cell size $c \approx 4.4$ mm has been selected for the refinement, that corresponds to at least 25 cells per cavity width at any time instant. The chosen time step size is $\Delta t = 1.28 \times 10^{-4}$ s or a rotation rate of 0.1 deg per time step, corresponding to about 45 time steps during the collapse. Design 2 appears to have a cavity size on the blade that is roughly half the size of the one on Design 1. Therefore, half the cell size has been selected for the volume refinement ($c \approx 2.2$ mm), and the time step size ($\Delta t = 0.64 \times 10^{-4}$ s or a rotation rate of 0.05 deg per time step), so that the same amount of cells are used along the cavity and the same number of time steps during the collapse. A wall resolved approach is used to better simulate the vapor volume and the cavity dynamics close to the wall, but also to get a good transition between the prism layer and the volume cells. The wall y^+ values on the blade are well below 1. Achieving even lower y^+ values would lead to either a worse transition between the prism layer and the volume cells or it would require a much larger number of prism layer cells increasing the total mesh size significantly. Table 6.4 shows the eventual number of cells in the domain, on the blade and in the prism layer region, while Fig. 6.8 and 6.9 illustrate the refined mesh on Design 1 and Design 2, respectively.

The convergence criterion, r, from Sec. 5.5 is employed to ensure the iterative convergence during each time step. The criterion is satisfied when the deviation between the

Table 6.4: Mesh information after the applied volume refinement on one of the blades, showing the total number of volume cells, surface cells on the refined blade, prism layers, and cells per cavity width along the maximum cavity size

	# cells total	# of cells on refined blade	# of prism layer cells	# of minimum cells per cavity width
Design 1	10.1 M	126 k	16	25
Design 2	18.5 M	303 k	16	25

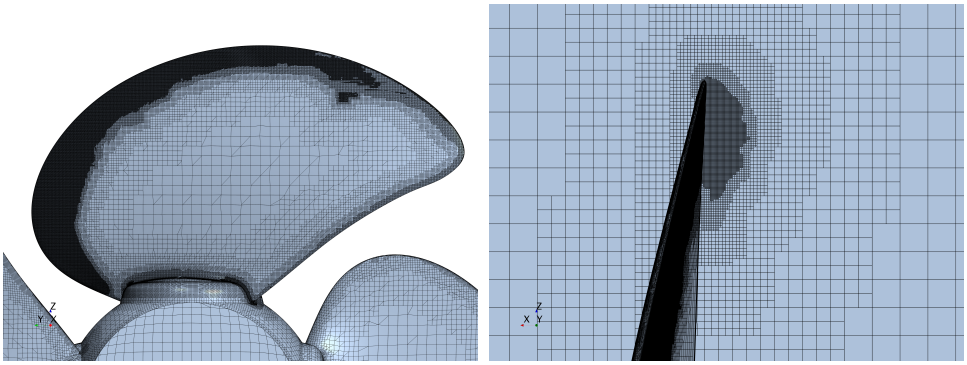

Figure 6.9: Representation of the mesh on the refined blade of Design 2

maximum and the minimum value of the total vapor volume fraction, α_v, over the last n iterations, divided by the average of α_v over the last n iterations is lower than 10^{-6}:

$$r = \frac{|\, max\{\alpha_v\}_{j=i-n+1}^{i} - min\{\alpha_v\}_{j=i-n+1}^{i} \,|}{\frac{1}{n}\sum_{j=i-n+1}^{i} \alpha_{v_j}} < 10^{-6} \tag{6.18}$$

where $i >= 5$ the iteration number during the time step. A value $n = 5$ is set in the simulations, together with a number of maximum inner iterations equal to 100 for Design 1, and 50 for Design 2 (the smaller time step size allows for half the maximum inner iterations during each time step).

6.4. RESULTS

6.4.1. WETTED FLOW - VERIFICATION

Self-propulsion simulations have been performed at 13.5 knots on the four generated grids from table 6.3 to assess the uncertainty in propeller thrust and torque of Design 2. Design 2 was selected for the sensitivity study over Design 1, since Design 2 was the one fitted on the vessel during the full-scale observations. Figure 6.10 illustrates the wall y^+ values on the hull and propeller wall surface for grid 3. An average value of $y^+_{avg} \approx 100$ was achieved on the hull, while on the propeller surface much higher values ($y^+_{avg} \approx 540$) are

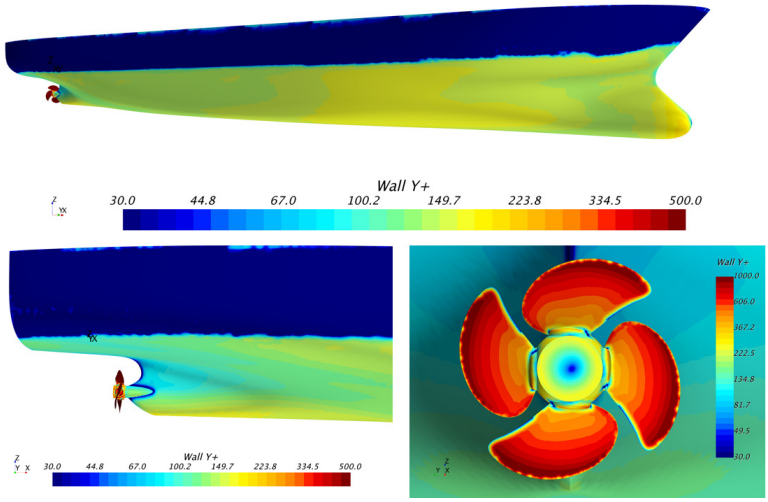

Figure 6.10: Wall y^+ Values on the hull and the propeller wall surface for grid 3

Table 6.5: Propeller thrust and torque values for four sets of grids with free surface, and for grid 3 using double body approach (no free surface)

	Thrust [kN]	% difference	Torque [kNm]	Power [kW]	% difference
G1 (VoF)	553.4	1.90 %	386.0	5417	3.38 %
G2 (VoF)	547.2	0.76 %	379.1	5319	1.51 %
G3 (VoF)	545.5	0.45 %	376.1	5278	0.72 %
G4 (VoF)	543.1	-	373.4	5240	-
G3 (DB)	544.5	0.26 %	375.7	5271	0.60 %

present due to the higher acceleration of the flow, and the propeller motion. A propeller rotation rate of 2 deg per time step has been used in each simulation, which is considered sufficient for all grids, combined with a second order time marching, and a second order upwind convection scheme. Looking at the results in Table 6.5, propeller torque is more sensitive to the grid density than thrust. However, both show less than 1% difference between the two finest grids. The generated free surface waves along the hull, for grid 3 are illustrated in Fig. 6.11, showing a quite low wave height. The bow and stern wave heights are also low, indicating that a symmetry plane may be used instead to improve the computational efficiency and stability. Indeed, the results obtained from the Double Body (DB) simulation, where the top boundary is at the free surface level, compare very well with the ones obtained with free surface. That indicates that even though the total resistance might be quite different between both simulations, the propeller working point and the propeller inflow seem to be very similar. This observation allows to estimate the erosion risk on the blades by neglecting the free surface effects, and therefore increasing the computational efficiency.

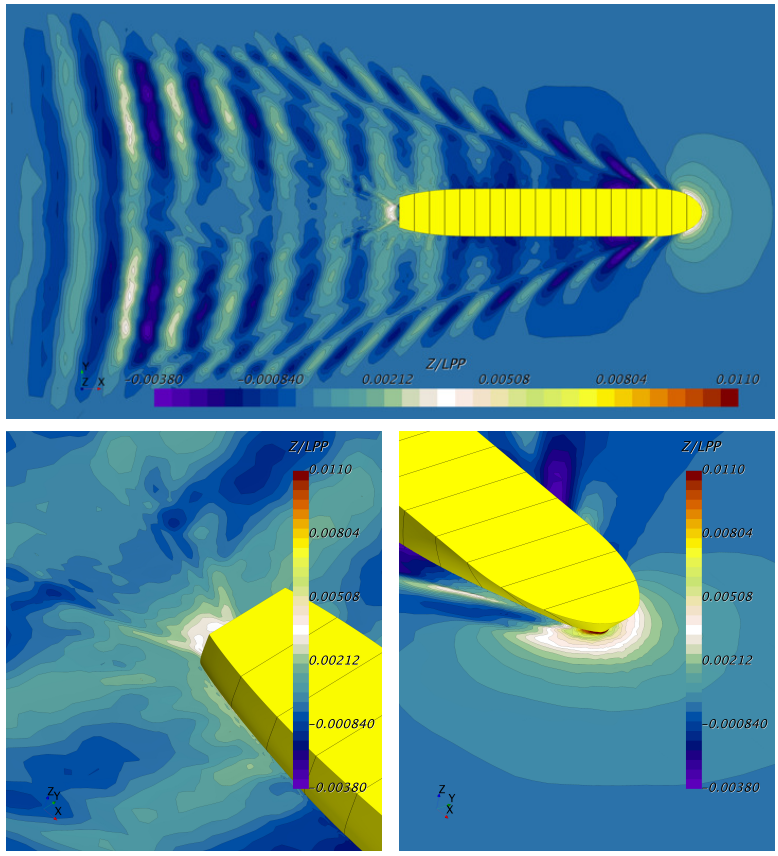

Figure 6.11: Representation of the free surface waves

Propulsion simulations have been performed on grid 3 to estimate the right operating condition for each design. For each propeller design, the performance at four ship speeds has been computed. Table 6.6 and table 6.7 present the results for Design 1 and 2, respectively. Comparing the CFD reults to the full-scale measurements (for design 2), quite some difference is observed on the power absorption at the same ship speed. A higher propeller torque was measured at 13.5 knots ship speed. However, this can be attributed to the fact that no added resistance for the hull and propeller roughness has been considered, that could increase the torque absorption significantly. Therefore, using the torque identity to match the measured power would lead to a ship speed quite lower than the trial speed (12.2 knots).

The measured delivered power of 5930 kW was also used in calculations with the lifting surface program MPUF-3A. A thrust coefficient is also derived from these calculations. Interpolating to match this thrust, leads to a ship speed closer to 13.5 knots for both designs, than interpolating to the delivered power of 5930 kW. Even though, thrust estimation may have a higher uncertainty than the power measurements, it was decided to use

Table 6.6: Propeller thrust and torque values for different ship speeds for Design 1 on grid 3

Ship speed [kn]	Thrust [kN]	K_T [-]	Torque [kNm]	K_Q [-]	Power [kW]
12.5	471.0	0.094	412.4	0.015	5787.3
13.0	427.6	0.085	400.0	0.014	5613.0
13.5	382.9	0.076	386.9	0.014	5429.5
14.0	338.1	0.067	373.7	0.013	5244.0
13.5 (MPUF-3A)		0.088			5930

Table 6.7: Propeller thrust and torque values for different ship speeds for Design 2 on grid 3

Ship speed [kn]	Thrust [kN]	K_T [-]	Torque [kNm]	K_Q [-]	Power [kW]
12.0	678.6	0.135	429.3	0.015	6027.7
12.5	636.8	0.127	412.8	0.015	5792.7
13.0	593.8	0.118	395.6	0.014	5551.3
13.5	544.5	0.108	375.7	0.013	5271.3
13.5 (measured)					5930
13.5 (MPUF-3A)		0.112			5930

the thrust identity to get the conditions for the erosion risk analysis. Interpolating to the thrust coefficient as derived from the MPUF calculations, leads to a ship speed of 12.8 knots for Design 1 and 13.3 knots for Design 2. Nevertheless, the difference in the vapor volume and its dynamics for small variations in ship speed did not seem to be very large, although higher speed means slightly higher pressure side cavitation.

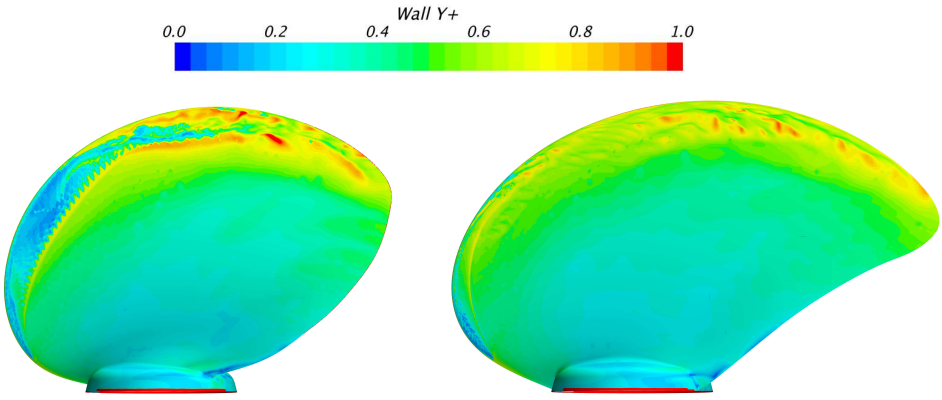

Figure 6.12: Wall y^+ values on the surface of the refined blade of Design 1 (left) and 2 (right) when the blades are at the top position

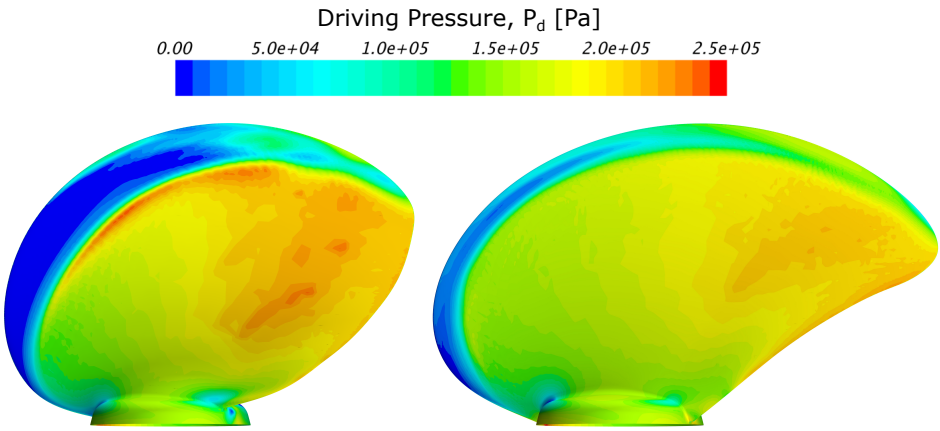

Figure 6.13: Time averaged pressure distribution on the surface of the refined blade of Design 1 (left) and 2 (right) after a sample time of one propeller revolution. A pronounced pressure gradient is observed over the cavitation free region of the blade.

6.4.2. EROSION RISK ASSESSMENT

The erosion risk on the propeller blades of Design 1 and 2 has been assessed for five propeller revolutions. The wall y^+ values on the blade surface for each design is depicted in Fig. 6.12. The wall y^+ values should be well below one for high fidelity predictions, especially when the k-omega SST turbulence model is used to model Reynolds stresses [25]. The average y^+ value over the refined blade is very similar for both designs, $y^+ = 0.41$ for Design 1 and $y^+ = 0.42$ for Design 2. Lower y^+ values would be desirable, but would lead to a larger number of prism layer cells that could increase the total number of cells significantly. Therefore, a compromise is made for somewhat larger y^+ values (only locally close to 1), but we ensure a better mesh quality, and computational efficiency. The pressure distribution on the blades, as a results of the moving average of the instantaneous pressure over one propeller revolution, is shown in Fig. 6.13. The pressure recovery gradient is more pronounced for Design 1, and thus more violent collapses should be expected, considering also the larger vapor volume on the blades. The depicted pressure distribution is at the top blade position, and it changes slightly with the blade position (sliding window equal to one revolution).

Figure 6.14 presents the total accumulated energy on the refined blade for each design, during each propeller revolution, without and with energy focusing. Even though the total accumulated energy is not directly related to the erosion risk levels, very often higher accumulated energy translates to higher erosion risk. The surface energy distribution and the energy density on the blades can possibly give more information about the aggressiveness of the implosion loads on the surface. From Fig. 6.14 the accumulated energy on the blade surface of Design 1 is almost two times larger than on Design 2. Moreover, we observe that for Design 1, higher energy is predicted without energy focusing. That is a common observation since the instantaneous release of energy usually leads to higher accumulated surface energy. Whether the surface energy will be higher or lower than the one predicted with energy focusing depends strongly on the dynamics and

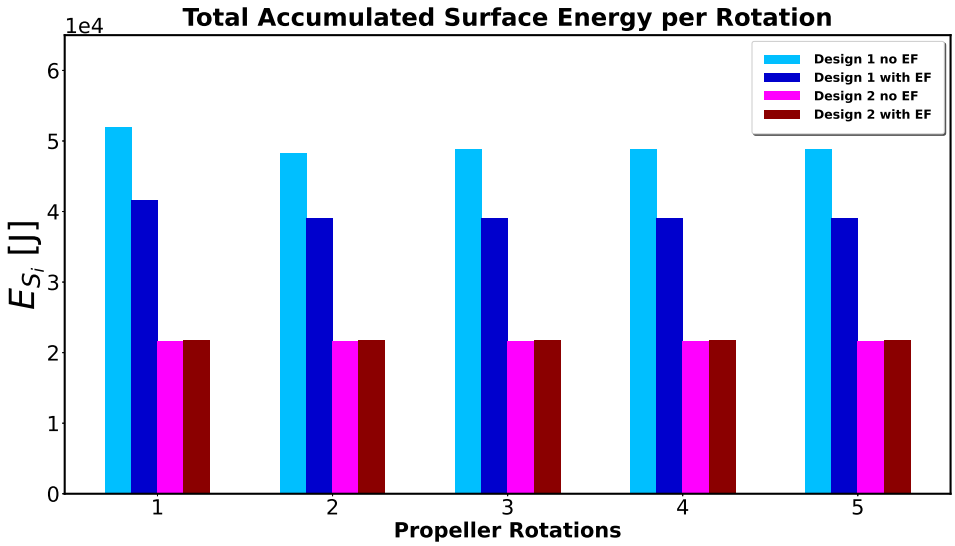

Figure 6.14: Total accumulated surface energy per propeller rotation, for five consecutive revolutions, for both designs, with and without energy focusing

the location of the radiation sources, as well as the curvature of the blade surface. Usually, the shedding of the sheet cavity happens very close to the surface, and the non-focusing model tends to produce larger amounts of energy on the surface. However, it can happen that the radiation sources with energy focusing are much closer to the surface than without focusing. Apparently, that happens to the second design where the surface accumulated energy is very similar for both approaches, and slightly higher in some revolutions, when energy focusing is applied.

Looking at the surface energy distribution on the blade, we can get a better insight into the locations of high implosion loads and the blade areas of higher erosion risk. Figure 6.15 illustrates the energy distribution on each design, without and with energy focusing. First of all, as in all the previous test cases, the energy focusing approach predicts higher implosion loads on the blades, the impacts on the surfaces are more scattered, and the main impacted areas are more distinct. Additionally, as the energy radiation takes place only at the final stage of the collapse, the involved advection has the tendency to stretch the surface energy distribution further downstream. Much less energy is predicted close to the leading edge and the energy is concentrated slightly further downstream in chordwise direction. On the other hand, when no energy focusing is applied the radiated energy is extended over a larger area and consequently, lower magnitudes are expected, and at locations closer to the leading edge. This observation is less pronounced on Design 2, as it shows more similar impact distributions with and without energy focusing. One possible explanation could be that, the vapor cavities, that are of smaller size, do not collapse very far from the point they are shed, and even though the pressure recovery gradient is not as pronounced as in Design 1 (see Fig. 6.13), it is still sufficient to cause rapid collapses, without letting the cavities travel long distances during their collapse. Thus, the effect of

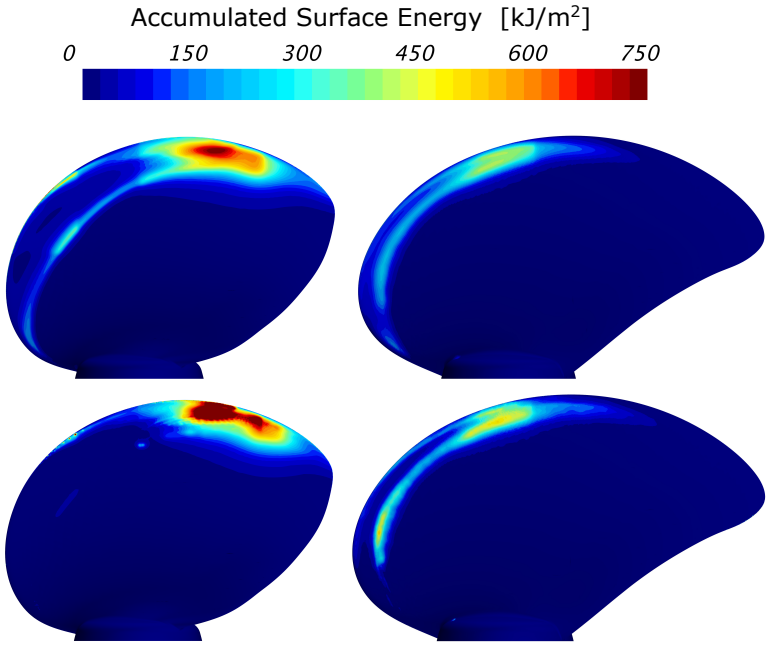

Figure 6.15: Surface specific accumulated energy on the refined propeller blade of Design 1 (left) and Design 2 (right), obtained without (top) and with (bottom) energy focusing, after five propeller revolutions

the focusing is mainly visible on the magnitude and not the location of the implosions.

On Design 1 almost no energy is predicted over the mid span of the blade with energy focusing. Most of the radiated energy is concentrated at the top of the blade and at higher radii. Much higher amplitudes of the implosion loads are predicted for Design 1, showing a higher erosion risk than Design 2, which compares well with both the MPUF calculations, and the overall observations on the real blades. Furthermore, Design 1 should experience erosion in a wide range of conditions, but it can be expected that at low speed the erosion risk is very high. On the contrary, Design 2 did not show any severe pressure side cavitation at 19 knots based on the full-scale observations, and therefore not a real risk for erosion, but at approximately 13.5 knots, both observations and simulations show some erosion risk on the blades, however, still lower compared to Design 1.

A filter has been applied to attenuate the low amplitude events, usually of high frequency, so that extreme events can be identified. Cavitation erosion can be a result of both repetitive events of low amplitude, and less frequent extreme events, but in most of the cases the extreme events are the ones mainly responsible for material damage. Both scenarios cause damage but in some cases at full scale the erosion tends to stop, probably the former scenario, while in other cases erosion just progresses, probably the latter scenario. Figures 6.16 and 6.17 present the filtered averaged surface impact distribution for Design 1 and 2, respectively, and for 5 variations of the intensity exponent (n=1.5,2,3,4 and 5). The filtered distribution attenuates the low amplitude events and amplifies the extreme events. Already for n=1.5 we observe that the impact scatter has

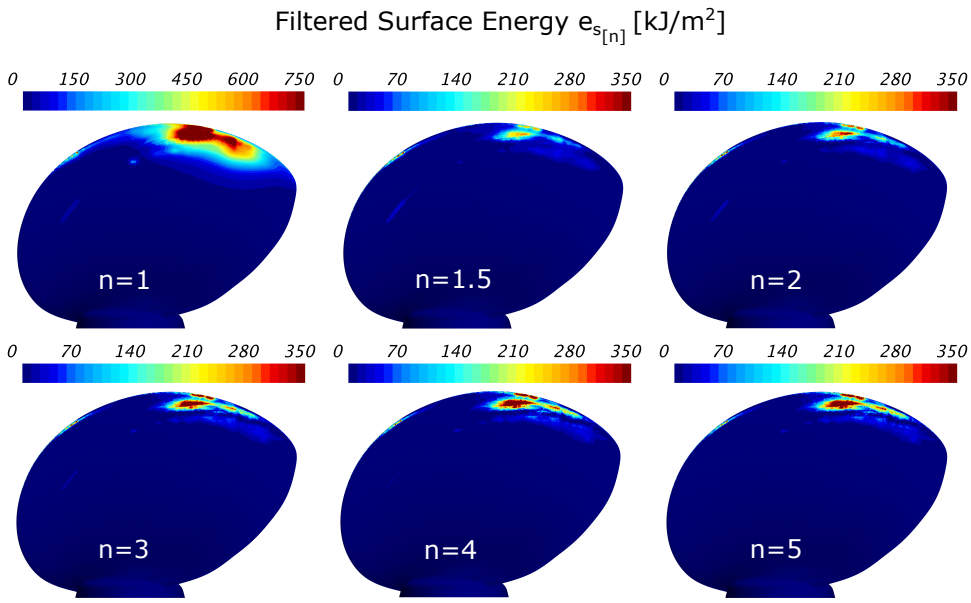

Figure 6.16: Filtered averaged surface impact distribution for different intensity exponents n, for Design 1, after 5 propeller revolutions

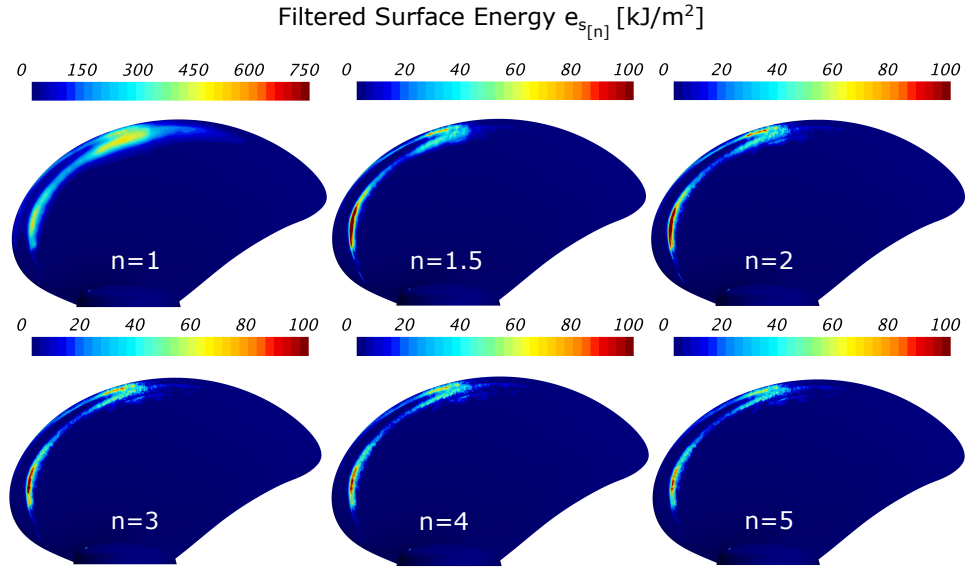

Figure 6.17: Filtered averaged surface impact distribution for different intensity exponents n, for Design 2, after 5 propeller revolutions

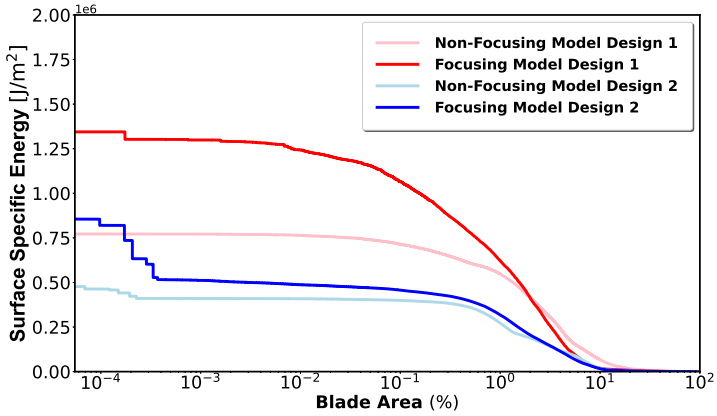

Figure 6.18: Surface specific energy over the blade area, showing the extent of the impacted blade area for each design, after five propeller revolutions, with and without energy focusing

increased compared to the unfiltered distribution (n=1). For large exponents (n>2) the filtered distribution looks very similar, without any significant change in the location of the extreme loads. That could mean that the high loads identified for large exponents, are much higher than the loads at other locations of the blade. The distribution obtained for large exponents, should give a better indication of the actual damage on the real blade, originated from these extreme events, although larger sample time (and revolutions) are needed for a statistical averaged solution, compared to the unfiltered distribution. Based on both the filtered and the unfiltered energy distribution, Design 1 indicates a very high risk for erosion at the identified locations, and from the filtered distribution it is illustrated that much higher impact loads occur on Design 1. The energy distribution on Design 2 identifies two main impact locations close to the leading edge, one at about 0.6R-0.75R, and one at 0.9R. From the unfiltered surface energy distribution (n=1) it is not clear which of the two locations has a higher erosion risk. On the other hand, the filtered surface energy distribution for high exponents identifies the impact at the lower radii to be of quite higher amplitude, and therefore indicating a higher risk of erosion in that region.

The surface specific energy over the percentage of the impacted area, confirms the conclusions of the analysis so far (see Fig. 6.18). The surface specific energy is higher when predicted with the focusing approach, compared to the one without energy focusing, for both designs. A similar percentage of blade area is impacted on each design (about 10%). However, design 1 exhibits 2-3 times higher implosion loads than design 2. The difference is smaller when no energy focusing is applied, indicating that energy focusing is essential for a fair comparison between the erosion risk of different designs (or even operating conditions). Consequently, the total accumulated surface energy, the blade impact distribution, and the surface specific energy plot indicate a higher erosion risk for Design 1, and based on the implosion load amplitudes, Design 1 should exhibit erosion damage quite quicker than Design 2, at the same operating condition.

Finally, we have compared the surface impact distribution obtained from the simula-

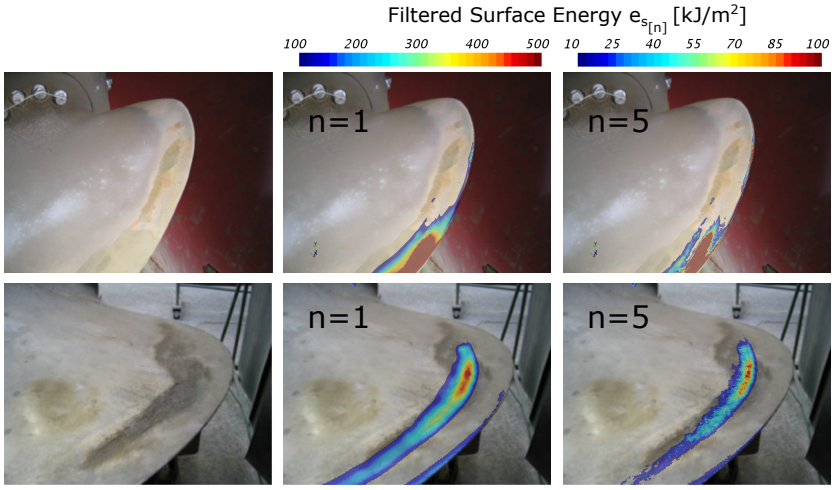

Figure 6.19: Comparison between the the simulated filtered surface energy and the actual damage on the real blade for Design 1 (top) and Design 2 (bottom). The filtered surface energy predicted with CFD is plotted on the snapshot of the real blade for two intensity components n=1 (unfiltered -total accumulated surface energy) and n=5.

tions to the actual damage on the real blades. Figure 6.19 presents snapshots of the blades of Design 1 and 2, where erosion damage is observed. Unfortunately, only a part of the blades is visible, but possibly only these parts suffered from erosion damage. The CFD solution has been plotted on the real blades for a fair and direct comparison. For a better illustration, only energy amplitudes above 100 KJ/m^2 and 10 KJ/m^2 are considered for the unfiltered (n=1) and filtered (n=5) surface specific energy distributions, respectively. It is important to note that the time after which the snapshots were taken is not known, and therefore the intensity of the damage is not representative. Based on the observations, and the simulations, for instance, Design 1 shows a higher risk, and more damage should be seen on the blades. However, the snapshot of Design 2 shows more severe erosion on the blade. Apparently, when the snapshot was taken, Design 2 was much longer in operation than Design 1. It has also been communicated by the owner that the blades of Design 1 were more frequently repaired, and the removed material was replaced by means of welding. Comparing the damage locations, the predicted impact distributions agree very well with some regions of the real damage on the blades. Especially on Design 2, where erosion takes place within a much smaller range of operating conditions than Design 1, the correlation between predictions and actual damage location is pretty good. Based on the unfiltered surface energy, a second location on the blade showed high accumulated energy, at higher radii and closer to the tip (see Fig. 6.15). Nevertheless, the filtered energy showed that the implosion events at lower radii are more extreme, and the erosion risk is much higher, agreeing well with the actual erosion on the real blade. Finally, the actual damage pattern on Design 1 is probably originated from a combination of conditions, since it exhibits pressure side cavitation over a longer range of operating conditions. A large area along the leading edge seems to be impacted from cavitation

erosion. Comparing the damage location with the predicted blade impact distribution, it agrees well with one region of the actual damaged area. However, no energy is predicted at lower radii, where material damage is detected on the real blade. Apparently, those locations have been impacted from operating at higher speeds and absorbed power, where a smaller amount of pressure side cavitation is present, and consequently higher impacts at lower radii are expected.

6.5. DISCUSSION AND CONCLUSIONS

From the analysis so far, in all test cases, energy focusing appears essential to have a quantitative high fidelity prediction of the cavitation implosion loads. Neglecting the energy focusing, usually leads to larger amounts of total accumulated energy on the blade surface, as well as lower amplitudes in critical areas of the blade. Due to the instantaneous energy radiation during any negative vapor volume change, energy is emitted at an earlier stage, way before the actual location of the final collapse, resulting in a wider and less intense energy distribution. Therefore, it is crucial for both the amplitude and the location of the implosion loads to always account for energy focusing, so that the overall as well as the instantaneous energy balance is always satisfied.

The erosive aggressiveness of the flow has been investigated by isolating extreme loads on the blade surface. For an intensity exponent n>2, the lower amplitudes are sufficiently attenuated, and the filtered energy distribution does not change for higher exponents. Very large values for the exponent n (n>5) may lead to precision errors due to excessive magnitudes of the amplified radiation terms. It is therefore recommended to always use exponent values between 2 and 5 (2<n<5) in order to filter low amplitude events from the surface impact distribution. Two main differences have been observed between the filtered an the unfiltered distribution. First, the filtered impacts are more scattered, since the extreme events are less frequent, but more pronounced. Second, the distribution looks slightly shifted towards the tip for both designs. Extreme events are more likely to occur at locations where the pressure has already recovered, such that the driving pressure is the largest. Therefore, by increasing n, the location of the impacts is tends to be correlated with locations of high driving pressures.

The erosion risk on Design 1 is clearly higher than the erosion risk on Design 2. First, the total accumulated energy on the blade during each propeller revolution is higher than for the second design. Furthermore, The surface impact distribution shows higher accumulated energy amplitudes at a distinct location for Design 1, and finally, a closer look at the surface specific energy indicates that Design 1 suffers from impact loads two orders of magnitude higher than the ones on Design 2. Nevertheless, the accumulated surface energy distribution on Design 2 is in better agreement with the actual erosion damage location on the real blade, than for Design 1. A possible explanation for this discrepancy is that Design 1 experiences erosion damage in a wider range of operating conditions than Design 2, while we only simulated the implosion loads for one operating condition. The erosion risk at low speed appears to be the highest, considering the larger vapor volume and the larger energy content within the collapsing cavities. This justifies also the fact that the damage location at this condition is predicted further downstream and at higher radii. At higher ship speeds, the amount of pressure side cavitation is considerably less, probably resulting in implosion loads closer to the leading edge and lower radii.

Therefore, the actual damage profile on the real blade of Design 1 is rather complicated to simulate exactly, as it should come from a combination of several conditions. However, the simulated damage location agrees well with one region of the actual damaged area on the real blade. On the other hand, Design 2 showed very little pressure side cavitation at high ship speeds, and based on the observations, only at low speed seemed to suffer from cavitation erosion. This explains why a very good agreement with the damage pattern is obtained, as the simulated operating condition is probably the one responsible for the erosion damage.

It should be noted that there is some uncertainty regarding the actual geometry of both sets of blades. It was reported that the blades of Design 1 have been repaired several times. During these repairs, the eroded areas have been ground out, and the areas on the blades where material has been removed, have been welded. Due to the erosion and the repairs, the leading edges of the blades have become much thinner and the chord of the blades has also been reduced. The thin and sharp leading edges may increase the amount of cavitation, and the severity of its dynamics. It is also not completely clear how often the blades of Design 2 have been repaired. It seems however, that they are closer to their original geometry (used in the simulations) than Design 1.

Finally, based on the results from this study, it is hypothesized that the proposed methodology, which accounts for energy focusing during the collapse, is able to capture the risk and location of cavitation erosion damage. The largest uncertainty in the actual damage is caused by the uncertainty of the operational profile and its consequences for risk and location of erosion damage.

REFERENCES

[1] C. S. Köksal, O. Usta, B. Aktas, M. Atlar, and E. Korkut, *Numerical prediction of cavitation erosion to investigate the effect of wake on marine propellers,* Ocean Engineering **239** (2021).

[2] G. Bark, J. Friesch, G. Kuiper, and J. Ligtelijn, *Cavitation erosion on ship propellers and rudders,* in *Proceedings of the* 9^{th} *Symposium on Practical Design of Ships and Other Floating Structures* (Luebeck-Travenmuende, Germany, 2004).

[3] D. Ponkratov and A. Caldas, *Prediction of cavitation erosion by detached eddy simulation (des) and its validation against model and ship scale results,* in *Proceedings of the* 4^{th} *International Symposium on Marine Propulsors* (Austin, Texas, USA, 2015).

[4] D. Ponkratov, *Des prediction of cavitation erosion and its validation for a ship scale propeller,* J. Phys. Conf. Ser. **656** (2015).

[5] A. Peters, U. Lantermann, and O. el Moctar, *Numerical prediction of cavitation erosion on a ship propeller in model- and full-scale,* Wear **408-409**, 1 (2018).

[6] F. G. Hammit, *Observations on cavitation damage in a flowing system,* J. Basic Eng **85**, 347 (1963).

[7] A. Vogel and W. Laterborn, *Acoustic transient generation by laser-produced cavitation bubbles near solid boundaries,* The Journal of the Acoustical Society of America **84**, 719 (1988).

[8] R. Fortes-Patella and J. L. Reboud, *A new approach to evaluate the cavitation erosion power,* Journal of Fluids Engineering **120**, 335 (1998).

[9] C. Flageul, R. Fortes-Patella, and A. Archer, *Cavitation erosion prediction by numerical simulations,* in *Proceedings of the* 14^{th} *International Symposium on Transport Phenomena and Dynamics of Rotating Machinery* (Honolulu, HI, USA, 2012).

[10] C. Leclercq, A. Archer, R. Fortes-Patella, and F. R. F. Cerru, *Numerical cavitation intensity on a hydrofoil for 3d homogeneous unsteady viscous flows,* Int. J. Fluid Mach. Syst. **10**, 254 (2017).

[11] R. Fortes-Patella, G. Challier, J. L. Reboud, and A. Archer, *Energy balance in cavitation erosion: From bubble collapse to indentation of material surface,* Journal of Fluids Engineering **135**, 011303 (2013).

[12] G. Bark, N. Berchiche, and M. Grekula, *Application of principles for observation and analysis of eroding cavitation, EROCAV observation handbook*, 3rd ed. (Department of Shipping and Marine Technology, Chalmers University of Technology, Sweden, 2004).

[13] S. Schenke, *Cavitation Implosion Loads from Energy Banalnce Considerations in Numerical Flow Simulations*, PhD Thesis, Delft University of Technology, Delft, The Netherlands (2020).

[14] T. Melissaris, S. Schenke, N. Bulten, and T. J. C. van Terwisga, *On the accuracy of predicting cavitation impact loads on marine propellers,* WEAR **456–457** (2020).

[15] T. Melissaris, S. Schenke, N. Bulten, and T. J. C. van Terwisga, *Cavitation erosion risk assessment on a full-scale steerable thruster,* Ocean Engineering **251** (2022).

[16] S. Muzaferija, M. Peric, P. Sames, and T. Schelin, *A two-fluid navier-stokes solver to simulate water entry,* in *Twenty-Second Symposium on Naval Hydrodynamics* (Washington, D.C, USA, 1998).

[17] B. P. Leonard, *The ultimate conservative difference scheme applied to unsteady one-dimensional advection,* Comput. Methods Appl. Mech. and Engng. **88**, 17 (1991).

[18] T. Waclawczyk and T. Koronowicz, *Modeling of the wave breaking with cicsam and hric high-resolution schemes,* in *European Conference on Computational Fluid Dynamics ECCOMAS CFD 2006* (Delft, The Netherlands, 2006).

[19] F. Menter, *Two-equation eddy-viscosity turbulence modeling for engineering applications,* AIAA Journal **32**, 1598 (1994).

[20] J.-L. Reboud and Y. Delannoy, *Two-phase flow modelling of unsteady cavitation,* in *Proceedings of the* 2^{nd} *International Symposium on Cavitation* (Tokyo, Japan, 1994).

[21] T. Melissaris, N. Bulten, and T. J. C. van Terwisga, *On the applicability of cavitation erosion risk models with a urans solver,* Journal of Fluids Engineering **141** (2019).

[22] G. H. Schnerr and J. Sauer, *Physical and numerical modeling of unsteady cavitation dynamics,* in *In Fourth International Conference on Multiphase Flow* (New Orleans, USA, 2001).

[23] M. Tinguely, D. Obreschkow, P. Kobel, N. Dorsaz, A. de Bosset, and M. Farhat, *Energy partition at the collapse of spherical cavitation bubbles,* Phys. Rev. E **86** (2013).

[24] Lord Rayleigh, *On the pressure development in a liquid during the collpapse of a spherical cavity,* Phil. Mag. **34**, 94 (1917).

[25] G. Vaz, T. Lloyds, and A. Gnanasundaram, *Improved modelling of sheet cavitation dynamics on delft twist11 hydrofoil,* in *Proceedings of VII International Conference on Computational Methods in Marine Engineering* (Nantes, France, 2017).

7

OUTLOOK

7.1. DISCUSSION OF THE RESEARCH FINDINGS

Quantitative prediction of the cavitation impact loads on mechanical components, already at an early design phase is key for optimizing their overall efficiency, as argued in the introduction. Since model tests are not able to provide such quantitative prediction, but solely a more qualitative assessment of the cavitation aggressiveness, it emphasizes the need for high fidelity numerical tools able to estimate the cavitation erosion risk in engineering applications. Thus, the main goal of this dissertation has been to apply an erosion model on full-scale marine propellers in behind condition using an Unsteady RANS incompressible solver to compute the implosion loads on the blade surface. The nature of incompressible solvers does not allow to resolve wave propagation due to the infinite speed of sound. Therefore, erosion models based on the prediction of peak pressures from the implosion of cavitating structures are not suitable, since the prediction of pressure amplitudes involve high uncertainties. However, kinematic quantities such as the shedding frequency and the cavity collapse time, can accurately be predicted with a pressure based RANS solver, and consequently, any erosion model based on the kinematics of the cavitating flow can be employed.

A novel erosion model based on the energy balance approach has been used to simulate the energy cascade during the collapse of large scale cavitating structures. During the collapse process, the potential energy initially contained in a cavity is continuously feeding into collapse induced kinetic energy. The distribution of the kinetic energy in the liquid is unknown, and therefore a model is employed that stores this energy at the cavity interface, until it is focused at the collapse center. At the final stage of the collapse, the energy stored at the collapse center is partitioned into acoustic, thermal and rebound energy. For relatively high driving pressures and by neglecting any non-condensible gas in the flow, the dissipative thermal energy and the rebound energy can be considered negligible (see Tinguely *et al.* [1]), so in the context of this study all the kinetic energy is converted into acoustic shock wave energy after the collapse.

High driving pressures also allow for the use of mass transfer models for the modeling of the phase transition from vapor to liquid. Mass transfer is modelled by the Schnerr-

Sauer cavitation model source term on the r.h.s of the vapor volume transport equation. Condensation and vaporization are controlled by the mass transfer coefficients $C_{c,SF}$ and $C_{v,SF}$, respectively. Relatively high values for the mass transfer coefficients are needed to ensure high steepness of the density-pressure trajectories ($C_{c,SF}$, $C_{v,SF} \geq 1$). However, very high values for the mass transfer coefficients may cause implications to the solution convergence, and therefore values of 1 or slightly higher are recommended.

To optimize the accuracy of the implosion load predictions, and to ensure energy conservation during the collapse process, special attention has been paid to four key aspects of the erosion model, the computation of the change in potential energy, the modeling of the conservative transport of the collapsed induced kinetic energy, the correct identification of the final collapse stages, and the correct projection of the radiated energy to the surrounding surfaces.

Cavitation erosion on marine propellers is a complex phenomenon. Material damage on the propeller blades depends on several factors, such as the frequency of the collapses, the transient temperature during the final stage of the collapse, and the radiated energy from the collapse mechanisms, as well as the static and dynamic pressure field distribution on the surface, the level of embrittlement of the material, the relative electropotential of the erosion site, the material mechanical properties, and the fracture modes. From the hydrodynamic side, however, energy conservation is the most important factor to achieve accurate quantitative predictions of the implosion loads, before we examine the material response. From a numerical point of view, energy conservation is achieved by first minimizing the iterative error, and then by accurately computing the change of potential energy. The iterative error can be controlled by a sufficient number of iterations during each time step, so that the vapor volume is adequately converged. On the other hand, the accurate prediction of the change in potential energy depends on the computation of the material derivative of the vapor volume, which is usually computed from the reconstructed velocity divergence, $\nabla \cdot \mathbf{u}$. In the present work, we have shown that the velocity divergence should be reconstructed from the the cavitation model source term, S_{α_v}, and not from the sum of the face fluxes given by $(\nabla \cdot \mathbf{u})_{center} = 1/V_{cell} \Sigma_f \mathbf{u}_f \cdot \mathbf{S}_f$. Even though both formulations should be equal by definition, the interpolation errors in the latter formulation seemed to be significant, especially in cases of high advective flow velocities. The higher the velocity the larger the error. Moreover, the interpolation error appears to be also influenced by the driving pressure, and for very large driving pressures the error should be low. However, since we mostly deal with driving pressure differences of around 1 bar, the error in most of the cases is likely to be significant.

The correct energy balance during the collapse involves the conversion of the potential energy into collapse induced kinetic energy, which is continuously being focused towards the collapse center. However, in complex flow simulations, the exact spatial distribution of the collapse induced kinetic energy is unknown, and therefore a model has been used for the conservative transport of the kinetic energy. Schenke [2] has shown that for an isolated bubble and for a collective collapse of a bubbly structure, the collapse induced kinetic energy distribution focuses towards the cavity interface. Therefore, the model assumes that all the kinetic energy is stored at the interface, and the transport of the kinetic energy is achieved by a destruction and a production term. Kinetic energy is destroyed right upstream from the interface, and the same amount of energy is absorbed

right into the interface at a rate proportional to the local potential energy reduction rate, so that an integral balance is achieved. Eventually, at the final stage of the collapse, all the potential energy has been converted into kinetic energy and, together with the interface, has been transported to the collapse center.

In order for the energy, focused at the collapse center, to be released, a criterion has been used, that identifies the final collapse stage. This criterion is based on the implication that pressure must be close to vapor pressure in the mixture regime, and that high amplitude pressure waves can only form in the liquid phase. That consideration, allows for the kinetic energy to be focused towards the collapse center, and at the moment of the collapse, where the volume cells are fully filled with liquid, and the pressure reaches (or surpasses) the ambient pressure, the energy can be released in the domain. Since the final collapse stage is not resolved, an entirely time accurate solution and the exact temporal distribution of the radiated energy cannot be expected from this method. Nevertheless, the energy focusing approach is supposed to provide an improved time accuracy of the acoustic power, in terms of a more realistic focusing of the impact towards the final collapse stage, while still satisfying the overall energy balance.

The correct projection of the energy to the surface is at least as important as the energy balance during the collapse. An error in the projected energy may disrupt the overall energy conservation in the system. The fraction of the radiated energy to impact the surface is computed using a fully continuous form of the solid angle. In unstructured meshes, the computation of the exact solid angle might be difficult to evaluate, since it may involve specific algebraic expressions. Therefore, an approximation of the solid angle has been used that depends only on the face area, its normal vector, and the distance vector between the face center and the radiation source. For sources very close to the surface, the approximated solid angle may lead to significant errors in the projected energy, and therefore the solid angle needs to be bounded to its maximum value in each case.

In the end, the erosion risk in cavitating flows can be assessed by several indicators. The total accumulated energy on the surface per cavity cycle gives a first indication of the amount of energy that is projected on the surface. The shedding frequency might also play a role in such cases, but for operating propellers the frequency is determined by the rotation rate. The exact surface impact distribution can show the location of the implosion loads. The areas with higher energy density show a much higher risk for erosion than areas with lower energy density. Using an intensity component, n, to amplify the surface impact power, can give additional information about the location of the extreme events. Even though the exact energy distribution in time is unknown, employing a statistical approach can identify extreme impact loads of lower frequency by filtering out implosion loads of higher frequency but lower amplitude. However, as we have seen in the thruster propeller case, both types of events may be responsible for erosion. Nevertheless, the material properties and response are still more than necessary to be able to compute the exact erosion rate in each case. Finally, the surface specific energy when plotted against the percentage of the impacted area indicates the maximum loads on the surface, as well as the extent of the impacted area. High energy density areas are definitely associated with higher erosion risk than areas of lower energy density.

7.2. SUMMARY OF THE MAIN FINDINGS

During the present work, we have used a novel erosion model for the prediction of the cavitation implosion loads using an incompressible URANS solver. The presented approach satisfies the energy balance during the collapse of cavitating structures, and it is energy conservative. The model has been verified and validated against a number of test cases. The main conclusions of this study are summarized as follows:

- Erosion models based on the overall integral energy balance can work well with incompressible Unsteady RANS. The kinematic parameters of collapsing cavities, such as the shedding frequency and the collapse time, as well as the vapor volume development and distribution of periodic cavitating flows can be reliably predicted. On the other hand, the most important limitation of pressure based incompressible solvers is the high uncertainty of the extreme pressure loads, which leads to unreliable estimations of the impact loads, and the fact that an infinite speed of sound is assumed does not allow for time accurate wave propagation. Therefore, erosion models based on the prediction of the peak pressures originated from the collapse of cavitating structures are not suitable for incompressible pressure based solvers.

- Non-equilibrium semi-empirical mass transfer models can give realistic predictions of the inertial dynamics of cavitating flows as long as the density-pressure trajectories obtained from the model are steep enough, such that the scale separation is physically satisfied. The steepness of the density-pressure trajectories is controlled by the evaporation and condensation coefficients of the cavitation model in use.

- Energy focusing during the collapse of a cavity is necessary for high accuracy predictions of the cavitation implosion loads. Neglecting the energy focusing often leads to larger amounts of surface accumulated energy. The instantaneous release of energy during each vapor volume variation results in radiated energy way before the final collapse stage, resulting in a wider energy distribution of lower amplitudes. When energy focusing is applied the instantaneous energy balance is satisfied, and acoustic energy is radiated at the final stage of the collapse, and therefore, a correct prediction of the location and the amplitude of the implosion loads is possible.

- Reconstructing the velocity divergence from the Schnerr-Sauer cavitation model source term showed the minimum error in the overall energy balance during the collapse, in StarCCM+. Using the cavitation rate to compute the change of potential energy allowed for high fidelity quantitative prediction of the radiated energy. The accuracy of the velocity divergence reconstruction may be solver and/or cavitation model dependent.

- When the fully continuous approximation of the solid angle is used due to difficulties in evaluating the exact topology of the surface cells, the approximated solid angle should be bounded to its maximum value, especially for sources very close to the surface, to avoid any significant errors in the surface energy projection.

- Results from the collapse of a single cavitation bubble showed that at least 20-25 cells per diameter, and a time step size that corresponds to at least 40 steps per

cavity collapse time are needed to obtain a grid and time step size independent solution. For a propeller, the bubble diameter is translated to the maximum width of the smallest dimension of the sheet cavity over one full revolution. Then, the collapse time can be estimated from the Rayleigh–Plesset collapse time of a spherical cavity with diameter equal to the maximum width of the sheet cavity on the blade.

- The presented erosion model, shows good potential for engineering applications and design optimization based on erosion risk analysis, and could possibly replace model scale cavitation observations in towing tanks in the future. The model satisfies the overall and the instantaneous energy balance during a cavity collapse, and it can provide quantitative predictions of the implosion loads, as well as different erosion risk levels, depending on the design or the operating condition.

7.3. OUTLOOK

The most important aspects that need further development are addressed here. The erosion model used in this study needs to be coupled to material response models. Even though quantitative predictions of the implosion loads are possible in discrete time increments, the actual erosion rate cannot be identified without information about the material properties and material response. Coupling the presented erosion model with material models could eventually lead to actual damage rates. Moreover, only design (smooth) surfaces have been considered in this study. Nevertheless, erosion damage on propellers often starts with a surface deterioration or roughening, followed by a plastic deformation of the blade, (known as orange peeling stage [3]). Such deformations on the blade surface can influence cavitation inception and cavitation dynamics, leading to different excitations compared to a smooth surface. Such deformation and roughness effects should be considered for an improved prediction of the excitation forces, as well as the material response.

The collapse driving pressure is the quantity that introduces the largest uncertainty in the erosion model. The reason is that the pressure field driving the collapse in complex flows is non-uniform and unsteady, rendering the computation of the exact driving pressure field difficult. In this study, we have shown that the moving average of the instantaneous pressure over a sufficient time window, can give a good impression of the pressure that the collapsing cavities experience on a statistical average. The size of the moving window should be at least equal to one cavity cycle. Even though this approach seems to capture most of the spatial and temporal effects as well as the effect of pressure recovery, a more detailed model with a more physical foundation would be desired.

In every test case of this dissertation, the presence of non-condensible gas in the flow has been neglected. The potential energy initially contained in the collapsing cavities has been fully converted into acoustic energy after the collapse, omitting any vapor generation from cavity rebounds. Nevertheless, in many occasions, and especially for smaller scales and low driving pressure differences, rebound energy may play a role in the overall energy balance during cavity collapse. Tinguely *et al.* [1] have investigated the rebound energy in relation to the non-condensible gas content within the cavity. High content in non-condensible gas means an increase of the rebound energy after the collapse, and therefore a decrease in the acoustic radiated energy. Fortes-Patella *et al.* [4] have also

studied the influence of gas content within the cavity in collapse efficiency, highlighting that it can play an important role in bubble dynamics. Therefore, it is recommended to include the effect of the gas content in the cavities on the overall energy balance, and thereby the increase in rebound energy after the collapse.

The implosion loads predicted from the presented erosion model are not time accurate. The exact energy distribution from the radiation sources is unknown, and only the energy content across the spherical wave front can be controlled. Also, since the solver is incompressible, the wave propagation speed is assumed infinite. Since the propagation of the wave front cannot be resolved, an additional modeling is needed to make the computed impact loads more accurate in time. With a modeling assumption about the wave passage time and an energy density distribution function across the wave front, the energy radiation could be computed in a more time accurate manner, rather than in discrete events, as happens in the present form [2].

The accuracy of the wakefield, and the propeller inflow, play an important role on the developed cavity dynamics on the blades. In this study the k-omega SST turbulence model has been used in the simulations, however, it is known that it does not provide the best prediction for the propeller wakefield. Reynolds stress models, for instance, are able to provide anisotropic turbulence predictions leading to more accurate estimation of the velocity fluctuations in space and time. Even though computationally less efficient, using the erosion model together with a more advanced turbulence model for the Reynolds Stresses, so that the inflow towards the propeller is captured more accurately, would be desirable.

REFERENCES

[1] M. Tinguely, D. Obreschkow, P. Kobel, N. Dorsaz, A. de Bosset, and M. Farhat, *Energy partition at the collapse of spherical cavitation bubbles,* Phys. Rev. E **86** (2013).

[2] S. Schenke, *Cavitation Implosion Loads from Energy Banalnce Considerations in Numerical Flow Simulations*, PhD Thesis, Delft University of Technology, Delft, The Netherlands (2020).

[3] J. Carlton, *Marine Propellers and Propulsion* (Butterworth-Heinemann, Kidlington, Oxford, 2019).

[4] R. Fortes-Patella, G. Challier, J. L. Reboud, and A. Archer, *Energy balance in cavitation erosion: From bubble collapse to indentation of material surface,* Journal of Fluids Engineering **135**, 011303 (2013).

ACKNOWLEDGEMENTS

I would like to thank Norbert Bulten for giving me the opportunity to start this journey of research in cavitation erosion by appointing me to this PhD position in Wärtsilä Netherlands. I highly appreciate it and thank you for all your help and guidance during this journey and especially during the first years. Your knowledge and passion in hydrodynamics and computational fluid dynamics gave me an extra push to always put some extra effort in my work and research, and gave me the opportunity to tackle problems from both scientific and commercial perspective. A big thank you also to Elias Boletis for giving me the first opportunity to join Wärtsilä Netherlands for my internship, and to my first supervisor Edgar Snelders.

I would also like to express my great gratitude to my promotor Tom van Terwisga. I am so grateful that we crossed each other's paths and I had the opportunity to work with you during all these years. I highly appreciate your guidance and all our discussions with you and Sören, trying to give our best to understand cavitation dynamics, but also discuss about life and personal well being. You have this magic skill to make work and research fun, but at the same time you make people around you thrive and excel. I made quite some progress with myself both personally and professionally since the beginning of this journey, and you played a big part in this. I would like to thank also Christian, my second promotor. Even though we did not spend too much time talking about research, I am glad we met during the CaFE project and I am very grateful for your feedback and remarks on my thesis.

I cannot express how grateful I am for my PhD-coworker and friend Sören Schenke. I am more than glad that we had the opportunity to work together, and I cannot thank you enough for all the knowledge and wisdom I gained from spending time with you. Without your unconditional help and assistance all these years I would not be the person and professional I am today. Your deep knowledge in physics, mathematics and fluid dynamics together with the long discussions we had gave always a different perspective on the problems we encountered and helped to find the best possible solutions. Thank you for everything you have done for me and all the good times we had during this period.

Special thank you to Manolis Gavaises and Amalia Petrova for organizing and managing the European ITN program CaFE. Thank you to all the supervisors and partners in the project for sharing your knowledge and for your continuous feedback to our research. Thank you Norbert and Petra for joining and accompanying me in the meetings. I would also like to thank all the ESR's, Daria, Prasanta, Shrey, Nikolaos, Magda, Stathis, Saad, Polina, Ebrahim, Mohammad, Akis, Sören, Max, Marco, Mithun, Ali, for all the nice meetings, nice discussions, nice excursions we had, and the nice trips with some of you. Special thanks to Marco and Max for teaching me how to ski. In general, this project was more than I could ever imagine. Thanks to these kind of projects, researchers can combine work with meeting people from all over the worlds and having fun. I hope European Union keep funding such projects that promote innovation, development, collaboration,

industrialization, sustainability, and multicultural activities.

A very big thank you to all my coworker at Wärtsilä, and especially my managers during all these years Norbert, Petra, and Iulia. Thank you Igor, Koen, Marc, Maarten, Bert, Ian, Robert, Stephan, Marilyne, Jannicke, Navneet, Joost. Thank you for all the discussions and all the help and support all these years. I would like to express my great gratitude to Maarten Bijlard, who has helped me a lot with the erosion model, and especially with post-processing and scripting. Your help is very much appreciated. Also, thank you Robert Goeijers for helping with the set-up of the single bubble collapse during your internship.

Also a big thank you to my dear colleagues at the university and the Ship Hydromechanics department or the Fluid Mechanics lab, Marco, Bart, Nikos, Maarten, Sören, Saad, Xiaobo, Lina, Gem, Jun, Cinq, Pranav, Swaraj, Tom. Thank you for all the great times, and all the dinners, activities and trips we had together. It was nice to feel a bit like a student again.

Furthermore, I would like to thank all my friends for being there for me. First, my beloved friends, and roommates for most of the time, Ammar and Mohannad. Living with you was a great experience, and especially during the COVID-19 lockdowns you kept me motivated and happy by spending time together and having fun. My friends in the Netherlands that I spent fruitful time with them these 7 years, Jürgen, Sebastiaan, Sam, Emiliano, Eefke, Stan, Sterre, Luc, Sandra, Jannina, Joël, Max, Katharina, Nikos, Jessie, Dora, Julian, Jullie, Konstantinos, Alexandra, Stavros, Giota, Navneet, Lara, Musse, Isotta, Nikos, Semina, Marco, Wenhua, Bart, Tasos, Vasia. Also, my friends from Greece, Kostas, Giannis, Pantelis, Marios, Panos, Marios, Spyros, Alex, Dominique, Efi, Sissy, Georgia, Iwanna, Eleni, Panos, Angelos, Rania, Dimitra, Angeliki, Kostas. Thank you all for making my free time more valuable, and thank you for all the vacation time we spent together. Letting some steam off every now an then was very crucial and important in this long journey. So, your contribution was very valuable.

Last, but not least, I would like to thank my family, who have been very supportive since the beginning. My dad, Giannis, who also helped me with stregthening my knowledge in hydrodynamics, my mom Dimitra, my sister Dora, my grandmother Mary, and all the rest of my family. Thank you deeply from the bottom of my heart for providing me the opportunity to first study marine engineering, fall in love with hydrodynamics, and further travel to the Netherlands and make one of my dreams come true.

CURRICULUM VITÆ

Themistoklis MELISSARIS

05-11-1992 Born in Athens, Greece.

WORK EXPERIENCE

2015–Present CFD Expert, Hydrodynamics
Department of Propulsion Technology
Wärtsilä Netherlands BV
Drunen, the Netherlands

2015 Erasmus+ Internship
Department of R&D Validation and Industrialization
Wärtsilä Netherlands BV
Drunen, the Netherlands

EDUCATION

2015–2022 PhD Research
Department of Propulsion Technology
Wärtsilä Netherlands BV
Drunen, the Netherlands
Department of Ship Hydromechanics and Structures
Delft University of Technology
Delft, the Netherlands

2010–2015 B.Sc & M.Sc. (Engineering Diploma) in Naval Architecture and Marine Engineering
National Technical University of Athens
Athens, Greece

AWARDS

2018 First Prize in Shipathon 2018 in future of smart and autonomous shipping

2015 Limmat Stiftung Award for graduating top 3 in the calendar year 2015

2011 First Prize in Electro-science Project Competition
by Institute of Marine Engineering, Science & Technology(IMAREST)

List of Publications

Themistoklis Melissaris

6. **T. Melissaris, S. Schenke, and T.J.C. van Terwisga**, *Cavitation erosion risk assessment for a marine propeller behind a RO-RO container vessel*, submitted to special topic in Physics of Fluids on "Cavitation" (2022).

5. **T. Melissaris, S. Schenke, N. Bulten, and T.J.C. van Terwisga**, *Cavitation erosion risk assessment on a full-scale steerable thruster*, Ocean Engineering **251**, 111019 (2022).

4. **T.J.C. van Terwisga, M. van Rijsbergen, E. van Wijngaarden, J. Bosschers, S. Schenke, and T. Melissaris**, *Cavitation Nuisance in Ship Propulsion: A Review of Developments*, in Cavitation and Bubble Dynamics, edited by P. Koukouvinis, and M. Gavaises, Academic Press (2021), pp. 73-109.

3. **T. Melissaris, S. Schenke, N. Bulten, and T.J.C. van Terwisga**, *On the accuracy of predicting cavitation impact loads on marine propellers*, WEAR **456–457**, 203393 (2020).

2. **S. Schenke, T. Melissaris, and T.J.C. van Terwisga**, *On the relevance of Kinematics for Cavitation Implosion Loads*, Physics of Fluids **31**(5), 052102 (2019).

1. **T. Melissaris, N. Bulten, and T.J.C. van Terwisga**, *On the Applicability of Cavitation Erosion Risk Models with a URANS Solver*, Journal of Fluids Engineering **141**(10), 101104 (2019).